



Trinity College Dublin
Coláiste na Tríonóide, Baile Átha Cliath
The University of Dublin

Computational Modelling and Design of Cathode Materials for Sustainable Energy Applications

by

Eric Mates-Torres

under the supervision of

Prof. Max García-Melchor

A thesis submitted in partial fulfilment
of the requirements for the degree of

Doctor in Philosophy

at the

University of Dublin, Trinity College

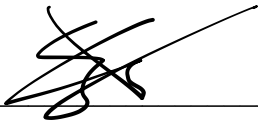
2022

Declaration of Authorship

I declare that this thesis has not been submitted as an exercise for a degree at this or any other university and it is entirely my own work.

I agree to deposit this thesis in the University's open access institutional repository or allow the Library to do so on my behalf, subject to Irish Copyright Legislation and Trinity College Library conditions of use and acknowledgement.

I consent to the examiner retaining a copy of the thesis beyond the examining period, should they so wish (EU GDPR May 2018).



Eric Mates-Torres

10 June 2022

Trinity College, The University of Dublin

Summary

If humanity strives to build a greener future, technologies to store renewably-generated energy and replace current polluting industrial processes are urgently needed. Over the past years, advances in photocatalytic and electrocatalytic systems have paved the way for using light and electricity to achieve this purpose through solar- and power-to-X applications, respectively. Particularly, Earth-abundant heterogeneous catalysts have shown great promise as cathode materials for sustainable energy applications, such as fuel cells or decarbonisation technologies; however, suitable Earth-abundant catalysts that rival precious metal-based approaches are yet to be found. Furthermore, the effects governing most key reactions involved in these processes are still under intense debate. Thus, this thesis aims at unravelling, by computational means, the activities and selectivities of three state-of-the-art materials used as catalysts for energy conversion, CO₂ utilisation and for the electrification of polluting industrial processes. In the following, the key concepts and main results obtained for each investigated catalytic system are summarised.

Firstly, we analysed the influence of N-dopants in the selectivity of a C-based electrode for the oxygen reduction reaction (ORR), which is the bottleneck process for the development of efficient fuel cells. Although high activities have been reported on similar systems, the effects driving the selectivity towards the 2-electron or the 4-electron products (hydrogen peroxide and water, respectively) and the nature of the active site are still poorly understood. Specifically, experiments performed by our collaborators in the group of Prof. Colavita in Trinity College Dublin revealed that amorphous C electrodes predominantly containing either graphitic or pyridinic N dopants were highly selective towards production of peroxide in alkaline media; in contrast, electrodes with a mixed composition of both N dopants displayed lower currents, which were attributed to higher selectivities towards the 4-electron oxygen reduction. Spurred by these results, we carried out a reactivity study of a proposed mechanism on three graphene cluster models containing only N_G (2N_G-Gr), only N_P (2N_P-Gr) or both N_G and N_P dopants (N_GN_P-Gr). This analysis revealed highly endergonic adsorptions of the HOO^{*-} and HOO* intermediates on 2N_G-Gr and 2N_P-Gr, respectively, which in both cases was predicted to hinder the selectivity. Interestingly, the predominant pathway on the N_GN_P-Gr model displayed an optimal energetic distribution of the reaction intermediates, which supported the higher selectivity and onset potential towards the 4-electron product observed in experiments. These results highlight the importance of a mixed N_G/N_P dopant composition to cooperatively enhance the selectivity and activity of C-based electrodes for the ORR.

Next, the influence of organic capping ligands for the photocatalytic activation of CO₂ and concomitant reduction (CO₂RR) to CO on ZnSe quantum dots (QDs) was investigated, in collaboration with the experimental group of Prof. Reisner from the University of Cambridge. In their studies, ZnSe QDs capped with imidazolium-based ligands were found to promote higher activities for CO formation compared to the bare

ZnSe QD. To rationalise these results, we conducted a computational investigation aimed at elucidating a proposed reaction mechanism facilitated by MEMI ligands. Our results showed that MEMI is able to stabilise the CO_2^{*-} intermediate in the presence of a photogenerated electron, which was determined to be the most endergonic step in the reaction pathway. Furthermore, simulations showed that this key stabilisation is owing to a set of attractive non-covalent interactions (NCIs) between the imidazolium ring and the O atoms of the adsorbed CO_2 , in line with previous theoretical studies. Encouraged by these results, we assessed the ability of dithiol ligands of different lengths to promote CO_2RR to CO on ZnSe QDs in the absence and presence of a Ni-based molecular co-catalyst. On the one hand, we found that ZnSe QDs capped with shorter dithiols are able to facilitate a surface-promoted mechanism, which explained the high CO yields observed by our collaborators. However, our simulations showed that these ligands fail at stabilising the reaction intermediates in the presence of the molecular co-catalyst due to their inability to reach the second coordination sphere of the adsorbed intermediates. On the other hand, we predicted that longer dithiols are able to stabilise intermediates adsorbed on the molecular co-catalyst through attractive NCIs, but their ability to facilitate a surface-promoted mechanism is sterically hindered, in line with experiments. Hence, these results provide a crucial insight for the development of novel ligand-based approaches for the light-driven CO_2 reduction using QDs.

Finally, the knowledge that novel 2-D carbides and nitrides (MXenes) can be terminated by electron-rich H coverages at relatively low negative potentials prompted us to study these materials as catalysts for the electrochemical hydrogenation (ECH) of terminal alkynes. To identify the most suitable MXene structures for this reaction, we conducted a thorough analysis of the surface coverage of all the MXenes with out-of-plane ordering synthesized to date under electrochemical conditions and in aqueous electrolyte. This analysis revealed that Ti, V and especially Mo-based MXenes display broad ranges of applied potentials at which H coverages are predominant and hold relatively good thermodynamical stabilities. Therefore, we then investigated the competence of H-terminated Ti_3C_2 MXenes for the coverage-mediated ECH of pentynol by elucidating a proposed Heyrovsky-type mechanism. Our calculations showed that pentynol is able to abstract terminal H atoms (which are negatively charged and behave as hydrides) in an asynchronous concerted transfer to produce pentenol and, subsequently, pentanol. Both hydrogenations were found to be characterised by transition state structures with low activation barriers. Our prediction was subsequently validated experimentally by our collaborators in the group of Prof. Colavita, who showed that Ti_3C_2 was active towards the ECH of pentynol. Interestingly, experiments yielded high selectivities towards the semi-hydrogenation product; further simulations are ongoing to untangle these results. In light of the activity of this MXene towards ECH, we then assessed the ability of Mo_2C , Mo_3C_2 , V_2C , V_3C_2 and Ti_3C_2 to hydrogenate acetylene via a similar mechanism. Interestingly, we showed that the semi-hydrogenation of acetylene to ethylene is achievable at low negative applied potentials through an asynchronous concerted H transfer governed by the coverage. Hence, this paves the way for the use of a broad range of MXenes as catalysts for the ECH of terminal alkynes, a green alternative to current industrial processes which does not require high temperatures or high H_2 pressures.

Abstract

Unravelling the activity and selectivity of novel heterogeneous catalysts requires a deep understanding of the effects unfolding at the catalytic surface. Particularly, this thesis emphasises the relevance of dopant distribution, ligand phase composition and surface coverage under electrochemical conditions for the theoretical study—supported by experiments—of photocatalytic and electrocatalytic systems for sustainable energy applications. To shed some light on the nature of these effects, three state-of-the-art electrocatalysts and their use for relevant reduction reactions were analysed computationally. Firstly, the role of N-dopants on the activity of metal-free C-based electrodes towards the oxygen reduction reaction were unveiled; next, we assessed the nature of the interactions driving photocatalytic CO₂ activation and reduction on ZnSe quantum dots capped with organic ligands. Finally, the surface coverage of novel 2-D carbides (MXenes) under electrochemical conditions was thoroughly investigated, serving as groundwork for the rational design of cost-effective cathode materials for the electrosynthesis of valuable chemical feedstocks.

Acknowledgements

First and foremost, I would like to start by thanking my supervisor, Prof. Max García-Melchor. While cleaning the shelves of our then newly inaugurated office, I remember him saying: “*By the time you finish your thesis, this room will be filled with people!*”—and he couldn’t have been more right. It has been an honour to see how, with your guidance, the CCEM group has grown from just us two to a diverse and inspiring team of researchers: Marconi, Arantxa, Alex, Ximo, Kevin, Michael, Anna, Manting and everyone that has been part of our extended family, specially Meriç and María; this wouldn’t have been possible without you. Also, I need to thank everyone that has led me to this path, especially Prof. Agustí Lledós, Prof. Jean-Didier Maréchal and everyone in the Universitat Autònoma de Barcelona. You taught me to love computational chemistry as much as you do.

I also want to thank everyone that has made my research possible, including the School of Chemistry and the Commercial Revenue Unit of Trinity College Dublin for funding my Ussher Postgraduate Scholarship, and the Royal Society of Chemistry for supporting me and allowing me to disseminate my research abroad. Also, I need to sincerely thank the Irish Centre for High End Computing for the technical support and provision of resources in the Fionn and Kay supercomputers, the Trinity Centre for High Performance Computing for allowing me to calculate in Dalton and Kelvin, and the IT4Innovations National Supercomputing Center of the Technical University of Ostrava for supplying computational time in Salomon and Karolina.

Last but not least, I want to thank my parents and my brother for the support and for believing in me. And most of all, I want to thank Sílvia: it has been the hardest, yet most fulfilling experience of my life, and it wouldn’t have been possible without you. I can’t wait to read the next chapter in our adventure.

Publications

Publications related to the contents of this thesis

- [1] Behan, J. A.‡; Mates-Torres, E.‡; Stamatini, S. N.; Domínguez, C.; Iannaci, A.; Fleischer, K.; Hoque, M. K.; Perova, T. S.; García-Melchor, M.; Colavita, P. E. *Small*, **2019**, *15*, 1902081.
- [2] Sahm, C. D.; Mates-Torres, E.; Eliasson, N.; Sokołowski, K.; Wagner, A.; Dalle, K. E.; Huang, Z.; Scherman, O. A.; Hammarström, L.; García-Melchor, M.; Reisner, E. *Chem. Sci.* **2021**, *12*, 9078-9087.
- [3] Sahm, C. D.; Ciotti, A.‡; Mates-Torres, E.‡; Sokołowski, K.; Neri, G.; Cowan, A. J.; García-Melchor, M.; Reisner, E. *Chem. Sci.* **2022**, *13*, 5988-5998.

Other publications

- [4] Craig, M. J.; Coulter, G.; Dolan, E.; Soriano-López, J.; Mates-Torres, E.; Schmitt, W.; García-Melchor, M. *Nat. Commun.* **2019**, *10*, 4993.
- [5] Kuznetsova, V. A.‡; Mates-Torres, E.‡; Prochukhan, N.; Marcastel, M.; Purcell-Milton, F.; O'Brien, J.; Visheratina, A. K.; Martínez-Carmona, M.; Gromova, Y.; García-Melchor, M.; Gun'ko, Y. K. *ACS Nano*, **2019**, *13*, 13560–13572.
- [6] Kehoe, D.; Mates-Torres, E.; Samokhvalov, P.; García-Melchor, M.; Gun'ko, Y. K. *J. Phys. Chem. C*, **2021**, *126*, 434–443.

Table of Contents

Declaration of Authorship	i
Summary	iv
Abstract	vi
Acknowledgements	vii
Publications	ix
List of Abbreviations	xiv
1. Introduction	1
1.1. Fundamentals of catalysis	1
1.1.1. Types of catalysis	4
1.1.2. Reactivity of heterogeneous catalysts.....	6
1.2. Electrocatalysis.....	8
1.2.1. Proton-coupled electron transfer	11
1.2.2. Photoredox catalysis	12
1.3. (Photo)(electro)catalysis for solar- and power-to-X conversion	13
1.3.1. Hydrogen evolution.....	14
1.3.2. Oxygen reduction reaction	15
1.3.3. CO ₂ reduction reaction.....	18
1.3.4. Electrosynthesis of commodity chemicals	20
2. Computational Methods	25
2.1. Uncovering the wavefunction.....	25
2.1.1. The Schrödinger equation.....	25
2.1.2. The Born–Oppenheimer approximation and the Hartree model.....	26
2.1.2.1. Polyelectronic systems in the Hartree model.....	27
2.1.3. Linear combination of atomic orbitals	30
2.2. Density functional theory	31
2.2.1. The Hohenberg–Kohn theorems	32
2.2.2. Kohn–Sham density functional theory.....	32
2.2.3. Exchange-correlation functionals	34
2.2.3.1. Local spin density approximation	34
2.2.3.2. Generalized gradient approximation.....	35
2.2.3.3. Limitations of GGA	36
2.2.3.4. Hybrid functionals	37
2.3. Description of solid state systems.....	38
2.3.1. The Bravais lattice	39

2.3.2.	The reciprocal space.....	41
2.3.3.	Periodic boundary conditions and Bloch's theorem	43
2.3.4.	Electronic band structure	45
2.4.	Basis sets	46
2.4.1.	Localised basis sets	46
2.4.2.	Plane wave basis sets	47
2.5.	Dispersion effects	48
2.6.	Simulation of the solvent.....	50
2.6.1.	The electrochemical water layer	50
2.6.2.	The universal solvation model	52
2.7.	Gibbs energy corrections.....	53
2.7.1.	Modelling of electrochemical reactions	55
2.7.2.	Calculation of the coverage in an aqueous electrolyte	56
2.8.	The potential energy surface	58
2.8.1.	Location of transition states in heterogeneous systems	59
2.9.	Structural optimisation and characterisation of solids	61
2.9.1.	The Birch–Murnaghan equation of state	61
2.9.2.	Generation of surface slabs	62
2.9.3.	Wulff constructions	63
2.9.4.	Analytical identification of surface sites.....	64
3.	Objectives	67
3.1.	N-doped Carbon Electrocatalysts for the Oxygen Reduction Reaction	67
3.2.	CO ₂ Photoreduction on Ligand-modified ZnSe Quantum Dots	68
3.3.	Coverage-led Design of MXenes for Electrocatalysis	68
3.4.	2-D MXenes for Electrochemical Hydrogenations.....	69
4.	N-doped Carbon Electrocatalysts for the Oxygen Reduction Reaction	71
4.1.	Introduction	72
4.2.	Experimental results	74
4.3.	Computational details	75
4.4.	N-doped carbon electrode surface model.....	76
4.5.	Assessing ORR activity.....	79
4.5.1.	Activity of 2N _G -Gr	81
4.5.2.	Activity of 2N _P -Gr	81
4.5.3.	Activity of N _G N _P -Gr.....	84
4.5.4.	Comparison of the ORR activity.....	85
4.6.	Assessing ORR selectivity	89
4.7.	Conclusions	90
5.	CO₂ Photoreduction on Ligand-modified ZnSe Quantum Dots	93
5.1.	Introduction	94
5.2.	Experimental results	96
5.3.	Computational details	101
5.4.	Modelling of ligand-functionalised ZnSe QDs	103

5.4.1.	ZnSe QD surfaces	103
5.4.2.	Ligand coverages.....	104
5.5.	Reactivity studies	107
5.5.1.	HER reactivity	107
5.5.2.	CO ₂ RR reactivity	108
5.6.	Ligand effects on CO ₂ RR selectivity	111
5.6.1.	Tailoring ligand-functionalised hybrid ZnSe QDs as CO ₂ reduction photocatalysts .	112
5.7.	Conclusions.....	116
6.	Coverage-led Design of MXenes for Electrocatalysis	119
6.1.	Introduction.....	120
6.2.	Computational details.....	123
6.3.	Coverage analysis of MXenes	125
6.4.	Relative stability of MXenes	128
6.5.	Electron conductivity of functionalized MXenes.....	132
6.6.	Coverage-dependent hydrogen evolution.....	134
6.6.1.	Kinetic and mechanistic study.....	135
6.6.2.	Basal plane <i>vs.</i> edge reactivity.....	139
6.6.3.	Coverage-driven HER at low overpotentials	140
6.7.	Conclusions.....	141
7.	2-D MXenes for Electrochemical Hydrogenations.....	145
7.1.	Introduction.....	146
7.1.1.	Rational design of electrochemical hydrogenation catalysts	147
7.2.	Computational methods	147
7.3.	Electrochemical hydrogenation of unsaturated alcohols	148
7.4.	Electrochemical hydrogenation of acetylene	152
7.4.1.	Semi-hydrogenation of acetylene	152
7.4.2.	Assessment of the selectivity	153
7.5.	Charge density difference analysis.....	154
7.6.	MXene stoichiometry and metal-dependence of acetylene hydrogenation	155
7.7.	Conclusions.....	159
8.	General Conclusions and Future Work	163
8.1.	Conclusions.....	163
8.2.	Future work.....	164
References		166
Appendix		175
Band diagrams of bare and covered <i>o</i> -MXenes.....		176

List of Abbreviations

AA	Ascorbic acid	PAW	Projector-augmented wave
BCC	Body-centred cubic	PCET	Proton-coupled electron transfer
BZ	Brillouin zone	PEM	Polymer electrolyte membrane
CB	Conduction band	PES	Potential energy surface
CG	Contracted Gaussian	PLS	Potential limiting step
CHE	Computational hydrogen electrode	PT	Proton transfer
CI-NEB	Climbing image - nudged elastic band	QD	Quantum dot
CO₂RR	CO ₂ reduction reaction	RDS	Rate determining step
DFT	Density functional theory	RHE	Reference hydrogen electrode
ECH	Electrochemical hydrogenation	RRDE	Rotating ring disk electrode
EOS	Equation of state	SA	Sacrificial [electron] acceptor
ET	Electron transfer	SC	Simple cubic
FCC	Face-centred cubic	SCF	Self-consistent field
GGA	Generalised gradient approximation	SD	Sacrificial [electron] donor
GHG	Greenhouse gas	SHE	Standard hydrogen electrode
GTO	Gaussian type orbitals	SIE	Self-interaction error
HCP	Hexagonal close packed	SMD	Solvation model based on the density
HER	Hydrogen evolution reaction	SP	Saddle point
HF	Hartree–Fock	SR	Short range
HOR	Hydrogen oxidation reaction	TCS	Three-component system
IHP	Inner Helmholtz plane	TOF	Turn-over frequency
IL	Ionic liquid	TON	Turn-over number
LCAO	Linear combination of atomic orbitals	TS	Transition state
L(S)DA	Local (spin) density approximation	TST	Transition state theory
LR	Long range	UEG	Uniform electron gas
MEP	Minimum energy path	UHF	Unrestricted Hartree–Fock
ML	Monolayer	VB	Valence band
NCI	Non-covalent interaction	WNA	Water nucleophilic attack
OER	Oxygen evolution reaction	XPS	X-ray photoelectron spectra
OHP	Outer Helmholtz plane	XRD	X-ray diffraction
ORR	Oxygen reduction reaction	ZPE	Zero-point energy

“ But censure is perhaps inevitable; for some are so ignorant, [...] and are chilled with horror at the sight of any thing, that bears the semblance of learning, [...] and should the spectre appear in the shape of a woman, the pangs, which they suffer, are truly abysmal. – Elizabeth Fulhame

Prologue to “An Essay on Combustion, with a view to a new art of dying and painting”, 1794

CHAPTER

1

Introduction

1.1. Fundamentals of catalysis

To grasp the importance of catalysis, one must understand the origin of life itself. From the findings of potentially biogenic ^{13}C -depleted graphite in sedimentary rocks,¹ it is believed that early life may have arisen on our planet around 4 billion years ago, at the beginning of the Archean Eon—the second geological age of the Earth. Despite the exact nature of the processes that yielded microbiological life are still under debate, most of the theories coincide in one key element: the presence of nitrogen. This is an essential constituent of nucleotides and amino acids, the building blocks from which life stemmed in the RNA world hypothesis² and the main component of protein structures in more developed life forms. Nitrogen in these compounds is found reacting with other atoms in its active form, which early life obtained from various sources of nitrogenated compounds in the atmosphere, such as nitrogen oxides (NO_x) or ammonia (NH_3). The majority of the nitrogen in the atmosphere, however, exists in its stable and unreactive diatomic form, N_2 ; the triple $\text{N}\equiv\text{N}$ bond in this molecule is one of the strongest atomic interactions in nature, with a bond dissociation energy of $941.69 \pm 0.04 \text{ kJ mol}^{-1}$.³ Due to the enormous amount of energy required to break this bond and produce nitrogenated compounds with reactive and usable nitrogen (a process known as *nitrogen fixation*), early life forms festered from the small amounts of nitrogen-containing species which were spontaneously formed by interaction of N_2 and CO_2 in the atmosphere, facilitated by highly energetic geothermal and atmospheric

events, such as volcanic activity and lightning.^{4,5} As demand for these compounds increased due to the development of higher plants, a shortage of activated nitrogen in the atmosphere may have forced early life forms to develop an alternative process,⁶ a way to effectively carry out a reaction in a microscopic scale which, otherwise, required lightning and volcanoes—by adapting to *catalyse* nitrogen fixation through a complex process involving a *nitrogenase* enzyme.⁷

In order to know how this was possible, we must introduce the concept of a catalyst and its influence on a chemical process. A catalyst is a substance that interacts with the constituents of a chemical reaction to increase its rate without modifying the reaction thermodynamics (the favourable or unfavourable nature of the reaction) or the composition of the initial and final state of the reaction (reactants and products, respectively). The role of the catalyst is thus not to change the total energy between reactants and products (the Gibbs energy of reaction, ΔG_r), but to lower the energy required to favour the kinetics of the forward and reverse reaction (the activation Gibbs energy, ΔG^\ddagger), as illustrated in Figure 1.1, all whilst itself remaining unaltered before and after the process. In a simple system, catalysts are able to do so by binding to the reactants (*A* and *B* in Figure 1.1); this binding (which shall not be too strong or too weak, but *just right*^{*}) is then followed by a reactivity step in order to form and stabilise intermediate species along the reaction (*I*), which enables a kinetically more favourable path towards the products (*P*). Depending on the number of intermediates, the catalysed reaction can involve more than one energy barrier, albeit none of the barriers of a catalysed reaction in an effective catalyst will span to higher energy values than those of the uncatalysed process. Finally, the products are desorbed and released into the environment. This is known as the *catalytic cycle*.

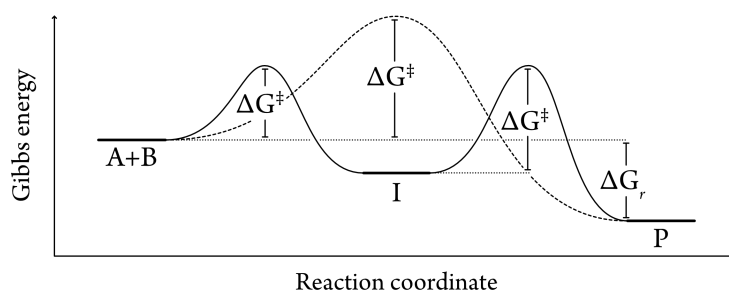


Figure 1.1 Reaction profile displaying the effect of the catalyst in the lowering of the activation barrier of an arbitrary exergonic reaction, $A + B \rightleftharpoons P$. Dashed and solid lines represent the energy paths of the reaction in the absence and presence of a catalyst, respectively.

One of the first instances of a study of a catalytic system was published by Louis Jacques Thénard in 1813, who discovered that ammonia was decomposed into nitrogen and hydrogen upon contact with various red-hot metals. Ever since, studies on the matter have tried to clarify the role of catalysts in the kinetics and efficiency

^{*} This is known as the Sabatier principle, often applied to heterogeneous catalytic systems—which we will discuss in the next chapters.

of the reaction, and several methodologies in order to determine the reaction rate in a catalytic system have been developed. In the following, we will describe some of these approaches.

In a general system, one of the simplest methods to relate the rate constant (k) with the activation energy and the absolute temperature (T) was described by Svante Arrhenius in 1889,⁸ who envisioned a system in which two colliding molecules in the gas phase with enough kinetic energy overcome an energy barrier with an activation energy E_a to yield the products. k can be calculated by means of the Arrhenius equation:

$$k(T) = \nu e^{-\frac{E_a}{RT}} = \nu e^{-\frac{E_a}{k_B T}} \quad (1.1)$$

Where ν is denoted as the pre-exponential factor, which in the Arrhenius interpretation of the rate constant is not dependent on the temperature. Eq. (1.1) can consider an activation energy per mol ($1 \text{ mol} = 6.022 \times 10^{23}$ molecules) by using the universal constant of ideal gases ($R = 8.314 \text{ J K}^{-1} \text{ mol}^{-1}$), or per molecule by using the Boltzmann constant ($k_B = 1.380 \times 10^{-23} \text{ J K}^{-1}$). The Arrhenius definition of the activation energy can be derived from Eq. (1.1):

$$E_a = RT^2 \frac{\partial \ln k}{\partial T} \quad (1.2)$$

The use of the Arrhenius equation to assess a system governed by collision theory, however, fails to correctly define the nature of the pre-exponential factor, which is rendered as a constant that is directly related to the collision frequency and is determined experimentally. An alternative approach that attempts to shed light on the exact nature of the pre-exponential factor is *transition state theory* (TST), developed by Eyring⁹ and Evans and Polanyi¹⁰ independently in 1935. TST considers that the reaction takes place by modification of a single parameter, the reaction coordinate (a bond length or an angle which changes along the reaction) which characterises the conversion of the reactants to the products. The structure corresponding to the highest energy point in the barrier is denoted as the *activated complex* or *transition state* (TS). In TST, a reaction such as that depicted in Figure 1.1 can be written as:



Which represents a situation where the TS (AB^\ddagger , where a \ddagger symbol denotes a structure which is characteristic of a saddle point in the energy profile) is in equilibrium with the reactants A and B with an equilibrium constant K^\ddagger , while the reaction is only allowed to proceed in the forward direction after surmounting the activation barrier with a rate constant k^\ddagger . The rate of formation of products can then be expressed as:

$$\frac{d[P]}{dt} = k^\ddagger [AB^\ddagger] \quad (1.4)$$

By relating k^\ddagger with the frequency of the vibrational mode of the reaction coordinate (e.g. stretching in an atomic bond) and considering i) the relation between the equilibrium constant and the thermodynamic properties of the energetic states of the reaction components, and ii) that the rate constant associated with the formation of products is solely dependent on the reaction coordinate, we can obtain the following definition for the thermodynamic form of the rate constant in TST, k_{TST} :

$$k_{TST} = \frac{k_B T}{h} K^\ddagger \quad (1.5)$$

This can be further expanded by taking the thermodynamic equations that relate the total available energy (the Gibbs energy) with the equilibrium constant and the enthalpy and entropy of the system:

$$\Delta G^\ddagger = -RT \ln K^\ddagger \quad (1.6)$$

$$\Delta G^\ddagger = \Delta H^\ddagger - T\Delta S^\ddagger \quad (1.7)$$

Combining Eqs. (1.6) and (1.7) into Eq. (1.5), we can reformulate the rate constant as:

$$k_{TST} = \frac{k_B T}{h} e^{\Delta S^\ddagger/R} e^{-\Delta H^\ddagger/RT} \quad (1.8)$$

Which can be expressed in terms of the activation energy defined by Arrhenius in Eq. (1.2), demonstrating that, in reality, the pre-exponential factor takes the form of a function of the temperature:

$$k_{TST} = \nu_{TST} e^{-\frac{E_{aTST}}{RT}} \quad \nu_{TST} = \frac{e k_B T}{h} e^{\Delta S^\ddagger/R} \quad (1.9)$$

As can be derived from Eq. (1.9), an increase in the entropy from the reactants to the TS results in a large pre-exponential factor that accelerates the reaction in the forward direction, which is inversely proportional to the effect of an increase in the activation energy.

From this introduction on the kinetics of a general catalytic system, it is obvious that in order to accurately define the rate of a reaction we need to determine the nature of the TS along the reaction profile; the strategies we have followed to describe and characterise these structures computationally will be discussed in Section 2.8.

1.1.1. Types of catalysis

Up to this point, we have described the influence of a catalyst on the molecular species that are involved in a reaction in the gas phase, by considering either collision theory and the Arrhenius equation or a general approach to TST. However, we have as of yet neglected the catalyst phase and the effect it has on chemical reactivity. In this section, we will discuss the three main types of catalysts, namely *bio catalysts*, *homogenous catalysts* and *heterogeneous catalysts*, and introduce the concepts that arise when the latter two interact with reacting molecular species.

In the first part of Section 1.1, we introduced the case of the biological nitrogen fixation to ammonia. This is an instance of a biocatalytic system, where reactivity occurs inside a protein complex denoted enzyme. Enzymes contain active centres (often including a metallic cofactor) acting as catalysts which are surrounded by amino acids that sterically determine the allowed geometry of the reactants (substrates), products and any transition states involved in the reaction. This renders enzymes as exceptionally selective catalysts towards very specific reactions involved in the functions of living organisms. For instance, metalloenzymes with Zn-based metal centres are able to catalyse alcohol oxidation and reduction (*via* alcohol dehydrogenases), hydrolysis of peptide bonds (*via* carboxypeptidases) or CO₂ conversion to carbonic acid (*via* carbonic anhydrases).¹¹ Due to the nature of this thesis, we are not going to discuss this type of catalyst in detail.

Homogeneous catalysts refer to those systems where both the catalyst and the reacting species are in the same phase—gaseous or, more commonly, in solution. Homogeneous catalysts, which coexist with the reactants in a molecular form in a substoichiometric mixture, are considered to be uniformly dispersed throughout the reaction media; thus, interactions with the surrounding reactive molecules are commonly portrayed using collision theory in an ideal gas (which is governed by diffusion in a liquid solution). This theory, however, is not without its downsides, e.g. neglecting the discrete chemical structure of the interacting molecules or considering that molecules do not interact until contact. Most homogeneous catalysts used in industry are organometallic catalysts, which contain metal-ligand bonds. In turn, reactivity usually occurs on the first coordination sphere of the metal centre, where bound molecules (ligands) are activated and undergo subsequent transformations.¹² Nonetheless, the broad use of homogeneous catalysts in industrial applications is hindered by their main characteristic, as the fact that products and catalyst are in the same phase forces the use of separation techniques that hamper scaling-up for a wide range of reactions.

The main type of system we are going to focus on in this thesis are heterogeneous catalysts, where the catalyst and the reacting species exist in different phases (usually, the former is a solid and the latter is a molecule in the gas or liquid phase). In contrast with single active site homogeneous catalysts, typical non-porous heterogeneous catalysts are composed of an impenetrable surface (e.g. metallic nanoparticle facet) terminated by a periodic distribution of surface atoms. These surface sites are often catalytically inert, and adsorption of reactants and intermediates predominantly occurs on sites neighbouring surface defects (e.g. vacancies, edges, kinks, steps).^{13,14} Hence, unravelling the nature of these active sites and their ability to selectively trigger a catalytic reaction is at the heart of heterogeneous catalysis.^{14–17} At the same time, the strength of the binding of the reactants onto these adsorption sites is one of the major determinants of the reaction rate in a heterogeneous catalytic system. This was demonstrated in the Sabatier principle formulated by Paul Sabatier, which states that *the interaction strength between a heterogeneous catalyst and the reactants must be neither too weak so that the reactants readily desorb without reacting, nor too strong so that the products fail to dissociate*. This concept has been widely applied in a number of theoretical studies on heterogeneous catalysts,¹⁸ which has led to the

development of activity descriptors and scaling relations between the binding energy of key reaction intermediates in some of the most relevant reactions, including the oxygen evolution,¹⁹ hydrogen evolution,²⁰ nitrogen reduction²¹ and CO₂ reduction.²² Finally, the distribution of the active sites and, therefore, the resulting activity of the system, is directly linked to the nature of the catalytic surface planes which are exposed to the reaction media, and/or the presence of surface defects. The analysis and optimisation of the structural properties of heterogeneous catalysts by computational means is discussed in Sections 2.3 and 2.9.

1.1.2. Reactivity of heterogeneous catalysts

There are two main mechanisms for the adsorption of reactant molecules (*adsorbates*) onto a surface and subsequent bimolecular reaction. The first kinetic model assumes that all reactant species are adsorbed on the surface and diffuse to react with each other, which is the most common scenario for the majority of reactions on heterogeneous catalysts. This is known as Langmuir–Hinshelwood kinetics, as displayed in Figure 1.2 (top), as it follows a reaction mechanism proposed by Irving Langmuir in his seminal series from 1916 to 1918²³ (who described a complete adsorption model on solid-liquid interfaces) which was formalised as a kinetic model for reactivity by Cyril Hinshelwood in 1926.²⁴ An instance of a widely studied mechanism following the Langmuir–Hinshelwood kinetic model is the Horiuti–Polanyi mechanism,²⁵ which describes the hydrogenation of alkynes and alkenes adsorbed on metallic surfaces by a sequential transfer of activated hydrogen atoms.²⁶ Alternatively, some catalysts can undergo a mechanism in which one of the species is adsorbed and accommodated onto a surface site, and reacts with another species in the reaction media to yield and desorb the product. This is known as the Eley–Rideal mechanism, depicted in Figure 1.2 (bottom). The stabilizing nature of the adsorbed intermediates on the Langmuir–Hinshelwood mechanism, however, results in the Eley–Rideal mechanism being unfavoured in most thermal catalytic systems.²⁷

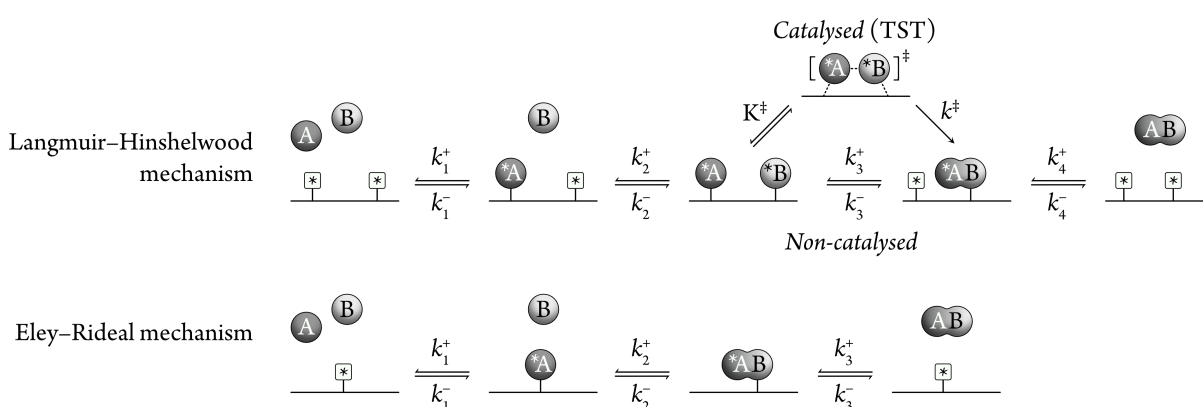


Figure 1.2 Schematic representation of the two predominant mechanisms in heterogenous catalysis, namely the Langmuir–Hinshelwood mechanism (top) and the Eley–Rideal mechanism (bottom). Horizontal lines represent the catalyst surface onto which reactants A and B are adsorbed to form product AB. A standalone asterisk symbol represents a free adsorption site, or an adsorbed species when preceding the reactants A or B or the product AB. The existence of a TS

structure in the third step of the Langmuir–Hinshelwood mechanism is included, which considers that the surface catalyses $*A + *B \rightleftharpoons *AB$ and forms an activated species $**AB^\ddagger$ as portrayed in TST.

Since a surface typically contains a very large amount of active sites atop which adsorption and reaction can occur, the kinetics of heterogeneous catalysts are formulated based on the fraction of active sites undergoing the chemical reaction. For instance, if we consider a system involving reactants in the gas phase, the first step in both the Langmuir–Hinshelwood and Eley–Rideal mechanisms (unimolecular associative adsorption of A from the gas phase with a pressure p_A onto the surface) can be defined by the rate of adsorption of species on sites A (θ_A):

$$\frac{d\theta_A}{dt} = p_A k_1^+ (1 - \theta_A) - k_1^- \theta_A \quad (1.10)$$

That is, the rate of adsorption is equal to the rate of sites that are being occupied minus those that are being depleted. Therefore, in a heterogeneous system in equilibrium, $d\theta_A/dt = 0$. In the Langmuir–Hinshelwood model, however, both A and B may be competing for the same adsorption sites; in this case, we can define the fractional coverage of each species (i.e. θ_A and θ_B) as follows:

$$\theta_A = \frac{K_1 p_A}{1 + K_1 p_A + K_2 p_B} \quad \theta_B = \frac{K_2 p_B}{1 + K_1 p_A + K_2 p_B} \quad (1.11)$$

Where $K_n = k_n^+/k_n^-$. Taking Eqs. (1.10) and (1.11) as reference, we can then write the rate equations for the Langmuir–Hinshelwood model. In many cases, calculating the full solution for the reaction rate considering all steps as equally relevant is an arduous task; this can be simplified by considering that the rate of reaction is predominantly governed by one elementary step. For instance, if we are to take the reactivity step ($*A + *B \rightleftharpoons *AB$) as the rate determining step (RDS, the step with the slowest reaction rate), the reaction rate becomes:

$$r = r_3 = k_3^+ \theta_A \theta_B - k_3^- \theta_{AB} \theta_* \quad (1.12)$$

Where θ_* corresponds to the fraction of free sites (so that $\sum_{A,B,AB,*} \theta_i = 1$ following the principle of conservation of sites). This equation can be generalised for all reaction steps by taking the fractional coverages of their respective initial and final species.

The thermodynamic form of TST can be applied to any step of the reaction on a heterogeneous catalyst. For instance, let us consider a catalyst that accelerates the aforementioned reactivity step; this is showcased with the appearance of an alternative reaction pathway from $*A + *B$ to $*AB$, going through an activated $**AB^\ddagger$ complex in the Langmuir–Hinshelwood mechanism as displayed in Figure 1.2. Applying Eq. (1.5) for a heterogeneous catalyst requires the equilibrium constant between the reactants and the TS, which now we can define as a function of the fractional coverages: $K^\ddagger = \theta_{AB^\ddagger}/\theta_A \theta_B$. Finally, the activity of a heterogeneous catalyst is quantified by the turn-over number (TON, which relates the amount of product obtained per active

site or per mass of catalyst) and by the turn-over frequency (TOF, which determines the amount of turn-over numbers per unit time):

$$TON = \frac{n_{AB}}{\sum \text{sites}} \equiv \frac{m_{AB}}{m_{\text{catalyst}}} \quad TOF = \frac{TON}{t} \quad (1.13)$$

Which is analogous to homogeneous catalysis, where the values of the TON and TOF are obtained as the mole of product per mole of catalyst.

Up until this point, we have—rather clumsily—described the concept of catalysis and how catalysts, and especially heterogeneous catalysts, influence the reaction rate. From this discussion, it is undeniable that the contributions from Langmuir, Eyring, Eley and co-workers have laid out the groundwork for the understanding of *all* heterogeneously catalysed reactions, such as the Horiuti–Polanyi mechanism; due to the relevance of this latter mechanism to unravel some of the elements of this thesis, this will be expanded in Section 1.3.4. Nonetheless, the work of Juro Horiuti and Michael Polanyi goes beyond their contributions to heterogeneous catalysis; this is best demonstrated by introducing an excerpt from their work published in *Nature* in 1933:²⁸

“It has been recently observed by M. L. Oliphant[†] that, when hydrogen is kept in contact with water for a few months, an exchange of atoms occurs between the hydrogen and the water. We have now found that this reaction can be catalysed by platinum black, such as is used in hydrogenation.”

Horiuti and Polanyi had just provided a formalism for *electrocatalysis*.

1.2. Electrocatalysis

Electrocatalytic processes have been in the heart of the metallurgic industry since the discovery of the Hall–Héroult process to extract aluminium from clay in 1886, which reduced the price of this metal by a factor of 200 and boosted its widespread use. The discovery of Horiuti and Polanyi drew a renewed attention to electrocatalysis and provided an accurate understanding of the general reactions involved in these processes. Horiuti and Ikusima attributed their observations to the following electrochemical reaction:²⁹



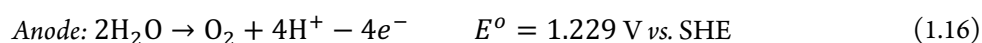
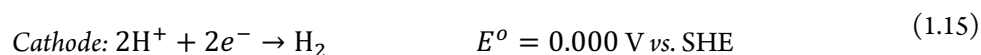
That is, protons and electrons in solution are in equilibrium with hydrogen in the gas-phase. In Oliphant’s experiments, any increase in the pressure of hydrogen gas inevitably induced the reaction going forward, following Le Chatelier’s principle. Accordingly, the use of Pt by Horiuti and Polanyi accelerated the reaction by facilitating hydrogen dissociation on the surface electrocatalytically. Here, electrocatalysis refers to the use of

[†] Sir Mark Oliphant discovered helium 3 and tritium, and was the first physicist to experimentally demonstrate nuclear fusion. He was a strong advocate for research on nuclear bombs, and his work was crucial for the development of the Manhattan Project.

catalysts (which can be either of the types presented in Section 1.1.1) to accelerate electrochemical reactions (reactions involving an exchange of electrons). Therefore, in the next few lines we will attempt to provide a summary of the fundamentals of electrochemistry.

Electrochemical reactions occur in an aqueous ionic conductor or *electrolyte* which interacts with a conductor, usually a solid surface or *electrode*. Reactions occurring at the electrode surface can either be *oxidations* or *reductions*, depending on whether the reactant species lose (oxidation) or gain electrons (reduction). Experimentally, these reactions are carried out in an electrochemical cell containing a pair of inter-wired electrodes separated by an ion-exchange membrane, each performing one *half-cell* reaction; in one electrode (the *anode*), a reactant species is oxidised and yields electrons, which are then transferred to the other electrode (the *cathode*) where a reduction takes place. Because of this, the electrode performing the electrochemical reaction of interest is denoted as the *working electrode*, while the other is referred to as the *counter electrode*. The facility with which the reductive species is oxidized at the anode and the oxidative species is reduced at the cathode determines the flow of electrons in the cell, and therefore, sets the cell potential, or the magnitude of the electromotive force that drives the electrons from the anode to the cathode. Because the cell potential cannot be determined for a single half-cell reaction and is always dependent on the difference between a reducing and an oxidating electrode, the reduction potential of a half-cell is determined with respect to a reference electrode, which is usually the *standard hydrogen electrode* (SHE) in which reaction in Eq. (1.14) takes place on a Pt electrode with all species having an activity of $a = 1$. To simplify its referential purpose, this cell is standardized to have a reduction potential of $E^o(\text{H}_2/\text{H}^+) = 0.0 \text{ V}^\ddagger$.

To showcase the effect of the potential, we are going to briefly discuss one of the most widely investigated reactions in literature, electrochemical water splitting, which will be used in subsequent sections for exemplification purposes. This reaction is composed of the following half-cell reactions in acid media:



The reactions occurring at the cathode and anode are known as the hydrogen evolution reaction (HER, which we will discuss in detail in the next sections) and the oxygen evolution reaction (OER), respectively. In order to carry out this reaction, we need to supply an external potential to surpass the thermodynamic potential of the OER, at which point water oxidation becomes spontaneous in an ideal catalytic system. In practice, however, the process is hampered by a potential limiting step (PLS) along the 4-step water nucleophilic attack

[‡] In reality, the absolute standard potential for the H_2/H^+ redox couple is defined as $E^o(\text{H}_2/\text{H}^+) = \phi^{\text{Hg}} + \Delta_{\text{H}_2\text{O}}^{\text{Hg}} \psi_{\sigma=0}^o - E_{\sigma=0}^{\text{Hg}}(\text{SHE})$, where the first, second, and third terms correspond to the electron work function of Hg, the contact potential difference at the metal-solvent interface, and the potential of zero charge of Hg, respectively. In water, and at the temperature of 298.15 K, $E^o(\text{H}_2/\text{H}^+) = 4.44 \pm 0.02 \text{ V}$.³⁰ Hence, E_{vac} (which corresponds to the reference vacuum energy level) can be defined as $E_{\text{SHE}} - 4.44$.

mechanism (WNA) followed by most OER electrocatalysts,^{31,32} requiring an additional energy input or *overpotential* η , which is the difference between the potentials at which the reaction becomes spontaneous in a real and an ideal system (E_{app} and E_{OER}^0 , respectively), so that $\eta = E_{app} - E_{OER}^0$. This will be further discussed in Section 1.3.2. Hence, modifying the cell potential externally one can tune the output of the desired reaction, for which the application of the thermodynamic potential plus an overpotential is necessary. In the case of water splitting, any applied voltage above $(1.23 + \eta_{OER}) V_{SHE}$ increases the rate of the anodic reaction, evidenced by a concomitant increase in the anodic current; similarly, any applied voltage below $(0.00 - \eta_{HER}) V_{SHE}$ results in an increase of the cathodic current. This is illustrated in Figure 1.3, where the potential-dependent relative energy of the electron level in the electrode allows for a cathodic or anodic electron flow.³³

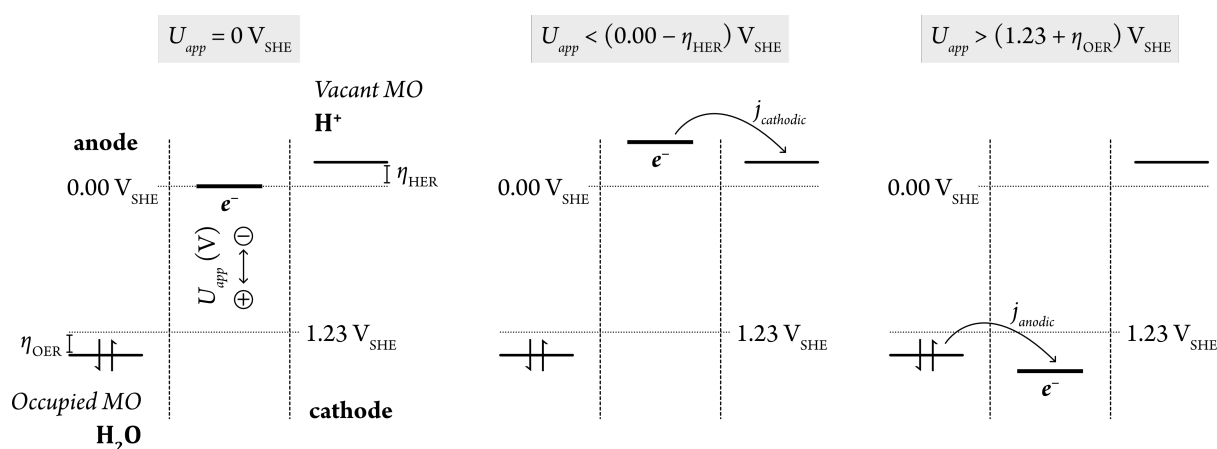


Figure 1.3 Representation of the effect of the application of an external potential on the energy level of the electrons in the cathode and anode in water electrolysis. If $U_{app} < (0.00 - \eta_{HER}) V_{SHE}$, the flow of electrons goes from the electrode to the oxidised species, increasing the cathodic current ($j_{cathodic}$); if $U_{app} > (1.23 + \eta_{OER}) V_{SHE}$, the flow of electrons occurs from the reduced species to the electrode, increasing the anodic current (j_{anodic}).

The relationship between the observed current density (j , indicative of the rate of reaction) and the applied overpotential in a reaction with a single rate-determining step is given by the Butler–Volmer equation:

$$j = j_{anodic} - j_{cathodic} = j_0 \left(\underbrace{e^{\frac{\alpha_a n e \eta}{k_B T}}}_{\text{anodic term}} - \underbrace{e^{\frac{\alpha_c n e \eta}{k_B T}}}_{\text{cathodic term}} \right) \quad (1.17)$$

Where j_0 is the exchange current (background current in the electrode at $U_{app} = 0 V$), α is the charge transfer coefficient (related to the potential difference present at the electrode-electrolyte interface), n is the number of exchanged electrons and η is the overpotential. In most heterogeneous electrocatalytic systems, j is reported as mA cm^{-2} . The overpotential at values of $|\eta| \gg k_B T / ne$ (where the dependence with j is logarithmic) can be plotted as a function of $\log(j)$ to obtain a curve with a slope (the *Tafel slope*, in mV decade^{-1}), which relates the rate of the reaction with the applied overpotential. Thus, there are two main figures of merit to measure the

activity of an electrocatalyst, namely the Tafel slope and the overpotential required to achieve a current density of 10 mA cm^{-2} at ambient temperature and 1 atm of O_2 , $\eta_{10\text{mA cm}^{-2}}$. This value, which is chosen by convention, corresponds to the current density of a solar water splitting cell with 10% efficiency irradiated with light of an intensity of 1 sun (1 kW m^{-2}).³⁴

Furthermore, electrochemical reactions often compete with one or several side reactions which in turn consume electrons, reducing the yield of the desired product. For instance, besides the 4-electron reduction depicted in Eq. (1.16), water can undergo a 2-electron oxidation to produce hydrogen peroxide.³⁵ To account for this, the Faradaic efficiency (FE) determines the selectivity of the catalyst (ability of the catalyst to predominantly yield a given product of interest) by assessing the charge that has gone to obtain this product (Q_{exp}) compared to the total charge transferred over a period of time (Q_{theo}):

$$\text{FE} = Q_{\text{exp}}/Q_{\text{theo}} = nF[P]/jt \quad (1.18)$$

Overall, a *good* heterogeneous electrocatalyst—either embedded onto or working as the electrode material—must be able to i) undergo the reaction of interest with a low overpotential to reduce the energy loss in allowing the reaction, ii) accelerate the reaction on the working electrode yielding a reasonable amount of current density upon varying the overpotential as quantified by the Tafel slope, and iii) selectively catalyse the reaction of interest with a high Faraday efficiency, all whilst remaining stable under experiment conditions. These are the main *figures of merit* of an electrocatalytic system. Importantly, finding an electrocatalyst that accomplishes these figures of merit to utilize the excess of renewably generated electricity for energy storage and production of chemical feedstocks is key for building a greener, more sustainable future.³⁶

1.2.1. Proton-coupled electron transfer

Proton-coupled electron transfer steps (PCET) are reactions in which, as the name suggests, a proton and an electron are jointly transferred from one species to another.³⁷ This elementary process is ubiquitous in most reactions in heterogeneous, homogeneous and bio electrocatalysis, and it is the common denominator of all reactions discussed in this thesis. For instance, there is a PCET at every step in the WNA mechanism of OER:³¹



There are several theories that support the concerted PCET over a sequential mechanism with a decoupled proton transfer (PT) and electron transfer (ET), ET/PT.^{37,38} For instance, multi-electron oxidations consisting of as-many distinct 1-electron steps benefit greatly from the absence of a charge build-up that could hinder the

feasibility of a subsequent oxidation step *via* Coulombic repulsions. This is especially relevant in fast, consecutive redox reactions such as Eqs. (1.19) to (1.22). PCET steps are also kinetically preferred over ET/PT: while the reaction profile of a coupled PCET may display only one energy barrier containing a single TS species, a decoupled step may display two distinct TS for each process together with a short-lived intermediate.^{39,40} Computationally, the consideration of a single process for both transfers simplifies calculations enormously; while determining the energetics of a single ET requires the use of less-developed applications of the Marcus theory,^{41,42} PCET steps can be assessed computationally by taking advantage of the reaction in Eq. (1.14) as implemented in the *computational hydrogen electrode* model (CHE), which is discussed in Section 2.7.1. Thus, in most of the electrochemical reactions studied in this thesis, electron and proton transfer events have been treated in a concerted fashion via PCET steps.

1.2.2. Photoredox catalysis

In electrocatalytic systems, oxidations and reductions are catalysed on the electrode surface and enabled by applying an external potential to the electrochemical cell, where electrons flow from the anode to the cathode in a closed electric circuit. Redox reactions can also be carried out photochemically on a solid semiconductor and in the presence of light (which is responsible for charge carrier generation). In photocatalytic systems, the reactants undergo chemical transformations in a very similar fashion to those using electrocatalysts.

Photocatalytic systems usually consist of a nanostructured semiconductor particle in solution, with a band gap E_g (the discussion of band gaps within the electronic band structure of solids is detailed in Section 2.3.4). Given that the particle is in contact with light of frequency ν , if $h\nu > E_g$, the photons will be able to excite an electron (e^-) from the valence band to the conduction band of the semiconductor particle (which acts as a *photosensitizer*), generating a hole (h^+) in the valence band.[§] Common semiconductors for photocatalysis include sulfides such as ZnS or CdS⁴³ and metal oxides, of which anatase TiO₂ stands out as the most active and versatile (in contrast with the rutile phase, which usually presents lower photocatalytic activities).⁴⁴ In contact with an oxidised and reduced species in solution, the e^-/h^+ pair either recombine releasing a photon, or interact with the reducing and oxidating species adsorbed on the surface. In that case, holes in the valence band can oxidise the reducing agent and, in turn, electrons in the conduction band reduce the oxidating agent. Similarly to electrocatalytic systems, in most cases we are only interested in investigating one half-reaction, rather than studying the whole system. In these situations, sacrificial electron donors (SD) or acceptors (SA) are often used, consisting of molecular species which undergo oxidation or reduction, respectively, and facilitate reduction or oxidation of the species of interest. Common SDs include triethylamine (TEA),⁴⁵ ethylenediaminetetraacetic acid (EDTA)⁴⁶ and ascorbic acid (AA), among others;⁴⁷ on the other hand, metallic

[§] These are the two charge carriers in a semiconductor, although due to their increased mobility, charge transfer is predominantly carried out by electrons. For instance, mobilities of electrons and holes in Si at 300 K are 1241 and 407 cm² V⁻¹ s⁻¹, respectively (Arora, Hauser and Roulston, 1982).

cations in solution are often used as SAs, mostly Ag^+ (although these have been shown to yield deposited Ag^0 atop the photocatalytic surface, potentially changing the chemical and optical properties of the system).^{1,2}

The combination of the semiconductor and SD (or SA) is usually insufficient to carry out the reaction of interest due to its slow kinetics on the photoelectrode surface. In these cases some strategies are followed, such as applying an external bias—leading to a photoelectrochemical system—or introducing an additional catalyst which utilises the charge carriers generated from irradiation of light to catalyse the redox process. This latter approach was first envisioned in the pioneering works by Fujishima and Honda in 1972,⁴⁹ who developed a photo-activated electrocatalytic water splitting system containing TiO_2 and Pt electrodes. Upon exposure to light, TiO_2 generated an e^-/h^+ pair; the h^+ promoted OER at the TiO_2 electrode, while the generated e^- was conducted to the Pt electrode where HER was catalysed. Current state-of-the-art photocatalysts, however, are usually formed by a three-component system (TCS)⁴⁷ in which the semiconductor and the SD/SA are accompanied by a co-catalyst that can be either a ligand with a metal centre coordinated to the photoelectrode surface, or a metal cluster.⁵⁰ For instance, a lot of effort has been put into designing a photochemical TCS that can efficiently catalyse water splitting^{51–53} (illustrated in Figure 1.4). In this regard, Al-doped SrTiO_3 photosensitizers with $\text{Rh}/\text{Cr}_2\text{O}_3$ and CoOOH -based co-catalysts for the HER and OER, respectively, have recently shown encouraging results with an outstanding *quantum yield*,⁵⁴ which is an indicator of the efficiency of the system. This is defined as the TOF for a heterogeneous system in mols of product per catalyst surface area and time, divided by the mols of photons *adsorbed* per unit time with respect to a reference system.

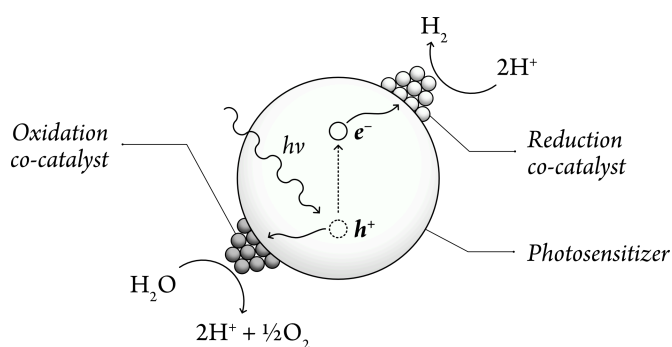


Figure 1.4 Schematic representation of a photocatalytic TCS for water splitting, where an e^-/h^+ pair is produced at the semiconductor particle. Here, water acts as a SD and is oxidised by holes at the oxidation co-catalyst, composed of a cluster of metal atoms on the photosensitizer, while protons are reduced by photogenerated electrons at the reduction co-catalyst.

1.3. (Photo)(electro)catalysis for solar- and power-to-X conversion

The most important conclusion we can draw from our discussion on electrocatalytic and photocatalytic systems is that the use of electricity in the former and of light irradiation in the latter can drive the thermodynamics for the catalysis towards a multitude of chemical compounds of interest. For instance, one can use electricity to

generate efficient and sustainable energy carriers or to produce relevant chemical feedstocks, or light to harvest usable fuels from highly polluting compounds. These concepts are known as *power-to-X* and *solar-to-X*, respectively (*X* denotes the obtained substance), which coupled with sustainable energy production strategies (such as wind power and solar irradiation), can provide a long-term solution for the energy crisis.^{55,56} For instance, power-to-hydrogen strategies—mostly water splitting technologies—are devoted to the production of green hydrogen gas, which can potentially store almost 4 times as much energy per kg than Li-ion batteries.⁵⁷ This hydrogen can then be converted back to ready-to-use power in *hydrogen-to-power* processes by means of fuel cells, yielding H₂O as the only by-product. Besides obtaining hydrogen gas as an energy carrier or *energy vector*, power-to-hydrogen technologies hold promise for the production of chemical compounds such as methane *via* interaction with hydrogen species.⁵⁸ Finally, other power-to-X processes have also been investigated for the generation of chemical feedstocks from green-house gases (GHG), such as the electrochemical conversion of CO₂ and water into CO and H₂⁵⁹ or to methane.⁶⁰ In the next sections, we will provide an overview of two reactions involved in power-to-hydrogen (the hydrogen evolution reaction or HER) and hydrogen-to-power (the oxygen reduction reaction or ORR), as well as introduce current approaches for the reduction of CO₂ (CO₂RR) to a variety of energy carriers via electrochemical and photochemical strategies. Finally, we will also discuss the potential use of other power-to-X strategies for the synthesis of valuable chemical feedstocks such as ethylene, which currently relies on highly polluting industrial processes. This will lay out the foundation for understanding the electrocatalytic and photocatalytic systems investigated in this thesis.

1.3.1. Hydrogen evolution

As we have already introduced in the previous sections, the HER is the reaction occurring at the cathode of water electrolyzers. HER in acidic media can occur via two different mechanisms—each undergoing two distinct elementary steps: one or two *Volmer* PCET steps in which one hydronium ion interacts with the surface and yields a *H species, followed by subsequent *Heyrovsky* or *Tafel* steps, wherein an adsorbed *H interacts with a H₃O⁺ from the electrolyte and an electron from the electrode through a second PCET, or two adsorbed *H species interact and desorb, respectively, to yield H₂.⁶¹ These mechanisms are illustrated in Figure 1.5.

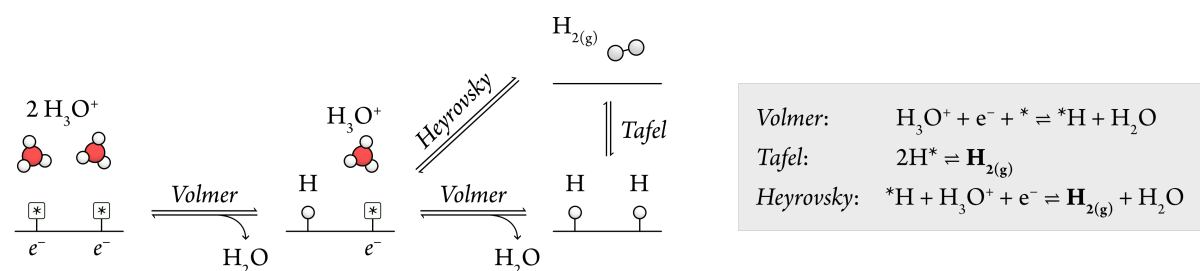


Figure 1.5 Schematic representation of the main reaction pathways for HER on an electrocatalyst surface.

Therefore, the HER can undergo *via* a Volmer–Heyrovsky mechanism or a Volmer–Volmer–Tafel mechanism. The nature of the kinetics involved in both mechanisms has been extensively studied,⁶² and several electrode materials have been proven to catalyse this reaction, mostly based on noble metals.⁶³ From of these, Pt-based catalysts stand out as the most active.⁶⁴ The exact nature of the Volmer, Heyrovsky and Tafel steps in the HER on noble metals has recently been discussed in a computational study,⁶⁵

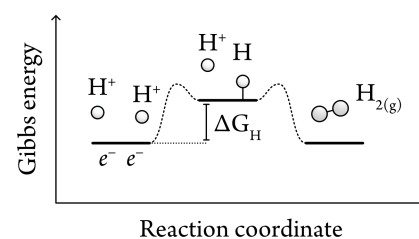


Figure 1.6 The binding energy of H atoms, ΔG_{H} , is considered to be a good descriptor for HER activity.

whereby simulation of the interactions between the inner and outer Helmholtz layers (as summarized in Section 2.6.1) confirmed that the Volmer–Heyrovsky mechanism was energetically favoured in most cases. Moreover, theoretical kinetic studies supported the basis for relating the catalytic HER activity to the binding energy of a H atom on the electrode surface, ΔG_{H} , in a direct application of the Sabatier principle. More specifically, electrocatalysts that display a strong ΔG_{H} may be limited by the Tafel or Heyrovsky steps, whereas catalysts with weak ΔG_{H} may be limited by the Volmer step. Therefore, ΔG_{H} (as represented in Figure 1.6) can be used as a reaction descriptor for the HER in acid, where catalysts with $\Delta G_{\text{H}} \approx 0$ eV, i.e. Pt and Pt alloys, are deemed to be the most active ones with an overpotential close to 0 and exceptional TOFs.^{20,66} This principle has been used in subsequent investigations for the rational design of HER electrocatalysts based on earth-abundant elements, such as nanostructured MoS₂, whose edge sites have been shown to be HER active.^{67–69} However, the use of such a simple descriptor, albeit suitable for understanding the trends in most heterogeneous catalysts, has some limitations, the major being its applicability in non-standard electrochemical conditions.^{1,2} In this regard, it has been shown that the activity of Pt catalysts decreases in alkaline pH in favour of Ir, wherein hydrogen production can occur through another route in which both *H and OH* binding energies are believed to be equally relevant.^{70–72} Another aspect in HER electrocatalysts often overlooked is the effect of the coverage resulting from under-potential deposited (UPD) H layers and the possibility that HER might be preceded by surface diffusion of H between active sites, which has also been posited to influence the reaction kinetics.⁷³ This knowledge has prompted a recent interest in understanding the factors driving HER in electrochemical conditions to rationally design cost-effective electrocatalysts for this process.

1.3.2. Oxygen reduction reaction

The main strategy to convert H_{2(g)} back into energy is through the use of fuel cells, wherein hydrogen gas is oxidised at the anode yielding protons and electrons via the so-called hydrogen oxidation reaction (HOR), and the airborne O₂ is reduced to water at the cathode through the oxygen reduction reaction (ORR), as outlined in Eqs. (1.22) and (1.23). In the most common fuel cells, protons diffuse from the anode to the cathode through a polymer electrolyte membrane (PEM),⁷⁴ where oxygen is reduced to water in the ORR. Electrons are

transported through a closed circuit, yielding charge current. The two half-cell reactions occurring at acidic pH are as follows:

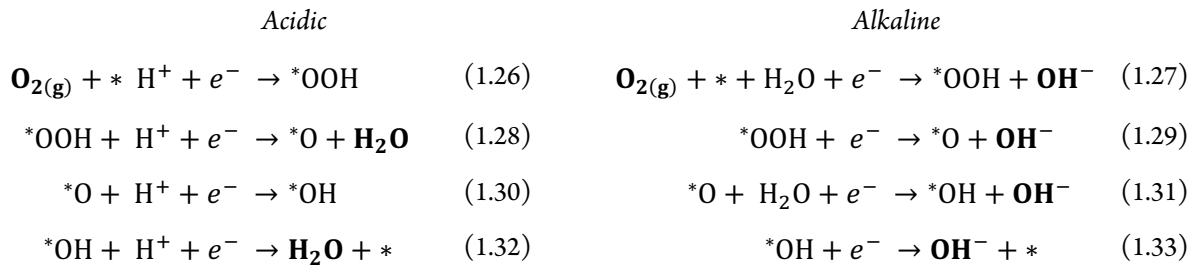


In an alkaline electrolyte, the cathodic reaction is:

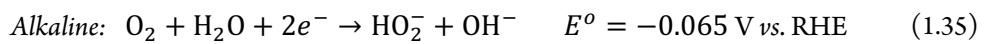


The overall reaction, therefore, is $\text{O}_2 + 2\text{H}_2 \rightarrow 2\text{H}_2\text{O}$, and has an thermodynamic cell potential of $+1.23 \text{ V}_{\text{SHE}}$, which indicates that this reaction is spontaneous. Thus, electric current can be generated as long as the cell is sourced with a continuous feed of hydrogen gas (the fuel). Because of the availability of the reactants and the lack of polluting by-products, PEM fuel cells have recently been identified as a key component for decarbonisation strategies.⁷⁵

The main bottleneck for the development of fuel cell technologies, however, is the slow kinetics of the ORR occurring at the cathode. This reaction can occur through a dissociative mechanism, where the O_2 bond is broken upon adsorption generating 2^*O species,^{76,77} or via an associative pathway undergoing a 4-electron process with the following steps in acidic and alkaline media:⁷⁸



Furthermore, the 4-electron ORR competes with a 2-electron process yielding hydrogen peroxide or hydroperoxide anions in an acidic and alkaline electrolyte, respectively:



The different steps of the main 4-electron and the competing 2-electron reactions in acidic and alkaline media are depicted in Figure 1.7.

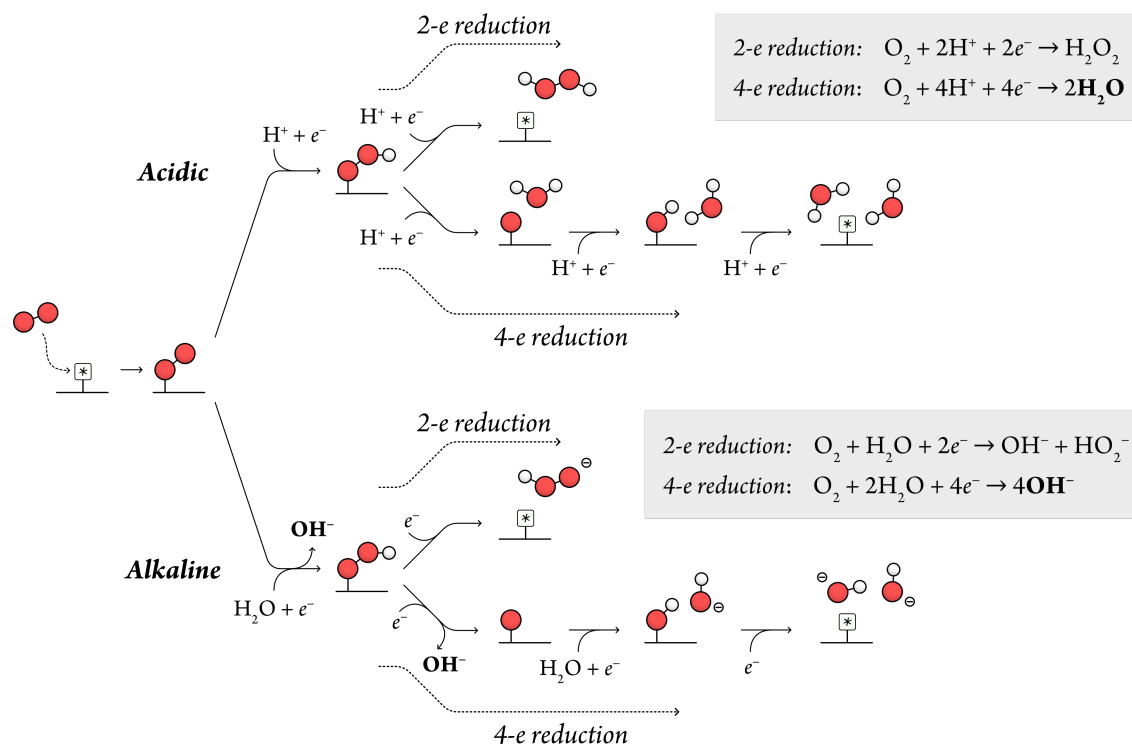


Figure 1.7 Representation of the two main associative mechanisms for the ORR in acidic and alkaline electrolyte.

In alkaline media, the reduction of $*OOH$ on the surface to a negatively charged $*OOH^-$ has been shown to determine the selectivity of the catalyst. A loosely bound $*OOH^-$ will desorb more easily facilitating the 2-electron pathway, whereas if it is too tightly adsorbed it will poison the surface and hinder the full 4-electron reaction. An intermediate binding of $*OOH^-$, therefore, will allow the subsequent reduction steps on the surface.⁷⁹ Due to the multitude of steps comprising the 4-electron ORR mechanism, careful examination of the reaction intermediates is required for an accurate mechanistic description.⁸⁰

In order for the ORR to be spontaneous and generate an electromotive force of $1.229 V_{SHE}$, the energy difference between consecutive electrochemical steps (depicted in Eqs. (1.26) to (1.33)) in an ideal catalyst must be of $\sim 1.23 eV$. This results in the total energy difference from $*O_2$ to $(* + H_2O)$ being $1.23 eV \times 4 = 4.92 eV$, as represented in the energy diagram of Figure 1.8 A. Therefore, $1.23 V_{SHE}$ is the highest potential at which the reaction is energetically feasible (grey line in Figure 1.8 A; the influence of the applied potential on the energy differences of electrochemical steps is derived in Section 2.7.1). However, a real catalyst at $U = 0 V_{RHE}$ will display an energy diagram such as the one represented in Figure 1.8 B (black line), where energy differences between intermediates diverge from the ideal value. In this case, the theoretical onset potential (which in a reduction is the highest potential at which the reaction can occur, represented by the orange line diagram in Figure 1.8 B) is determined by the theoretical overpotential:

$$U_{onset}^{ORR} = 1.23 - \eta_{theor} \quad (1.36)$$

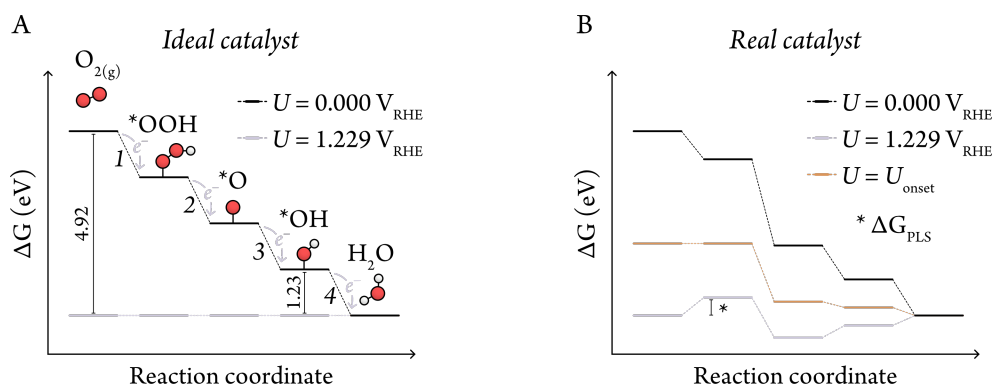


Figure 1.8 Gibbs energy diagrams of the ORR pathways in acid depicted in Figure 1.7, with an ideal catalyst (A) and an arbitrary system (B), at 0.0 and 1.23 V_{RHE} . In B, the energy pathway at the onset potential from which the reaction becomes endergonic is represented in orange. The PLS in B is the highest energy difference between consecutive intermediates at $U = 1.23 V_{RHE}$, which defines the theoretical overpotential of the electrocatalytic system.

η_{theor} in (1.36), in turn, can be obtained by calculating the potential limiting step (PLS) at $U = 1.23 V_{RHE}$, which in the arbitrary energy diagram of Figure 1.8 B is denoted as the first step and can be generally defined as:³²

$$\Delta G_{PLS}^{ORR} = \max\{\Delta G_1, \Delta G_2, \Delta G_3, \Delta G_4\} @ U = 1.23 V_{RHE} \quad \boxed{\eta_{theor}^{ORR} = \Delta G_{PLS}^{ORR} / e} \quad (1.37)$$

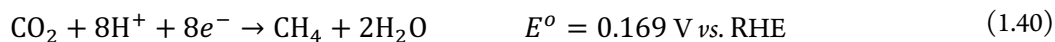
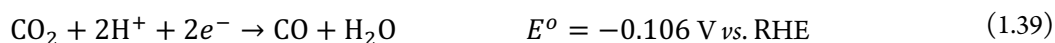
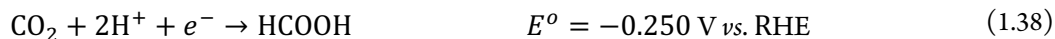
Therefore, an efficient catalyst that facilitates the ORR in a fuel cell must display an overpotential as close as possible to 0 V_{RHE} in order to optimise the output potential and minimise energy loss.

1.3.3. CO_2 reduction reaction

Capturing CO_2 —one of the major pollutants contributing to climate change—and either storing it or converting it into usable chemical feedstocks is a necessary step in order to cut anthropogenic GHG emissions and achieve the 1.5°C target set by the Paris agreement and ratified at the COP26 conference.^{81,82} Although big oil and technological companies are heavily investing in CO_2 capturing technologies, efficient strategies for implementing large-scale CO_2 conversion are urgently needed. Thus, CO_2RR is one of the most investigated reactions in the literature, and a myriad of approaches have been undertaken to catalyse this reaction either with solar-to-X or power-to-X technologies.^{83,84} Due to the complexity of this reaction and the broad areas of coverage that define some of the concepts that surround it, this and the subsequent related sections intend to provide a general overview of the main factors to consider when investigating heterogeneous catalysts for the CO_2RR , while focusing on the aspects relevant to this thesis.

The main bottleneck for the development of electrochemical and photochemical approaches for catalysing this reaction is that the vast majority of catalytic systems are hindered by two common drawbacks, namely poor activity and lack of selectivity.⁸⁵ This can be attributed to two predominant reasons: the high energy required to break the C=O bond in the linear CO_2 molecule ($798.9 \pm 0.4 \text{ kJ mol}^{-1}$),³ and the wide range of products to

which CO₂ can be reduced. For instance, CO₂ can be converted to C1 species such as formic acid or carbon monoxide via a 2-electron reduction pathway, or to methane via an 8-electron reduction process:



The selectivity of heterogeneous catalysts towards a specific product is determined by a wide range of factors, such as the presence of an aqueous solvent enabling the competing HER,⁸⁶ the porosity of the catalyst,^{87,88} the morphology of the active surface,⁸⁹ pH,⁹⁰ or the presence of promoters or surface ligands which stabilize certain CO₂RR intermediates.⁹¹ The catalyst material has also been shown to influence the activity and product distribution in the CO₂RR; generally, the majority of transition metal electrocatalysts can be divided in two groups, primarily yielding either CO (e.g. mainly Au and Ag, but also Pd, Pt or Zn) or formate (e.g. Cd, Sn or Pb).¹⁻³ Nonetheless, one of the most investigated transition metals for the electrochemical CO₂RR is Cu, due to its remarkable ability to produce a wide range of valuable hydrocarbons, including C₂H₂ and CH₄, as well as aldehydes and alcohols.⁹³ This reaction predominantly occurs on undercoordinated surface sites, such as in the vicinities of vacancies or at steps and edges⁹⁴—for instance, the activity of Cu electrodes for the CO₂RR towards CH₄ is increased in a stepped (211) facet compared to a flat (111) surface.^{95,96}

The CO₂RR towards any reaction product is widely believed to involve a series of ET and/or PCET steps, forming radical and/or negatively charged intermediates. The binding strength of these intermediates may depend on the geometry of the active site, the surface coverage, and the interactions in the second coordination sphere. However, the nature of the first intermediate in both electrocatalytic and photocatalytic CO₂RR (activation and chemisorption of CO₂ onto the catalyst surface), which is the RDS in most cases, is still under intense debate.⁹⁷ CO₂ adsorption can occur through two main reaction pathways, either accepting an electron from the surface yielding a coordinated *CO₂⁻, or via a PCET to yield *COOH. In any case, CO₂ is activated on the surface by exchanging charge through the O or C atoms, leading to a bent *CO₂ molecule with negative charge density and radical build-up. This activated species has a lower energy barrier to yield the subsequent reaction intermediates compared to its linear geometry.^{98,99} Therefore, effective stabilization of this first intermediate onto the catalyst surface is key for the reduction process. To this aim, inclusion of an excess of organic ligands in the solution can favour the stabilization of *CO₂⁻ through a set of non-covalent interactions (NCIs, which span a variety of interactions ranging from H bonds to steric repulsions), which will be discussed in further detail in Chapter 5.

The adsorption mode of the initial *CO₂⁻ intermediate is a key factor influencing the major product in the CO₂RR. It has been proposed that CO₂ can be adsorbed through an oxygen atom, a carbon atom, or a mixed coordination where a C and one O atom are both anchored to the surface. In the former, steric availability of C will favour an initial hydrogenation of this atom, yielding formate as the major product.⁸³ On the contrary, steric

hindrance in the carbon and mixed coordination modes hampers an initial hydrogenation of the C atom, which instead is more likely to occur on the O atoms, generating $^*\text{COOH}$. This species can then undergo an ET to yield OH^- and a $^*\text{CO}$ intermediate. Consequently, the adsorption strength of the $^*\text{CO}$ species is an indicator of the behaviour of the system: catalysts that display a weak adsorption for this intermediate will readily desorb CO, which will be the major product. In contrast, a strong CO adsorption facilitates further reduction of this species to subsequent products, such as CH_4 .⁹⁶ A representation of four possible coordination-dependent mechanisms towards some relevant CO_2RR products on heterogeneous catalysts is depicted in Figure 1.9.⁹⁹

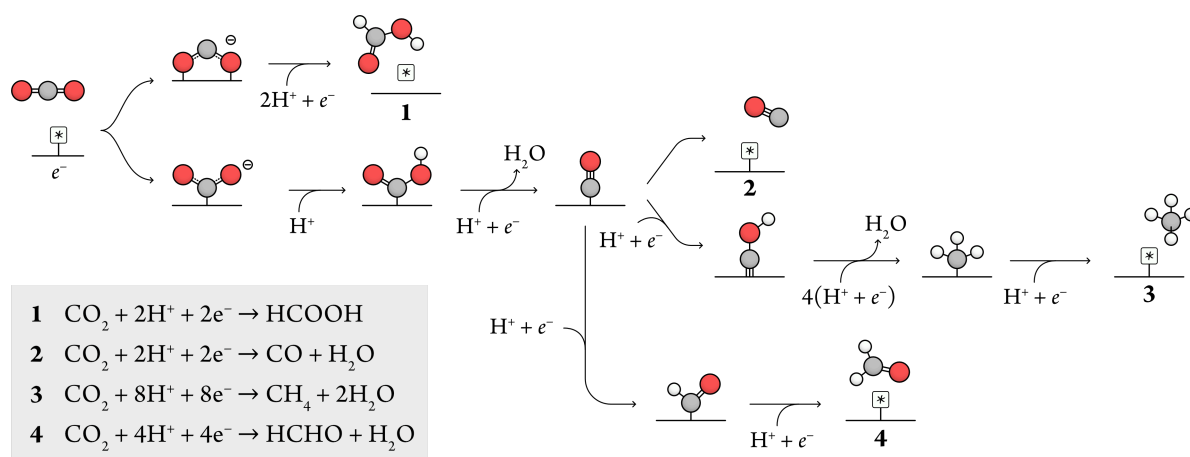


Figure 1.9 Proposed pathways in acid for the CO_2RR towards HCOOH (1), CO (2), CH_4 (3) and HCHO (4).

Hence, a good understanding of the nature of the intermediates that conform the CO_2RR mechanism towards the product of interest, as well as a thorough investigation of the catalyst nature and its environment, are keystone steps in the development of active photocatalysts and electrocatalysts for the CO_2RR .

1.3.4. Electrosynthesis of commodity chemicals

A basic literature search of studies on electrocatalytic systems for the generation of industry-relevant chemical feedstocks proves that the strategies followed are predominantly centred around the reduction of CO_2 .¹⁰⁰ So far, however, less effort has been put into investigating ways to *electrify* current industrial processes and mitigate their impact on emissions. For instance, an immensely relevant process that should be addressed is the synthesis of ethylene, one of the most important chemical feedstocks to produce pharmaceutical and commodity chemicals. The selective hydrogenation of acetylene (C_2H_2) to ethylene (C_2H_4), therefore, is a keystone process in chemical industry. This reaction is industrially carried out in steam crackers by means of heterogeneous catalysts based on precious metals, mainly metal-doped Pd.¹⁰¹ In addition to their high cost, Pd-based catalysts tend to form subsurface hydride and carbide species compromising their hydrogenation ability and affinity towards acetylene adsorption.^{102,103} Other limitations of this thermal process include oligomerization of the generated alkene and poisoning of the catalyst surface due to the presence of CO in the

steam cracking process, leading to catalyst deactivation.¹⁰³ More specifically, the adsorption of the reactants on the surface using thermal catalysts often leads to deposition of carbonaceous products yielding surface coke, which has been shown to reduce catalytic activity and selectivity towards the semi-hydrogenated product.^{104,105} To overcome these issues, several approaches have been undertaken, namely doping Pd with Bi and Sn,^{106,107} catalyst nanostructuring,¹⁰⁸ modifying the surface with a self-assembled monolayer of ligands,¹⁰⁹ and the use of alloys with a combination of Pd and other transition metals.¹¹⁰ In the quest for non-precious metal-based catalysts, cerium oxide has proven to be able to activate H₂ with relative ease¹¹¹ and to hydrogenate terminal alkynes with excellent selectivity at moderately high temperatures and pressures.^{112–115} Likewise, nanostructured graphene has been shown to promote the hydrogenation of acetylene to ethylene with remarkable selectivity and stability.¹¹⁶ Yet, all industrially used hydrogenation catalysts require moderately high temperatures and pressures, as well as highly pure H₂ as hydrogen source. Hence, the development of highly active and selective electrocatalysts that can perform the electrochemical hydrogenation (ECH) of acetylene which are based only on abundant elements, do not require highly pure H₂, operate at mild conditions, and overcome the main drawbacks of current hydrogenation catalysts, is of utmost importance.

Most works investigating the electrocatalytic hydrogenation of organic molecules have focused on scarce precious metals such as Pt and Pd.^{117,118} Nonetheless, state-of-the-art electrocatalysts for the ECH of acetylene have been developed which are mainly based on Cu. In the first instance of such a system, T. Zhang et al.¹¹⁹ recently developed a cathode containing a diffusion gas layer and a microporous layer that can selectively hydrogenate C₂H₂ contained in C₂H₄-rich feeds over a Cu-based layered double hydroxide catalyst with an onset potential of $-0.39 V_{\text{RHE}}$. This system yielded nearly 100% conversion of C₂H₂ with a selectivity of over 93% for C₂H₄ and high current densities. In addition, the onset potential for the ECH of C₂H₂ was found to be 0.21 V higher than that for HER, which limited the generation of H₂ as a by-product and hinted at a hydrogen gas-free mechanism. Another recent study of the ECH of C₂H₂ by J. Zhang et al.¹²⁰ on electrodeposited Cu nanoparticles forming dendrites displayed Faradaic efficiencies of 93% towards C₂H₄ in an ethylene-rich feed at $-0.6 V_{\text{RHE}}$, yielding current densities of over 150 mA cm⁻² at $-0.8 V_{\text{RHE}}$. In both studies, selectivity is directly linked to the ability of the catalyst material to exothermically adsorb acetylene and desorb ethylene, while displaying high kinetic and thermodynamic barriers for the over-hydrogenation to ethane. In both catalytic systems, acetylene hydrogenation occurs *via* a Horiuti–Polanyi mechanism (see Figure 1.10), where acetylene is adsorbed on the Cu catalyst and undergoes sequential hydrogen transfers from the surface H atoms, primarily sourced from protons generated from the OER occurring at the anode. As discussed before, this is regarded as the most common hydrogenation mechanism on heterogeneous catalysts. However, an alternative mechanism has also been proposed on thermal Ag and Au catalysts, where H₂ cleavage is very difficult.^{121,122} In these systems, hydrogen cleavage and alkyne hydrogenation occurs upon interaction of H₂ with the chemisorbed alkyne in an associative mechanism, as shown in Figure 1.10. This eventually leads to activation of the triple C–C bond and the generation of a non-negligible amount of oligomers compromising the catalyst selectivity, which has been

identified as a major drawback and reviewed recently.¹²³ The Horiuti–Polanyi and associative mechanisms may however not be applicable to heterogeneous catalysts whose resting state consists of a fully H-covered surface, as the chemisorption of the alkyne may be hindered due to the lack of available adsorption sites. In this case, hydrogenation may proceed instead via alkyne physisorption on the H-covered surface, followed by its hydrogenation with H atoms sourced by the surface coverage, or using protons from the electrolyte under electrochemical conditions. This Heyrovsky–type mechanism, depicted in Figure 1.10, is envisioned to facilitate the desorption of the produced alkene due to the weak substrate-catalyst interaction, preventing the formation of undesired oligomers.¹²⁴ Enabling such pathway can therefore provide an alternative approach for the hydrogenation of acetylene and a wide range of organic molecules with terminal alkynes at ambient conditions.

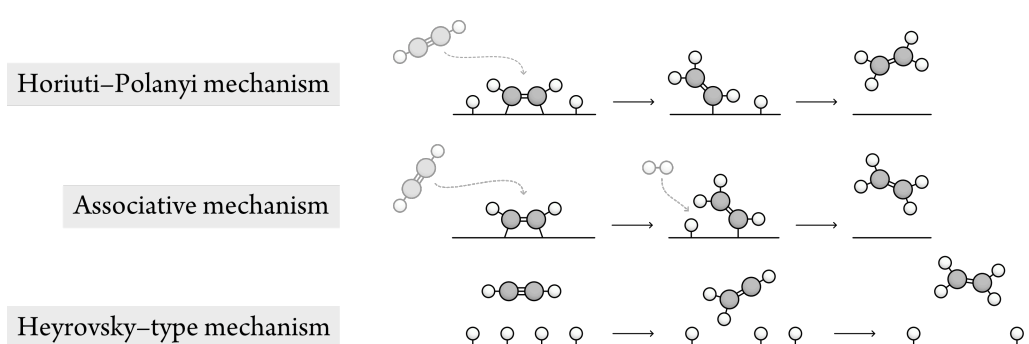


Figure 1.10 Proposed mechanisms for the hydrogenation of acetylene on heterogeneous catalysts. The Horiuti–Polanyi mechanism is the predominant pathway but alternative mechanisms include an associative mechanism in thermally activated processes and a Heyrovsky–type mechanism on an electrode surface with a high H coverage under electrochemical conditions.

“ *If it is not true it is very well invented.* – **Giordano Bruno**

De gli heroici furori, 1585

CHAPTER

2

Computational Methods

2.1. Uncovering the wavefunction

2.1.1. The Schrödinger equation

For centuries, physics has established that the properties of macroscopic systems in classical mechanics abide by Newton's laws and are ruled by the conservation of energy and momentum. For instance, Newton's Second Law allows us to predict the acceleration of an object given its mass and the external force applied onto it. These principles, however, are not applicable to certain systems, such as those involving objects travelling close to the speed of light—where relativistic effects play a big role—or in atomic-scale structures—where quantum effects come into action. In this chapter, the basis for the theories and methods developed to describe the properties of single molecules and periodic crystals will be discussed, including those presented in this work.

This discussion led Erwin Schrödinger to develop his famous equation in 1926, which has been the foundation for the study of particles in quantum mechanical systems. The time-independent form of the Schrödinger equation is as follows:

$$\left\{ -\frac{\hbar^2}{2m} \nabla^2 + V \right\} \Psi(\mathbf{r}) = E\Psi(\mathbf{r}) \quad (2.1)$$

Where \hbar is Planck's constant divided by 2π , m is the mass of the particle and V (the potential energy operator) is the time-independent potential field such as that generated by a proton in an atom under which the particle moves with an energy E . The motion of the particle is defined by the wavefunction, Ψ , which itself has no physical representation and is more often used in its quadratic form (integrated with its complex conjugate), which shows the probability of finding the electron in a region in space. ∇^2 (also known as the kinetic energy operator) is the Laplace operator which, in the Schrödinger equation, determines the divergence of the gradient of the wavefunction across the three cartesian coordinates. The terms in brackets jointly form the Hamiltonian operator, H , which in one electron system (e.g. H, He⁺ ...) is:

$$H = -\frac{1}{2}\nabla^2 - \frac{Z}{r} \quad (\text{a.u.}) \quad (2.2)$$

Where Z is the charge of the nucleus. This approach has been extensively used for the calculation of the energies of mono-electronic systems, such as H₂⁺; however, this is not applicable for solving more complex molecular and crystallographic structures with more than one electron. If we are to calculate the properties of such systems, we need to make use of a series of approximations, which will be discussed below.

2.1.2. The Born–Oppenheimer approximation and the Hartree model

The basis for the Born–Oppenheimer approximation relies on the fact that the nuclei have a considerably larger mass than any number of surrounding electrons (being the ratio in the lightest nucleus, ¹H, $m_{\text{H}}/m_e \approx 1836$). With this in mind, we assume that the movement of electrons and nuclei can be decoupled, and that the electronic wavefunction does not depend on the momenta of the nuclei. Therefore, neglecting the effect of the kinetic energy of the nuclei with respect to that of the electrons, and not including constant nuclear-nuclear interactions, H , becomes:

$$H = - \underbrace{\sum_i^N \frac{1}{2} \nabla_i^2}_{T_e} - \underbrace{\sum_A^M \sum_i^N \frac{Z_A}{r_{iA}}}_{V_{eN}} - \underbrace{\sum_{i>j}^N \frac{1}{r_{ij}}}_{V_{ee}} \quad (2.3)$$

Where T_e corresponds to the kinetic energy of the electrons, V_{eN} corresponds to the interactions between the electrons and the nuclei and V_{ee} to the electron–electron repulsions for N electrons and M nuclei. Solving this last term, however, is not analytically possible since we have to consider the trajectories of all electrons relative to each other.

An initial approach to this problem is the Hartree model published by D. R. Hartree in 1928,¹²⁵ which assumes that the Hamiltonian is composed of the sum of each 1-electron Hamiltonian with the form:

$$H = \sum_i^N h(i) = \sum_i^N \left\{ -\frac{1}{2} \nabla_i^2 + \sum_A^M \frac{1}{r_{iA}} \right\} \quad (2.4)$$

However, this approximation does not contemplate electron-electron interactions present in polyelectronic systems. To solve this, Hartree made use of the Born interpretation of the wavefunction, which states that its square yields the probability distribution. In the case of electrons, as with all fermions, the wavefunction contains a spatial component, ψ_i , and a spin component, α or β , so that $\chi_N = \psi_i\alpha$ or $\chi_N = \psi_i\beta$. Taking this into account, if we include the probability distribution of electron x_2 in its spin orbital χ_2 , the energy ε_1 of electron x_1 in spin orbital χ_1 in a two-electron system is represented by:

$$\left\{ -\frac{1}{2} \nabla^2 - \frac{Z}{r_1} + \int \frac{\chi_2^2(x_2)}{r_{12}} \partial\tau \right\} \chi_1(x_1) = \varepsilon_1 \chi_1(x_1) \quad (2.5)$$

Solving Eq. (2.5) requires an initial set of trial functions for χ_1 and χ_2 , which in turn changes the density function and the total energy and yields a new set of spin orbitals. This process is repeated until the input functions are equal to the output orbitals, which is known as the Hartree Self-Consistent Field (SCF).

2.1.2.1. Polyelectronic systems in the Hartree model

In the Hartree model, the wavefunction describing a general system containing N electrons is known as the *Hartree product*:

$$\Psi^{\text{HP}} = \chi_i(x_1)\chi_j(x_2) \cdots \chi_\eta(x_N) \quad (2.6)$$

Four years after Hartree's postulate, V. A. Fock noticed that this wavefunction did not follow the antisymmetry principle, which states that the wavefunction of any system containing fermions (in this case, electrons) must be antisymmetric (i.e. change sign) upon interchange of the coordinates of any two electrons. Instead of the Hartree product, Fock improved upon Hartree's work (thus developing the Hartree–Fock approximation, HF) and employed a determinant containing all electrons in all spin orbitals with a normalization factor $1/\sqrt{N!}$ (which stems from the orthonormality of spin orbitals and the necessity that the probability density be equal to 1 in all space) to act as the antisymmetric wavefunction, which is known as a Slater determinant, with the form:

$$\Psi^{\text{SD}} = \frac{1}{\sqrt{(N!)}} \begin{vmatrix} \chi_i(x_1) & \cdots & \chi_\eta(x_1) \\ \vdots & \ddots & \vdots \\ \chi_i(x_N) & \cdots & \chi_\eta(x_N) \end{vmatrix} \quad (2.7)$$

Eq. (2.7) is often written as a single-row determinant by specifying the diagonal of the matrix and leaving out the normalization factor, which is assumed:

$$\Psi^{\text{SD}} = |\chi_i(x_1)\chi_j(x_2) \cdots \chi_\eta(x_N)| \quad (2.8)$$

The Hamiltonian associated to this wavefunction is:

$$H = \left(-\frac{1}{2} \sum_{i=1}^N \nabla^2 - \underbrace{\frac{1}{r_{1A}} - \frac{1}{r_{1B}} \dots + \frac{1}{r_{1M}}}_{\text{Sum over electron and nuclei}} + \underbrace{\frac{1}{r_{12}} \dots + \frac{1}{r_{1N}}}_{\text{Electron-electron terms}} \right) \quad (2.9)$$

The energy of the system can be calculated with the following expression:

$$E = \frac{\int \Psi H \Psi d\tau}{\int \Psi \Psi d\tau} \quad (2.10)$$

The orthonormal nature of spin orbitals results in many of the terms of the integral expansion going to 0, but expanding the integrals in real systems is a very time-consuming task, as many interacting electrons are involved. For this reason, a more generic form is adopted, where the three types of interactions arising from these calculations are explicitly denoted.

Firstly, the kinetic energy and the electron-core interaction energy of a single indistinguishable electron (1) in a spin orbital χ_1 under the influence of M nuclei, H_{ii}^{core} , can be written as:

$$H_{ii}^{core} = \int d\tau_1 \chi_1(1) \left(-\frac{1}{2} \nabla^2 - \sum_{A=1}^M \frac{Z_A}{r_{1A}} \right) \chi_1(1) \quad (2.11)$$

Yielding a favourable (negative) energy contribution from N electrons so that:

$$E_{total}^{core} = \sum_{i=1}^N H_{ii}^{core} \quad (2.12)$$

Next, we obtain an Coulombic interaction between pairs of electrons (electron in coordinates 1 and electron in coordinates 2), J_{ij} :

$$J_{ij} = \iint \chi_i(1) \chi_i(1) \left(\frac{1}{r_{12}} \right) \chi_j(2) \chi_j(2) d\tau_1 d\tau_2 \quad (2.13)$$

The resulting energy arising from this electrostatic repulsion is unfavourable (positive), and its expression including an electron in orbital χ_1 interacting with all other electrons can be written as:

$$E_i^{Coulomb} = \sum_{j \neq i}^N J_{ij} \quad (2.14)$$

The total energy from all Coulombic interactions from the possible combinations of orbitals with all other orbitals is:

$$E_{total}^{Coulomb} = \sum_{i=1}^N \sum_{j=i+1}^N J_{ij} \quad (2.15)$$

Finally, pairs of electrons with parallel spins contain a non-zero term arising from the integral expansion, which corresponds to the exchange interaction K_{ij} :

$$K_{ij} = \iint \chi_i(1)\chi_j(2) \left(\frac{1}{r_{12}} \right) \chi_i(2)\chi_j(1) d\tau_1 d\tau_2 \quad (2.16)$$

This term has no physical meaning and arises from the Pauli exclusion principle—two electrons with the same spin tend to avoid each other so as to not occupy the same space (creating an exclusion area known as the *exchange hole*), therefore decreasing their repulsive Coulombic interaction compared to that expected from the interaction of their average electron densities. Due to orthogonality of the orbitals, integrals in which electrons 1 and 2 have different spins are 0. As with the energy due to electron-electron Coulombic repulsions, the exchange energy between the electron in orbital χ_1 and all other orbitals is:

$$E_i^{Exchange} = \sum_{j \neq i}^N K_{ij} \quad (2.17)$$

While the total energy of the exchange interaction between all electrons corresponds to:

$$E_{total}^{Exchange} = \sum_{i=1}^N \sum_{j=i+1}^N K_{ij} \quad (2.18)$$

The sum of the total kinetic, coulombic and exchange energies in a polyelectronic system yields the total energy of the electrons in the trial spin orbitals. However, most polyelectronic systems are close-shell, i.e. all spin orbitals contain two opposite-spin electrons. In these cases, the energy can be assessed by contemplating a model consisting of a core surrounded by 2 spatial orbitals, ψ_i and ψ_j , each containing two electrons with spins α and β . As represented in Figure 2.1, there are 4 possible Coulombic J_{ij} interactions between the electrons in the different spatial orbitals (which are independent of the spin sign) and only 2 possible exchange $-K_{ij}$ interactions between electrons of identical spin. In addition, we also must consider a J_{ii} interaction between electrons in the same spatial orbital (between which there exists no exchange as they have opposite spins) and the kinetic and potential energy of both

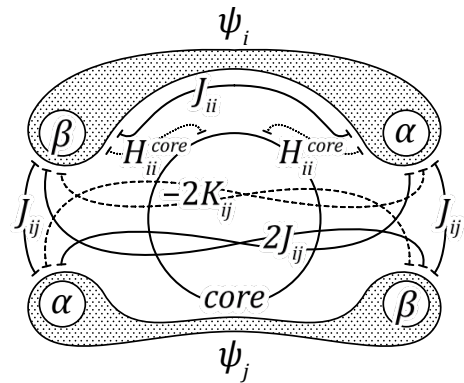


Figure 2.1 Source of all Coulombic (continuous line), exchange (dashed line), kinetic and potential electron-core (dotted line) interactions in a close-shell model system with 2 spatial orbitals. Electron-electron and core-electron interactions in ψ_j have been omitted for clarity.

electrons in each spin orbital under the influence of the core, $2H_{ii}^{core}$. Therefore, the resulting energy for a close-shell system of N electrons in $N/2$ orbitals can be written as:

$$E = 2 \sum_{i=1}^{N/2} H_{ii}^{core} + \sum_{i=1}^{N/2} \sum_{j=i+1}^{N/2} (4J_{ij} - 2K_{ij}) + \sum_{i=1}^{N/2} J_{ii} \quad (2.19)$$

This approach, which substantially simplifies the calculation of the electronic energy, is known as restricted Hartree–Fock (RHF, in contrast to calculating each electronic interaction individually, which is known as unrestricted Hartree–Fock, UHF). RHF can also be partly used alongside UHF in open-shell systems, where Eq. (2.19) is used to assess the interactions between spatial orbitals containing paired electrons, and Eqs. (2.11) to (2.18) are used between the electrons in single-occupied spatial orbitals and the rest; this is referred to as restricted open-shell Hartree–Fock (ROHF).

2.1.3. Linear combination of atomic orbitals

In order to solve the aforementioned HF equations for the description of molecular systems, we must expand on the concept of spatial molecular orbital. We can define each spatial molecular orbital as a linear combination of (spatial) atomic orbitals (the LCAO approach), where each of the atomic orbitals is multiplied by a scalar which determines its weight in the atomic orbital so as to minimize the energy of the wavefunction:

$$\psi_i(\mathbf{r}) = \sum_{v=1}^K c_{iv} \phi_v(\mathbf{r}) \quad (2.20)$$

Each molecular orbital ψ_i (basis set, whose exact analytical form will be discussed in the following chapters) is defined by K atomic orbitals ϕ_v (basis functions) and must, at least, contain the necessary number of basis functions to describe all the electrons in the molecular system. The addition of more basis functions on top of the minimal basis set will lower the energy of the system up to a minimum at which the energy remains invariable (the HF limit). The overall electron density $\rho(\mathbf{r})$ for $N/2$ molecular orbitals is then defined as:

$$\begin{aligned} \rho(\mathbf{r}) &= 2 \sum_{i=1}^{N/2} \psi_i^*(\mathbf{r}) \psi_i(\mathbf{r}) = 2 \sum_{i=1}^{N/2} \left(\sum_{\mu} c_{i\mu}^* \phi_{\mu}^*(\mathbf{r}) \right) \left(\sum_{\nu} c_{i\nu} \phi_{\nu}(\mathbf{r}) \right) \\ &= \sum_{\mu} \sum_{\nu} \underbrace{\left(2 \sum_{i=1}^{N/2} c_{i\mu}^* c_{i\nu} \right)}_{P_{\mu\nu}} \phi_{\mu}^*(\mathbf{r}) \phi_{\nu}(\mathbf{r}) \end{aligned} \quad (2.21)$$

Where $P_{\mu\nu}$ is the electronic *density matrix*, which describes the complete charge density of the system and is extremely useful for the analysis and identification of covalent and non-covalent interactions.¹²⁶

If we introduce the LCAO into the HF formulation of the electronic energy, the equations of the one-electron terms now become as follows:

$$\begin{aligned} H_{ii}^{core} &= \int \psi_i(1) h(i) \psi_i(1) d\tau_1 = \sum_{\mu} \sum_{\nu} c_{i\mu}^* c_{i\nu} \int \phi_{\mu}(1) h(i) \phi_{\nu}(1) d\tau_1 \\ &= \sum_{\mu} \sum_{\nu} c_{i\mu}^* c_{i\nu} H_{\mu\nu}^{core} \end{aligned} \quad (2.22)$$

For the two-electron terms, as now we are involving four molecular orbitals, we will use a shorthand notation in which each pair of orbitals that act upon electron 1 and 2 are written on the left and on the right side of a dividing line, respectively, and enclosed by parentheses:

$$\int \int \phi_{\mu}(1) \phi_{\nu}(1) \frac{1}{r_{12}} \phi_{\lambda}(2) \phi_{\sigma}(2) d\tau_1 d\tau_2 \equiv (\mu\nu|\lambda\sigma) \quad (2.23)$$

Rewriting the Hartree–Fock equations in terms of atomic orbitals and using this notation for J_{ij} and K_{ij} gives:

$$\begin{aligned} J_{ij} &= \sum_{\mu} \sum_{\nu} \sum_{\lambda} \sum_{\sigma} c_{\mu}^i c_{\nu}^j c_{\lambda}^k c_{\sigma}^l (\mu\nu|\lambda\sigma) \\ K_{ij} &= \sum_{\mu} \sum_{\nu} \sum_{\lambda} \sum_{\sigma} c_{\mu}^i c_{\nu}^j c_{\lambda}^k c_{\sigma}^l (\mu\lambda|\nu\sigma) \end{aligned} \quad (2.24)$$

Equation (2.19) for a close-shell system can be solved in terms of the LCAO by means of the Roothaan–Hall method,¹²⁷ which reformulates the molecular HF equations as matrices with which we can operate using conventional operations; this will not be further explored in this thesis.

2.2. Density functional theory

Up to this point, we have discussed all the main interactions present in a molecular system and how we can assess them analytically by means of the HF equations using the electronic wavefunction to solve the time-independent Schrödinger equation. A major advantage of the electronic description of HF lies on the fact that the electronic spin correlation is built into the method by means of the exchange interaction term; however, HF fails to describe electron-electron correlation accurately, as it neglects the effect that the Coulombic repulsion that individual electrons exert upon each other has on their movement, and instead treats the potential generated by all electrons as a mean field. There have been approaches to include the correlation energy into the HF formulation, but these are deemed too computationally demanding and still require the use of a multi-determinant wavefunction. We have previously defined the *HF limit*, i.e. the minimum energy achievable by using the HF approximation, which is invariable with the increase of the number of basis functions used for the description of the basis set; specifically, the Löwdin interpretation of the correlation energy describes it as the difference between the exact energy and the energy at the HF limit:

$$E_C = E_{exact} - E_{HF} \quad (2.25)$$

In addition, the HF approach fully relies on the use of the wavefunction which is rather abstract and is not observable. Its square, however, does have a physical interpretation (the electron density) and can be easier to work with, as it is a 3-dimensional property that does not depend on the coordinates of each individual electron.

2.2.1. The Hohenberg–Kohn theorems

Based on the groundwork laid by Thomas and Fermi in 1927,¹²⁸ in 1964 Hohenberg and Kohn built the foundation for the *Density Functional Theory* (DFT) by developing the Hohenberg–Kohn theorems, which are as follows:

- 1) *The ground state of any set of interacting particles is a unique functional (a function of a function) of the electron density $\rho(\mathbf{r})$, so that $\Psi_{GS} = \Psi[\rho_0(\mathbf{r})]$. Therefore, the energy and the properties of any polyelectronic system depend on the overall electron density—the energy, E , is also a functional of $\rho(\mathbf{r})$.*
- 2) *There exists a true ground state electron density that minimises the total energy and results in the ground state energy obtainable through the Schrödinger equation. Therefore, this can be achieved through a variational principle.*

The energy functional dependent on the density is as follows:

$$E[\rho(\mathbf{r})] = \int V_{ext}(\mathbf{r})\rho(\mathbf{r})d\mathbf{r} + F[\rho(\mathbf{r})] \quad (2.26)$$

In this formulation, $V_{ext}(\mathbf{r})$ contains all potentials under which the electron moves, such as those created by the nuclei. $F[\rho(\mathbf{r})]$, also known as the *Hohenberg–Kohn universal functional*, is defined as the sum of the kinetic energy of all the electrons and the electron-electron interactions. In contrast with HF's interpretation of the energy contributions, $F[\rho(\mathbf{r})]$ does not have a clear definition and, as we will see in the next sections, must be approximated.

2.2.2. Kohn–Sham density functional theory

In 1965, Kohn and Sham redefined Hohenberg–Kohn's theorem in terms of a fictitious non-interacting system of electrons moving under an external potential (the Kohn–Sham potential). Under the Kohn–Sham scheme, this non-interacting system of electrons (the Kohn–Sham system) has the same ground energy as the fully interacting system of electrons. More importantly, they re-assessed Hohenberg and Kohn's formulation of the energy potential by re-considering the electron density, $\rho(\mathbf{r})$, as the sum of the squares of one-electron non-interacting orthonormal orbitals—the *Kohn–Sham orbitals* (χ_i^{KS}):

$$\rho(\mathbf{r}) = \sum_i^N |\chi_i^{KS}(\mathbf{r})|^2 = \rho_0(\mathbf{r}) \quad (2.27)$$

This provided a way of clearly defining the kinetic energy of the electrons based on the wavefunction, while considering the total electron density for the electron-electron and electron-core interactions. With this in mind, $F[\rho(\mathbf{r})]$ can be defined as:

$$F[\rho(\mathbf{r})] = T_s[\rho(\mathbf{r})] + E_H[\rho(\mathbf{r})] + E_{xc}[\rho(\mathbf{r})] \quad (2.28)$$

Where $T_s[\rho(\mathbf{r})]$ is the kinetic energy of the electron in the non-interacting system, which is expressed in an identical fashion to the HF formulation:

$$T_s[\rho(\mathbf{r})] = \sum_{i=1}^N \int \chi_i^{KS}(\mathbf{r}) \left(-\frac{1}{2} \nabla^2 \right) \chi_i^{KS}(\mathbf{r}) d\mathbf{r} \quad (\text{a.u.}) \quad (2.29)$$

$E_H[\rho(\mathbf{r})]$ is the pair-wise Coulombic interaction (also known as the Hartree electrostatic energy) between electron densities:

$$E_H[\rho(\mathbf{r})] = \frac{1}{2} \iint \frac{\rho(\mathbf{r}_1)\rho(\mathbf{r}_2)}{|\mathbf{r}_1 - \mathbf{r}_2|} d\mathbf{r}_1 d\mathbf{r}_2 \quad (2.30)$$

And $E_{xc}[\rho(\mathbf{r})]$ corresponds to the non-classical exchange and correlation electron-electron interactions defined previously, which can be written as follows:

$$E_{xc}[\rho(\mathbf{r})] = \underbrace{\{T[\rho(\mathbf{r})] - T_s[\rho(\mathbf{r})]\}}_{T_C[\rho(\mathbf{r})]} + \underbrace{\{E_{ee}[\rho(\mathbf{r})] - E_H[\rho(\mathbf{r})]\}}_{E_{NC}[\rho(\mathbf{r})]} \quad (2.31)$$

Where the correlation contribution to the kinetic energy, $T_C[\rho(\mathbf{r})]$, corresponds to the difference between the true kinetic energy and the kinetic energy of the non-interacting system of electrons, and the term containing non-classical electronic interactions, $E_{NC}[\rho(\mathbf{r})]$, results from the difference between all electron-electron interactions and the Coulombic interactions between the electron densities. Hence, the total electronic energy for a system with N electrons within the Kohn-Sham formulation is:

$$\begin{aligned} E[\rho(\mathbf{r})] &= \sum_{i=1}^N \int \chi_i^{KS}(\mathbf{r}) \left(-\frac{1}{2} \nabla^2 \right) \chi_i^{KS}(\mathbf{r}) d\mathbf{r} \\ &\quad + \frac{1}{2} \sum_{i=1}^N \sum_{j=1}^N \iint |\chi_i^{KS}(\mathbf{r}_1)|^2 \left(\frac{1}{r_{12}} \right) |\chi_j^{KS}(\mathbf{r}_2)|^2 d\mathbf{r}_1 d\mathbf{r}_2 + E_{xc}[\rho(\mathbf{r})] \quad (2.32) \\ &\quad - \sum_{i=1}^N \int \sum_{A=1}^M \frac{Z_A}{r_{1A}} |\chi_i^{KS}(\mathbf{r}_1)|^2 d\mathbf{r} \quad (\text{a.u.}) \end{aligned}$$

It is worth highlighting that, while electron-electron interactions and electron-nuclei interactions are represented by terms which are dependent on the electron density, the kinetic energy is that of a non-interacting system of electrons and, thus, a known function which is solely dependent on the wavefunction. In an identical fashion to the SCF method in HF, solving this equation requires applying a variational principle, in which a

series of trial orthonormal molecular orbitals are used to consistently minimise the energy (taking into account Kohn and Sham's definition of the electron density in Eq. (2.27)). The one-electron Kohn–Sham equations are then:

$$\left\{ -\frac{1}{2}\nabla^2 + \left[\int \frac{\rho(\mathbf{r}_2)}{r_{12}} d\mathbf{r}_2 + V_{xc}(\mathbf{r}_1) - \sum_{A=1}^M \frac{Z_A}{r_{1A}} \right] \right\} \chi_i^{KS}(\mathbf{r}_1) = \varepsilon_i \chi_i^{KS}(\mathbf{r}_1) \quad (\text{a.u.}) \quad (2.33)$$

Where V_{xc} is the exchange-correlation functional, which is the gradient of the exchange energy defined in Eq. (2.31), $V_{xc}(\mathbf{r}) = \delta E_{xc}[\rho(\mathbf{r})]/\delta\rho(\mathbf{r})$. In a similar approach to the UHF approach for open-shell systems discussed previously, in systems with an electron density which is characterised by a spin density which is predominant to the other (defined by the difference of densities of electrons with spins α and β , $\sigma(\mathbf{r}) = \rho_\alpha(\mathbf{r}) - \rho_\beta(\mathbf{r})$), V_{xc} depends on both the electron density and the spin density, leading to two different sets of equations. This approach will be applied computationally in the majority of the systems discussed in this thesis.

2.2.3. Exchange-correlation functionals

If we are to find a solution to the Kohn–Sham equations using a self-consistent field and a set of trial wavefunctions, we must find an approach to reveal the nature of $E_{xc} = E_x + E_c$. To do this, two main approximations are used, namely the local density approximation (LDA, which in open-shell systems is also dependent on the spin densities—LSDA) and the generalised gradient approximation (GGA).

2.2.3.1. Local spin density approximation

This approach, introduced by Kohn and Sham, builds upon the idea that the electron density is constant in all space, a concept which was firstly envisioned by Thomas and Fermi and is referred to as the *uniform electron gas* (UEG) model. Despite the real electron density not being by any means homogeneous, Kohn and Shan defined it as a *collection* of constant electron densities, each described by that of a UEG. Each point in space contains a given electron density that, in turn, is defined by an exchange-correlation energy, a function of the density of the UEG, ε_{xc} , so that the total exchange correlation energy, E_{xc} , results from integrating it in all space:

$$E_{xc}[\rho_\alpha(\mathbf{r}), \rho_\beta(\mathbf{r})] = \int \rho(\mathbf{r}) \varepsilon_{xc}[\rho_\alpha(\mathbf{r}), \rho_\beta(\mathbf{r})] d\mathbf{r} \quad (2.34)$$

ε_{xc} is defined as a known analytical function and is usually divided into the exchange and correlation terms separately. For instance, the Slater description of the exchange energy for the LSDA approximation takes the following form:

$$\varepsilon_x^{LSDA}[\rho_\alpha(\mathbf{r}), \rho_\beta(\mathbf{r})] = -\frac{3}{2} \left(\frac{3}{4\pi} \right)^{\frac{1}{3}} \int [\rho_\alpha^{4/3}(\mathbf{r}) + \rho_\beta^{4/3}(\mathbf{r})] d\mathbf{r} \quad (2.35)$$

The correlation term $\varepsilon_c^{L(S)DA}$ has been calculated using quantum Monte Carlo, and has been tabulated for close-shell and open-shell systems. This parametrized analytical function is always solely dependent on the local Wigner-Seitz radius r_s , where $r_s^3 = 3/\{4\pi\rho(\mathbf{r})\}$.

2.2.3.2. Generalized gradient approximation

Despite the simplicity of the approach, using a UEG as the source for exchange and correlation often yields unrealistic results—it tends to overestimate binding energies and provide unrealistic bond lengths. The solution to this was to approximate the electron density not only to a constant dictated by the UEG, but also considering the nature of the electron density at each point in space—introducing functions of $\nabla\rho(\mathbf{r})$. This approach is known as the generalized gradient approximation (GGA), and is the basis of the functionals used for the calculation of solid state structures in this thesis. The exchange term in GGA is defined by the exchange energy per particle, ε_x , integrated over all space, with an enhancement factor F_x (which varies from functional to functional). This equation, for an open-shell system, is as follows:

$$E_x^{GGA}[\rho_\alpha(\mathbf{r}), \rho_\beta(\mathbf{r})] = \int \varepsilon_x^{LSDA}[\rho_\alpha(\mathbf{r}), \rho_\beta(\mathbf{r})]\rho(\mathbf{r}) F_x(s) \quad (2.36)$$

Where s is the reduced density gradient

$$s(\mathbf{r}) = \frac{1}{2(3\pi^2)^{\frac{1}{3}}} \frac{|\nabla\rho(\mathbf{r})|}{\rho(\mathbf{r})^{\frac{4}{3}}} \quad (2.37)^{**}$$

The GGA correlation energy usually takes the following form:

^{**} The visualization of s with respect to ρ in Eq. (2.37) has a direct pseudo-quantitative interpretation for the identification of all interactions in molecular and supramolecular complexes.^{126,129} Specifically, electron density regions where the reduced density matrix tends to zero are characterised by a density gradient which also tends to zero, indicating an inflection point between two density maxima. The actual electron density at these points can be related to the interaction strength: the larger the electron density, the more intense the interaction is. Finally, the attractive or repulsive nature of the interaction can be assessed by investigating the *curvature* of the electron density, $\nabla^2\rho$. Since the overall curvature is dominated by attractive electron-core interactions, the local curvatures in the diagonalised Hessian of the electronic density matrix in Eq. (2.21) (containing the second order partial derivatives) are considered. Specifically, the second eigenvalue, λ_2 , is found to be a good indicator of the interaction behaviour, as it appears negative when the interaction is attractive and positive when it is repulsive. Therefore, by analysing the reduced density gradient in all points of the electron density and plotting s vs. $\text{sign}(\lambda_2)\rho$, we can identify the interactions as *peaks* in the electron density. The non-covalent interactions of the systems discussed in this thesis, characterised by peaks near the origin—as they are far weaker than covalent bonds—, have been analysed with this methodology.

$$E_c^{GGA}[\rho_\alpha(\mathbf{r}), \rho_\beta(\mathbf{r})] = \int \rho(\mathbf{r})[\varepsilon_c^{LSDA} + H(r_s, \zeta, t)] d\mathbf{r} \quad (2.38)$$

$\zeta = (\rho_\alpha(\mathbf{r}) - \rho_\beta(\mathbf{r}))/\rho(\mathbf{r})$ is the relative spin polarization and

$$t = \frac{|\nabla\rho(\mathbf{r})|}{2\phi k_s \rho(\mathbf{r})}, \text{ where } \phi(\zeta) = \frac{[(1+\zeta)^{2/3} + (1-\zeta)^{2/3}]}{2} \quad (2.39)$$

and $k_s = \sqrt{\frac{4k_F}{\pi a_0}}$, where $a_0 = \frac{\hbar^2}{me^2}$ is the Bohr radius.

k_F is the Fermi momentum for the UEG. Similarly to the enhancement factor in the exchange energy, the correlation contribution function $H(r_s, \zeta, t)$ also varies depending on the functional.

The main functional used for the study of periodic structures in this thesis is the Perdew–Burke–Ernzerhof (PBE) exchange–correlation functional,¹³⁰ developed in 1996. PBE builds upon the Perdew–Wang 91 (PW91) exchange–correlation functional,¹³¹ which contains a deeply parametrized F_x factor, with the form:

$$F_x^{PW91}(s) = \frac{1 + 0.19645s \sinh^{-1}(7.7956s) + (0.2743 - 0.1508 e^{-100s^2})s^2}{1 + 0.19645 \sinh^{-1}(7.7956s) + 0.004s^4} \quad (2.40)$$

The PBE functional sought to decrease the dependence of PW91 on so many empirical parameters (and only rely on those which can be calculated with quantum mechanical methods), as well as to correct the asymptotic behaviour of F_x so that it spans through larger values of s in order to account for the exchange potentials at larger interelectronic distances. With this in mind, F_x in the PBE functional has a much simpler form:

$$F_x^{PBE}(s) = 1 + \kappa - \frac{\kappa}{1 + \left[\frac{\mu s^2}{\kappa}\right]} \quad (2.41)$$

Where $\kappa = 0.804$ and $\mu \simeq 0.21951$. As for the correlation energy, $H(r_s, \zeta, t)$ takes the form:

$$H = \frac{e^2}{a_0} \gamma \phi^3 \times \ln \left\{ 1 + \frac{\beta}{\gamma} t^2 \left[\frac{1+At^2}{1+At^2+A^2t^4} \right] \right\}, \text{ where } A = \frac{\beta}{\gamma} \left[-e^{-\frac{\varepsilon_c^{LDA}}{\gamma \phi^3 e^2 / a_0}} - 1 \right]^{-1} \quad (2.42)$$

$$\beta \simeq 0.066725 \text{ and } \gamma \simeq 0.031091$$

2.2.3.3. Limitations of GGA

Despite its applicability to a wide range of materials and the large number of GGA and LDA functionals developed, we have to consider the major and interconnected drawbacks with the use of GGA and LDA-based methodologies compared to HF. Firstly, while HF deals with an approximate form of the wavefunction for the molecular orbitals and draws an exact solution to it based on the variational principle (and adding more determinants to the wavefunction brings the solution closer to the HF limit), the approach in DFT is inverse: we begin with the *exact* density function (2.27) as the unimprovable object to which exchange and correlation are approximated. These exchange and correlation terms are readily embedded in the formulation of DFT but

their nature are unknown, and therefore, the approaches to the exchange and correlation energies are necessarily inexact. This gives rise to the final and most limiting downsides of DFT, which is the *self-interaction error* (SIE). In HF, the Coulombic and exchange terms in Eq. (2.19) are cancelled out when $J_{ii} = K_{ii}$, and therefore, the spurious interaction of an electron with itself is avoided. Because of the approximate nature of the exchange and correlation functional in DFT, the self-interaction error is non-zero and has to be accounted for:

$$E_{SIE} = \left| \frac{1}{2} \iint \frac{\rho(\mathbf{r}_1)\rho(\mathbf{r}_2)}{|\mathbf{r}_1 - \mathbf{r}_2|} d\mathbf{r}_1 d\mathbf{r}_2 - E_{xc}[\rho(\mathbf{r})] \right| > 0 \quad (2.43)$$

Some approaches have been developed in order to mitigate the effect of the SIE in GGA, the two predominant ones being DFT+ U and the use of hybrid functionals. Due to the nature of the contents of this thesis, the latter will be discussed.

2.2.3.4. Hybrid functionals

This method attempts to replace all or part of the exchange energy in GGA with the exact HF exchange energy term as a function of the Kohn–Sham molecular orbital:

$$E_x^{HF} = \sum_{i=1}^{N/2} \sum_{j=i+1}^{N/2} \iint \psi_i(\mathbf{r}_1)\psi_j(\mathbf{r}_1) \left(\frac{1}{r_{12}} \right) \psi_i(\mathbf{r}_2)\psi_j(\mathbf{r}_2) d\mathbf{r}_1 d\mathbf{r}_2 \quad (2.44)$$

The final DFT exchange-correlation term will then contain a fraction a of the HF exchange:

$$E_{xc} = (1 - a)E_{xc}^{DFT} + aE_x^{HF} \quad (2.45)$$

For instance, one of the most widely used hybrid functionals, B3LYP, contains an exchange-correlation energy with contributions from the Becke 88 exchange functional¹³² and the Lee–Yang–Parr (LYP) correlation functional,¹³³ with the following form:

$$E_{xc}^{B3LYP} = (1 - a)E_x^{LSDA} + aE_x^{HF} + b\Delta E_x^B + (1 - c)E_c^{LDA} + cE_c^{LYP} \quad (2.46)$$

Where a , b and c are 0.20, 0.72 and 0.81, respectively. Other hybrid functionals (*range separated functionals*, as opposed to *global functionals* which contain a constant fraction of HF exchange) mix different ratios of HF exchange at different regions, using a larger E_x^{HF} contribution at long range interactions (LR)—from which an accurate definition of the exchange hole is harder to achieve using GGA functionals—, and keeping the GGA or LDA approach for the exchange for short range interactions (SR).^{††} The exchange- correlation energy for long range-corrected (LC) functionals is:

^{††} Some range-separated hybrid functionals, however, mix exchange terms the other way round—including HF it in the short range interactions, while only considering the GGA approach for long range, such as the Heyd–Scuseria–Ernzerhof (HSE) functional.

$$E_{xc}^{LC-DFT} = E_x^{LR-HF} + E_x^{SR-DFT} + E_c^{DFT} \quad (2.47)$$

To achieve this, the operating term $1/r_{12}$ in (2.44) is divided into two terms:

$$\frac{1}{r_{12}} = \frac{1 - [\alpha + \beta(1 - \omega_{RSF}(\gamma, r_{12}))]}{\underbrace{r_{12}}_{SR-DFT}} + \frac{\alpha + \beta(1 - \omega_{RSF}(\gamma, r_{12}))}{\underbrace{r_{12}}_{LR-HF}} \quad (2.48)$$

These functionals use a soft *separating* function, $\omega_{RSF}(\gamma, r_{12})$, that controls the manner in which the HF and DFT exchanges intersect and mix as a function of the range. This function usually takes the form of the complementary error function $\text{erfc}(\omega r)/r$ for SR and the error function $\text{erf}(\omega r)/r$ for LR. α , β and γ are mixing parameters, which are parametrized against observed data for each functional.

One major aspect in the calculation of the ground state properties of molecular systems is the need for a *good* functional which correctly characterises the exchange and correlation energies and that can accurately describe long-range vdW interactions, which play a key role in reactivity and in the formation of supramolecular complexes. Accordingly, $\omega B97XD$,^{134,135} developed by Chai and Head-Gordon in 2008, builds upon Becke's B97 functional¹³⁶ to create a range-corrected (ω), hybrid (X) and dispersion-corrected (D) functional, which includes an expansion of the electron density and its first derivative in the definition of the exchange-correlation energy. Initially, the parameters of the used B97 exchange were tailored so as to fit the calculated atomization energies, ionization potentials, electron affinities, total atomic energies and proton affinities to a dataset of experimental values, obtaining a ten-parameter fitting equation with an accuracy beyond B3LYP for the tested type systems. Based on this functional, $\omega B97XD$ contains an exchange correlation energy formed by B97 SR exchange and correlation, while including both LR and SR HF exchange.

$$E_{xc}^{\omega B97X} = E_x^{LR-HF} + c_x E_x^{SR-HF} + E_x^{SR-B97} + E_c^{B97} \quad (2.49)$$

Optimal values for ω and the various coefficients were obtained by fitting to a training set of 412 experimental and theoretical data, including similar types of parameters to those in B97. As will be discussed in Section 2.5, Chai and Head-Gordon also included the E_{disp}^{D2} correction with the tailor-made f_{damp}^{CHG} damping function in addition to the expression for the exchange and correlation, which yields a more accurate asymptotic behaviour of the energy at LR. Due to the completeness of this methodology and the satisfactory results obtained in previous theoretical studies from our group and others,^{137,138} $\omega B97XD$ will be used for the calculation of the properties of all molecular species in this thesis.

2.3. Description of solid state systems

One could argue that the physical definition of a molecule is relatively simple: a delimited *cluster* of bonded atoms, each characterised by a set of spatial coordinates. In the DFT approach, the electronic energy of a

molecule is defined by considering a set of non-interacting electrons, where the trial functions used in the self-consistent field calculations are usually functions with a *localised* range of impact (as we will discuss in Section 2.4.1). Some of the structures presented in this thesis, however, are not molecules but *crystals*, large arrangements of atoms which are closely packed together and distributed in a patterned fashion, displaying motifs of a repeating unit (*unit cell*) throughout the structure. Due to the vast number of atoms forming the crystal (there are *ca.* 10^{18} atoms in a grain of salt), it is usually more feasible to consider it not as an immense structure with an orderly distribution of atoms and defined edges surrounded by vacuum (a *cluster model*), but rather as an *infinite* structure with a given periodicity, which simplifies the calculations to study these materials. In this section, a comprehensive overview of how periodic systems are defined and their properties calculated will be provided.

2.3.1. The Bravais lattice

Crystals are defined by two aspects: the atoms or molecules that form them and their underlying lattice structure onto which the atoms are positioned. This base structure is equivalent from all positions, i.e. the distribution of the neighbouring lattice points is the same regardless of the chosen crystallographic centre (as displayed in Figure 2.2). Every point in this grid is then defined by a lattice vector \mathbf{R} :

$$\mathbf{R} = n_1\mathbf{a}_1 + n_2\mathbf{a}_2 + n_3\mathbf{a}_3 \quad (2.50)$$

Where \mathbf{a}_1 , \mathbf{a}_2 and \mathbf{a}_3 are basis vectors in cartesian coordinates that describe the real space of the crystal lattice, and n_{1-3} are integers that define all possible lattice points that can be built as multiples of the basis vectors. This configuration of lattice points is defined by a *primitive cell* (dashed line in Figure 2.2), a unit describing the smallest building block of the periodic structure with which, by stacking with identical primitive cells, we can build the entire crystal lattice without overlaps.

An inherent property of all periodic structures is *symmetry*. We can apply symmetry operations to the structure (rotations, reflections and inversions) so that the resulting structure remains unaltered. In the case of the honeycomb lattice in Figure 2.2 (which has the P6mm group in the Hermann–Mauguin notation^{139,140}), we can easily see that there is a C_6 symmetry axis at the middle of the hexagons, as well as a C_2 symmetry axis in the middle of the chosen primitive cell, among others. In some 3-D crystal structures, however, these symmetry operations are more clearly seen not by using the primitive cell, but a unit cell that contains other symmetrically equivalent lattice points to facilitate visualization. All 3-D crystals in nature, in turn, can be categorised based on their

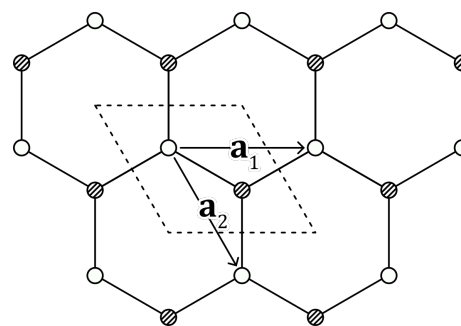


Figure 2.2 Representation of a 2-D honeycomb lattice. The equivalence between lattice points is illustrated by shaded and clear atoms—these represent the two different *sublattices* inside the crystal. A chosen primitive cell is delimited with a dashed line.

translational and rotational symmetries, giving rise to a total of 7 categories and 14 possible configurations, the Bravais lattices, represented in Figure 2.3.

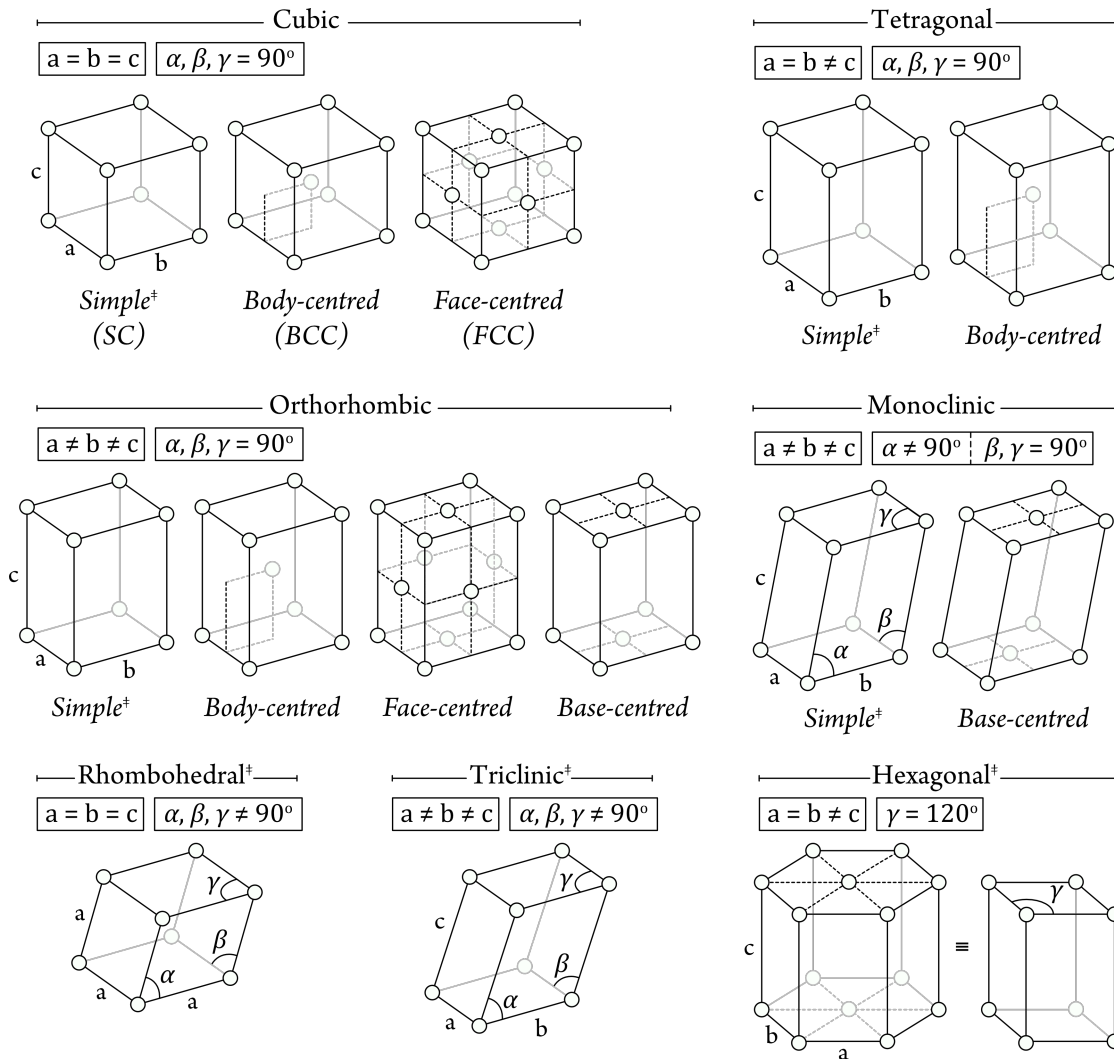


Figure 2.3 Schematic representation of the 7 categories and 14 Bravais lattice types. Each lattice is defined by their lattice parameters a , b and c and angles α , β and γ . The symbol \dagger indicates lattice types which are represented by their primitive unit cells, while all others are conventional unit cells with multiple lattice points. The leftmost representation of the hexagonal Bravais lattice highlights its distinct honeycomb pattern, while its primitive unit cell is displayed on the right. Crystals that have the hexagonal lattice usually display a layered structure to optimise the packing efficiency (*hexagonal close packing, hcp*).

However, both mono-elemental and multi-elemental crystals can be formed by a combination of two or more sublattices, each one represented by a Bravais lattice type. This is the case of the zinc blende structure (F-43m symmetry group) that has been studied in this thesis, which is formed by two intersecting FCC lattices.

In addition to the aforementioned primitive and unit cells, a third type of unit cell which we can build from a given lattice is the *Wigner–Seitz cell*. This is a special case of primitive cell which is not necessarily made up of parallel planes and contains only one lattice point, and is comprised of a Voronoi diagram around the central lattice point—forming a geometrical shape whose planes are equidistant from the central lattice point and the rest. The Wigner-Seitz cell of a BCC lattice is represented in Figure 2.4.

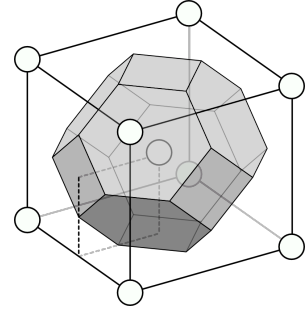


Figure 2.4 In grey, Wigner–Seitz primitive cell of a BCC lattice.

2.3.2. The reciprocal space

In order to describe how to approach the calculation of periodic structures, we first need to understand the experimental strategies followed in the characterisation of these systems. The structure of a crystal is determined by X-ray diffraction (XRD), where a beam of X-ray is irradiated onto a crystal (usually in powder form) and the scattered light is analysed. In 1913, William Henry Bragg and his son, William Lawrence Bragg, were the first to discover that the irradiation reflected by the crystal displayed very characteristic ring-like patterns, or *peaks* if the bisection of the ring was plotted.¹⁴¹ They speculated that these peaks were the result of constructive interactions between the reflected waves of parallel planes in the crystal, separated by a distance d . Max von Laue later introduced a more formal description of this interaction by considering two scatterer lattice points separated by a vector \mathbf{T} . The incident ray, with a wavelength λ , is defined by a plane wave $e^{i\mathbf{k}\mathbf{R}}$ with a wavevector $\mathbf{k} = 2\pi/\lambda \hat{\mathbf{k}}$, while the scattered light has a plane wave $e^{i\mathbf{k}'\mathbf{R}}$ with a wavevector $\mathbf{k}' = 2\pi/\lambda \hat{\mathbf{k}'}$. The condition for constructive interaction from the scattering of the two atoms is:

$$(\hat{\mathbf{k}}' - \hat{\mathbf{k}}) \cdot \mathbf{T} = m\lambda \rightarrow \underbrace{(\mathbf{k} - \mathbf{k}') \cdot \mathbf{T}}_{\mathbf{G}} = 2\pi m \quad (2.51)$$

Where m is an integer and \mathbf{G} is a reciprocal lattice vector $\mathbf{G} = m_1\mathbf{b}_1 + m_2\mathbf{b}_2 + m_3\mathbf{b}_3$ (analogous to \mathbf{R} in Eq. (2.50)) which represents any vector that satisfies Eq. (2.51). The collection of these vectors forms the *reciprocal lattice* in the reciprocal or k -space, with units of length^{-1} and basis vectors \mathbf{b}_1 , \mathbf{b}_2 and \mathbf{b}_3 , which are related to the basis vectors of the *real* (direct) lattice in (2.50) by the following equivalences:

$$\mathbf{b}_1 = 2\pi \frac{\mathbf{a}_2 \times \mathbf{a}_3}{\mathbf{a}_1 \cdot (\mathbf{a}_2 \times \mathbf{a}_3)} \quad \mathbf{b}_2 = 2\pi \frac{\mathbf{a}_3 \times \mathbf{a}_1}{\mathbf{a}_1 \cdot (\mathbf{a}_2 \times \mathbf{a}_3)} \quad \mathbf{b}_3 = 2\pi \frac{\mathbf{a}_1 \times \mathbf{a}_2}{\mathbf{a}_1 \cdot (\mathbf{a}_2 \times \mathbf{a}_3)} \quad (2.52)$$

A simple approach to understand the diffraction peaks observed in XRD is by envisioning a sphere of radius $1/\lambda$ in the reciprocal space (an *Ewald sphere*)¹⁴² delimiting a set of reciprocal lattice points (represented as an empty circle in Figure 2.5). This sphere, of which we will consider a bisection along the X-Y plane for simplification purposes ($\mathbf{b}_3 = 0$), intersects with two points in the reciprocal lattice equidistant to the centre of the circle. If we take one of the points as our scatterer at the origin, we can describe another point (represented by a reciprocal lattice vector $\mathbf{G} = 0\mathbf{b}_1 + 2\mathbf{b}_2 + 0\mathbf{b}_3$, (020) in Figure 2.5) which represents the scattering point at the reciprocal plane closest to the incident beam. This point is, by definition, a scatterer which satisfies Eq. (2.51) and, therefore, will display a

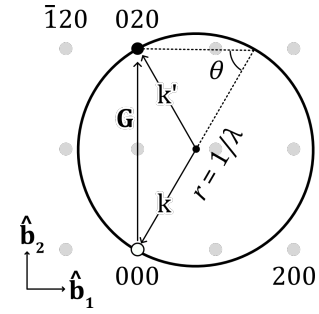


Figure 2.5 Representation of an Ewald sphere, with points in the reciprocal lattice denoted as dots.

maximum in the X-ray reflection ring. This condition will be met by *any* reciprocal point inside the sphere, as we can rotate the angle of incidence and change the orientation of the sphere taking (000) as the pivotal origin. This effect is sought with the use of powdered crystals, since using a powder allows for the random orientation of all containing crystals so that constructive interaction can occur with all possible points inside the Ewald sphere. As for the choice of wavelength for the incident beam (which determines the Ewald sphere radius), this must be small enough so that the Ewald sphere encompasses enough reciprocal points, but not so small that it includes too many constructive interactions and over-represents peaks (hence the use of X-rays with a wavelength of $\sim 1 \text{ \AA}$). Hence, the distance between scattering Bragg planes displaying a peak must be a multiple of the scattered beam wavelength $\lambda_G = 2\pi/|\mathbf{G}|$. We then can relate the interplanar distance with the reciprocal lattice vector \mathbf{G} within the Ewald construction scheme:

$$d_{hkl} = d_{000 \rightarrow 020} = \frac{1}{|\mathbf{G}|} = \frac{1}{|h\mathbf{b}_1 + k\mathbf{b}_2 + l\mathbf{b}_3|} \quad (2.53)$$

Where integers h , k and l are Miller indices, which represent the coordinates of the plane hkl normal to the shortest reciprocal lattice vector that satisfies this condition. From this construction, Bragg's law¹⁴¹ is straightforward to derive:

$$\sin \theta = \frac{1}{\frac{2d_{hkl}}{\frac{1}{\lambda}}} \rightarrow \lambda = 2d_{hkl} \sin \theta \quad (2.54)$$

The hkl plane, which denotes a characteristic plane in the crystal, can be drawn by imagining the Miller indices as indicators of where the plane intersects with the basis vectors \mathbf{a}_1 , \mathbf{a}_2 and \mathbf{a}_3 ; for instance, plane (100) will only be intersected once by vector \mathbf{a}_1 in the unit cell. Three examples of planes in the SC lattice (represented in Figure 2.3) are displayed in Figure 2.6.

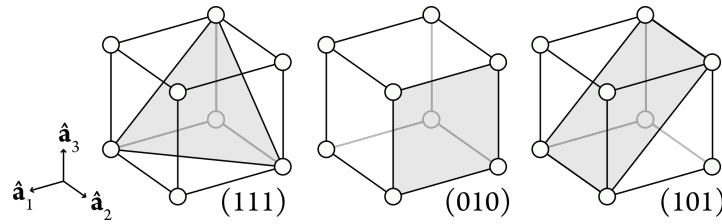


Figure 2.6 Lattice planes with Miller indices (111), (010) and (101) in a SC unit cell displayed as shaded surfaces.

Similarly to the case with the direct lattice, we can build a Wigner–Seitz primitive cell around a central point (Γ) in the reciprocal lattice, which is known as the *first Brillouin zone* (1st BZ). This is represented for a BCC cell in Figure 2.7. The primitive cell in the reciprocal space contains a set of high-order symmetry or *critical* points, which are points of interest that define the shape of the Wigner–Seitz cell and vary depending on the investigated Bravais lattice. For a BCC’s 1st BZ, these points are Γ , N, H and P, which are at the centre of the Wigner–Seitz cell, the centre of a face, and at the intersection of four and three edges, respectively.

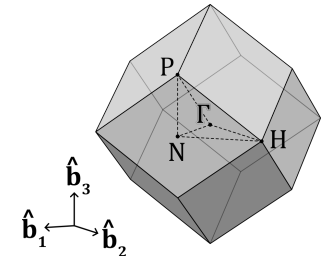


Figure 2.7 First Brillouin zone of the BCC unit cell. Γ , N, H and P denote high symmetry points in the reciprocal lattice.

2.3.3. Periodic boundary conditions and Bloch’s theorem

If we are to investigate the properties of the electrons in crystals, we must adapt Eq. (2.1) for a periodic system. With this aim, we first consider the nature of the external potential $V(\mathbf{r})$ which, since the source of potential will be the perfectly ordered nuclei, displays the same periodicity as the Bravais lattice, so that $V(\mathbf{r} + \mathbf{R}) = V(\mathbf{r})$, where \mathbf{R} is any vector in the crystal lattice. The periodicity of the system, hence, allows us to use an expression for the wavefunction as a plane wave times a periodic function:

$$\psi_{\mathbf{k}}(\mathbf{r}) = e^{i\mathbf{k}\cdot\mathbf{r}}u_{\mathbf{k}}(\mathbf{r}) \quad (2.55)$$

$$u_{\mathbf{k}}(\mathbf{r}) = u_{\mathbf{k}}(\mathbf{r} + \mathbf{R}) \quad (2.56)$$

This is known as *Bloch’s theorem*. One important consequence of Eq. (2.55) is that any vector \mathbf{k}' outside the 1st BZ will have the same function as a point in the 1st BZ with the same vector \mathbf{k} with respect to the relative centre ($\mathbf{k}' = \mathbf{k} + \mathbf{G}$). This has a great implication on the complexity of the problem, since instead of having to deal with a solution for all space, the sampling is now delimited to those points within the 1st BZ.

If we include this notion, it is obvious that Bloch’s theorem must make use of a boundary condition in order to account for the periodicity of the system. The wavefunction at any point \mathbf{r} will be periodic with a period equal to the basis vectors \mathbf{a}_i times an integer N :

$$\psi(\mathbf{r} + N_i \mathbf{a}_i) = \psi(\mathbf{r}) \quad (2.57)$$

This is the *Born–Von Karman boundary condition*. The modulation term A can be expressed as a plane wave $e^{iN_i \mathbf{k} \cdot \mathbf{a}_i}$, so that:

$$\psi(\mathbf{r} + \mathbf{R}) = e^{iN_i \mathbf{k} \cdot \mathbf{a}_i} \psi(\mathbf{r}) \quad e^{iN_i \mathbf{k} \cdot \mathbf{a}_i} = 1 \quad (2.58)$$

\mathbf{k} is any vector in the 1st BZ $\mathbf{k} = m_1 \mathbf{b}_1 + m_2 \mathbf{b}_2 + m_3 \mathbf{b}_3$, being the basis vectors defined by (2.52). Importantly, this results in a set of allowed wavevectors which satisfy Eq. (2.58):

$$\mathbf{k} = \sum_{j=1}^3 \frac{m_j}{N_j} \mathbf{b}_j \quad (2.59)$$

As with any periodic function, we can write both $V(\mathbf{r})$ and $\psi(\mathbf{r})$ as Fourier series—a linear combination of sinusoidal waves:

$$V(\mathbf{r}) = \sum_{\mathbf{G}} V_{\mathbf{G}} e^{i\mathbf{G} \cdot \mathbf{r}} \quad \psi(\mathbf{r}) = \sum_{\mathbf{G}} c_{\mathbf{G}}^{\mathbf{k}} e^{i(\mathbf{k} + \mathbf{G}) \cdot \mathbf{r}} \quad (2.60)$$

Where \mathbf{G} is any vector in the reciprocal space, and $V_{\mathbf{G}}$ and $C_{\mathbf{G}}^{\mathbf{k}}$ are the Fourier coefficients. Including Eq. (2.60) into Eq. (2.1), we obtain the following expression (after a series of variable transformations thoroughly discussed in literature):

$$\sum_{\mathbf{G}} \left(\frac{1}{2} (\mathbf{k} + \mathbf{G})^2 - E_{n\mathbf{k}} \right) c_{\mathbf{G}}^{\mathbf{k}} e^{i(\mathbf{k} + \mathbf{G}) \cdot \mathbf{r}} + \sum_{\mathbf{G}'} \sum_{\mathbf{G}} V_{\mathbf{G}'} c_{\mathbf{G} - \mathbf{G}'}^{\mathbf{k}} e^{i(\mathbf{k} + \mathbf{G}) \cdot \mathbf{r}} = 0 \quad (2.61)$$

Where $\mathbf{G}' = \mathbf{Q} + \mathbf{G}$ so that \mathbf{Q} is a wavevector inside the 1st BZ. Since we are interested in finding a solution for Eq. (2.61), we can then simplify the equation as follows:

$$\left(\frac{1}{2} (\mathbf{k} + \mathbf{G})^2 - E_{n\mathbf{k}} \right) c_{\mathbf{G}}^{\mathbf{k}} + \sum_{\mathbf{G}'} V_{\mathbf{G}'} c_{\mathbf{G} - \mathbf{G}'}^{\mathbf{k}} = 0 \quad (2.62)$$

This is called the *central equation*, which simply represents the Schrödinger equation of a periodic system making use of the Fourier series of both the external potential and the wavefunction. At this point, an approximation can be made: we must take into account that the potential experienced by the electrons in metals and heavy atoms is relatively small, due to the existence of a certain amount of *shielding* of the core electrons that hinders the effect of the core charge on the valence electrons. Therefore, a simple model was developed where the potential term in Eq. (2.62) was neglected—the *nearly-free electron model*. If we consider this case, the kinetic energy of the electron in \mathbf{k} is:

$$E_{n\mathbf{k}} = \frac{1}{2}(\mathbf{k} + \mathbf{G})^2 \quad (2.63)$$

We note that Eq. (2.63) runs over all reciprocal lattice vectors \mathbf{G} , and therefore, there will be as many solutions to the Schrödinger equation—and hence, energy values—as vectors \mathbf{G} in the reciprocal lattice (each labelled with an index n) for a given wavevector \mathbf{k} .

2.3.4. Electronic band structure

In the nearly-free electron model, electrons are portrayed as those in an *empty* lattice, where they experience a negligible external potential. This is in contrast to the *tight binding model*, where electrons are subject to a potential so intense from the nucleus of their own atom that any interaction with surrounding atoms is negligible. Due to its relevance for the contents of this thesis, in the next section we will focus on the nearly-free electron model.

One interesting consequence of Eq. (2.63) is that we can plot a set of energy points for a given value of \mathbf{G} by varying \mathbf{k} . This is known as the *electronic band structure*, formed of a set of n continuous bands. The chosen values of continuous \mathbf{k} vectors for which the energy is analysed is known as the *k-path*. However, the choice of how to draw this *k-path* along the axes in the reciprocal lattice is not trivial. To achieve a proper understanding of the band structure of the crystal, we must primarily investigate those points in the reciprocal lattice (from hereafter, *k-points*) that more accurately represent the 1st BZ. As the geometrical representation of such, these correspond to the high-symmetry points in the reciprocal lattice Wigner–Seitz cell discussed in Section 2.3.1. Taking as an example the case of the Wigner–Seitz cell of the 1st BZ of the BCC crystal lattice from Figure 2.7, a rational choice for the *k-path* would be Γ –H–N– Γ –P–H|P–N, where H|P denotes a discontinuous step in order to assess all possible unique paths throughout the cell. A sample band structure of a BCC structure resulting from evaluating Eq. (2.63) at discrete points along this *k-path* is represented in Figure 2.8.

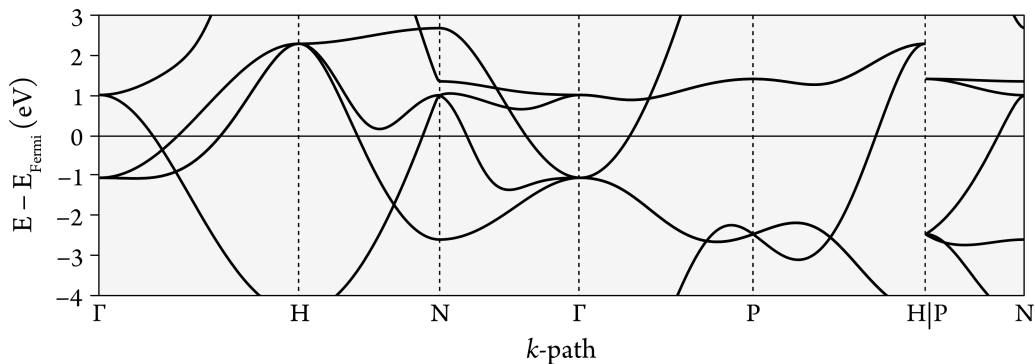


Figure 2.8 Arbitrary electronic band structure of bulk Cr (chosen for illustration purposes), which displays a BCC Bravais lattice. Adapted from Materials Project (id: mp-90), distributed under a CC BY 4.0 license.

An important piece of information that we can extract from the electronic band structure is the nature of the material—whether it is metallic, semiconductor or insulator; semiconductors and insulators display a *gap* between the highest occupied band (valence band) and the lowest unoccupied band (conduction band), where no occupied energy states exist. This energy difference represents the external energy required to excite an electron from the valence band to the conduction band. In the case of metals the valence band diffuses into the conduction band, and therefore, electrons can conduct freely. Usually, the origin in the energy axis of the band structure in metals will be located at the Fermi level—the energy of the highest occupied states; in insulators and semiconductors, however, the Fermi level is usually located close to centre of the gap.

Importantly, direct visualization of the band structure allows us to characterise the material based on their band gap—or absence thereof. Some materials, however, display relativistic effects that we also need to take into account. For instance, *topological insulators*¹⁴⁸ display a gap-containing band structure for their bulk atoms, while also containing conductive bands in their shell atoms. In short, this is due to *spin-orbit coupling*, where the spin of the electrons interacts with their orbit around a heavy core, leading to a generation of local magnetic moments that influence the conductivity of the surface states. This effect is usually accounted for by running non-collinear calculations, where the spin quantum number is not constrained to a given projection (α or β) and is allowed to point at any direction. This approach will be followed in the investigation of some of the 2-D structures presented in this thesis.

2.4. Basis sets

2.4.1. Localised basis sets

Up to this point, we have assessed the different ways in which we can describe the ground state energy of molecular and periodic structures using the electron density. As has already been discussed, DFT, similarly to HF, follows a variational principle that, in practice, requires a SCF in order to be solved. This SCF is reliant on *trial* functions which, if we are to follow the LCAO approach for the description of the Kohn–Sham orbitals, have to be similar in shape to the real atomic orbitals. The electron wavefunctions are then represented by *basis sets*, composed of *basis functions* which, similarly to the Schrödinger equation for monoelectronic atoms, should ideally display an exponential decay and the correct cusp at $r = 0$. Initially, Slater-type orbitals (with a radial part of the form $Ae^{-\zeta r}$, where A is a constant, ζ is a function of the effective nuclear charge and r is the electron-core distance) were used to simplify the solution for the Schrödinger equation of the H atom. Due to the complexity of using this method for Hartree–Fock (because of the large number of integrals arising from the two-electron terms), a more convenient form of the basis function is commonly employed, wherein atomic orbitals are approximated as gaussian-type functions (gaussian type orbitals, GTOs). Using GTOs in the description of molecular orbitals simplifies the two-term integrals in HF, since the product of two gaussian

functions results in a third gaussian function with a displaced centre. We can express a GTO in cartesian coordinates as:

$$g(\mathbf{r}) = A(x^i y^j z^k) e^{-\alpha r^2} = A(x^i y^j z^k) e^{-\zeta(x^2+y^2+z^2)} \quad (2.64)$$

These simple functions are called *primitive* GTOs. In practice, atomic orbitals are usually defined as a linear combination of GTOs (each multiplied by a contracting coefficient c_i) in order to form a *contracted* gaussian (CG), which emulates the radial part of the STOs:

$$G(\mathbf{r}) = \sum_{i=1}^N c_i g_i(\mathbf{r}) \quad (2.65)$$

Each atomic orbital is then defined by, at minimum, one CG (minimal basis set); usually, however, more than one CG is used (forming the double, triple or quadruple- ζ basis sets). Many modern calculations use the Pople split-valence basis sets, denoted as X - YZG , where 1 CG comprised of X primitive GTOs is used for the representation of each core atomic orbital, while valence orbitals are described with 2 CGs, each containing Y and Z primitive GTOs. These are called valence double- ζ basis sets; valence triple and quadruple- ζ basis sets of the form X - $YZVG$ and X - $YZVWG$, respectively, have also been developed.

In addition to the valence and core, further basis functions are usually included into the basis set. For instance, a function is usually applied to the $n + 1$ highest occupied angular momentum—e.g. p and d functions are used for H and O, respectively—, and is preferably denoted in brackets after the basic Pople notation, such as 6-31G(d). To account for all atoms in systems which include H, a second term inside the bracket is used to indicate the polarization functions which are applied solely onto the description of H: 6-31G(d, p). If we also want to account for a diffuse electron density and more accurately describe the tail of the atomic orbitals, we can include single diffuse functions (characterised by a very small exponent and a long decay) which are denoted with a *plus* sign in Pople's basis sets: 6-31+G(d, p).

Finally, for transition metals and heavy elements, which see their core electron configurations unaltered in reactivity, a common approach is to have their core electrons—up to a certain radius—replaced by an *effective core potential* that acts on the valence orbitals.

2.4.2. Plane wave basis sets

In our previous discussion regarding the study of periodic systems that satisfy Bloch's theorem, we introduced the idea of using a Fourier series for the description of the wavefunction, as shown in Eq. (2.60). By using this approach, we are approximating the electron wavefunction to a linear combination of discrete plane waves. In turn, there will be as many plane-waves as vectors \mathbf{G} in our reciprocal lattice, which in our case, results in an infinite number of terms. Therefore, using the as-is Fourier expansion of periodic plane waves as our basis set is

not feasible. However, we know that the bulk of the weight of the basis set will correspond to the plane waves with bigger $c_{\mathbf{G}}^{\mathbf{k}}$ coefficients; these will typically be those with a smaller $|\mathbf{k} + \mathbf{G}|$ and, thus, with a smaller kinetic energy in Eq. (2.63). In order to obtain a more manageable (albeit incomplete) basis set, the expansion of plane waves are truncated with a cut-off to the energy of the considered plane waves:

$$E_{cut} \geq \frac{1}{2}(\mathbf{k} + \mathbf{G})^2 \quad (2.66)$$

Which corresponds to a sphere around \mathbf{k} in the reciprocal space. A common practice to obtain a sufficiently accurate basis set is to choose a value of the cut-off energy over which the electronic energy of the overall system becomes invariable under a reasonable threshold (e.g. 1 meV per atom).

The use of plane wave basis sets, however, presents some drawbacks. Most importantly, atoms in higher periods contain valence orbitals with convoluted nodal features near the core; attempting to fine-tune the basis sets to replicate the *true* wavefunction shape near the nucleus is very resource-demanding, due to the number of gaussians required. Two strategies are usually followed to solve this issue. In the first approach, as is the case behind the reasoning of the use of effective core potentials, an accurate description of the behaviour of core electrons is deemed to be unnecessary for reactivity. In the *frozen core* approach, the electron density associated to these electrons is computed once and considered a constant in subsequent iterations in the self-consistent field.

The second approach is to use pseudopotentials—plane waves that display the shape of the exact function at larger distances from the nuclei, where interactions actually occur, but being nodeless at shorter distances from the core. In this thesis, the *projector-augmented wave* (PAW) method¹⁴⁹ has been used. This method contains two parts: firstly, a smooth plane wave pseudo-wavefunction ($\tilde{\Psi}$, which is related to the true wavefunction by a transformation operator T , so that $\Psi = T\tilde{\Psi}$) is used for the description of the short-range features of the wavefunction. This function behaves as the true wavefunction beyond a certain radius around the core (the *augmentation sphere*). Since the use of this pseudo-wavefunction removes the nodal features around the core, the PAW method includes another set of localised basis functions (*partial waves*, which are described as functions on a radial grid multiplied with spherical harmonics) inside the augmentation sphere. Similarly to the densities in the frozen core, the partial waves are pre-computed.

2.5. Dispersion effects

Although the use of exact HF exchange substantially improves the description of the LR exchange energy in hybrid LC DFT functionals, one drawback associated with the inherently poor definition of long-range interactions in GGA and LDA is that dispersion or van der Waals (vdW) interactions are often misrepresented.

To account for these interactions, the dispersion-corrected DFT (DFT-D) scheme was developed,¹⁵⁰ whereby a correction is added to the total DFT energy:

$$E_{DFT-D} = E_{KS-DFT} + E_{\text{disp}} \quad (2.67)$$

One of the most widely adopted methods to calculate E_{disp} is through the (so-called) Grimme's dispersion scheme, which is an atomic-pairwise correction based solely on empirical parameters. This correction provides a cost-efficient solution which can be applied to any hybrid, GGA or LDA functional. Grimme's DFT-D2¹⁵¹ method and its newer DFT-D3¹⁵² counterpart are the two main approaches used in the majority of calculations of molecular and periodic structures, and they serve as the foundation for the development of more sophisticated DFT-D methods. Grimme's DFT-D2 dispersion correction to the energy in a system containing N atoms takes the form:

$$E_{\text{disp}}^{D2} = -s_6 \sum_{A=1}^N \sum_{B<A}^N \left(\frac{C_{6,AB}}{R_{AB}^6} \right) f_{\text{damp}}^{D2}(R_{AB}) \quad (2.68)$$

$$f_{\text{damp}}^{D2}(R_{AB}) = \left[1 - e^{-d(R_{AB}/R_{0,AB}-1)} \right]^{-1}$$

Where R_{AB} is the pair-wise interatomic distance, s_6 is a global scaling parameter which has been tailored for some GGA and hybrid functionals (e.g. $s_6^{PBE} = 0.75$), $C_{6,AB} = \sqrt{C_{6,A}C_{6,B}}$ are tabulated atomic parameters and $R_{0,AB}$ is the sum of the vdW radii from atoms A and B , and d is an additional parameter. Given that this equation unrealistically diverges by a factor of R^{-6} in SR (similarly to a Lennard-Jones potential), a damping function f_{damp}^{D2} , which approaches 0 as $R \rightarrow 0$ is used for small values of R to avoid collapse of the function. DFT-D2 was used as the basis for the dispersion correction developed by Chai and Head-Gordon in 2008 for the formulation of the dispersion-corrected range-separated hybrid ω B97XD functional,¹³⁸ with a modified damping function:

$$f_{\text{damp}}^{CHG}(R_{AB}) = \left[1 + a(R_{AB}/R_{0,AB})^{-12} \right]^{-1} \quad (2.69)$$

Grimme's D3 method improves the accuracy of DFT-D2 by including geometry-dependent parameters which are modified depending on the coordination number and interatomic distances. Grimme's D3 original dispersion expression, known as the *zero-damping* DFT-D3(0) method (since the damping functions, similarly to DFT-D2, approach 0 as $R \rightarrow 0$), is as follows:

$$E_{\text{disp}}^{D3} = - \sum_{A=1}^N \sum_{B<A}^N \left[s_6 \left(\frac{C_{6,AB}}{R_{AB}^6} \right) f_{\text{damp},6} + s_8 \left(\frac{C_{8,AB}}{R_{AB}^8} \right) f_{\text{damp},8} \right] \quad (2.70)$$

$$f_{\text{damp},n}^{D3(0)}(R_{AB}) = \left[1 + 6 \left(\frac{R_{AB}}{s_{r,n} R_{0,AB}} \right)^{\beta_n} \right]^{-1}$$

Where $\beta_6 = 12$ and $\beta_8 = 14$, $s_{r,6}$ is a functional-dependent parameter and $s_{r,8} = 1$, and $C_{6,AB}$ and $C_{8,AB}$ take the same form and function as the tabulated atomic parameters in the DFT-D2 method. It is worth mentioning that DFT-D3 has recently been improved by including an empirical charge-dependent parameter which is independent of the functional, as implemented in the DFT-D4 approach.¹⁵³

Grimme's DFT-D3(0) dispersion corrections have been used in all the periodic systems in this thesis in which long-distance vdW interactions are envisioned to play a major role.

2.6. Simulation of the solvent

So far, our discussion has focused on defining molecular structures in the gas phase—without considering the influence that the solvent may have on their energetics, overall geometry and charge distribution. However, we know that this scenario is not realistic, since experiments are usually not carried out in a vacuum but inside a certain media. Hence, to obtain a more realistic description of the systems studied in this thesis, we ought to include these effects in our calculations.

Solvent effects can be accounted for in two different ways. On the one hand, we can simulate an *explicit* solvent, where actual models of the solvent molecules are introduced in the system surrounding the atomic species in the calculation. This gives rise to accurate solvent-solute interactions; however, the addition of the explicit solvent molecules often requires a high computational cost, and therefore simplification of the model or the use of less computationally demanding methods are needed. On the other hand, we can include solvent effects *implicitly*, whereby the presence of solvent molecules is accounted for as a correction to the energy of the system through a function that depends on the dielectric constant of the solvent and the charge density of the solute. In the following sections, we will discuss both approaches and introduce the main methodologies used in the calculation of some molecular and solid structures of this thesis.

2.6.1. The electrochemical water layer

If we want to achieve an accurate representation of the solvation of the model, usually, a considerably large number (in the order of hundreds) of solvent molecules surrounding the solute needs to be introduced in the calculation. However, modelling these big systems using quantum mechanical (QM) methods requires a prohibitive amount of computational resources. This problem can be circumvented using molecular mechanical methods—by means of *force fields*. These can be used to calculate the entirety of the system (molecular mechanics, MM) or used in conjunction with QM methods, where the solvent phase is calculated

using a force field and the solute-solvent interface, along with the solute, are calculated with QM methods leading to the so-called hybrid QM/MM methods.¹⁵⁴

In the simulation of heterogeneous electrochemical systems, consideration of the solvent is crucial for the accurate description of processes that involve electrode-electrolyte interactions—such as PCET steps between hydronium ions on the outer Helmholtz plane (OHP, the ion-containing solvent plane closest to any adsorbates on the surface) and either the inner Helmholtz plane (IHP, containing any ions bound to the surface) or the bare surface itself. Because of this, instead of considering the entirety of the solvent phase, most efforts dedicated to investigate electrode-electrolyte interactions have focused on characterising the structure at the electrochemical interface, IHP and OHP, where any relevant interactions can influence the catalytic activity.

The arrangement of water molecules at the electrode-electrolyte interface was spectroscopically characterised by Nilsson et al. in 2002.¹⁵⁵ In their observations, water molecules adsorbed on a Pt(111) surface at 100 to 120 K were predominantly distributed in an ice-like structure where they formed a bi-layered hexagonal pattern stabilized by H-bonding, with half of the waters displaying one H atom pointing towards the surface (Figure 2.9 A, B). This model has been used to simulate the stabilization of ORR intermediates on metal surfaces,¹⁵⁶ and more recently, to describe electrochemical interfaces containing hydronium ions (as shown in Figure 2.9 C), with the aim to investigate reactions involving an electrochemical proton discharge from the electrolyte to the electrode.¹⁵⁷ Work carried out by Nørskov et al. in 2018¹⁵⁸ shed light on the localisation of the positive charge due to the added proton into a multi-layered water electrochemical interface. In their model, consisting of a Pt(111) surface and an OHP with 3 stacked water bi-layers, the protonation of the water molecule closest to the IHP yielded a reasonable charge localisation on the proton, with a net Bader charge of *ca.* +0.7 *e*. From this knowledge, a single protonated water bi-layer with the H₃O⁺ cation arranged as shown in Figure 2.9 C has been shown to provide a good representation of the aqueous electrochemical interface for the calculation of proton transfer steps without the need of considering the entire solvent structure, as reported by Chan et al. in 2020.⁶⁶ In their work, the modelling of a water bi-layer representing the OHP provided a simple yet sufficiently accurate starting point for the calculation of the kinetics involved in the Volmer and Heyrovsky steps in HER on a series of metal surfaces with partial and full *H and *OH coverages.

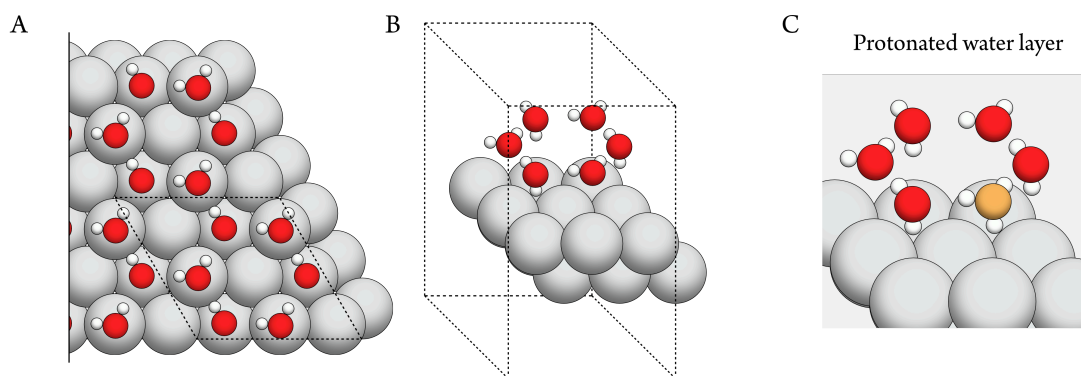


Figure 2.9 A) Top and B) isometric view of a single electrochemical water layer on an arbitrary surface. Oxygens and hydrogens are represented as red and white spheres, respectively. C) Representation of the electrochemical water layer with an additional proton added onto a water, yielding one H_3O^+ ion (highlighted in orange).

2.6.2. The universal solvation model

In implicit solvation models, the Gibbs energy of solvation (ΔG_{solv}) is typically divided into 3 main terms:

$$\Delta G_{solv} = \Delta G_{cav} + \Delta G_{disp} + \Delta G_{elec} \quad (2.71)$$

ΔG_{cav} corresponds to the energy required to form the solvation cavity, i.e. to rearrange the solvent molecules around the solute, which is unfavourable and hence this term is always positive; ΔG_{disp} corresponds to the NCIs between the solute and solvent, and ΔG_{elec} corresponds to the electrostatic interactions between solute and solvent which yields a charge density redistribution inside the molecular species.

The implicit model used in this thesis is called the *universal solvation model* (SMD,¹⁵⁹ which stands for *solvation model based on density*, since it utilises the full electron density of the solute). This model contains two distinct components for the calculation of the solvation energy, namely the electrostatic and non-electrostatic contributions. The electrostatic contribution builds upon the *polarizable continuum model*,^{160,161} which defines the solvation cavity volume as that formed by the overlap of the van der Waals radii of the atoms, and then solves the Poisson equation^{††} to integrate the charge of the system in a continuum dielectric using a generalized Born approach,^{§§} giving rise to the free energy of polarisation that can be expressed as follows:

^{††} The Poisson equation relates the second derivative of the potential with the spatial charge density, $\nabla^2 V = -\rho/\epsilon$.

^{§§} This is a generalisation of the Born equation, which is expressed as the energy required to charge a species from gas phase to solution:

$$G_p = -\frac{1}{2} \left(1 - \frac{1}{\epsilon} \right) \frac{q^2}{\alpha}$$

In this equation, using the permittivity of the vacuum ($\epsilon = 1$) cancels out the middle term; therefore, solvation energy contributions in the gas phase are rendered null.

$$G_P = -\frac{1}{2} \left(1 - \frac{1}{\epsilon_r}\right) \sum_{k,k'}^{atoms} q_k q_{k'} \gamma_{kk'} \quad \gamma_{kk'} = \frac{1}{\left(r_{kk'}^2 + \alpha_k \alpha_{k'} e^{r_{kk'}/d_{kk'}} \alpha_k \alpha_{k'}\right)^2} \quad (2.72)$$

The energy for this first contribution, which is formed from the sum over pair-wise atoms, depends on the relative permittivity of the solvent, ϵ_r ($\epsilon_r = 1$ for vacuum, and $\epsilon_r \approx 80$ for water), the charge of the individual atomic centres in the cavity, q , and the radii of the atoms, α . This charge distribution is used to calculate the overall solvation energy, which in turn changes the charge distribution which, then, requires recalculation of the solvation energy in an iterative process (i.e. *self-consistent reaction field*), until convergence is reached.

The second contribution to the solvation energy in the SMD model contains the energy required for cavitation, dispersion and structural rearrangement (CDS) of the solvent (equivalent to the first two terms in Eq. (2.71)) and it takes the following form:

$$G_{CDS} = \sum_k^{atoms} A_k \left(\sigma_k + \sum_{k'}^{atoms} \sigma_{kk'}(\mathbf{R}) \right) \quad (2.73)$$

Where A_k is the accessible surface area of the solvent—the area around the cavity where solvent-solute interactions occur—and σ are microscopic surface tensions, which in the case of SMD, are linear combinations of a series of per-atom parameters or descriptors, including solvent index of refraction, solvent surface tension, acidity or basicity, or the existence of carbon aromaticity.

2.7. Gibbs energy corrections

It is important to note that the energy obtained from DFT does not contain any thermochemical values. Knowing the electronic energy is not sufficient to investigate chemical reactivity, and we must take into account several aspects to unravel the true *available energy* of the system—the total energy associated with any chemical process, the *Gibbs energy*. The Gibbs energy is defined as:

$$G = H - TS = U + pV - TS \quad (2.74)$$

Where H is the enthalpy (exchange of heat at constant pressure), T is the temperature of reaction, S is the entropy (amount of energy of a closed thermodynamic system which is unavailable to do useful work), U is the internal energy, p is the pressure, and V is the volume. Knowing the difference in Gibbs energy between products and reactants in a chemical process (ΔG_R) allows to identify whether the reaction is spontaneous in the forward ($\Delta G_R < 0$, *exergonic*) or reverse direction ($\Delta G_R > 0$, *endergonic*), or if the reaction is in equilibrium ($\Delta G_R = 0$). In this next section, we will briefly describe the methods used to calculate thermodynamic corrections to the electronic energy in order to obtain the Gibbs energy.

The main methodology used in this thesis for the study of molecular systems assumes that molecular species are non-interacting particles, therefore behaving as an *ideal gas*. In this approximation, the contributions to the enthalpy and entropy terms can be separated into translational, rotational, vibrational and electronic contributions:

$$H_{tot} = E_{elec} + E_{ZPE} + \int_0^T C_P dT \quad (2.75)$$

$$S_{tot} = S_{trans} + S_{rot} + S_{vib} + S_{elec} - k_B \ln\left(\frac{P}{P_0}\right) \quad (2.76)$$

The first two terms in Eq. (2.75) correspond to the electronic energy and zero-point energy ($E_{ZPE} = \sum_i 1/2 h\nu_i$ for each vibrational mode). C_P is the heat capacity at constant pressure; this can be obtained using the constant-volume heat capacity C_V plus the Boltzmann constant k_B , $C_P - C_V = k_B$. In turn, C_V can be further divided into its translational, rotational, vibrational and electronic parts. Hence, C_P can be defined as:

$$C_P = C_V^{trans} + C_V^{rot} + C_V^{vib} + C_V^{elec} + k_B \quad (2.77)$$

All entropic and heat capacity terms in Eqs. (2.76) and (2.77) can be calculated using the molecular partition functions $q(V, T)$:

$$S_i = k_B + k_B \ln(q_i(V, T)) + k_B T \left(\frac{\partial \ln q_i}{\partial T} \right)_V \quad (2.78)$$

$$E_i = k_B T^2 \left(\frac{\partial \ln q_i}{\partial T} \right)_V \quad C_V^i = \left(\frac{\partial E_i}{\partial T} \right)_{N,V} \quad (2.79)$$

whose translational (q_{trans}), rotational (q_{rot}), vibrational (q_{vib}) and electronic (q_{elec}) partition functions are given by:

$$q_{trans} = \left(\frac{2\pi m k_B T}{h^2} \right)^{\frac{3}{2}} \quad q_{elec} = \sum_i^{levels} g_i e^{-\frac{\varepsilon_i}{k_B T}} \quad q_{vib} = \prod_k \frac{e^{-\frac{h\nu_k}{2k_B T}}}{1 - e^{-\frac{h\nu_k}{k_B T}}} \quad (2.80)$$

$$q_{rot}^{linear\ molecule} = \frac{2Ik_B T}{\hbar^2} \quad q_{rot}^{non-linear\ molecule} = \left(\frac{k_B T}{hc} \right)^{\frac{3}{2}} \sqrt{\frac{\pi}{\tilde{A}\tilde{B}\tilde{C}}}$$

Where g_i and ε_i in q_{elec} are the degeneracy and energy of the energy level, respectively, ν_k is the frequency of vibrational mode k , and two terms for q_{rot} are independently used for linear or non-linear molecules, where I is the moment of inertia, c is the speed of light and \tilde{A} , \tilde{B} and \tilde{C} are rotational constants.

In the calculation of adsorbates bound to a surface, however, it is usually assumed that there are no rotational and translational contributions to the energy. In addition, in contrast to the ideal gas approximation where expansion can occur, the Gibbs energy in a surface + adsorbate system is computed at constant volume. This yields the *Helmholtz free energy*, F :

$$F = U - TS \quad (2.81)$$

If we consider the pV term in Eq. (2.74) to be negligible, we can approximate F to G . Each term in Eq. (2.81) is defined as:

$$U = E_{elec} + E_{ZPE} + \int_0^T C_{V,vib} dT \quad (2.82)$$

$$S = S_{vib} \quad (2.83)$$

In all structures containing adsorbates, the Helmholtz energy has been computed following this approximation.

2.7.1. Modelling of electrochemical reactions

In addition to the corrections mentioned in the previous section, calculating the Gibbs energies of electrochemical steps requires a tailor-made approach which accounts for the role of the applied bias. Furthermore, most electrochemical steps such as a PCET demand an accurate description of both the proton and the electron. To address these issues in the study of the ORR, Nørskov et al. developed the CHE (see Section 1.2.1) in 2004.^{82,162} In the CHE model, the main assumption is the use of the SHE (as introduced in Section 1.2) as the reference electrode for the calculation of reduction potentials. As mentioned previously, the SHE is based on a half-cell containing a Pt surface in a solution of 1 M H^+ in equilibrium with $\text{H}_2(\text{g})$ (as portrayed in Eq. (1.14)) at standard conditions ($p_{\text{H}_2} = 1\text{ atm}$ and $T = 298\text{ K}$). By considering the reaction equilibrium depicted in Eq. (1.14), we can relate the Gibbs energy of the proton-electron couple with the Gibbs energy of the hydrogen molecule:

$$G(\text{H}^+ + \text{e}^-) = \frac{1}{2} G(\text{H}_2) \quad (2.84)$$

The cell potential of the redox couple in Eq. (1.14) can be written with the Nernst equation:

$$U = U^o - \frac{k_B T}{2e} \ln \left(\frac{a_{\text{H}^+}^2}{p_{\text{H}_2}} \right) \quad (2.85)$$

Where U^o is the standard potential of the reaction ($E^o(\text{H}^+/\text{H}_2)$), and a_{H^+} is the activity of protons (usually, the concentration). At standard conditions, $U = U^o = U_{\text{SHE}} = 0$, which defines the potential of the SHE electrode. Any variation of these conditions, however, results in the rightmost term in (2.85) not cancelling out, and requires careful consideration of each parameter; for this purpose, the reference hydrogen electrode (RHE)

is used which denotes a hydrogen electrode similar to the SHE under conditions other than the standard. Nonetheless, most theoretical studies of electrochemical systems are carried out considering standard temperatures and p_{H_2} , whilst the pH of the electrolyte, determined by the proton activity, may vary.¹⁶³ Therefore, a relation between U_{SHE} and U_{RHE} may be written as follows:

$$U_{\text{RHE}} = U_{\text{SHE}} + \frac{k_B T}{e} \ln(10) \times \text{pH} \approx U_{\text{SHE}} + 0.059 \times \text{pH}/e \quad (2.86)$$

Moreover, at a given pH, the relation between the Gibbs energy of Eq. (1.14) and the cell potential is:

$$\Delta G = eU_{\text{RHE}} = eU_{\text{SHE}} + 0.059 \times \text{pH} \quad (2.87)$$

This knowledge allows us to establish the building guidelines of the CHE model, which have been followed in all electrochemical steps of the reactions discussed in this thesis:

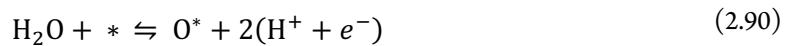
- 1) Eq. (2.84) allows us to calculate reactions in which PCET steps are involved by considering the Gibbs energy of the hydrogen molecule instead of the more convoluted energy of a solvated proton and electron.
- 2) If we wish to investigate a reaction at $\text{pH} > 0$, we must include a correction to the Gibbs energy of H^+ :

$$\Delta G(\text{pH}) = k_B T \ln(10) \times \text{pH} \quad (2.88)$$

- 3) The effect of the applied bias U is included as a correction $\pm neU$ in all electrochemical steps ($+neU$ for reductions, $-neU$ for oxidations¹⁶²), where n is the number of electrons exchanged in the process, e is the electron charge and U is the applied bias.

2.7.2. Calculation of the coverage in an aqueous electrolyte

Consequent to the use of the SHE is that at standard conditions, protons and water are in equilibrium on the electrode surface. Therefore, oxygen, hydroxide and hydrogen species may be adsorbed onto the surface through the following reactions:



Wherein the O^* species is formed by an initial adsorption of HO^* and subsequent dehydrogenation. In Eqs. (2.89) to (2.91), $*$ denotes a surface active site. Considering the CHE model, the Gibbs energy of adsorption of HO^* , O^* and H^* onto a surface site can be written in terms of the Gibbs energies of H_2 and H_2O , so that:

$$\Delta G_{\text{HO}^*} = G_{\text{HO}^*} - \left(G_{\text{H}_2\text{O}} - \frac{1}{2} G_{\text{H}_2} \right) - G_* - k_B T \ln(10) \times \text{pH} - eU \quad (2.92)$$

$$\Delta G_{O^*} = G_{O^*} - (G_{H_2O} - G_{H_2}) - G_* - k_B T \ln(10) \times \text{pH} - 2eU \quad (2.93)$$

$$\Delta G_{H^*} = G_{H^*} - \frac{1}{2}G_{H_2} - k_B T \ln(10) \times \text{pH} + eU \quad (2.94)$$

The Gibbs energies of the most stable adsorptions of HO^* , O^* and H^* on the surface can be plotted as a function of U_{SHE} at a given pH,¹⁵⁶ giving rise to a multi-line plot such as the one represented in Figure 2.10 A. As seen from the last terms in Eqs. (2.92) to (2.94), application of a reductive or oxidating cell potential will vary the Gibbs energy of the adsorbates and, therefore, will determine the relative stability of the surface covered with either H^* , O^* or HO^* . Hence, assuming that in an aqueous electrolyte the reactions in Eqs. (2.89) to (2.91) are competing, at each value of U_{SHE} the surface will be predominantly covered by either O^* , HO^* or H^* —whichever displays the lowest Gibbs energy of adsorption per adsorbate at that potential. We can then build a surface Pourbaix diagram, such as the one in the rightmost panel of Figure 2.10 B, which indicates the regions of stable coverages as a function of U_{RHE} and pH. This is constructed by obtaining the value of the minimum energy intersects at pH 0, m_n in Figure 2.10 A, which correspond to the origin of the region limits; the coverage stability regions are then delimited by this intercept and a line with a slope $-k_B T \ln(10) \sim 0.059 \text{ V pH}^{-1}$.

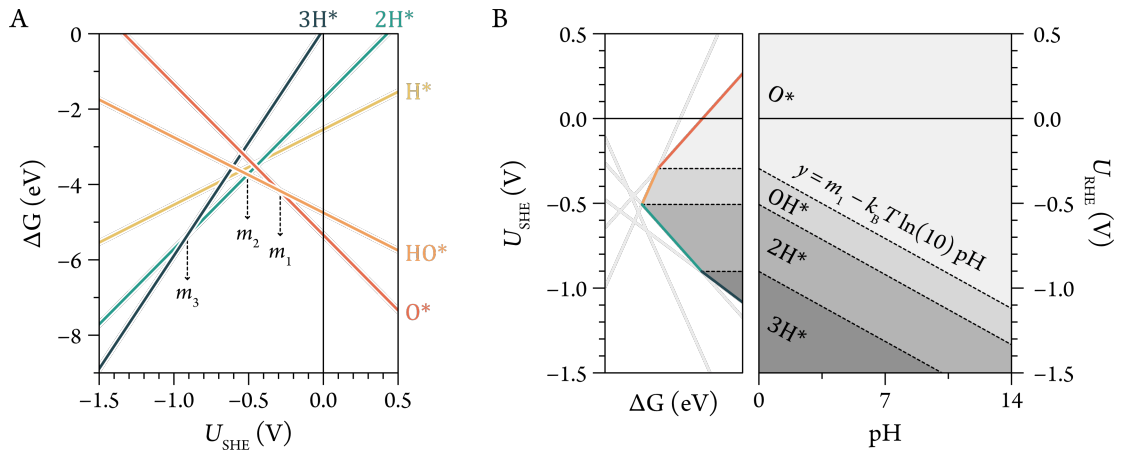


Figure 2.10 A) Diagram displaying the Gibbs energy of adsorption of 1 O^* , 1 HO^* and 1, 2 and 3 H^* per unit cell as a function of U_{SHE} at pH 0. Minimum energy intersects are denoted as m_1 , m_2 and m_3 , which are used to generate a surface Pourbaix diagram depicted in B. This diagram displays regions of U_{RHE} vs. pH at which competing coverages of O^* , HO^* , 2H^* and 3H^* are predominant.

Further coverage stability phases can be included in the surface Pourbaix diagram in Figure 2.10 B by considering mixed coverage phases (e.g. a mix of O^* and HO^* adsorbates in a unit cell).

2.8. The potential energy surface

The use of the Born–Oppenheimer approximation for the calculation of the energy of molecular and solid systems allows us to separate nuclear and electronic energies. While the former will be directly dependent on the structural coordinates of the atoms, the latter will vary with the relative positions of the electrons with respect to the nuclei. With this in mind, we can assume that the overall energy of the system will be mainly dependent on the position of the atoms. Therefore, we can describe the energy as a multidimensional function of $3N - 6$ internal coordinates of the system (interatomic distances, torsion angles and dihedral angles, which is $3N - 5$ for linear molecules) or $3N$ Cartesian coordinates—the *potential energy surface* (PES). Visual exploration of such a multidimensional function is an impossible task; for simplification purposes, the PES is usually represented as a 3-D surface where the energy is dependent on only 2 coordinates of interest, R_1 and R_2 , as seen in Figure 2.11 A. The most relevant points in the 3-D PES are those for which the gradient of the energy is 0, $g = \nabla E = 0$. These points correspond to energy minima and n^{th} order saddle points (SPs). In Figure 2.11 A, 1st order SPs are a maximum along one coordinate but a minimum along the other, while the 2nd order SP corresponds to a maximum in the 2-D PES along both directions.

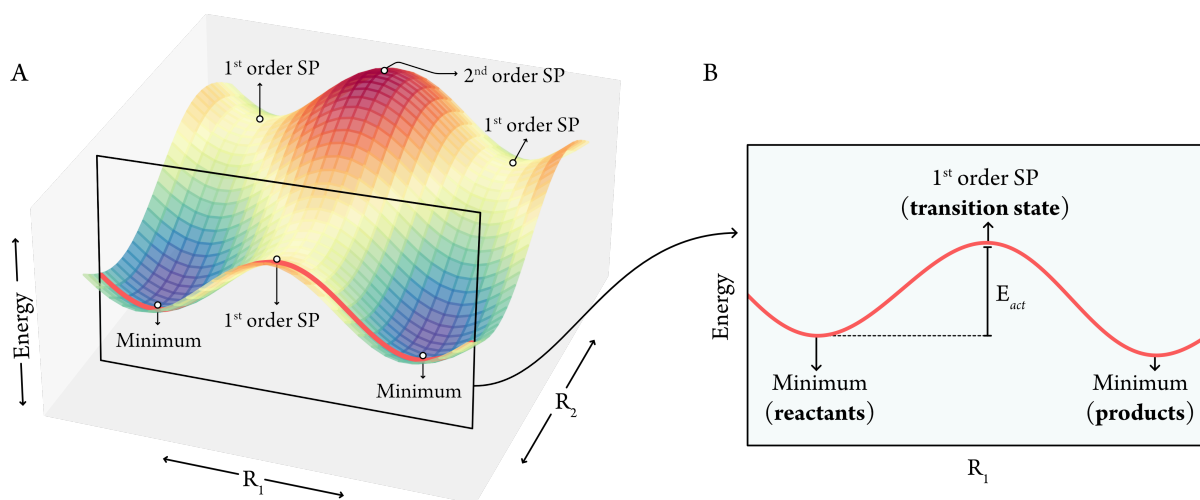


Figure 2.11 A) Representation of an arbitrary 3-D PES with 2 reaction coordinates, R_1 and R_2 . Points of interest (minima and saddle points) are denoted with a white dot. B) Cross-section of the plane in which the two minima in the 3-D energy surface in A) reside, effectively displaying a 2-D PES where the energy of the system is dependent on only one reaction coordinate. In this representation, the two minima are denoted as reactants and products (depending on the direction of the reaction) and the 1st order SP is the TS. The activation energy (E_{act}) is denoted as the energy difference between the reactants and the TS.

To identify whether the points with $g = 0$ are minima or saddle points, one must look at the curvature—the second derivative of the energy with respect to the internal coordinates, $\nabla^2 E = \nabla g$, which in a system with $3N$ cartesian coordinates corresponds to a diagonalised $3N \times 3N$ matrix. If all second derivatives in the matrix

positive, the investigated point will correspond to a minimum in energy, as displacing it along any coordinate will require an increase in energy. If any of the second derivatives are negative, however, this will correspond to a n^{th} order SP (n being the number of negative eigenvalues). Physically, the curvature of the PES along the coordinates of the system is proportional to the vibrational frequencies; hence, any negative (imaginary) frequency will denote a SP along the characteristic coordinate of that vibrational mode. Furthermore, any 2 contiguous minima along one dimension in the PES will be necessarily connected by one 1st order SP through a minimum energy path (MEP), which will display only one negative second derivative along one reaction coordinate. If we consider this, it is usually more convenient to display a 1-D PES where any 2 minima of interest are connected by a 1st order SP, a *transition state* (TS); any increase or decrease in the magnitude of the chosen coordinate will lead to convergence of the TS towards one or the other minimum, which we denote as the *reactants* or the *products*, depending on the direction of the process. The difference between the reactants and the TS indicates the energy barrier that needs to be overcome to carry out the reaction. This is highlighted in the 2-D PES presented in Figure 2.11 B.

Several methods have been used to find energy minima and SPs in the PES, by analysing either the first^{164,165} or second derivatives^{166,167} of the energy. In the next section, however, we are going to focus our discussion on a method which aims to find 1st order SPs in both molecular and heterogeneous systems, although only the latter has been used in this thesis.

2.8.1. Location of transition states in heterogeneous systems

Finding the MEP between two minima is not straightforward, and requires a rational exploration of the PES. In this regard, some of the simplest approaches to identify the reaction-determining TS are based on *chain-of-state* methods, where a linear interpolation (chain) of images (states) is performed, each image containing a progressive change in the coordinates of the system to accommodate conformational changes in between the atomic coordinates in the energy minima. In the linear synchronous-transit method (LST),¹⁶⁸ the images—kept at a constant distance from each other along the reaction path—are optimised so as to approach the *true* MEP. This method, along with its predecessors, proved to be extremely efficient for parallel computing, as multiple images could be optimised at the same time. LST was later improved by considering an elastic band connecting neighbouring images, with a spring force so that convergence of the pathway to the MEP was not subject to a rigid constraint. Results based on both these methods, however, did not give an accurate representation of the MEP, and usually required classical optimisation algorithms on the highest energy point to describe it with more accuracy.¹⁶⁹

To overcome this issue, Jónsson et al. developed the *nudged elastic band* method (NEB, represented in Figure 2.12).^{170,171} Similarly to the earlier chain-of-states methods, the NEB method begins with a linear interpolation of images between minima, which are elastically held together by a spring constant. The novelty of this method, however, lied in the fact that the force to which the images are subject due to the elastic band, F_{\parallel}^K , is only applied

in the parallel direction to the reaction path (black arrows in Figure 2.12). Furthermore, this force is detached from the tangent force that drives the images towards the MEP, F_{\perp}^r (red arrows in Figure 2.12). Distinct projection of both F_{\parallel}^k and F_{\perp}^r (referred to as *nudging* in Ref. ¹⁷¹) provides a substantially better representation of the MEP compared to previous methods.

In some cases, however, the highest energy image from the resulting path after an NEB calculation may slightly fall short of depicting the *true* TS. In this case, a modification of the NEB is used (the *climbing-image* nudged elastic band, CI-NEB)¹⁷², where i) variable spring constants are used to increase the density of points at higher energies, and ii) the highest energy image in the MEP is subject to an extra force so as to make it *climb* in the direction of the lowest energy path and converge it to the highest saddle point along the MEP. This is schematised in the topmost image on the MEP in Figure 2.12.

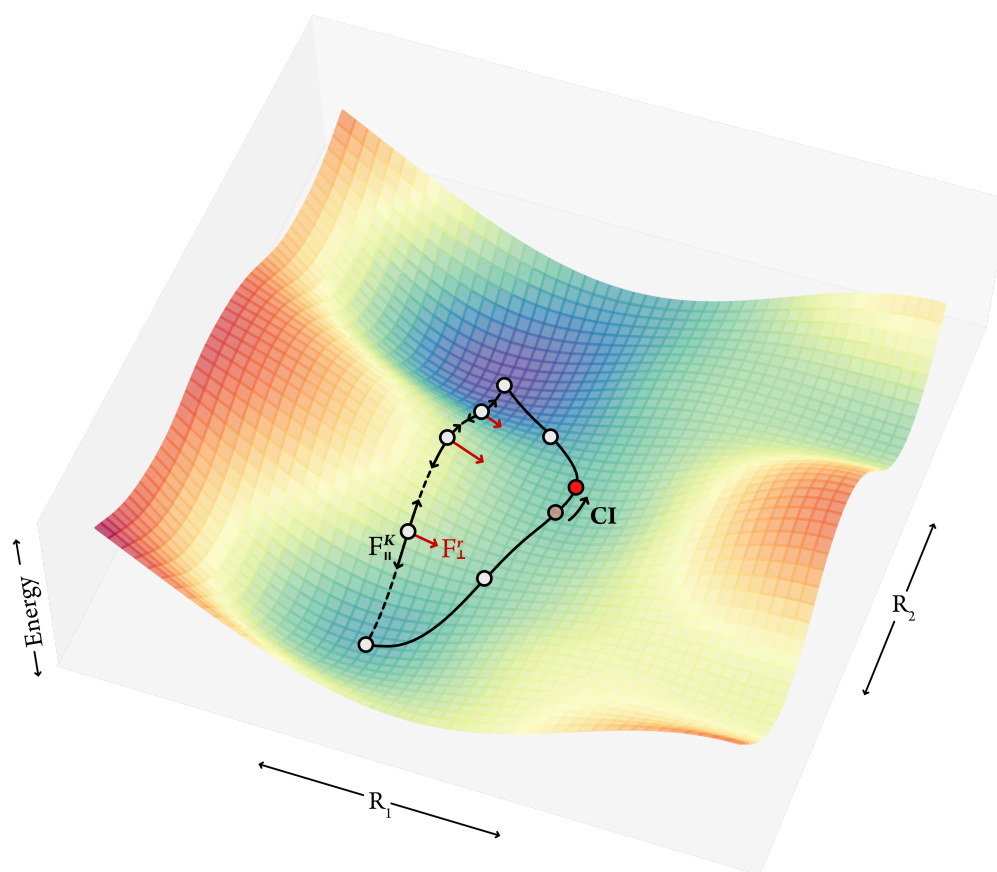


Figure 2.12 3-D PES displaying white spheres on a dashed line to represent the images on the initial linear interpolation between two energy minima using the NEB method. Each image along the initial interpolation is subject to two sets of forces: a spring force in the direction of the neighbouring images (F_{\parallel}^k , black arrows), and a force normal to the interpolation path and in the direction where the energy is minimised (F_{\perp}^r , red arrows). The resulting MEP is displayed as a continuous line, with its corresponding images as white spheres. The image with the highest energy (pale red sphere) is brought in the ascending direction along the MEP using the CI-NEB method, resulting in an image which is more representative of the true TS (bright red sphere).

2.9. Structural optimisation and characterisation of solids

2.9.1. The Birch–Murnaghan equation of state

To optimise the lattice parameter of a given unit cell, one common approach is to use an *equation of state* (EOS), which relates state functions such as pressure, energy and volume. In the simplest EOS, the volume of a gas experiencing an external pressure can be related to a temperature change with the ideal gas law, $PV = nRT$, where R is the ideal gas constant and n denotes the number of moles. In solids, however, a change in volume associated with a variation of the external pressure depends on the resistance of the solid towards compression at a given temperature, the *Bulk modulus* (B), which can be defined using the following isothermal EOS:

$$B = -V \left(\frac{\partial p}{\partial V} \right)_T \quad (2.95)$$

One of the earliest EOS for solids, developed by Francis D. Murnaghan in 1944,¹⁷³ builds upon Eq. (2.95) and depicts B as being linearly dependent on p , so that $V = V_0(1 + B'p/B_0)$, where B_0 is the bulk modulus at equilibrium and B' is the derivative of B with respect to p . Francis Birch then built upon Murnaghan's work and developed the Birch–Murnaghan higher-order EOS,¹⁷⁴ with which we can represent the internal energy as:

$$E(V) = E_0 + \frac{9V_0B_0}{16} \left\{ \left[\left(\frac{V_0}{V} \right)^{\frac{2}{3}} - 1 \right]^3 B'_0 + \left[\left(\frac{V_0}{V} \right)^{\frac{2}{3}} - 1 \right]^2 \left[6 - 4 \left(\frac{V_0}{V} \right)^{\frac{2}{3}} \right] \right\} \quad (2.96)$$

Usually, the parameters of interest are E_0 , V_0 and B_0 (the energy, volume and bulk modulus at equilibrium, respectively). In order to obtain these terms, the energies ($E(V)$) of a series of points are calculated in which the volume of the unit cell (V) is varied while allowing α , β and γ parameters to change; the parameters of the structure at equilibrium are extracted by fitting these points to Eq. (2.96), as shown in Figure 2.13.^{***}

^{***} This method is preferred for the obtention of accurate lattice parameters in periodic systems calculated with plane waves. This is due to the errors associated with zero-pressure optimisations in most common approaches, i.e. plane wave basis sets are incomplete in regard to changes in the volume. Unless complete convergence has been achieved, this yields to incorrect diagonal components in the stress tensor (called *Pulay stress*). More information can be found in the VASP supporting documentation website.

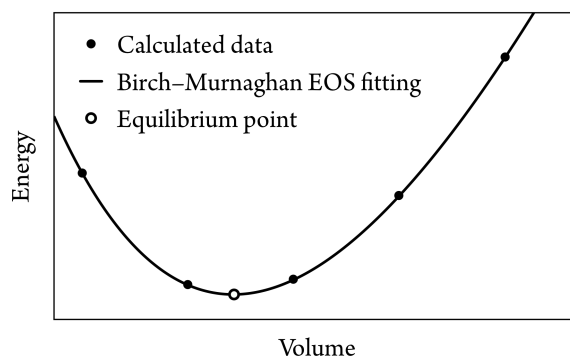


Figure 2.13 Schematic representation of a fitting of V and E of computationally calculated structures (filled dots) to the Birch–Murnaghan EOS (continuous line). The minimum in energy—the equilibrium point—from which E_0 , V_0 and B_0 are derived is represented as an empty dot.

2.9.2. Generation of surface slabs

As discussed in the previous sections, the main particularity of heterogeneous catalysts lies in the fact that reactivity occurs on the interface between the solid and its environment. Therefore, the modelling of reactions in periodic crystals focuses on describing the chemical events occurring at the surface of the solid catalyst, comprised of the outermost atomic layers of the studied crystal. This surface structure can be constructed from a conventional unit cell (as shown in Figure 2.14 A, which is expanded into a $(3 \times 3 \times 3)$ *supercell*—formed by 27 conventional unit cells—in Figure 2.14 B) by cleaving the crystal structure along a (hkl) lattice plane (Figure 2.14 C) parallel to the terminating surface plane, and including a number of atomic layers within a set distance from this plane. To enable periodicity along the \hat{a}_1 and \hat{a}_2 directions, the surface structure is then aligned so that the vector orthogonal to the surface plane is parallel to \hat{a}_3 ; furthermore, a vacuum is included along this axis to minimise the interactions between neighbouring unit cells in that direction. The resulting structure (Figure 2.14 D) is denoted as a surface *slab* model, which is periodic along 2 of the axes and is able to describe the geometry of the catalyst interface (as opposed to the *bulk* model represented by the conventional cell in Figure 2.14 A, which is periodic along the three directions and describes the *inside* of the crystal). The periodicity of the slab is often indicated as $p(m \times n)$, where $p(1 \times 1)$ is the smallest unit that can represent the surface; calculation of surfaces with large adsorbates often requires consideration of larger slab models, where $m, n > 1$ in order to avoid overlapping between adsorbates in neighbouring unit cells.

Given that it is comprised of a film of atomic layers with a delimited thickness, the as-is slab model is able to describe 2-D materials that exist as flakes or free-standing layers, where reactivity can occur on both sides of the slab. In these cases, the slab model is usually allowed to relax freely in response to the inclusion of any adsorbate or any structural change in the calculation. However, this model falls short of providing a good description for structures where the number of comprising atomic layers is high, such as nanoparticles; in these systems, free relaxation of the surface atoms is hindered by the constraints imposed by rigid inner atoms (*bulk effects*). In order to reproduce this phenomenon, the slab model is altered by including more atomic layers and fixing

the coordinates of a number of atoms in the bottom layers (which simulates the more rigid bulk), while allowing the atoms in the remaining surface layers to relax.

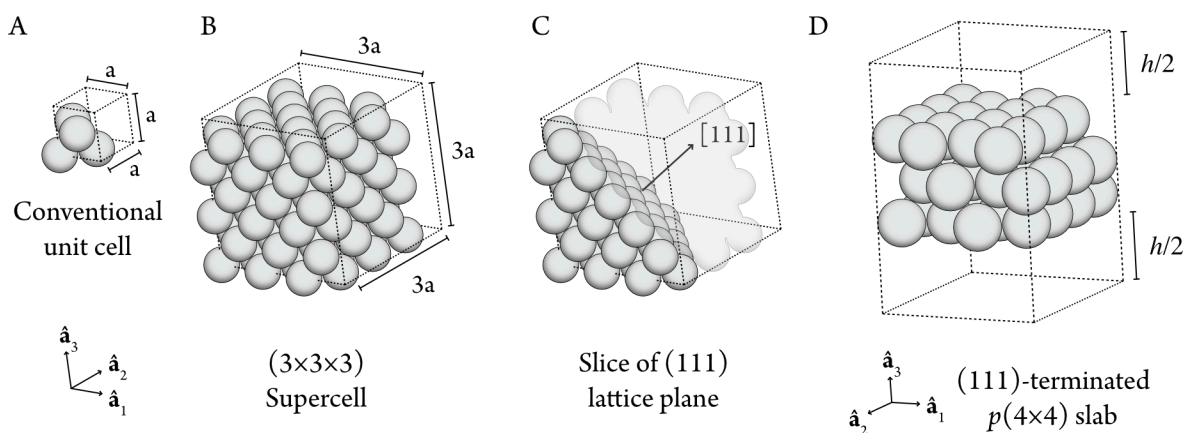


Figure 2.14 A) Representation of a conventional unit cell of a FCC crystal describing the bulk. B) $(3 \times 3 \times 3)$ supercell of the unit cell in A). C) Slicing of the bulk along the (111) lattice plane. D) Representation of an arbitrary slab model with periodicity $p(4 \times 4)$ which includes 3 atomic layers and a vacuum h , wherein $[111]$ is aligned with \hat{a}_3 . It is worth mentioning that the slicing and generation of the slab is usually carried out with the unit cell; in this image, this is carried out with the $(3 \times 3 \times 3)$ supercell for illustration purposes.

2.9.3. Wulff constructions

An essential aspect to consider when simulating heterogeneous systems representing nanoparticles is that, in reality, these structures usually expose not one, but many surface facets onto which reactivity can occur. Therefore, an accurate assessment of the reactivity on these systems must start with a precise determination of the lattice planes that are likely to conform the nanoparticles, which will be inherently governed by their morphology.

The concept of geometry in heterogeneous systems was first discussed by Willard Gibbs between 1875 to 1878. In his 1876 publication as part of the complete work *On the Equilibrium of Heterogeneous Substances*,¹⁷⁵ he introduced the concept of *neutral equilibrium* to define the state at which a heterogeneous system, in contact with a liquid phase, maximises the entropy and minimises the surface tension of the exposed facets. Therefore, he theorised that as a particulate system approaches equilibrium, it converges to a polyhedral structure displaying a limited number of lattice planes, in crystallographic systems, represented by Miller indices (hkl) . The mathematical interpretation of this principle (the Gibbs–Wulff theorem) was later developed by George Wulff,¹⁷⁶ who suggested that the shape of particles in neutral equilibrium can be envisioned as the volume inside all crystal planes (hkl) , at a distance h_{hkl} from the centre which is proportional to the surface energy of the lattice plane, $h_{hkl} = c \cdot \gamma_{hkl}$. Here, c is an arbitrary constant, and γ_{hkl} is the surface energy of the plane, the energy per unit area required to create a slab with a terminal lattice plane of Miller indices (hkl) from a bulk structure of the crystal, as discussed in Section 2.9.2.

$$\gamma_{hkl} = \frac{E_{slab} - NE_{bulk}}{2A} \quad (2.97)$$

Where E_{slab} is the electronic energy of the slab, E_{bulk} is the energy of the starting bulk material, A is the area of the resulting slab, and N is the number of bulk units included in the slab, also defined as $N = N_{atoms}^{slab}/N_{atoms}^{bulk}$. The equilibrium shape of the crystal particle is, therefore, a function of the relative surface energies of all represented lattice planes, and it can be constructed by only knowing the Miller indices of these planes and their surface energies (as represented for a 2-D system in Figure 2.15 A). This methodology, known as a *Wulff construction*, has been widely applied in the computational study of nanoparticle morphology,^{177,178} whose equilibrium shapes correspond to 3-D polyhedrons with the same symmetry as that of the Bravais lattice of the underlying crystal (with similar shapes to the construction in Figure 2.15 B), and has been used for the prediction of the reactive surfaces of ZnSe-based quantum dots (QDs) in this thesis.

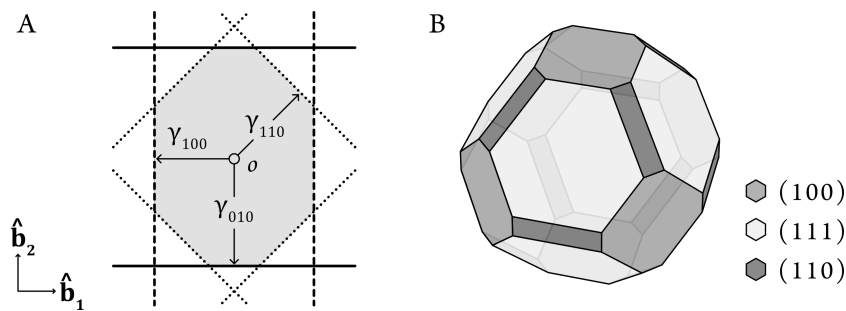


Figure 2.15 A) Representation of a Wulff construction for an arbitrary 2-D system, taking into account lattice planes with Miller indices (100), (010) and (110). The equilibrium shape, given by the area delimited by the closest planes to the centre (O) at each point is represented in grey. B) Schematic representation of the equilibrium shape of a 3-D particle with surface energies of 1.10, 1.00 and 1.15 eV/Å² for lattice planes with Miller indices (100), (111) and (110), respectively.

2.9.4. Analytical identification of surface sites

The theoretical determination of the resting state and activity of any heterogeneous system in any media requires an exhaustive structural analysis of the active surface. This surface will bind adsorbates in a determined configuration, which depends on both the nature of the atoms that make up the active surface, and the availability of surface sites. In the latter, adsorbates can bind in the *fcc*, *hcp*, *top* or *bridge* sites. The *fcc* site is characterised by being on a hollow site in the topmost layer, which in turn is atop a further hollow site from the second topmost layer, which lies above an atom in the third topmost layer; the *hcp* site is located on a hollow site in the topmost layer that lies on an atom directly located on the same position in the second topmost layer; the *top* site is located directly atop a surface atom in the topmost layer; finally, the *bridge* site lies atop the bisection between two neighbouring atoms in the topmost layer. A schematic representation of the adsorption sites in a (111)-terminated FCC surface is depicted in Figure 2.16.

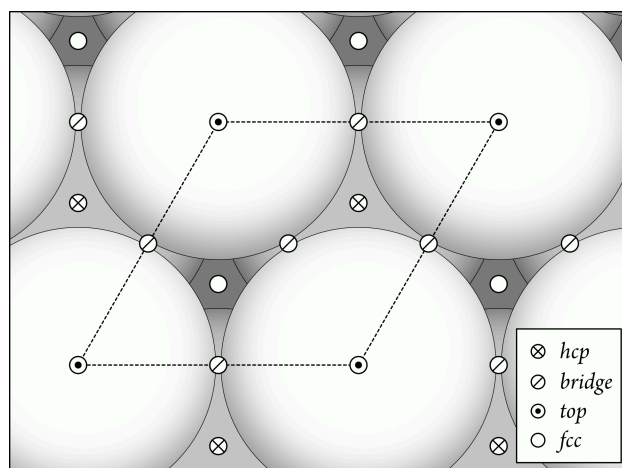


Figure 2.16 Top view representation of the adsorption sites present in a surface of a FCC lattice terminated by the (111) plane. The primitive unit cell, which fully encloses 3 *bridge*, 1 *fcc*, 1 *hcp* and 1 *top* full sites, is delimited with a dashed line.

To investigate the lowest energy configuration for an adsorbate on any surface, we must consider all available adsorption sites which are not symmetrically equivalent. In crystal systems with large unit cells that lack symmetry or display non-conventional adsorption sites (e.g. on kinked or stepped surfaces), this is not straightforward. In these cases, surface sites can be identified by means of a *Delaunay triangulation* network and forming a 2-D Voronoi diagram from the coordinates of the surface atoms, as implemented in the Python-based software *pymatgen*;¹⁷⁹ the surface adsorption sites have been shown to reside atop the given surface site coordinates, at the midpoints of the edges in the network and at the centre of the Voronoi cells.¹⁸⁰ This generic method based on the geometry of the surface sites allows for the simplification and automatization of coverage analyses on systems with multiple symmetrically non-equivalent adsorption sites, and has been applied procedurally in all adsorption studies carried out in this thesis.

“ *A problem is grand in science if it lies before us unsolved and we see some way for us to make some headway into it.* – **Richard Feynman**

Letter to a former student, 1966

CHAPTER 3

Objectives

The main aim of this thesis is to use periodic DFT calculations to investigate relevant reduction reactions in (photo)electrocatalytic systems, to understand the effects driving the catalytic activity and selectivity and to drive the discovery of more efficient (photo)electrocatalysts for solar- and power-to-X technologies. Specifically, the results discussed in this thesis focus on gaining a deeper insight into the ORR, CO₂RR, HER and ECH of terminal alkynes on three different catalytic systems. Below, we will explore the rationale behind the studies presented herein and the key objectives that were set for each of them.

3.1. N-doped Carbon Electrocatalysts for the Oxygen Reduction Reaction

Despite N-doped C materials having been extensively studied for their use as metal-free electrodes for the ORR, the fundamental understanding of the effect that different N-dopants have on the ORR activity and selectivity is still lacking. To shed some light on the reactivity and rationalise the experimental findings from our collaborators in the group of Prof. Paula Colavita in Trinity College Dublin, we sought to perform a thorough investigation by means of DFT calculations. With this in mind, we aimed at accomplishing the following objectives:

- Design cluster models representative of the C electrodes employed in experiments.
- Establish the N-dopant distribution and multiplicities of the C clusters containing predominantly graphitic or pyridinic N dopants, and of the cluster containing a homogeneous mixture of both.

- Uncover the energetics of a proposed ORR pathway on all C sites of the three cluster models to locate the predominant active site for this reaction.
- Assess the ORR activity and selectivity of the designed cluster models.
- Compare our theoretical results with the reduction currents observed in experiments.

3.2. CO₂ Photoreduction on Ligand-modified ZnSe Quantum Dots

Colloidal metal chalcogenide QDs are among the most investigated systems for the photocatalytic conversion of CO₂ into C-based fuels, and several strategies have been adopted to try to improve their activity and selectivity. In particular, the introduction of organic capping ligands has shown great promise, although the factors responsible for the ligand-led enhancement are still under intense debate. To determine the scope of the ligand's influence on the CO₂RR activity to CO using QDs, in this thesis we aimed at untangling the reaction mechanism on ZnSe QDs using imidazolium capping ligands, as well as dithiol-based ligands in the absence and presence of a Ni-based molecular co-catalyst. This study was carried out in close collaboration with our experimental collaborators in the group of Prof. Erwin Reisner at the University of Cambridge. To unravel the photocatalytic CO₂RR activity and selectivity on ligand-capped ZnSe QDs, we established the following goals:

- Determine the morphology of the ZnSe QD particles and ligand concentration under reaction conditions.
- Propose and elucidating a reaction mechanism on the ZnSe QD surface, and relating the energetics of the proposed pathway with the experimental results.
- Analyse the effect of ligand capping on the CO selectivity and HER suppression observed experimentally.
- Assess the influence of the imidazolium-based ligands on the reaction intermediates by uncovering all non-covalent interactions.
- Determine the effect of the dithiol ligand length on the stabilisation of key reaction intermediates in the absence and presence of the Ni-based molecular co-catalyst, and examine the non-covalent interactions to rationalise the CO yields and selectivities obtained in experiments.

3.3. Coverage-led Design of MXenes for Electrocatalysis

The consideration of the coverage of the electrode surface under reaction conditions is essential for understanding the activity and selectivity of most heterogeneous catalysts. One of the most promising materials for electrocatalytic applications, 2-D MXenes, have been shown to be covered by various terminations at different conditions of pH and U . Nonetheless, most theoretical studies of MXene-based electrocatalysts often neglect the surface coverage under electrochemical conditions, thus leading to a misrepresentation of the reaction mechanisms and surface reactivity. Hence, in this thesis we aimed to use periodic DFT calculations to

accurately assess the surface coverages of most MXenes synthesized to date, and to employ the acquired knowledge to tailor their applications for electrocatalysis. To achieve this, we set the following goals:

- Determine the predominant surface coverages of all the experimentally known MXenes with out-of-plane ordering at different electrochemical conditions.
- Establish a procedure to determine the optimal conditions of pH and U for a certain surface coverage based on its thermodynamic stability.
- Assess the electron conductivity of the MXenes with different terminations and benchmark our results with those reported in the literature.
- Uncover the activity of MXenes towards the HER based on the energetics of their surface coverages, at different conditions of applied potential and pH.

3.4. 2-D MXenes for Electrochemical Hydrogenations

Based on our study on the surface coverages, we then sought to investigate the viability of electron-rich H-covered 2-D MXenes as electrocatalysts for the ECH of organic substrates. Thus, we focused on performing a thermodynamic investigation of the ECH of a common liquid alkyne, 4-pentyn-1-ol, on a readily available MXene, i.e. $Ti_3C_2T_x$. This electrocatalytic system, which is intended to serve as a proof of concept, was investigated in collaboration with the experimental group of Prof. Paula Colavita. Subsequently, we aimed at determining the competence of a broader range of H-covered MXenes as catalysts for the selective ECH of acetylene to the industry-relevant ethylene. Both goals were broken down into the following objectives:

- Propose and elucidating the reaction mechanism for the H-coverage-led ECH of 4-pentyn-1-ol to 4-penten-1-ol and 1-pentanol.
- Rationalise the energetics of the proposed mechanism with the experimental results from our collaborators.
- Determine the most promising candidates for the ECH of small terminal alkynes based on their range of predominance of H coverages and their corresponding thermodynamic stabilities.
- Propose a reaction mechanism for the H-coverage-led ECH of acetylene on 2-D MXenes.
- Assess the activity and selectivity for the ECH of acetylene to industry-relevant ethylene on a range of MXenes.

“ I believe that water will one day be employed as fuel, that hydrogen and oxygen which constitute it, used singly or together, will furnish an inexhaustible source of heat and light, of an intensity of which coal is not capable. – **Jules Verne**

The mysterious island, 1874

CHAPTER

4

N-doped Carbon Electrocatalysts for the Oxygen Reduction Reaction



4.1. Introduction

In the 60s, the necessity of generating power in space missions during the years of the space race boosted a mainstream interest for investigating the ORR as the most important and rate-limiting reaction in PEM fuel cells,¹⁸¹ by means of a safe and efficient process which only required lightweight fuels. In turn, ORR research was also motivated by the prospect of generating potable water for crew consumption and cabin humidity as the only by-product in the energy production process. This led NASA to develop a fuel cell for the Gemini mission, which ran for more than 1,000 hours and served as a proof of concept for the development of more advanced fuel cells for the Apollo missions. In this fuel cell, both the anode and the cathode consisted of electrodes with deposited Pt catalysts, which could catalyse the HOR and ORR at room temperature. For decades thereafter, Pt catalysts have been overwhelmingly considered as the primary systems capable of performing this reaction,¹⁸² and many efforts have been put into unravelling the activity of these catalysts⁸² and designing better electrodes by alloying^{183,184} or nanostructuring Pt.¹⁸⁵

The results discussed in this section have been published and highlighted on the front cover of the 48th issue of *Small*

Behan, J. A.‡; **Mates-Torres, E.‡**; Stamatina, S. N.; Domínguez, C.; Iannaci, A.; Fleischer, K.; Koque, Md. K.; Perova, T. S.; García-Melchor, M.; Colavita, P. E. *Small*, **2019**, 1902081.

Metal-free C-based catalysts have been identified as promising candidates to replace Pt for the ORR.¹⁸⁶ For instance, electrochemical studies of the ORR activity on highly-oriented pyrolytic graphite (HOPG) showed that the edges of this material displayed enhanced catalytic properties.¹⁸¹ Despite several C-based electrode modification strategies having been investigated for the selective ORR towards the 2-electron pathway to generate hydrogen peroxide,¹⁸⁷ most studies in the past decades have been devoted to obtaining better C-based catalysts for the 4-electron ORR in alkaline media for applications in fuel cell technologies. The most relevant advancement in this field was the discovery that N-doping of a wide range of C materials (e.g. graphene, fullerenes or carbon nanotubes) dramatically increased their catalytic activity and selectivity towards the 4-electron ORR product,¹⁸⁸⁻¹⁹² achieving current densities similar to those obtained using Pt/C catalysts. Since then, theoretical and experimental studies have focused on understanding the effect of the N-doping on the enhancement of the catalytic performance and determining the active site.^{16,193}

The exact nature of the active site is directly linked to the type of dopant present on the catalytic surface. Accordingly, N moieties in N-doped graphene-like carbon materials can be either graphitic (N_G), located at the basal plane or valley sites, or pyridinic (N_P), located at the edges or surrounding carbon vacancies, as displayed in Figure 4.1. There has been a lot of controversy around the importance of the presence of either or both in catalytic systems.¹⁸⁶ In the early stages of these investigations, N_G was deemed as the main promoter of the increase in ORR activity;^{194,195} however, recent studies suggest that oxygen species are preferentially adsorbed and reduced on carbon atoms with increased Lewis basicity in the vicinities of N_P sites.¹⁶ The true nature of the N dopants in current state-of-the-art C-based electrocatalysts for the ORR probably lies in-between: both N_G and N_P are believed to play an important role in effectively catalysing this reaction in a synergetic way,^{196,197} and the predominancy of either one or the other may become more relevant at different values of pH.¹⁹⁸ While the practical effects of this N-dopant mixing is somewhat understood,¹⁹⁹ the role of the interplay between these two dopants in the reaction mechanism is still under intense debate.

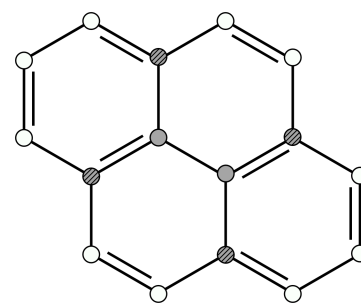


Figure 4.1 Carbon scaffold with edge, basal and valley sites, depicted as white, plain grey and striped grey spheres, respectively.

In order to improve our understanding of the cooperative effects between N_P and N_G in N-doped carbon electrodes, in this section we will present a comprehensive theoretical approach to rationalize the findings of our experimental collaborators led by Prof. Paula Colavita, who observed an enhanced selectivity towards the 4-electron ORR product in alkaline media using N-doped carbon electrodes containing mixed $N_P:N_G$ dopant compositions. Our computational results will also shed light on the good activity of pure N_P and N_G -doped systems for the 2-electron pathway revealed in the experiments, and determine the nature and location of the surface active sites in all investigated model electrodes.

4.2. Experimental results

In order to elucidate the influence of the N-dopant in the ORR, three C electrodes were prepared consisting of a geometrically well-defined glassy carbon disk sputtered with amorphous carbon using two different methods. On the one hand, nitrogenation of the carbon scaffold was achieved by using a N₂/Ar plasma during the sputtering process, followed by the annealing of the deposited film at 900 °C under a N₂ atmosphere, yielding nitrogenated amorphous carbon films on the glassy carbon disk. This system is referred to as a-C:N 900. On the other hand, amorphous carbon was sputtered in the absence of N₂ on two glassy carbon disks, and N-doping was introduced by treating the surface with a N₂/NH₃ atmosphere at temperatures of 700 and 900 °C. These electrodes are referred to as a-C NH₃ 700 and a-C NH₃ 900, respectively. Deconvoluted X-ray photoelectron spectra (XPS)^{†††} of the three electrodes show two peaks centred at ~ 398 and 401 eV, corresponding to surface N_G and N_P, respectively. As shown in Figure 4.2 A, a-C:N 900 contained predominantly N_G surface species (with a composition of [74 ± 8]% vs. [26 ± 8]% of N_G and N_P, respectively). On the other hand, a-C NH₃ 700 displayed a predominant electron count corresponding to N_P species ([39 ± 9]% and [64 ± 9]% of N_G and N_P, respectively). Finally, a-C NH₃ 900 showed a nearly 1:1 composition of N_G and N_P ([43 ± 6]% and [56 ± 6]% of N_G and N_P, respectively). Further analyses of the Raman spectra of these electrodes indicated that they possessed a highly graphitized carbon network with small graphite cluster sizes.

The ORR activity in alkaline media (pH = 14) was examined by using a rotating ring disk electrode (RRDE).^{†††} The onset potentials for the ORR (potential corresponding to a 0.1 mA cm⁻² current density) were found to be 0.83, 0.77, and 0.73 V_{RHE} for a-C NH₃ 900, a-C:N 900 and a-C NH₃ 700, respectively. The current generated at the ring disk was demonstrated to be caused by HO₂⁻ generation, which was the only species detectable through the RRDE. Hence, the ring current density (shown in Figure 4.2 B) could be used to determine the amount of HO₂⁻ produced, and the selectivity of the catalyst towards the 4-electron product, as seen in Figure 4.2 C. Specifically, a-C:N 900 shows the highest yield of HO₂⁻ (70 % at 0.3 V_{RHE}) with an average of exchanged electrons of $n = 2.4$. This indicates that the ORR on the a-C:N 900 electrode occurs predominantly through the 2-electron pathway. This is in contrast with a-C NH₃ 900, which displays a HO₂⁻ yield of as low as 6 % at 0.3 V_{RHE} with $n = 3.9$, demonstrating a high selectivity towards the 4-electron pathway. Finally, experiments show that both the 2- and 4-electron pathways operate in a-C NH₃ 700, with $n = 3.1$. Altogether, these results highlight the importance of the presence of both N_G and N_P in the C scaffold for effectively driving the ORR towards the desired 4-electron product.

^{†††} XPS uses the photoelectric effect and displays the number of electrons with a specific binding energy on the surface, effectively determining the type and number of surface elements and their coordination.

^{†††} In a RRDE, the electrode is made to rotate and is surrounded by a ring. In the case of the ORR, this allows for O₂ to be reduced at the electrode with its products subsequently sliding to the ring in a laminar flow, where they may be detected and oxidised. Analysing the current density at the ring quantifies the amount of a given product obtained.

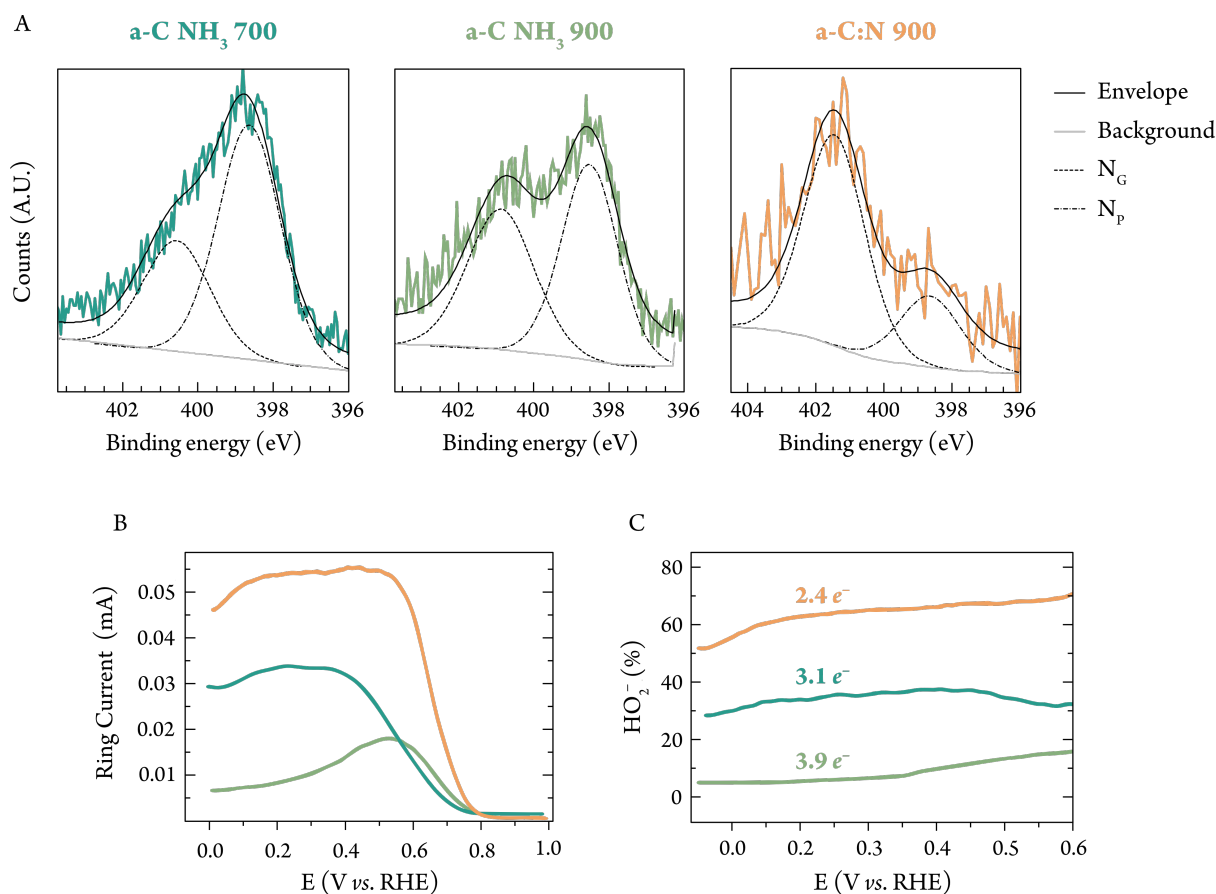


Figure 4.2 A) Deconvoluted XPS spectra of the three amorphous C electrodes, namely a-C NH₃ 700, a-C NH₃ 900 and a-C:N 900. B) Observed ring current in a linear sweep from 0.0 to 1.0 V_{RHE} with the three catalytic systems. C) HO₂⁻ yield detected with each electrode from 0.0 to 0.6 V_{RHE}, specifying the number of exchanged electrons at the ring disk electrode. Panels B and C follow the colour code for each electrode depicted in A.

Based on the above experimental results, we set out to unravel the activity of the three systems using computational models, which will be described in the following sections.

4.3. Computational details

All DFT calculations were carried out using the dispersion-corrected range-separated hybrid ω B97XD functional,¹³⁸ described in Section 2.2.3.4, as implemented in the Gaussian09 software.²⁰⁰ The 6-31G(d, p) basis set was used for C and H atoms, with the addition of diffuse functions in 6-31+G(d, p) for O atoms. The aqueous electrolyte was simulated as an implicit solvent with dielectric constant, $\epsilon = 78.3553$, by means of the SMD universal solvation model,¹⁵⁹ discussed in Section 2.6.2. All converged calculations were confirmed to be energy minima in the PES through vibrational frequency analysis. The Gibbs adsorption energies (ΔG_{ads}) of the reaction intermediates were calculated at experimental conditions (298 K, 1 atm, and pH = 14) using the CHE model,⁸² and fixing the Gibbs energy of the overall reaction to the experimental value of 4.92 eV (as schematised in Figure 1.8). Therefore, the resulting ΔG_{ads} in the proposed mechanism are calculated in a similar

fashion to Eq. (2.92) in the Computational Methods. However, it must be noted that the one-electron transfer involved in the $\text{HOO}^\cdot \rightarrow \text{HOO}^-$ transition is approximated to the solvation energy of the proton, which is related to the absolute potential of the standard hydrogen electrode. In this thesis, the value of 4.44 eV recommended by the International Union of Pure and Applied Chemistry (IUPAC) has been used. This corresponds to a 1 M gas phase to 1 M solution standard-state aqueous proton solvation Gibbs energy of $-261.7 \text{ kcal mol}^{-1}$.^{30,201} In addition, the Gibbs energy of the hydroxide anion required to describe the adsorption energies of the intermediates is defined as:

$$G_{\text{OH}} = G_{\text{H}_2\text{O}} - G_{\text{H}} = G_{\text{H}_2\text{O}} - \frac{1}{2}G_{\text{H}_2} + k_B T \ln(10) \times \text{pH} \quad (4.1)$$

The reaction PLS in each model system was calculated by determining the maximum Gibbs energy associated to the elementary steps ΔG_{1-4} in the proposed mechanism at the thermodynamic potential (i.e. $1.23 V_{\text{RHE}}$ or $0.404 V_{\text{SHE}}$ at $\text{pH} = 14$), as displayed in Eq. (1.37). These relative energies are given by the following equations:

$$\Delta G_1 = \Delta G_{\text{I}_1} - \Delta G_{\text{O}_2} \quad (4.2)$$

$$\Delta G_2 = \Delta G_{\text{I}_2} - \Delta G_{\text{I}_1} \quad (4.3)$$

$$\Delta G_3 = \Delta G_{\text{I}_3} - \Delta G_{\text{I}_2} \quad (4.4)$$

$$\Delta G_4 = 0 - \Delta G_{\text{I}_3} \quad (4.5)$$

Where I_1 , I_2 and I_3 are the first, second and third intermediates in the proposed mechanism for the 4-electron ORR, which will be discussed in subsequent sections. A model energy diagram for this reaction is shown in Figure 1.8 for exemplification purposes.

4.4. N-doped carbon electrode surface model

To shed light on the activity of the three different catalysts for the ORR, three cluster models were designed with the aim to simulate the N-dopant distribution at the electrode surface observed by XPS. The undoped initial structure (referred to as Gr) consisted of a medium-sized 48-C graphene monolayer (illustrated in Figure 4.3), which was deemed large enough to limit interactions between the multiple N-dopants to be introduced in the doped systems. These models were deemed to be good representations of the local structure of the amorphous C electrodes, wherein effects taking place at edges and kinks were expected to play a major role. To simulate the various dopant ratios at the carbon electrodes, three structures were modelled: a graphene system containing 2 N_G dopants (denoted as $2\text{N}_G\text{-Gr}$, which emulates the dopant composition in the a-C NH_3 700 electrode), 2 N_P dopants (labelled as $2\text{N}_P\text{-Gr}$, which only contains the predominant N dopants found in the a-C:N 900 electrode), and a structure containing 1 N_G and 1 N_P (denoted as $\text{N}_G\text{N}_P\text{-Gr}$, replicating the mixed composition of the a-C NH_3 900 electrode). Firstly, an analysis on the dopant distribution was carried out by considering all combinations of atoms at edge and basal plane graphitic and pyridinic N atoms (basal plane pyridinic N dopants were accompanied by a neighbouring vacancy). This analysis revealed that the most stable

N-doped structures in all cases correspond to all dopants located on edge and valley sites, and as far apart as the geometry allowed. Thus, the most stable structures for the $2N_G$ -Gr, $2N_P$ -Gr and $N_G N_P$ -Gr models, which present carbon substitutions in positions C32 and C89, C12 and C109, and C32 and C109, respectively, are depicted in Figure 4.4 A.

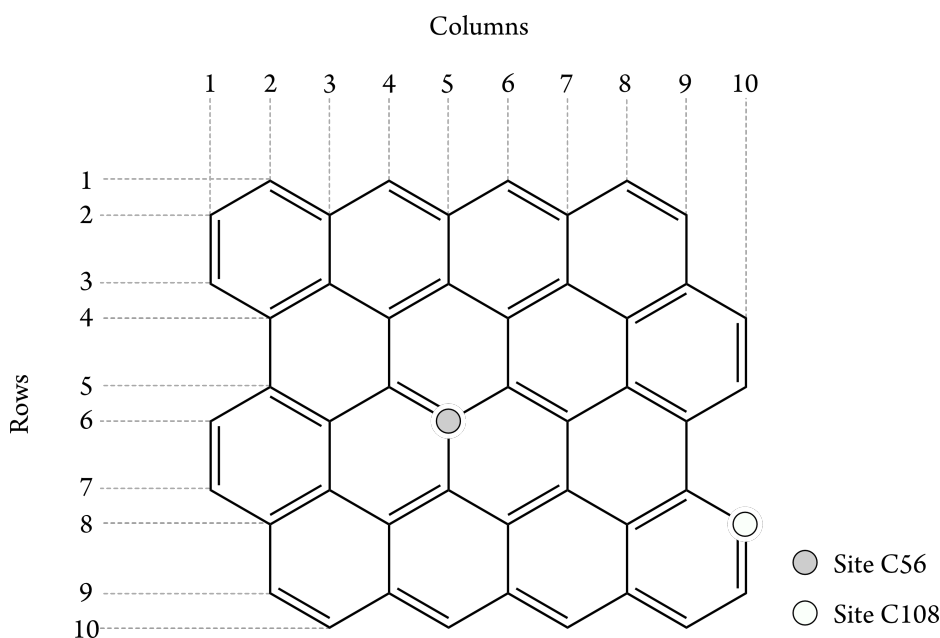


Figure 4.3 Schematic representation of the pristine Gr model of the bare graphene used in simulations, including the column-row notation adopted to label the sites considered for the benchmark of the different N-dopant distributions inserted by substitution. This notation was also used to denote the location of the ORR intermediates in the activity and selectivity studies described in subsequent sections. Two arbitrary points in the graphene scaffold are indicated as grey and white filled circles for exemplification purposes.

Furthermore, at the potential window of interest (positive values up to $1.23 V_{RHE}$), we predict that these N-doped graphene clusters can be present in either their neutral or oxidised form; restricting the possible oxidised forms to only one state with a charge of +1, we can identify several configurations of charge and multiplicity arising from the possible combinations of electrons around the N sites. These combinations are represented in Figure 4.4 B, where the possible local environments of the N-dopants in the neutral and oxidised forms of three cluster models is represented. In all cases, the oxidised form with the smallest multiplicity is found to be the most energetically favoured configuration, as can be seen in Table 4.1, which also includes some larger multiplicities than the ones shown in Figure 4.4 resulting from electron recombination between neighbouring carbon atoms.

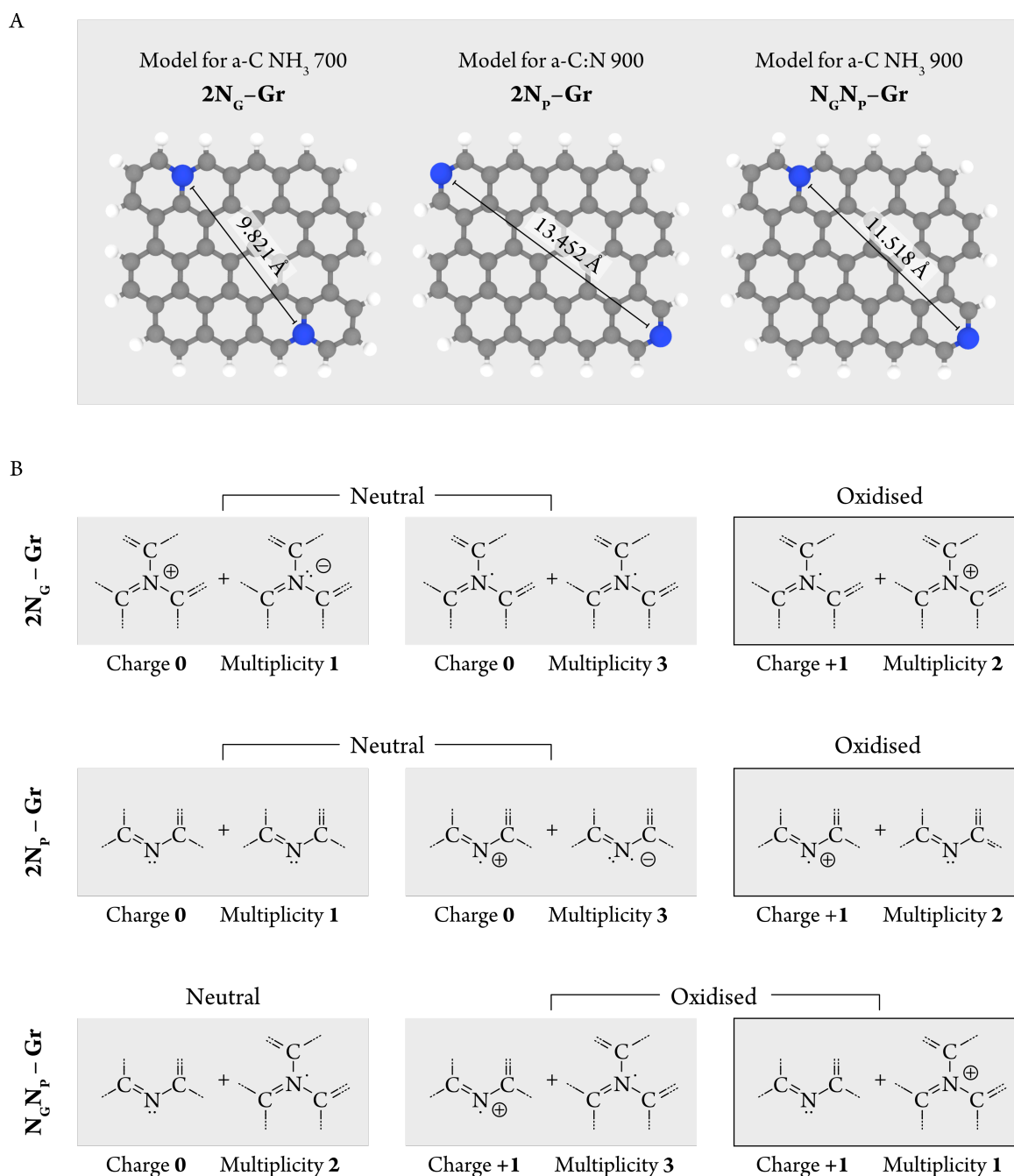


Figure 4.4 A) Graphene models used to simulate the surfaces of the three electrodes, containing only N_G or N_P dopants (2N_G-Gr and 2N_P-Gr, respectively), or a 1:1 composition of each (N_GN_P-Gr). Carbon, hydrogen and nitrogen atoms are depicted as grey, white and blue spheres, respectively. At the working potentials, we expect these structures to be present in either neutral or oxidised forms with different multiplicities, arising from the combinations represented in B). The most stable configurations used for reactivity studies are denoted with a black overline.

Table 4.1 Relative Gibbs energies (in eV) for the neutral and oxidized forms of the most stable pristine 2N_G-Gr, 2N_P-Gr and N_GN_P-Gr clusters shown in Figure 4.4 A at 0 V_{RHE}. The values of the most stable structures in each model are highlighted in bold.

2N _G -Gr			2N _P -Gr			N _G N _P -Gr		
Charge	Multiplicity	ΔG	Charge	Multiplicity	ΔG	Charge	Multiplicity	ΔG
0	1	0.00	0	1	0.00	0	2	0.00
	3	1.08		3	0.03		4	1.03
1	2	-0.94	1	5	2.20	1	1	-0.57
	4	0.25		2	-0.21		3	-0.48

To assess the ORR activity and selectivity of each catalyst model, we performed a thorough mechanistic analysis of the possible C active sites surrounding the N dopants present on the surfaces of the resting states obtained for each cluster model.

4.5. Assessing ORR activity

In order to unravel the ability of the C electrodes to selectively promote the 2-electron or 4-electron ORR, we carried out a thorough computational investigation of the mechanism. In addition, following experimental evidence that suggest that a weak HO₂⁻ adsorption yields a lower 4-electron selectivity, HOO*⁻ was considered as a reaction intermediate in the proposed reaction pathway.⁸¹ Therefore, we investigated the 4-electron ORR with a proposed mechanism consisting of the initial adsorption of O₂ onto the active site and its subsequent protonation to a hydroperoxo intermediate (HOO*), as in Eq. (4.6), followed by an ET step to generate HOO*⁻, as depicted in Eq. (4.7). This intermediate can then undergo a further 2-electron reduction to yield OH⁻ species to complete the 4-electron reaction according to Eqs. (4.8) and (4.9), or desorb from the surface to produce the hydroperoxide anion HO₂⁻ detected at the RRDE.



In the above proposed mechanism, the generation of the 2-electron product is believed to occur *via* direct desorption of the hydroperoxyl radical after a ET step, as in Eq. (4.10), or *via* interaction of the hydroperoxo intermediate with a superoxide species O₂^{•-} resulting from the O₂ reduction in an outer-sphere electron transfer which is known to occur in alkaline media,²⁰² as in Eq. (4.11).



Therefore, an accurate assessment of the binding energies of the reaction intermediates is crucial to determine the PLS of each system and derive the activity of the catalysts, which will subsequently reveal their selectivity towards the 2-electron and the 4-electron products. Locating the active site onto which these intermediates are bound is not straightforward. Despite there being consensus on the basis that reactivity occurs on the C atoms near the N dopants,¹⁶ an accurate assessment demands individual analysis of the mechanism on every possible site. Therefore, for each modelled N-doped C scaffold, we mapped out all edge and basal plane C atoms atop which the reaction intermediates could potentially bind. During this process, the inversion symmetry of the $2N_G$ -Gr and the $2N_P$ -Gr models allowed for the reduction of the amount of sites to be considered for reactivity (for instance, the site C109 in $2N_G$ -Gr was considered to be the same as the site C12, and thus the mechanism was only assessed on the latter). This resulted in 17 sites analysed for $2N_G$ -Gr, 16 for $2N_P$ -Gr and 19 for $N_G N_P$ -Gr. The activity of each site was examined by modelling the binding of the HOO^* , HOO^{*-} and HO^* intermediates, resulting in structures similar to the ones presented in Figure 4.5 for site C41 of the $2N_G$ -Gr cluster.

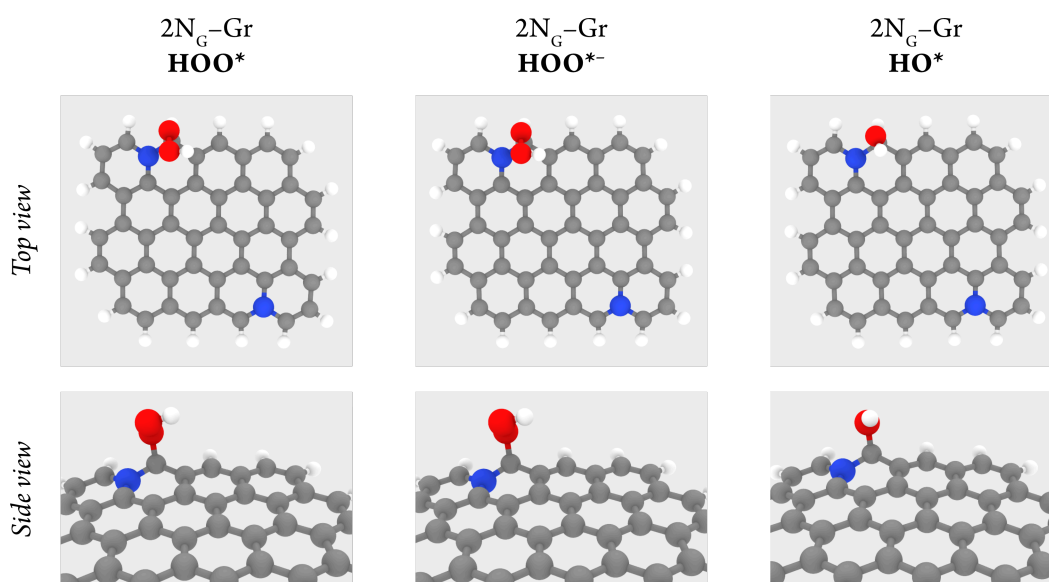


Figure 4.5 Top and side view representations of the optimised OOR intermediates involved in the proposed mechanism, namely HOO^* , HOO^{*-} and HO^* , on the C41 site of the $2N_G$ -Gr cluster model. Carbon, hydrogen, nitrogen and oxygen atoms are depicted as grey, white, blue and red spheres, respectively.

As discussed in Section 1.3.2, in order to determine the theoretical onset potential we must analyse the reaction mechanism at the thermodynamic potential of $1.23 V_{RHE}$ ($0.404 V_{SHE}$ at $pH = 14$) and identify the PLS (see computational methods for more details). Hence, we will devote the following sections to the study of the activity of the three cluster models to reveal the location of the primary active sites and the effect of the N-dopant composition on the OOR reactivity.

4.5.1. Activity of 2N_G-Gr

With the aim of obtaining a good representation of the activity of the 2N_G-Gr cluster, the adsorption of the 3 intermediates in the 4-electron reaction was modelled on a total of 9 edge sites (C16, C13, C12, C21, C41, C61, C81, C92 and C104), 5 valley sites (C24, C25, C52, C72 and C93) and 3 basal sites (C33, C36 and C44). Of these, 8 sites failed at adsorbing one or more intermediate species and were discarded as potential active sites. The energy diagrams obtained at the thermodynamic potential on all the other sites are displayed in Figure 4.6.

A careful examination of the intermediate adsorption energies from the mechanistic studies on all sites in N_G-Gr reveals that the four most active sites, with PLS of 0.87, 0.96, 0.98 and 1.06 eV correspond to the sites in positions C41, C61, C21 and C13, respectively—that is, on the edge sites closest to N_G—, in agreement with previous theoretical data on N_G-predominant C clusters.²⁰³ These sites are denoted with an orange dot in their Gibbs energy diagrams and in the C scaffold schematic at the bottom of Figure 4.6. Furthermore, we predict that these sites will present the same trends in their Gibbs energy diagrams at 1.23 V_{RHE}: an endergonic adsorption of HOO*, followed by an exergonic ET to HOO*⁻ and subsequent formation of HO*, and a final endergonic formation of HO⁻. While the final step is the PLS on site C41, edge sites further from the N_G dopant are less able to stabilise the HOO* and HO* intermediates, which see their adsorption energies increase. This results in the PLS shifting from the last step to the first on sites C61, C21 and C13.

This potential stabilising effect of the N_G dopant on the HOO* and HO* reaction intermediates at neighbouring edge sites is further demonstrated by studying the reaction on the farthest edge sites (i.e. sites C16, C81, C104 and C92) and a basal plane site (C33). These display a common energy trend wherein the HOO* formation is very endergonic, followed by a very exergonic ET to HOO*⁻ and an endergonic and exergonic formation of HO* and an HO⁻, respectively, and are indicated with a dark blue spot in Figure 4.6. In all instances, HOO* formation constitutes the PLS with values of 1.88, 1.97, 2.00, 2.02 and 2.28 eV for C16, C33, C81, C104 and C92, respectively. We conclude that these large PLS hinder the ability of O₂ to undergo the 4-electron ORR on these sites; therefore, we predict the ORR reactivity of the 2N_G-Gr cluster models to occur predominantly on the edge sites highlighted in orange in Figure 4.6, which display a more energetically feasible distribution of the Gibbs energies of the reaction intermediates.

4.5.2. Activity of 2N_P-Gr

Similarly to 2N_G-Gr, we analysed the reactivity on 2N_P-Gr by examining the adsorption of the ORR intermediates on 9 edge sites (C21, C41, C61, C81, C92, C13, C16, C17 and C29), 5 valley sites (C32, C52, C24, C25 and C28) and 2 basal plane sites (C33 and C53). Of these, 3 valley C sites were deemed to be inactive since they failed at adsorbing one or more intermediates. The Gibbs energy diagrams at 1.23 V_{RHE} obtained for the remaining sites are displayed in Figure 4.7.

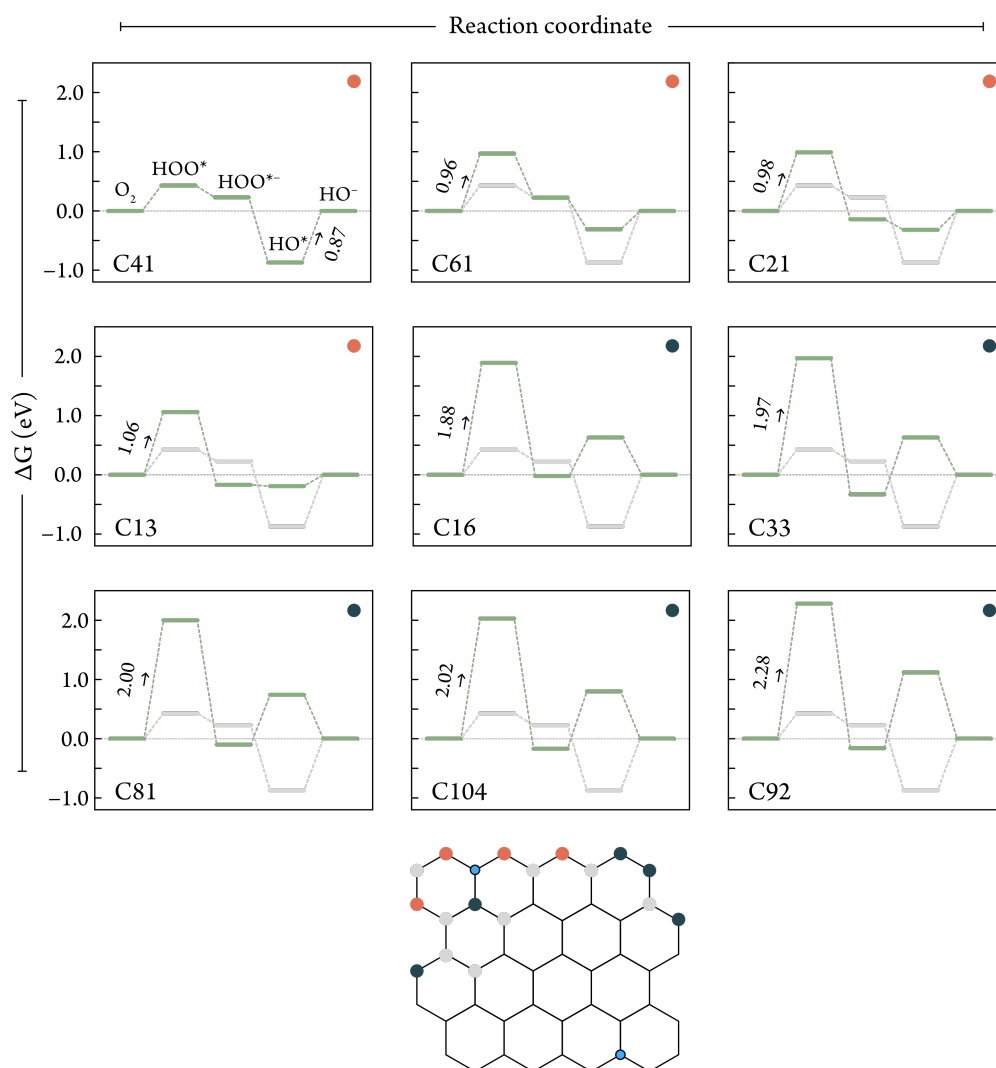


Figure 4.6 Gibbs energy diagrams at 1.23 V_{RHE} for the proposed mechanism on the C sites of 2N_C-Gr that are able to adsorb all the ORR intermediates. The coordinates of the studied site in the carbon scaffold is included as an inset at the bottom left of each energy diagram. The first energy diagram, corresponding to the pathway on the C site that displays the lowest PLS, is included in grey below subsequent diagrams for reference, which in turn are arranged in ascending order (left to right and top to bottom) based on the value of their PLS (which is identified with an ascending black arrow along with its value). The reaction intermediates are common to all energy diagrams, and therefore, are only specified in the first one. Inset (below): Schematic representation of all analysed sites in the cluster, where the two groups of studied sites displaying common energetic trends in their corresponding energy pathways are highlighted in orange and dark blue, both in the scaffold and in the energy diagrams. The sites excluded as active sites due to their inability to adsorb one or more intermediates are highlighted in grey. Hydrogen atoms and double bonds have been omitted for clarity; N dopants are depicted in light blue.

Firstly, an assessment of the PLS for each of the sites indicates that the one exhibiting the lowest values are the same as those in $2N_G\text{-Gr}$, *i.e.* sites C41, C13, C61 and C21 with PLS values of 0.82, 1.05, 1.07 and 1.14 eV, respectively. The identical location of the most active sites between $2N_G\text{-Gr}$ and $2N_P\text{-Gr}$ may be due to the similar position of the N dopants in both cases. The energetic trends in the Gibbs energy pathways, however, differ considerably in the current case. For all the aforementioned sites, the formation of HOO^* corresponds to the PLS, and is followed by a very exergonic ET step to yield HOO^{*-} , and two endergonic steps to HO^* and HO^- . The four cases that display this energy trend are indicated as orange spots in Figure 4.7.

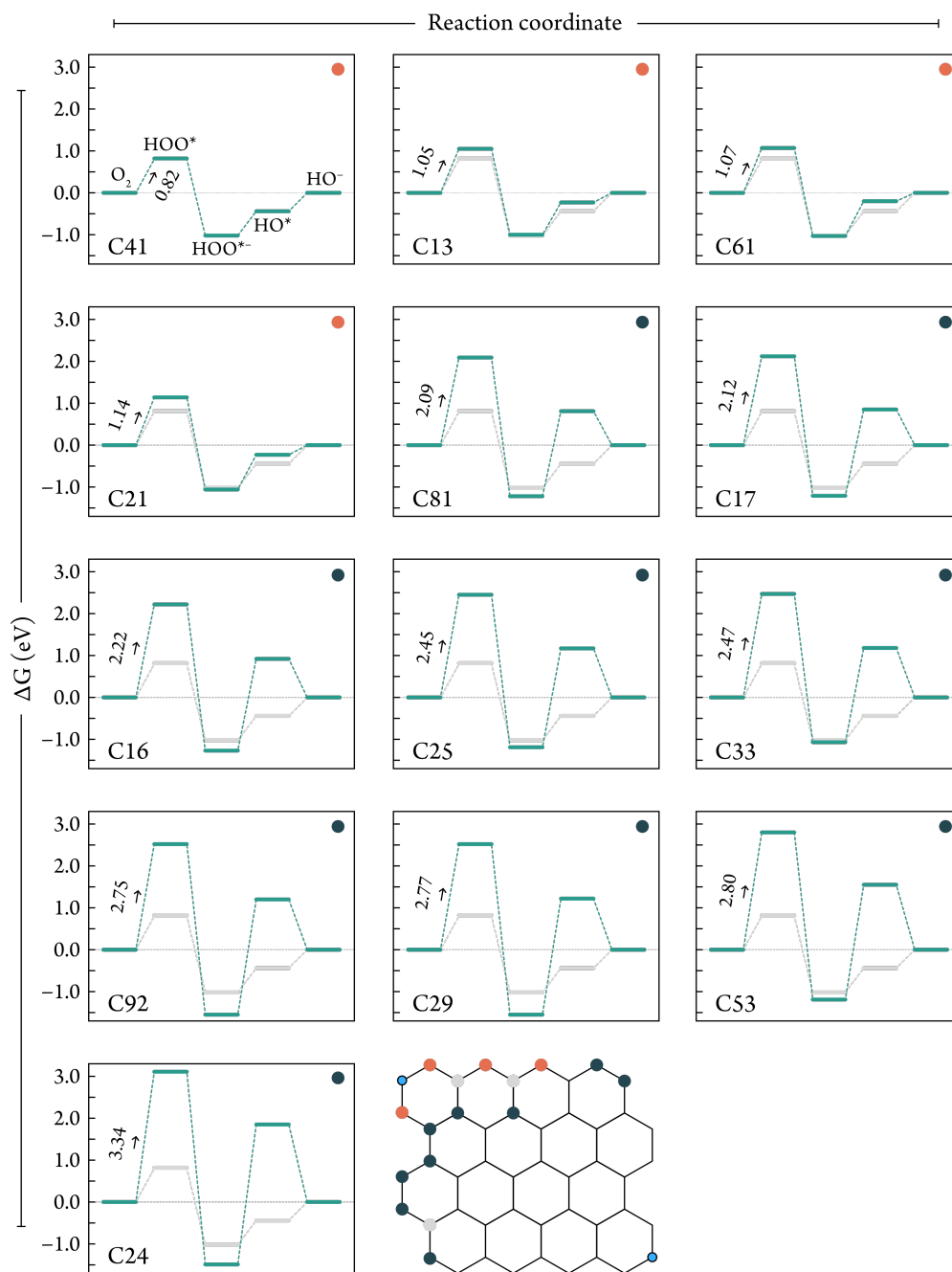


Figure 4.7 Gibbs energy diagrams at $1.23 V_{\text{RHE}}$ for the proposed mechanism on the C sites of $2N_P\text{-Gr}$ that are able to adsorb all the ORR intermediates. Further relevant information can be found in the caption of Figure 4.6.

Therefore, our results suggest that the presence of the N_P dopant in $2N_P$ -Gr stabilises the HOO^{*-} intermediate more efficiently compared to N_G . Furthermore, similarly to $2N_G$ -Gr, the edge site closest to the N_P dopant (C41) displays a lower adsorption for HOO^* and HO^* , which indicates that the dopant may have a certain influence in the stabilisation of these intermediates, effectively lowering the PLS. This is also evident from the analysis of the basal, valley and further edge sites onto which HOO^* and HO^* adsorptions become substantially more endergonic, in identical fashion to $2N_G$ -Gr. These sites, which are denoted with a dark blue spot in the Gibbs energy diagrams and the schematic of the C scaffold of Figure 4.7, share a similar energy trend to that discussed on $2N_G$ -Gr, where an endergonic formation of HOO^* is followed by an exergonic ET to HOO^{*-} , an endergonic formation of HO^* and an exergonic desorption to HO^- . In these cases, however, the endergonicity of the HOO^* and HO^* formation is increased with respect to the equivalent sites in $2N_G$ -Gr, which supports the superior ability of N_G to stabilise these intermediates even on sites which are not especially active.

4.5.3. Activity of $N_G N_P$ -Gr

Based on the knowledge acquired by studying the site-dependent activity on the two aforementioned clusters, we performed a similar investigation on $N_G N_P$ -Gr, where mainly edge sites near the N_G and N_P dopants were considered while excluding most valley and basal plane sites. This resulted in a total of 14 edge sites, 2 valley sites and 3 basal plane sites (2 near each dopant and 1 equidistant from both). Of these, the centremost basal plane and the valley sites were deemed inactive due to one or more intermediates desorbing from the surface.

The Gibbs energy diagrams of the 4-electron ORR at 1.23 V_{RHE} on the aforementioned sites are represented in Figure 4.8. From these, we can discern a group of sites, corresponding to C710, C510, C108, C61, C910, C13 and C41. These sites display a similar energetic trend consisting of an initial endergonic HOO^* formation (which is the PLS in all cases except for sites C710 and C41), followed by an exergonic ET to HOO^{*-} , exergonic formation of HO^* , and an endergonic desorption of HO^- (which is the PLS in C710 and C41). Interestingly, this energy pattern resembles the one observed for the most active sites seen in $2N_G$ -Gr, which may indicate that this dopant is still partly responsible for a major stabilisation of the HOO^* and HO^* intermediates. Contrary to that system, however, the formation of HOO^{*-} is much more exergonic in $N_G N_P$ -Gr, which may be caused by the influence of the neighbouring N_P site, similarly to the effect observed in $2N_P$ -Gr. Interestingly, the energetic trends on the sites in the vicinity of each N dopant in $N_G N_P$ -Gr are found to be noticeably influenced by either N_G and N_P , which can be seen in the comparison of the opposite sites C710 and C41. The former, which is closer to N_P , displays a much more endergonic adsorption of HOO^* and HO^* compared to C41, which nears to N_G and has these intermediates stabilised. On the other hand, the supporting effect on the HOO^{*-} intermediate on C710 due to the proximity to N_P is considerably smaller on C41. These effects can be better observed in the Gibbs energy diagram for C41 which has the diagram for C710 underlaid for comparison. In addition, the cooperative effect between N dopants is distinguishable in all active sites on the $N_G N_P$ -Gr cluster, leading to PLS values which are lower than the most active sites predicted for $2N_G$ -Gr and $2N_P$ -Gr.

Nonetheless, the most active sites are surrounding N_P , as can be seen in the inset of Figure 4.8. The most active sites displaying this similar energy trend are denoted with a yellow or orange spot if they are neighbouring either N_G or N_P , respectively.

Finally, analysis of the remaining less active sites (denoted with a dark blue spot in Figure 4.8) yields similar results to $2N_G$ -Gr and $2N_P$ -Gr, wherein HOO^* and HO^* are bound very weakly, resulting in a much more endergonic energy pathway for the 4-electron ORR. Hence, our simulations predict that the reactivity of the $N_G N_P$ -Gr cluster will predominantly occur on the sites near the N dopants represented in orange and yellow in Figure 4.8, wherein the most active site corresponds to the edge site C710 neighbouring N_P with a PLS of 0.67 eV at 1.23 V_{RHE} .

4.5.4. Comparison of the ORR activity

In the previous sections, we assessed the role of the N_G and N_P dopants on the $2N_G$ -Gr and $2N_P$ -Gr clusters in the stabilisation of the reaction intermediates, and the cooperative effect upon introduction of both dopants in the $N_G N_P$ -Gr cluster. The values of the relative Gibbs energies associated to each of the elementary steps calculated on the sites discussed in the previous sections, as well as the predicted theoretical onset potentials, are reported in Table 4.2. The most relevant results from the three clusters are summarised in Figure 4.9, which shows the most active sites in each system and their associated onset potentials.

As mentioned in the previous sections, our simulations show that the most active site in $2N_G$ -Gr (Figure 4.9 A) corresponds to C41. This site is located at a distance of 1 bond from the N_G dopant and displays a theoretical onset potential of 0.36 V_{RHE} , which is dictated by the last step in the 4-electron reduction. Similarly, the most active site in the $2N_P$ -Gr cluster is C41, which is at a distance of 3 bonds from the N_P dopant and exhibits a theoretical potential of 0.41 V_{RHE} ; however, in this case the PLS is determined by the HOO^* formation. Interestingly, sites at closer and farther distances from N_P are predicted to be far less active than C41. Finally, in the mixed $N_G N_P$ -Gr system, the most active site C710 features a similar configuration to that found in $2N_P$ -Gr. This site is located 3 bond lengths away from N_P and displays a theoretical onset potential of 0.56 V_{RHE} , which is governed by the last reaction step. Further edge sites near N_P are also deemed as very active, as indicated by the C sites highlighted in green at the bottom right of the cluster in Figure 4.9 C. Besides these highly active sites, an edge site located 3 bonds away from the N_G dopant shows an onset potential of 0.41 V_{RHE} , which is comparable to the most active site in the pure $2N_G$ -Gr cluster.

Overall, our calculations predict a larger onset potential for $N_G N_P$ -Gr compared to $2N_G$ -Gr and $2N_P$ -Gr, which is in good agreement with the experimental observations. In addition, we predict that the most active sites in all clusters will be predominantly on edge positions 1 to 3 bonds away from the N-dopant. Importantly, our results indicate that the catalytic activity is only dependent on edge sites near the N dopant, while basal plane, valley and edge sites farther from the N_G and N_P dopants will contribute to a lesser degree.

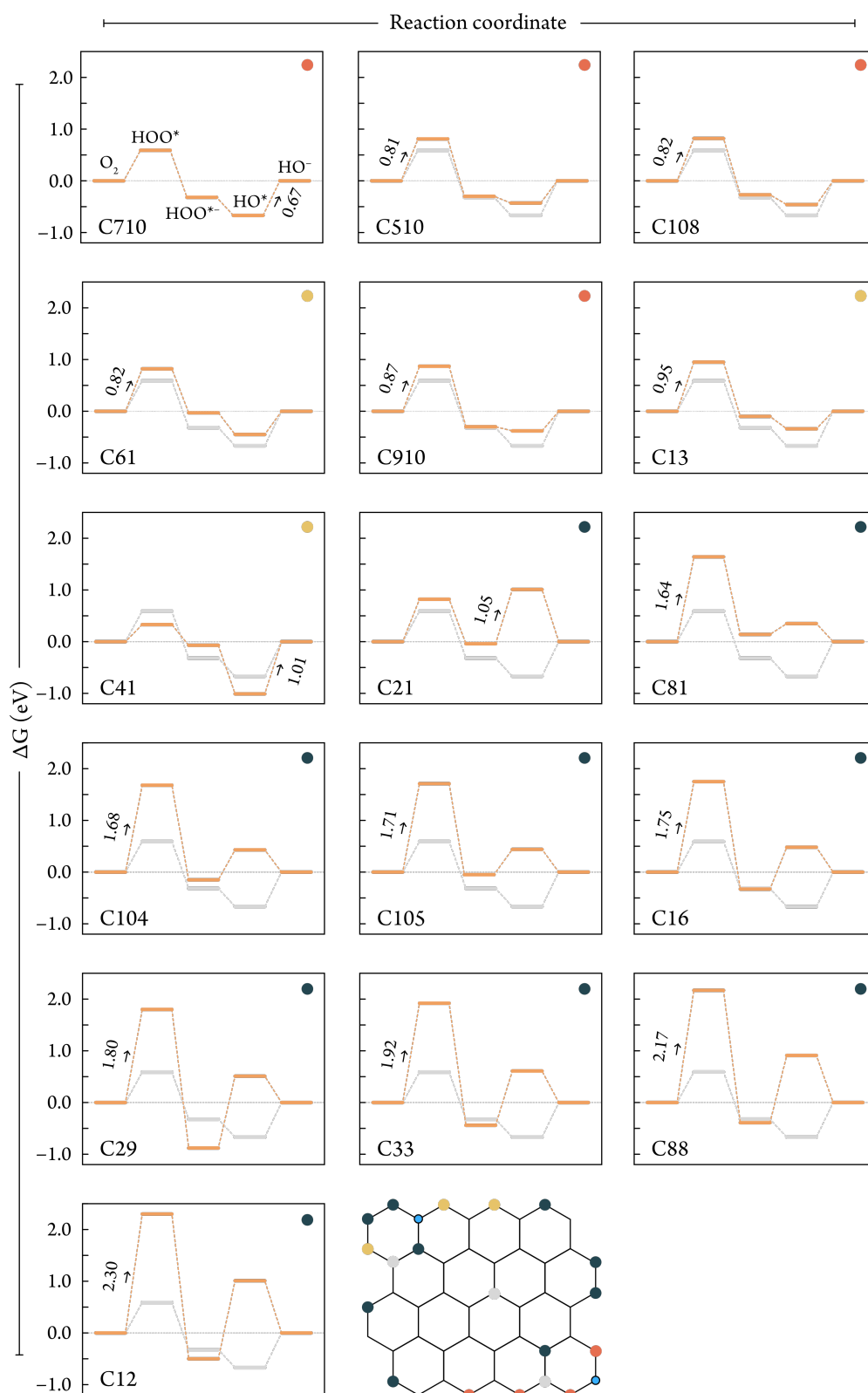


Figure 4.8 Gibbs energy diagrams at 1.23 V_{RHE} for the proposed mechanism on the C sites of $\text{N}_6\text{N}_p\text{-Gr}$ that are able to adsorb all intermediates. Further relevant information can be found in the caption of Figure 4.6. In this case, groups of studied sites with common energetic trends in their corresponding energy pathways are highlighted in dark blue and in orange or yellow; these two latter groups display similar energetic trends but differ in their location on the cluster, either neighbouring N_G (in yellow) or N_P dopants (in orange).

Table 4.2 Computed relative Gibbs energies (in eV) at 1.23 V_{RHE} and theoretical onset potentials of active sites with successful adsorptions of all intermediates in the 4-electron ORR mechanism on the three simulated cluster models. The PLS on each site is depicted in bold. Values of the theoretical potentials are colour coded as in Figure 4.9.

	Active site	ΔG_1 (eV) $O_2 \rightarrow HOO^*$	ΔG_2 (eV) $HOO^* \rightarrow HOO^{*-}$	ΔG_3 (eV) $HOO^{*-} \rightarrow HO^*$	ΔG_4 (eV) $HO^* \rightarrow OH^-$	Theoretical onset potential (V _{RHE})
2N _G -Gr	C41	0.43	-0.20	-1.10	0.87	0.36 ●
	C61	0.96	-0.75	-0.53	0.31	0.27 ●
	C21	0.98	-1.13	-0.17	0.32	0.25 ●
	C13	1.06	-1.23	-0.02	0.19	0.17 ●
	C16	1.88	-1.91	0.66	-0.63	-0.65 ●
	C33	1.97	-2.31	0.96	-0.63	-0.74 ●
	C81	2.00	-2.10	0.84	-0.74	-0.77 ●
	C104	2.02	-2.19	0.97	-0.80	-0.79 ●
	C92	2.28	-2.45	1.28	-1.12	-1.05 ●
2N _P -Gr	C41	0.82	-1.84	0.57	0.44	0.41 ●
	C13	1.05	-2.05	0.77	0.23	0.18 ●
	C61	1.07	-2.09	0.83	0.20	0.16 ●
	C21	1.14	-2.20	0.83	0.23	0.09 ●
	C81	2.09	-3.31	2.03	-0.81	-0.86 ●
	C17	2.12	-3.33	2.07	-0.85	-0.89 ●
	C16	2.22	-3.48	2.19	-0.92	-0.99 ●
	C25	2.45	-3.63	2.36	-1.17	-1.22 ●
	C33	2.47	-3.54	2.24	-1.18	-1.24 ●
	C92	2.52	-4.06	2.75	-1.20	-1.52 ●
	C29	2.52	-4.06	2.77	-1.22	-1.54 ●
	C53	2.80	-4.00	2.74	-1.55	-1.57 ●
	C24	3.11	-4.60	3.34	-1.85	-2.11 ●
N _G N _P -Gr	C710	0.59	-0.90	-0.35	0.67	0.56 ●
	C510	0.81	-1.12	-0.12	0.43	0.42 ●
	C108	0.82	-1.09	-0.18	0.46	0.41 ●
	C61	0.82	-0.85	-0.42	0.45	0.41 ●
	C910	0.87	-1.17	-0.08	0.38	0.36 ●
	C13	0.95	-1.05	-0.24	0.34	0.28 ●
	C41	0.33	-0.40	-0.94	1.01	0.22 ●
	C21	0.82	-0.86	1.05	-1.01	0.17 ●
	C81	1.64	-1.50	0.21	-0.35	-0.41 ●
	C104	1.68	-1.83	0.58	-0.43	-0.45 ●
	C105	1.71	-1.76	0.49	-0.44	-0.48 ●
	C16	1.75	-2.07	0.81	-0.48	-0.52 ●
	C29	1.80	-2.68	1.39	-0.51	-0.57 ●
	C33	1.92	-2.36	1.04	-0.61	-0.69 ●
	C88	2.17	-2.56	1.30	-0.91	-0.94 ●
C12	2.30	-2.80	1.50	-1.01	-1.07 ●	

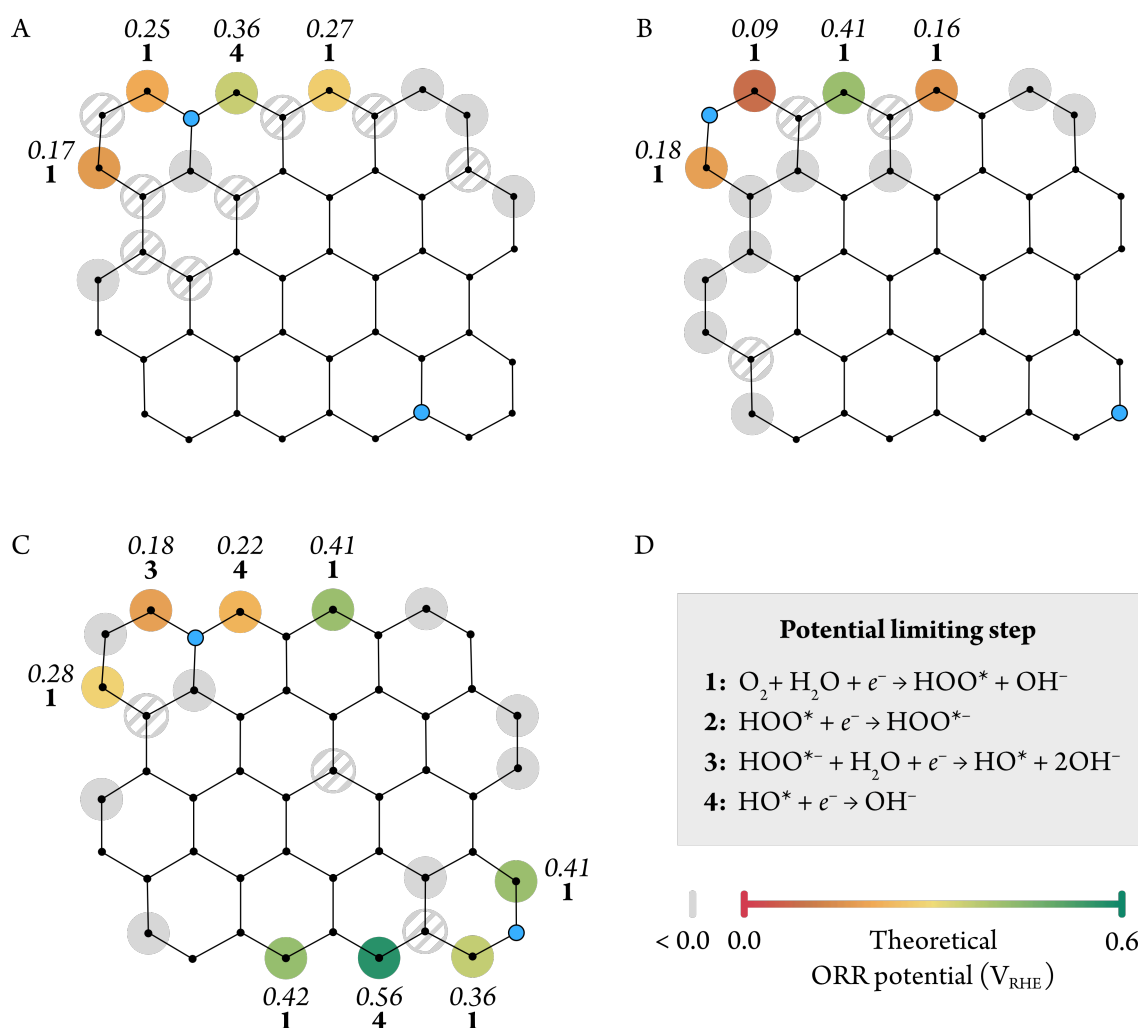


Figure 4.9 A–C) Schematic representation of the $2\text{N}_G\text{-Gr}$, $2\text{N}_P\text{-Gr}$ and $\text{N}_G\text{N}_P\text{-Gr}$ clusters, respectively. The most active of the investigated sites for the 4-electron ORR are highlighted with a colour code based on the predicted ORR onset potential (in V vs. RHE) shown in D. The carbon sites that can bind all reaction intermediates but display a poor activity are highlighted with a filled grey patch, while sites that fail at adsorbing one or more intermediates are marked with a striped grey patch. Relevant active sites are accompanied by the value of their predicted onset potential in italics and the ordinal number of the PLS, detailed in D. Hydrogen atoms and double bonds have been omitted for clarity, while N dopants in the scaffold are depicted in blue.

To rationalise the observed activities, we performed an analysis of the difference between α and β spin densities of the $2\text{N}_G\text{-Gr}$, $2\text{N}_P\text{-Gr}$, and $\text{N}_G\text{N}_P\text{-Gr}$ systems. This study reveals that the sites with the lowest theoretical overpotential depicted in Figure 4.9 are those which display the most positive spin density (dark blue regions in the heatmap) in Figure 4.10. This is in good agreement with theoretical studies which theorise that the location of the most active sites for the ORR on N-doped C electrodes arises from a π -spin delocalisation induced by the N dopants; specifically, it has been suggested that C sites with relatively more positive spin density are able to more evenly stabilise the intermediates and, consequently, display higher activities.^{204,205}

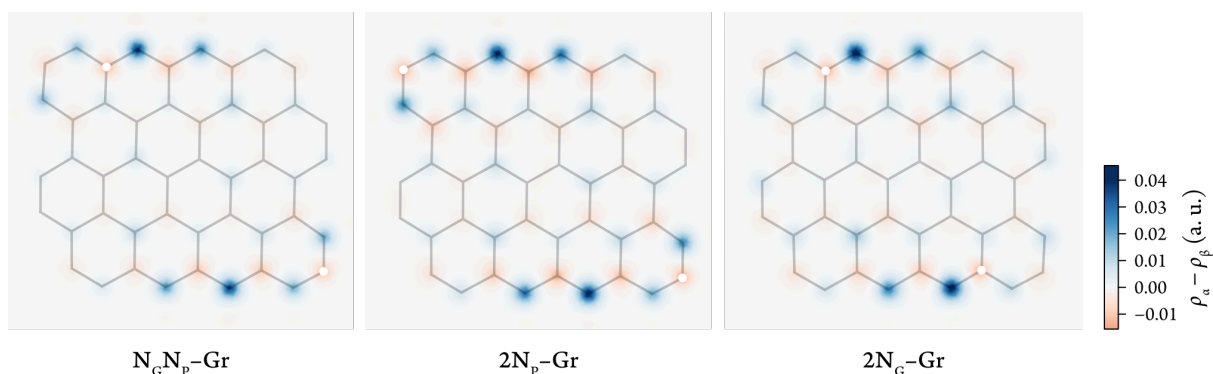


Figure 4.10 Heatmaps representing the difference between α and β spin densities of $2N_G$ -Gr, $2N_P$ -Gr, and $N_G N_P$ -Gr on their respective scaffolds, normalised by the number of unpaired electrons. The location of the N dopants in the clusters is depicted with a white dot. Hydrogen atoms and double bonds have been omitted for clarity. Given that the calculated resting state for $N_G N_P$ -Gr is a singlet, spin densities for this structure have been introduced by considering an alternative triplet configuration.

4.6. Assessing ORR selectivity

In order to rationalise the selectivity towards the 4-electron or the 2-electron products observed experimentally we must analyse the energetics of the most feasible reaction pathway on each cluster, which is given by the most active site predicted in our calculations, *i.e.* C41 in both $2N_G$ -Gr and $2N_P$ -Gr, and C710 in $N_G N_P$ -Gr. The Gibbs energy diagrams for the 4-electron reduction process on these sites are shown in Figure 4.11.

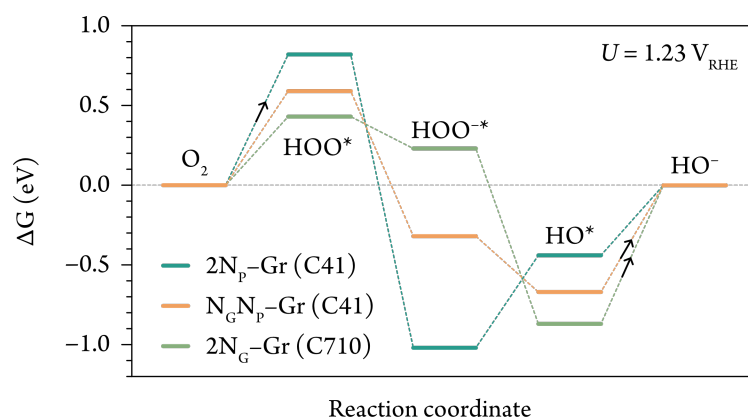


Figure 4.11 Gibbs energy diagrams at $1.23 V_{RHE}$ for the proposed 4-electron ORR mechanism on the most active sites of the modelled $2N_G$ -Gr, $2N_P$ -Gr and $N_G N_P$ -Gr clusters (corresponding to the first diagrams in Figure 4.6, Figure 4.7 and Figure 4.8). The PLS in each diagram is indicated with a black arrow.

As discussed in previous sections, Figure 4.11 demonstrates the stabilising effect of the N_G dopant on the HOO^* and HO^* intermediates in $2N_G$ -Gr compared to $2N_P$ -Gr. In addition, the effect from the N_P dopant on the stabilisation of HOO^{*-} in $2N_P$ -Gr is highlighted by the *ca.* 1.25 eV difference between this system and the $2N_G$ -

Gr cluster. Interestingly, calculations predict that the most active site in the mixed $N_G N_P$ -Gr cluster displays binding energies of the intermediates which are in-between $2N_G$ -Gr and $2N_P$ -Gr. Therefore, the presence of both dopants greatly determines the PLS of the most active site, which in turn dictates the catalyst selectivity.

According to our calculations, the weakest binding for the HOO^{*-} intermediate occurs on the $2N_G$ -Gr cluster, in the absence of the N_P dopant that stabilises it. This larger endergonic adsorption suggests that HO_2^- desorption following (4.10) will compete more effectively with the subsequent steps in the 4-electron reduction process. On the other hand, the most endergonic binding of the HOO^* intermediate is observed with $2N_P$ -Gr, as it lacks the stabilising effect from the N_G dopants. Hence, in this case the HOO^* will be more prone to desorb into HOO^* on this cluster competing in a similar fashion with the complete 4-electron reduction. In both cases, desorption of HO_2^- and HOO^* will result in an increase in the currents at the ring due to the oxidation of the hydroperoxide anion, either by direct detection of the product in the former, or by reaction with a superoxide species as in Eq. (4.11) in the latter. This is in good agreement with experiments, wherein a higher yield of HO_2^- is observed with the electrodes a-C NH_3 700 and a-C:N 900 which predominantly contain N_P or N_G sites, respectively.

Importantly, our theoretical results indicate that the co-presence of both N-dopants in similar concentrations is essential for the effective distribution of the energetics of the ORR intermediates to yield the 4-electron product. As shown in Figure 4.11, the $N_G N_P$ -Gr cluster displays a HOO^* binding which is stronger than $2N_P$ -Gr to avoid the desorption of HOO^* , while also showing a stronger HOO^{*-} binding compared to $2N_G$ -Gr, thus avoiding the desorption of this species. Furthermore, HOO^{*-} is not as tightly bound as in $2N_P$ -Gr, which is predicted to be the PLS of the overall process. All these factors are expected to favour the 4-electron pathway over the 2-electron process when both N-dopants coexist, which is supported by the lower amount of HO_2^- detected at the RRDE with the a-C NH_3 900 electrode.

4.7. Conclusions

The results discussed in this section shed light on the key factors involved in the development of efficient N-doped carbon materials for the ORR. To support the experimental data which suggests that a mixed composition of N_G and N_P dopants improves the selectivity and activity of C electrodes towards the 4-electron process, three models consisting of a middle-sized graphene cluster doped with either N_G or N_P , and a mixture of both were simulated. A thorough computational study of the reactivity of the possible active sites on the surface reveals that, in all cases, the most active site is located 1 to 3 bonds away from the N-dopant and in an edge position. Interestingly, our simulations show that N_G and N_P dopants have different effects on the energetics of the ORR intermediates; while N_G stabilises the HO^* and HOO^* intermediates, N_P favours the binding of HOO^{*-} . We thus predict N_G -doped and N_G -doped clusters to display different energetically distributed intermediates, albeit portraying an identical location for the most active sites. This leads to a shift in

the PLS in $2N_P$ -Gr from the first to the last step upon exchanging the dopant to a graphitic position in $2N_G$ -Gr. In the mixed $N_G N_P$ -Gr cluster, a cooperative effect between N_G and N_P is observed whereby HOO^* , HOO^{*-} and HO^* are equally stabilised, resulting in a much better distribution of the energetics of the ORR intermediates which greatly improves catalytic activity. Thus, the theoretical onset potential of the clusters follows the trend: $N_G N_P$ -Gr > $2N_G$ -Gr \approx $2N_P$ -Gr, which is in good agreement with the experimental results. In addition, our results show that the distribution of the binding energies determines the selectivity of the clusters towards the 2-electron or 4-electron process. While $2N_G$ -Gr and $2N_P$ -Gr display a relatively high endergonic adsorption of the HOO^* and HOO^{*-} intermediates, which in both cases is believed to result in an energetically favoured desorption and generation of HO_2^- (*via* direct desorption or by reaction with an O_2^- species in alkaline media competing with the full 4-electron reduction), the mixed $N_G N_P$ -Gr cluster displays an optimal distribution of the energy of the ORR intermediates that avoids the desorption of intermediate species and facilitates hydroxide generation. This is also in agreement with the experimental results, and highlights the necessity of introducing both types of N-dopants to cooperatively stabilise the reaction intermediates.

Overall, besides providing key information to rationalise the cooperative effects between N_G and N_P dopants in the considered metal-free C electrodes, this theoretical work deepens the understanding of the nature and consequences of these effects. Specifically, our calculations reveal the exact location and energetics of the most active sites for the 4-electron ORR in N_G , N_P and N_G/N_P -doped C clusters. Therefore, this study provides valuable insights for the future rational design of carbon materials with precisely located N-dopants with enhanced ORR activity/selectivity. To facilitate this process, future investigations should focus on obtaining a better insight of the physical interactions between N-dopants and the C active sites.

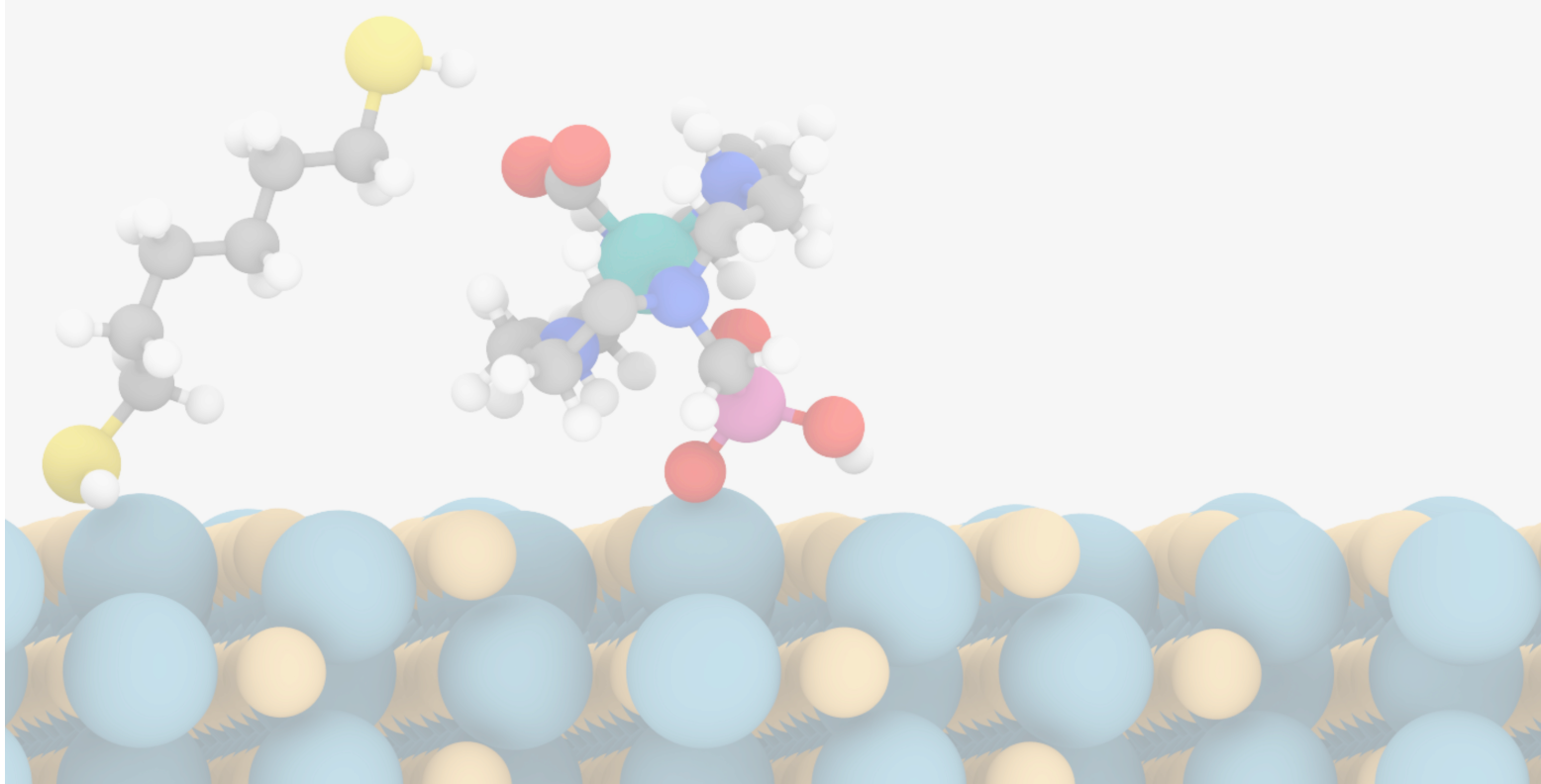
“ But the amount [of sunlight] that strikes the surface is still a staggering one, and it is a pity that man has made so little progress in turning it to direct use. – Cecilia Payne

In “Introduction to Astronomy”, 1954

CHAPTER

5

CO₂ Photoreduction on Ligand-modified ZnSe Quantum Dots



5.1. Introduction

The use of semiconductor QDs for the photocatalytic reduction of CO₂ into valuable C-based fuels such as CO, as discussed in Section 1.3.3, has received considerable attention over the past decade due to the potential ability of semiconductor particles to simultaneously generate an e^-/h^+ pair and effectively activate the C=O bond.²⁰⁶ Of the most investigated materials for photocatalytic CO₂RR in solution,^{§§§} chalcogenide QDs (mainly Cd-based) have shown the most potential due to their ability to absorb visible and UV light.²⁰⁷ However, early studies concluded that these materials are inactive towards CO₂RR in their bare form,²⁰⁸ and therefore, several strategies are required to trigger their catalytic activity with an increased selectivity (since most photocatalytic colloidal QDs for the CO₂RR are also highly active towards HER). For instance, the introduction of Ni²⁺

The results discussed in this section have been included in the following research articles:

Sahm, C. D.; **Mates-Torres, E.**; Eliasson, N.; Sokołowski, K.; Wagner, A.; Dalle, K. E.; Huang, Z.; Scherman, O. A.; Hammarström, L.; García-Melchor, M.; Reisner, E. *Chem. Sci.* **2021**, *12*, 9078–9087.

Sahm, C. D.; Ciotti, A.†; **Mates-Torres, E.†**; Sokołowski, K.; Neri, G.; Cowan, A. J.; García-Melchor, M.; Reisner, E. *Manuscript submitted*

§§§ In CO₂RR photocatalysis in solution, the QDs are in colloidal state and an organic solvent such as dimethylformamide (DMF) is usually employed to increase the solubility of CO₂.

dopants into CdS QDs has shown to trap the photoexcited electrons on the surface, hindering e^-/h^+ recombination and suppressing HER while promoting CO₂RR to CO and CH₄ with high selectivities.²⁰⁹ Transition metal co-catalysts have also been used to enhance CO₂RR activity. For instance, CdS QDs decorated with Pt nanoparticles have been found to increase the production rate of CO from 0.12 $\mu\text{mol g}^{-1} \text{h}^{-1}$ on the bare CdS QD to 2.99 $\mu\text{mol g}^{-1} \text{h}^{-1}$. In addition, metal complexes have been developed to co-catalyse this reaction alongside chalcogenide QDs forming a hybrid system, particularly by means of Ni-based molecular catalysts. Recently, a hybrid system with a $[\text{Ni}(\text{terpy})_2]^{2+}$ complex immobilised on CdS has shown to promote CO₂RR to CO with an outstanding selectivity.²¹⁰

Besides the above promising developments on Cd-based QDs, current investigations on photocatalytic QDs for the CO₂RR are starting to sway away from Cd in favour of more benign and inexpensive solutions, particularly earth-abundant Zn chalcogenides which display similar optical and structural properties.²¹¹ Accordingly, ZnSe QDs have been reported for the photocatalytic CO₂RR as photosensitizers in combination with molecular Ni-based co-catalysts. In particular, the group of Prof. Erwin Reisner has found that anchoring ZnSe QDs with $[\text{Ni}(\text{cyclam})]^{2+}$ —a molecular electrocatalyst which has been shown to selectively reduce CO₂ to CO²¹²—through a phosphonic acid group allows the photogeneration of CO with 3.4% selectivity and a 1:2 CO:H₂ ratio.²¹³

A less-explored but nonetheless very promising strategy to improve the photocatalytic CO₂RR activity of QDs—which has already been briefly introduced in Section 1.3.3—is the use of organic ligands in ionic liquids (ILs), which have been extensively used in the electrochemical CO₂RR.^{214–216} For instance, in the case of CdS QDs, the introduction of mercaptopropionic acid has shown to improve the rate of CO₂RR to HCOOH and, residually, to CO and CH₄, which is facilitated by an modification of the energy gap leading to an improvement in the e^-/h^+ pair separation upon functionalisation of the QD. Of the most relevant organic ligands for the electroreduction of CO₂, imidazolium-based ligands such as 1-ethyl-3-methylimidazolium cation ($[\text{EMIM}]^+$) are the most versatile and effective for promoting activity and selectivity mainly towards electrocatalytic CO and HCOOH production.^{93,217} These ligands are usually accompanied by BF_4^- as a counterion forming $[\text{EMIM}][\text{BF}_4]$, and has been extensively studied in conjunction with molecular and heterogeneous electrocatalysts. However, the nature of the effect derived from the inclusion of imidazolium groups is still under debate, and three main theories have been proposed. In the first one, the adsorbed EMIM on the electrode surface is believed to react with CO₂ via complexation and subsequently convert it to CO at low overpotentials.²¹⁸ In the second one, formation of a carbene in the imidazolium motif has also been theorised to induce the adsorption and activation of CO₂ to either $^*\text{CO}_2^-$ through a carboxylation²¹⁹ or through a PCET to yield $^*\text{COOH}$.^{220,221} However, recent studies have shown that imidazolium motifs are more likely to promote CO₂RR by stabilising the activated $^*\text{CO}_2^-$ species on the electrode surface by means of electrostatic

interactions through the protons at C4 and C5 positions⁹³ or by forming a favourable electric field²²² or local stabilising microenvironment.²¹⁴

Despite their recent applications in electrocatalytic CO₂RR, the use of imidazolium-based ILs on photosensitizer QDs for the photoreduction of CO₂ has been, to our knowledge, seldom explored in literature. Therefore, in this chapter, we will untangle the effects of an imidazolium-based ligand on a ZnSe QD for the photoreduction of CO₂ to CO by describing the design of a theoretical model including mechanistic and structural studies to support the results obtained by our experimental collaborators in the group of Prof. Erwin Reisner. With the acquired knowledge, we will then introduce a subsequent collaboration focusing on the influence of the introduction of dithiol ligands on the stabilisation and activation of the initial *CO₂⁻ intermediate on the ZnSe QD, both in the absence and the presence of a Ni(cyclam)²⁺-based co-catalyst. In both projects, the ligand coverage and structural properties of the QD are predicted to play a critical role, which will be demonstrated through a comprehensive analysis of the NCIs.

5.2. Experimental results

The photocatalytic potential of metal chalcogenides towards the ligand-facilitated CO₂RR was investigated by the group of Prof. Reisner by synthesizing ZnSe QDs with weakly coordinating BF₄⁻ capping ligands. This yielded ZnSe–BF₄ QDs consisting of pseudo-spherical particles with a radius of 4.5 ± 0.7 nm, as observed using transmission electron microscopy with a zinc blende structure as confirmed by XRD, and displaying an adsorption maximum peak at 416 nm. BF₄⁻ capping ligands were exchanged with a thiol-modified EMIM molecule (MEMI), which could effectively bind to the QD surface, as revealed by ¹H-NMR spectroscopy studies; these revealed that each ZnSe–BF₄ QD could accommodate up to 12 MEMI molecules on its surface. MEMI is believed to influence the CO₂RR via interactions in the second coordination sphere of the reaction intermediates adsorbed on the ZnSe surface.⁹³ The EMIM and MEMI molecules are portrayed in Figure 5.1 A and B, respectively.

Photocatalytic studies were carried out under a constant flow rate of CO₂ and irradiation of UV light ($\lambda > 400$ nm) in a 0.1M solution of AA at pH = 6.5, which is oxidated to dehydroascorbic acid (DHA) acting as the SD. The bare ZnSe–BF₄ QDs under these conditions produced a marginal, albeit detectable, 0.64 ± 0.11 mmol g_{ZnSe}⁻¹ of CO after 10 h of irradiation with a selectivity of 3% (defined as the moles of CO divided by the total moles of product, containing both CO and H₂ from the competing HER). Addition of EMIM (ZnSe | EMIM) was found to increase the formation of CO to 1.06 ± 0.06 mmol g_{ZnSe}⁻¹ after 10 h and CO selectivity to < 5%.

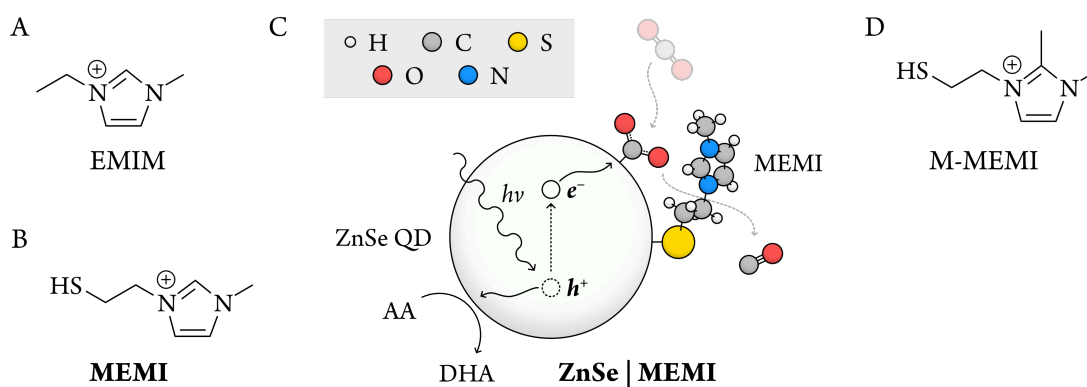


Figure 5.1 A) Structure of [EMIM]⁺ IL. B) Structure of the MEMI ligand used for reactivity studies. C) Representation of the proposed stabilising effect of MEMI to promote the CO₂RR on the ZnSe | MEMI system. D) M-MEMI ligand used to investigate the ability of MEMI to coordinate with CO₂.

Subsequent studies showed that the biggest change occurred upon addition of MEMI ligands, where the MEMI-functionalised QDs (ZnSe | MEMI, as represented in Figure 5.1 C) displayed a CO production of 1.78 mmol g_{ZnSe}⁻¹ after 10 h with a selectivity of 5.8%, yielding only traces of formate. Analyses of the activity of ZnSe | MEMI at different ligand concentrations revealed that CO production remained above 1.41 ± 0.10 mmol g_{ZnSe}⁻¹ at MEMI loadings from 25 μM and peaked at 50 μM, where HER was further suppressed potentially due to dynamic ligand/QD interactions (as shown in Table 5.1). In addition, studies at higher and lower pH values showed that CO production yields are pH-independent. The activity of the system was ceased entirely in the dark or without the presence of the QD or the AA SD, indicating that all parts in the system are essential. Further analyses with monothiol BuSH ligands forming a ZnSe | BuSH system showed similar results to the bare ZnSe QD, revealing that the thiol group acts solely as an anchoring group and that the imidazolium group is the main promoter of CO production.

To unravel the role of the imidazolium motif in the enhancement of CO₂ reduction and determine whether the interaction with CO₂ occurs by coordination onto a carbene species formed in situ, photocatalytic experiments were repeated using a modified methyl protected MEMI ligand on the imidazolium C2 position (M-MEMI, represented in Figure 5.1 D). If the catalytic activity arises from an initial coordination of CO₂ with that carbon site, it would be expected that CO production on the M-MEMI-functionalised ZnSe QD (ZnSe | M-MEMI) would be hindered. On the contrary, this system displayed an even larger production of CO up to 2.38 mmol g_{ZnSe}⁻¹ after 10 h of irradiation, with a selectivity of 12%. In view of the ability of the bare ZnSe QD to slightly catalyse CO production, this result hints at the possibility that the imidazolium group facilitates a surface mechanism by stabilising the CO₂RR intermediates, potentially via NCIs in the second coordination sphere. All aforementioned relevant figures of merit for the studied systems are gathered in Table 5.1.

Finally, charge carrier dynamics experiments revealed that the effect of the MEMI ligand on the enhancement of the CO₂RR was not caused by a generation of hole trap states upon adsorption of the ligands on the surface,

and therefore, this was most probably caused by the interactions between the MEMI and the reaction intermediates. In conclusion, experimental results on the ZnSe | MEMI system hinted at a QD-surface pathway promoted by secondary coordination sphere interactions between the MEMI ligand and the reaction intermediates adsorbed on a surface active site.

Table 5.1 Production yields of H₂ and CO and CO selectivities after 10 h of irradiation using a QD concentration of 0.5 μM in a 0.1 M AA/NaHCO₃ solution at pH 6.5 under constant CO₂ flow. For the ZnSe | MEMI system, results for 4 different ligand loadings are included.

System	Ligand loading (μM)	n(H ₂) (mmol g _{ZnSe} ⁻¹)	n(CO) (mmol g _{ZnSe} ⁻¹)	CO selectivity (%)
ZnSe	0	71.8 ± 19.7	0.64 ± 0.11	0.9% ± 0.3
ZnSe EMIM-BF ₄	50	40.2 ± 6.06	1.06 ± 0.06	2.6% ± 0.5
ZnSe MEMI	12.5	46.9 ± 8.15	1.18 ± 0.22	2.5% ± 0.7
	25	38.6 ± 13.0	1.41 ± 0.10	3.8% ± 1.1
	37.5	26.0 ± 1.69	1.52 ± 0.14	5.5% ± 0.3
	50	29.9 ± 8.52	1.78 ± 0.23	5.8% ± 1.1
ZnSe M-MEMI	50	17.3 ± 0.87	2.38 ± 0.19	12% ± 1.1
ZnSe BuSH	50	72.1 ± 27.6	0.69 ± 0.19	1.1% ± 0.5

Motivated by these results, and in view of the importance of the NCIs in the second coordination sphere, our experimental collaborators then sought to investigate the ability of alkanedithiol capping ligands to stabilise the reaction intermediates through more directional H-bonding arising from interaction with a dangling thiol group (assuming that the most stabilising NCIs are mainly H bonds). In order to demonstrate this, the influence of dithiol ligands on the catalytic activity was investigated on a ZnSe QD in the absence and the presence of a phosphonic-acid functionalised Ni-cyclam (Ni(cycP)) molecular catalyst for the CO₂ reduction introduced in Section 5.1, which is schematised in Figure 5.2. In their approach, interactions within the second coordination sphere were theorised to play an important role in the facilitation of either a surface-promoted mechanism in which the CO₂RR intermediates are stabilised onto surface Zn sites via interaction with shorter ligands (as schematised in Figure 5.3 A), or through a co-catalyst promoted pathway where longer dithiols are expected to have a greater impact (as in Figure 5.3 B). Thus, the catalytic activity towards the CO₂RR on the bare QD (ZnSe hereafter) and the Ni(cycP)-functionalised QD (ZnSe | Ni(cycP)) was assessed by including dithiol ligands of different lengths: 1,2-ethanedithiol (EDT), 1,4-butanedithiol (BuDT), 1,6-hexanedithiol (HexDT) and 1,8-octanedithiol (OctDT) (Figure 5.3 C), which were adsorbed onto the QD in different concentrations as confirmed by ¹H-NMR.

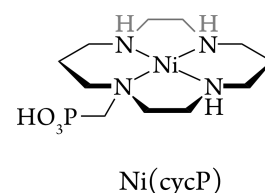


Figure 5.2 Schematic representation of the Ni(cycP) molecular co-catalyst.

The obtained product yields after 10 h of irradiation on the ZnSe and the ZnSe | Ni(cycP) systems are summarised in Table 5.2. The addition of 50 μM of each dithiol ligand in a solution containing a colloidal dispersion of the bare ZnSe QD was shown to suppress HER independently of the dithiol considered, from 16.7 μmol of H₂ produced on the bare ZnSe QD to *ca.* 5 to 8 μmol on the QD capped with dithiol ligands. However, CO production levels differed more noticeably between of each dithiol-containing system, where the ZnSe | EDT system displayed the highest CO production of 0.95 $\mu\text{mol}_{\text{CO}}$, a 6-fold increase compared to a 0.15 $\mu\text{mol}_{\text{CO}}$ yield on the bare ZnSe QD.

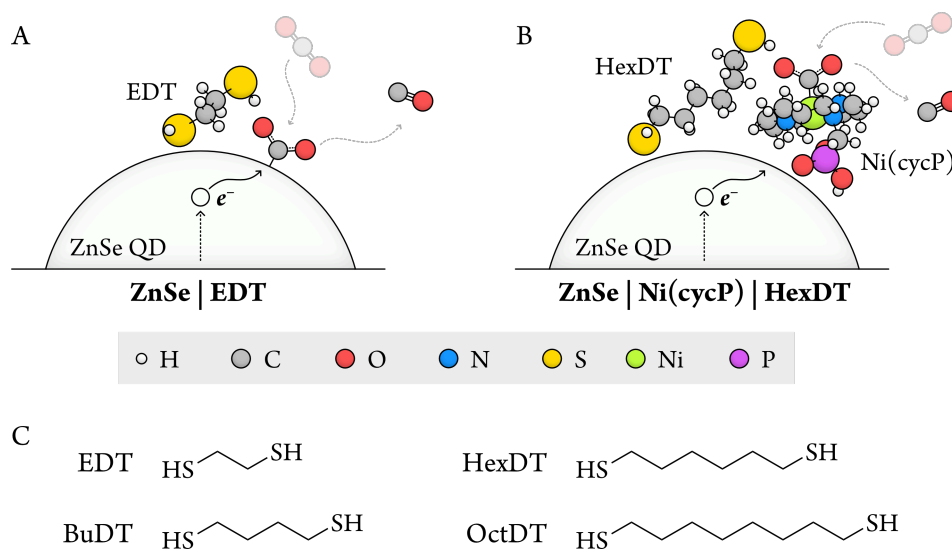


Figure 5.3 Representation of the photocatalytic systems consisting of ZnSe QD modified with dithiols in which the visible light-driven reaction is believed to occur through A) a surface-promoted mechanism or B) through a co-catalyst promoted pathway in a ZnSe QD functionalised with Ni(cycP) (ZnSe | Ni(cycP)). C) Representation of the dithiol ligands of various lengths used for reactivity studies.

As can be seen from the experimental results, the effect of longer dithiols on the catalytic performance of the bare ZnSe QD is not as noticeable as when using EDT; however, this behaviour is reversed upon inclusion of the Ni(cycP) co-catalyst. As shown in Table 5.2, the ZnSe | Ni(cycP) | HexDT system displays a nearly 4-fold increase in CO production compared to the ligand-free ZnSe | Ni(cycP) (4.05 *vs.* 1.09 $\mu\text{mol}_{\text{CO}}$), and outperforms the rest of the catalytic systems with different dithiol ligands. This is in contrast with ZnSe | Ni(cycP) | EDT, which displays activities within the margin of error of those on the ZnSe | Ni(cycP) in the absence of ligands.

Next, our experimental collaborators sought to determine whether the flexibility of the alkanedithiols and the presence of a dangling thiol are necessary for the enhancement of CO production. This was achieved by carrying out a similar investigation using analogous ligands with either hindered flexibility (benzene-1,4-dithiol, BenzDT) or containing only one thiol group (using monothiol such as HexSH). Experimental results of the ZnSe | Ni(cycP) | BenzDT and ZnSe | Ni(cycP) | HexSH systems in Table 5.2 display similar CO production

yields compared to the ligand-free ZnSe | Ni(cycP) system, while efficiently achieving HER suppression. Thus, these results suggest that any influence on the CO₂RR is derived from the presence of two terminal moieties capable of H-bonding. This hypothesis was further corroborated by assessing the effect of introducing mercaptoalcohols such as mercaptohexanol (HO-HexSH) on the ZnSe | Ni(cycP) system, which displayed a production of 3.10 μmol_{CO} comparable to the observed yields using OctDT (2.97 μmol_{CO}).

Table 5.2 Production yields of H₂ and CO after 10 h of irradiation and selectivities towards CO on the bare ZnSe QD and the ZnSe | MEMI systems, using a QD concentration of 0.5 μM in a 0.1 M AA/NaHCO₃ solution at pH 6.5 (w/o co-catalyst) or 0.1 M AA pH 5.5 (w/ co-catalyst), under constant CO₂ flow.

System	Ligand loading (μM)	Catalyst loading (μM)	Dithiol length (Å)	Ligands per QD	n(H ₂) (μmol)	n(CO) (μmol)	CO selectivity (%)
ZnSe	0	0	0	–	16.7 ± 4.60	0.15 ± 0.02	0.9% ± 0.1
ZnSe EDT	50	0	4.3	100	5.29 ± 0.79	0.95 ± 0.19	15.1% ± 2.6
ZnSe BuDT	50	0	6.8	25–50	5.84 ± 0.99	0.46 ± 0.06	7.4% ± 0.4
ZnSe HexDT	50	0	9.3	25–50	8.18 ± 1.23	0.14 ± 0.03	1.7% ± 0.3
ZnSe OctDT	50	0	11.7	50–100	4.21 ± 0.63	0.27 ± 0.04	5.9% ± 0.5
ZnSe BenzDT	50	0	6.4	–	7.49 ± 0.97	0.19 ± 0.01	2.6% ± 0.3
ZnSe BuSH	50	0	–	–	16.8 ± 6.38	0.17 ± 0.04	1.1% ± 0.6
ZnSe NiCycP	0	10	0	–	25.7 ± 3.69	1.09 ± 0.18	4.0% ± 0.2
ZnSe NiCycP EDT	25	10	4.3	100	17.6 ± 2.64	1.21 ± 0.18	6.4% ± 0.3
ZnSe NiCycP BuDT	25	10	6.8	25–50	11.6 ± 1.74	3.78 ± 0.46	24.5% ± 2.0
ZnSe NiCycP HexDT	25	10	9.3	25–50	6.19 ± 0.93	4.05 ± 0.25	39.6% ± 1.9
ZnSe NiCycP OctDT	25	10	11.7	50–100	5.82 ± 0.87	2.97 ± 0.24	33.8% ± 1.8
ZnSe NiCycP BenzDT	25	10	6.4	–	11.7 ± 0.59	1.45 ± 0.07	10.9% ± 0.5
ZnSe NiCycP HexSH	25	10	–	25–50	17.9 ± 0.89	1.15 ± 0.06	6.0% ± 0.3
ZnSe NiCycP HO-HexSH	25	10	–	< 25	22.4 ± 1.51	3.10 ± 0.16	12.2% ± 0.6

In conclusion, the aforementioned experimental results from the group of Prof. Erwin Reisner hint at the importance of the interactions in the second coordination sphere that drive the CO₂RR on ZnSe QDs functionalised with capping ligands. To determine the nature of these interactions and their role on the energetics of the process, in the next sections we will first describe a theoretical investigation including a thorough ligand coverage analysis and a reactivity study of the reaction mechanism on the ZnSe | MEMI system, which will be further supported by assessing the interactions between the ligand and the highest energy reaction intermediates in the second coordination sphere. Finally, we will discuss the role of the NCIs in promoting the CO₂RR in the bare ZnSe and the ZnSe | Ni(cycP) systems in the presence of the aforementioned alkanedithiol ligands.

5.3. Computational details

Periodic DFT calculations reported in this study were performed using the PBE functional¹³⁴ as implemented in the VASP software, version 5.4.4.^{223,224} The core electrons of Zn, Ni, Se, P, S, O, N, and C atoms were replaced by PAW pseudopotentials,¹⁴⁹ while their valence electrons were expanded in plane waves with a kinetic energy cut-off of 500 eV. Structures were optimised using a maximum step size of 0.05 Å and a force-based convergence criteria of 0.015 eV Å⁻¹. Dispersion corrections were added using the zero-damping DFT-D3 method by Grimme¹⁵² to account for NCIs. The bulk structure of ZnSe was retrieved from the Materials Project database,²²⁵ and the equilibrium lattice constant was optimized by fitting the energy of a number of bulk ZnSe structures with lattice parameters ranging between ± 5% of its initial value to the Birch–Murnaghan EOS, sampling the reciprocal space using Γ -centred k -point grids of 3×3×3, 5×5×5, 7×7×7 and 9×9×9. Ultimately, a Γ -centred k -point grid of 5×5×5 was selected for bulk calculations, following a convergence criterion of 1 meV atom⁻¹, yielding a k -point density of 28.7 Å³ which was used for subsequent surface calculations. Molecules in the gas-phase were calculated at Γ -point with at least 15 Å of vacuum along the three axes.

The energies of the 4-layered slabs of all considered facets were calculated with a vacuum of at least 15 Å perpendicular to the surface to avoid interaction between slabs in neighbouring cells. The bottom two layers of the calculated surfaces were fixed to their bulk positions, whereas the two topmost layers were allowed to relax. Surface energies were calculated as in Eq. (2.97). Determination of the surface resting state was simulated by computing the adsorption energies of the MEMI and dithiol ligands as follows:

$$\Delta E_{n \times *L} = E_{n \times *L} - E_* - n \times E_L \quad (5.1)$$

Where $E_{n \times *L}$ is the energy of n ligands adsorbed on the surface sites, E_* is the energy of the bare surface and E_L the energy of the ligand molecule in the gas phase. The analysis of the coverage of the MEMI and dithiol ligands, which will be further discussed in the following sections, was assessed by investigating the saturation point at which inclusion of more ligands on the surface was predicted to be endothermic (in the former) or by considering the concentration of ligands contained on the ZnSe QD under experimental conditions (in the latter). The ligand coverage on the modelled surface was related to the experimentally observed number of ligands per QD (Table 5.2) using the approximation in Eq. (5.2):

$$\frac{n_{\text{ligands}} \text{ QD}^{-1}}{4\pi r_{\text{QD}}^2} = \frac{n_{\text{ligands}} \text{ unit cell}^{-1}}{A} \quad (5.2)$$

Where r_{QD} is the radius of the ZnSe QD (*ca.* 2.27 nm), and A is the area of the simulated surface unit cell. Adsorption energies of H atoms on the surface were calculated following the CHE model, wherein the energy of the hydrogen was replaced by one half of the energy of molecular hydrogen (as in Eq. (2.70)).

Gibbs corrections to the energy were computed including the ZPE, vibrational enthalpy and entropy terms obtained by means of the Thermochemistry module implemented in the Atomic Simulation Environment (ASE) package,²²⁶ at the experimental temperature of 298 K. In the calculation of the Gibbs energy corrections for the different molecules, we considered a pH of 6.5, partial pressures of CO₂ of 1 atm and H₂O of 0.035 bar (which is the pressure at which the gas and liquid phases of H₂O are in equilibrium at 300 K), and the experimentally detected concentration of CO of 3 μM. Adsorption Gibbs energies of the reaction intermediates on the ZnSe | MEMI system were computed by following the CHE model to account for the energy of PCET steps in a similar process to the one described in Section 2.7.2—in this case using CO₂ as a reference—and considering either the neutral or negatively charged slab as reference for calculating the adsorption energies of systems in the absence or the presence of a photogenerated electron, respectively, which was simulated by increasing the number of electrons in the calculation by one.^{****} The Gibbs energy of the overall reaction was calculated as follows:

$$\Delta G_R = G_{\text{CO}} + G_{\text{H}_2\text{O}} - (G_{\text{CO}_2} + G_{\text{H}_2}) \quad (5.3)$$

NCIs stabilising the reaction intermediates in ZnSe | MEMI and ZnSe | Ni(cycP) | nDT (nDT = EDT, HexDT and OctDT) were assessed by taking the geometry of the adsorbed species optimized in VASP and computing their electron density via single-point calculations with the dispersion-corrected hybrid exchange-correlation functional ω B97XD¹³⁸ (discussed in Section 2.2.3.4) using the Gaussian09 software.²⁰⁰ In these calculations, Ni atoms were described with the effective core potential Lanl2dz and an additional f-polarization function (exponent = 3.130),²²⁷ while the 6-31G(d, p) basis set was used to describe the C and H atoms, with an additional p-diffuse function to represent the electrons of the more electronegative S, N, P and O atoms. The reduced density gradient $s(\mathbf{r})$ (defined in Eq. (2.37)) arising from these calculations was plotted as a function of the electron density ρ using the software Critic2,²²⁸ in a method discussed in Section 2.2.3.2. Electron density regions are associated to the observed peaks in the $s(\mathbf{r})$, denoting maxima in the electron density and depicting individual NCIs, by performing subsequent NCI analyses wherein the plotted range of $\text{sign}(\lambda_2)\rho$ was delimited to only include points of interest. In the results presented herein, only the minima in the $s(\mathbf{r})$ (*i.e.* the outline of the NCI peaks) is represented to facilitate visualization.

^{****} This was used to simulate the local environment where the charge carrier of the photogenerated exciton lies; however, this approach suffers from a major drawback: due to the unrealistic nature of a charged unit cell (which would theoretically lead to an infinitely charged crystal), VASP adds a background charge to achieve neutrality. This, in turn, requires *a posteriori* energy corrections which, in slabs, are dependent on the width of the vacuum due to the generated electrostatic potential between the slab and the background charge. Therefore, these calculations yield total and even relative energies which are not representative of experiments. Other approaches to tackle this issue include the addition of sacrificial electron donors or acceptors in the form of cations at the top or the bottom of the surface slab, itself presenting issues such as generating local dipoles within the slab which may also alter the energy surface. In our case, due to the similar geometry of the compared intermediate species (the surface is unmodified in all cases and the vacuum is kept constant), we expect the aforementioned energy correction to remain similar in all instances; therefore, we believe this gives rise to relative energies that provide a fairly accurate chemical understanding of the experimental results due to error cancellation.

5.4. Modelling of ligand-functionalised ZnSe QDs

In view of the importance of an accurate description of the surface morphology and the ligand phase for understanding the activity of the ZnSe QD, the following sections will be devoted to assessing the surface structures used for adsorption and reactivity studies, as well as discussing the approaches taken for achieving an accurate representation of the ligand coverages on the surface, which play a major role in promoting the reaction.

5.4.1. ZnSe QD surfaces

To untangle the catalytic activity of the ZnSe QD, we proceeded to build a model depicting the surface of the nanoparticle. Firstly, optimisation of the ZnSe bulk was performed by means of a Birch–Murnaghan EOS. Ultimately, a bulk structure (Figure 5.4 A) with a lattice constant of 5.74 Å, *ca.* 1% larger than the experimentally reported value of 5.66 Å in literature²²⁹ was obtained and used for subsequent calculations. To identify the most predominant surface on the ZnSe QD, the surface energies of 4-layered slabs with lattice planes characteristic typically observed in XRD spectra of zinc blende (i.e. (111), (200), (220), and (311)) were computed (Table 5.3) and used for the Wulff construction method. This yielded an equilibrium shape consisting of a rhombic dodecahedron exposing exclusively the facet with Miller indices (220), as represented in Figure 5.4 B. This equilibrium shape was found to be predominant in zinc blende structures in previous theoretical studies.²³⁰ Interestingly, the (220) surface is characterised by containing a large amount of undercoordinated Zn and Se surface sites onto which the binding of reaction intermediates and capping ligand may be favoured. The optimised $p(1\times 1)$ -(220) surface cell used for adsorption and reactivity studies is represented in Figure 5.4 C.

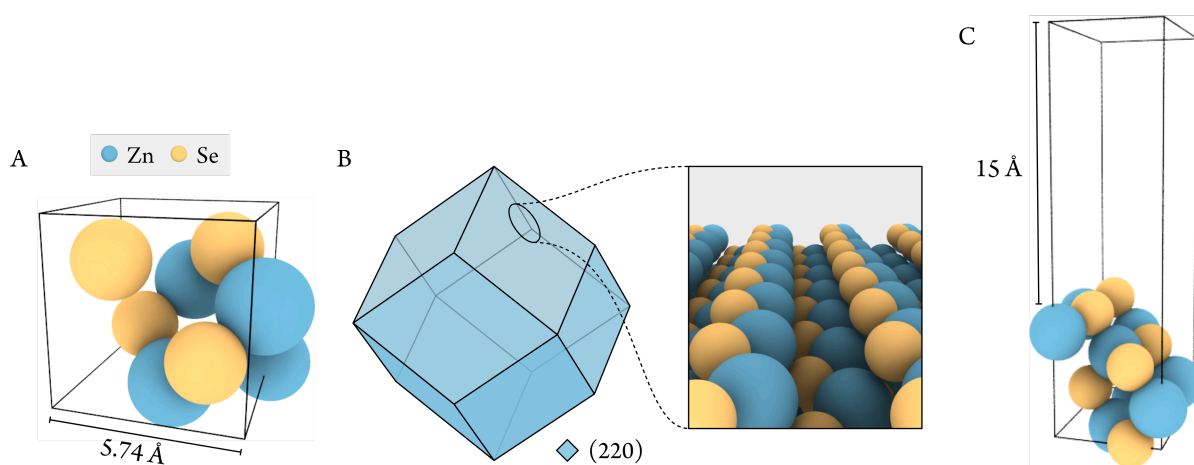


Figure 5.4 A) Modelled bulk ZnSe QD structure with a cubic lattice. B) Schematic representation of the Wulff construction obtained by assessing the surface energies of the (111), (200), (220) and (311) lattice planes. The final morphology of the equilibrium crystal displays uniquely the (220) plane, shown in blue. The characteristic stepped morphology of this surface with rows of undercoordinated sites is represented in the inset. C) $p(1\times 1)$ -(220) surface used for coverage and reactivity analyses, with 15 Å of vacuum along the direction perpendicular to the surface.

Having elucidated the nature of the predominant surface on the QD, we then sought to determine its resting state in the presence of either MEMI ligands or the Ni(cycP) co-catalyst and dithiol ligands.

Table 5.3 Computed surface energies for the predominant planes in XRD spectra.

Surface facet	Unit cell area (Å ²)	γ (J m ⁻²)
(111)	57.083	1.00
(200)	32.957	1.33
(220)	46.608	0.49
(311)	109.305	0.93

5.4.2. Ligand coverages

Firstly, the resting state of the ZnSe | MEMI system was determined by assessing the coverage of MEMI ligands on the ZnSe(220) surface. In order to obtain the most stable coverage at the experimental conditions, we determined the maximum number of MEMI ligands that could be exothermically adsorbed onto the ZnSe surface. This was achieved by simulating the adsorption of MEMI ligands (which only bind through the thiol group onto surface Zn sites) on ZnSe(220) surfaces with periodicities $p(2\times 1)$, $p(2\times 2)$ and $p(4\times 2)$ (as represented in Figure 5.5 A), which effectively allowed us to investigate different surface coverages. Accordingly, coverages of 12.5% and 25% (described as the percentage of Zn sites functionalised by MEMI) were investigated by adsorbing 1 MEMI ligand on $p(4\times 2)$ -(220) and $p(2\times 2)$ -(220) surfaces, respectively, while coverages of 50% and 100% consisted of 2 MEMI ligands on the most stable positions on $p(2\times 1)$ -(220) and $p(2\times 1)$ -(220) surfaces, respectively. A schematic representation of these distributions of MEMI ligands is depicted in Figure 5.5 B. Assessing the adsorption energies of these ligands revealed that producing a 12.5% MEMI coverage from a clean surface is exothermic by -2.50 eV. Similarly, going from a 12.5% to a 25% and from a 25% to a 50% MEMI coverage was also predicted to be exothermic, with relative adsorption energies of -3.21 eV and -5.16 eV, respectively. However, going from a 50% to a 100% MEMI coverage was found to be endothermic by 2.16 eV. Hence, our calculations predict that a 50% MEMI surface coverage is the most likely one; therefore, we selected this coverage for subsequent studies on the ZnSe | MEMI system.

In order to investigate the effect of the dithiol length on the surface and co-catalyst promoted pathways, we modelled the ZnSe and ZnSe | Ni(cycP) systems containing three representative ligands of different sizes, namely EDT, HexDT and OctDT. The surface ligand concentrations of these systems were determined by Eq. (5.2) and considering the number of ligands per QD assessed by ¹H-NMR as depicted in Table 5.2. All symmetrically non-equivalent adsorption sites and dentations were considered. Therefore, ZnSe(220) surfaces with periodicities $p(2\times 1)$, $p(2\times 3)$ and $p(6\times 1)$ containing 1 ligand of EDT, HexDT and OctDT (in a bidentate

configuration where both thiol groups were predominantly bound to Zn) were used to simulate the ZnSe | EDT, ZnSe | HexDT and ZnSe | OctDT systems, respectively, in the absence of the Ni(cycP) co-catalyst. These dithiol-covered surfaces were subsequently used to assess the interactions between the covered ligands and the reaction intermediates in the surface-promoted mechanism.

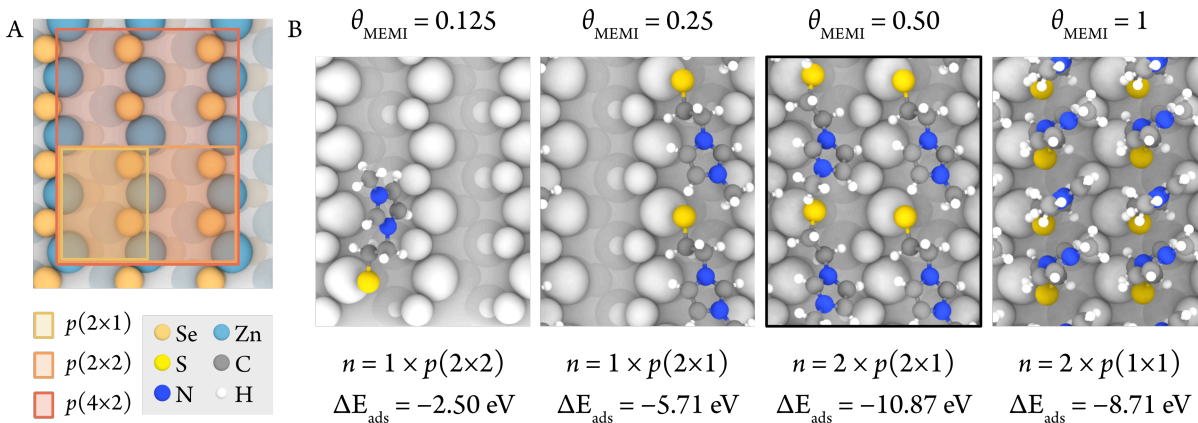


Figure 5.5 A) Representation of the surface cells with different periodicities used for the coverage analysis of MEMI. B) Top view representations of the modelled surface coverages, consisting of 12.5%, 25% 50% and 100% of the Zn adsorption sites covered by MEMI ligands via the thiol group. The number of MEMI ligands per surface cell periodicity (n) required to reach the specified surface coverage and the overall adsorption energies of the ligand phases are depicted at the bottom. Surface Zn and Se are represented in white to distinguish the atoms in the adsorbed ligands. The surface coverage used for subsequent reactivity studies on ZnSe | MEMI is depicted with an outline.

The ligand coverage on the ZnSe | Ni(cycP) was calculated by considering the presence of the Ni(cycP) co-catalyst on a $p(4 \times 3)$ –(220) surface (Figure 5.6 A), which was preferentially adsorbed onto a surface Zn site (site I in Figure 5.6 B); a side view of the adsorbed co-catalyst on that site is shown in Figure 5.6 C. To accurately describe the concentration of dithiols observed in experiments, 2 EDT, 2 HexDT and 2 OctDT ligands were adsorbed on the remaining surface sites. In ZnSe | Ni(cycP) | HexDT and ZnSe | Ni(cycP) | OctDT, the first ligand is predicted to bind in a stable bidentate conformation, in which both thiol groups are bound to surface Zn sites. Calculations revealed that energy differences between bidentate and monodentate configurations of subsequently adsorbed ligands are smaller; hence, we envision the presence of monodentate adsorption modes of the second ligand in the surface cell, with a non-binding thiol group that can effectively interact with the second coordination sphere of the intermediates on the Ni centre of the Ni(cycP) co-catalyst. An analysis of the binding energies of the bidentate + monodentate ligands, as well as the independent monodentately and bidentately bound dithiol ligands, reveals that the adsorbed ligands can be considered as non-interacting species at a distance of *ca.* 5 Å in the majority of combinations ($\Delta E_{\text{ads}}^{\text{bi+mono}} \approx \Delta E_{\text{ads}}^{\text{bi}} + \Delta E_{\text{ads}}^{\text{mono}}$). After determining that the ligands bound bidentately to Zn sites on the surface fail at stabilising the reaction intermediates on the Ni(cycP) co-catalyst, we focused on assessing the activity of the ZnSe | Ni(cycP) system in the presence of a

monodentately bound EDT, HexDT or OctDT ligand that could readily reach the second coordination sphere of the Ni metal centre.

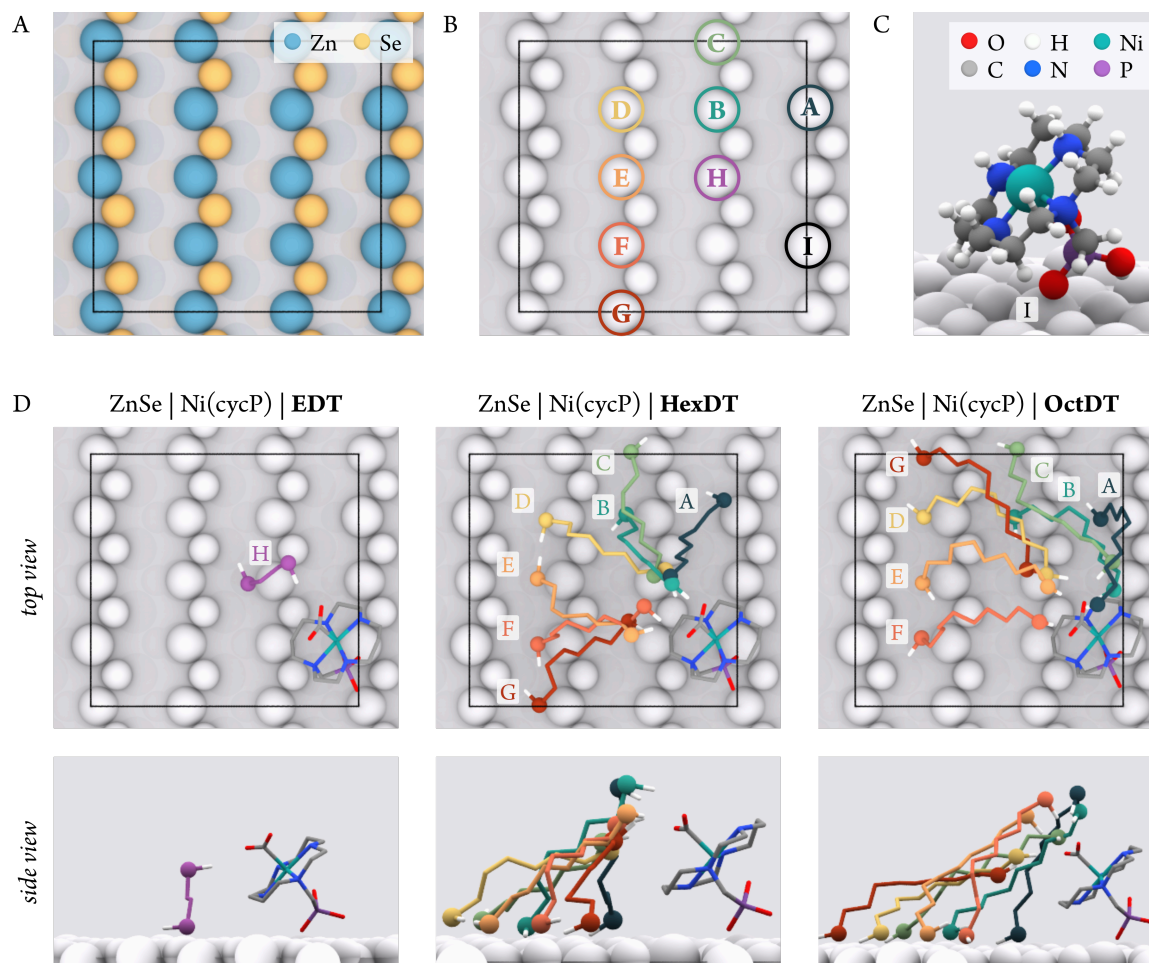


Figure 5.6 A) Top view representation of the $p(4 \times 3)$ surface used for the adsorption of EDT, HexDT and OctDT on the ZnSe and ZnSe | Ni(cycP) systems. Relevant undercoordinated atoms in the topmost surface layer are coloured, whereas non-interacting Zn and Se atoms in lower layers are shaded. B) Representation of the surface denoting the Zn atoms considered for ligand and co-catalyst adsorption. C) Most stable configuration for the adsorption of the Ni(cycP) co-catalyst, on site I. D) Top and side view representations (topmost and bottom panels, respectively) of the EDT, HexDT and OctDT ligands adsorbed on sites A to H, considered based on their potential proximity to the second coordination sphere of the intermediates on the Ni centre. Of all possible sites for the adsorption of EDT on the surface, only site H was deemed suitable for this purpose, whereas HexDT and OctDT displayed a wider range of adsorption sites from which they could influence the reaction through NCIs. All figures in C display the ligands interacting with the first intermediate in the CO₂RR on the Ni(cycP) co-catalyst (represented as sticks), to more easily depict their interacting nature. The dithiol ligands are represented as coloured chains based on their adsorption site, where S atoms are represented as larger spheres. Only H atoms in the thiol groups are included; all other H atoms are omitted for clarity.

Thus, of all possible positions onto which the considered ligands can be adsorbed, the ZnSe | Ni(cycP) | EDT system was studied by considering EDT bound onto Zn site H in Figure 5.6 B. All other configurations were

deemed too distant for the ligand to have any effect on the activity of the co-catalyst. In contrast, the ZnSe | Ni(cycP) | HexDT and ZnSe | Ni(cycP) | OctDT systems contained a total of 7 sites each (A to G in Figure 5.6 B) from which their respective monodentately coordinated ligands could interact with the intermediates and influence their stabilisation. Schematic representations of the studied configurations for the monodentate dithiols adsorbed on the $p(4\times 3)$ -(220) ZnSe surface in the presence of the Ni(cycP) co-catalyst are depicted in Figure 5.6 D. To better visualize the interacting nature of the ligands with the intermediates on the Ni centre, Figure 5.6 D represents the calculated structure of the ligands interacting with the $^*CO_2^-$ intermediate of the co-catalyst promoted pathway.

After elucidating the nature of the ligand coverage on the ZnSe | MEMI and the ZnSe | Ni(cycP) | nDT systems, in the next section we will assess the activity of the catalyst by studying a proposed surface mechanism for the CO₂RR, along with the competing HER, on the bare ZnSe and the ZnSe | MEMI system. These results will provide insight into the improved performance of the ZnSe | Ni(cycP) | nDT system, whose activity will be rationalised based on a thorough NCI analysis.

5.5. Reactivity studies

5.5.1. HER reactivity

First, the ability of the MEMI ligand to suppress HER on the ZnSe QD surface (lowering the H₂ yield from 71.8 to 29.9 mmol g_{ZnSe}⁻¹) was investigated by assessing the H binding on all possible adsorption sites on the bare ZnSe surface and the surface with a 50% MEMI coverage, both in the absence and presence of a photogenerated electron. Due to the stepped nature of the (220) lattice plane, the adsorption sites on the $p(2\times 1)$ -(220) surface were identified through a Delaunay triangulation based on the atomic centres of the surface atoms, as described in Section 2.9.4. After removing symmetrically equivalent sites, this resulted in 10 potential adsorption sites depicted as black crosses in Figure 5.7 A. The most favourable Gibbs energies of adsorption of H on the bare ZnSe (atop surface undercoordinated Zn and Se sites) are displayed in Figure 5.7 B. Our simulations revealed that the introduction of a photogenerated electron is essential to lower the H adsorption energy with respect to the neutral system, from 2.04 eV to 1.38 eV atop Se sites and from 2.15 eV to 0.36 eV atop Zn sites. As discussed in the previous sections, an adsorption energy close to thermoneutrality is believed to favour HER;²⁰ thus, our simulations predict that HER on the bare ZnSe QD only occurs atop surface Zn sites and in the presence of a photogenerated electron, in agreement with experiments.

After assessing the nature of the active sites towards HER, we next explored the influence of the MEMI ligands to rationalise the HER suppression observed in experiments. Similarly, the Gibbs energy of adsorption of a H atom on the most stable configuration atop surface Zn and Se sites in the ZnSe | MEMI system is reported in Figure 5.7 C. Noticeably, both in the neutral and charged surfaces we see that the presence of a MEMI ligand

favours the adsorption of H, which is *ca.* 0.2 eV lower than on the bare ZnSe. Thus, we predict that, in the presence of a photogenerated electron, the Gibbs energy of adsorption of H on a surface Zn site is 0.15 eV, which indicates that these sites are also potentially active towards HER.

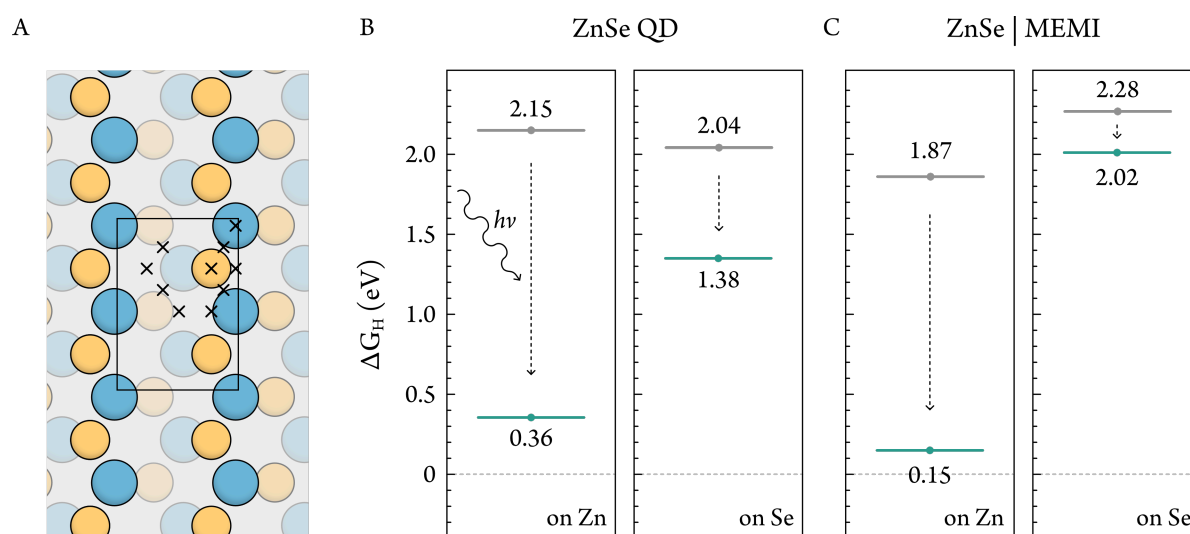


Figure 5.7 A) Potential surface adsorption sites identified on the $p(2\times 1)-(220)$ ZnSe surface. B and C) Gibbs energies of the most favourable adsorption of a H atom on the bare ZnSe (B), and the ZnSe | MEMI (C) systems onto a surface Zn (left) or Se (right) site. Adsorption energies are depicted in the absence (grey) and presence (turquoise) of a photogenerated electron in the simulation.

Hence, in view of the low adsorption energies for H on both ZnSe and ZnSe | MEMI systems, we conclude that the suppression of HER leading to a higher catalytic performance of ZnSe | MEMI stems from the stronger binding of the MEMI ligands to the surface compared to H, which are both predominantly adsorbed on the same Zn surface sites. Therefore, we predict that higher coverages of MEMI ligands will further hinder H adsorption and reduce the yield of H₂ with respect to the bare ZnSe, as observed in experiments.

5.5.2. CO₂RR reactivity

Having elucidated the nature of the competing HER, we then turned our attention to investigating the CO₂RR on the surface of the bare ZnSe and the ZnSe | MEMI systems. Firstly, the ability of surface Se and Zn sites to activate CO₂ was assessed with and without the presence of a photogenerated electron. On the bare $p(2\times 1)-(220)$ surface, all attempts to activate CO₂ in its bent configuration were unsuccessful resulting in CO₂ desorbing away from the surface into the gas phase, which indicated that the bare ZnSe QD is unable to efficiently activate CO₂ and subsequently reduce it, which is in good agreement with the experimental results.

Interestingly, our calculations showed that CO₂ can be activated in its bent form (with a O–C–O angle of 137.7° and C–O bond lengths of 1.234 and 1.238 Å—up from 1.16 Å in the gas phase) atop free surface Zn sites on the ZnSe | MEMI system exclusively in the presence of a photogenerated electron. This suggests that both the electron and the stabilising MEMI ligands around the second coordination sphere are necessary to activate CO₂

on the surface. To confirm this, further studies on the activated CO₂ revealed that removing either the MEMI ligands or the additional electron yielded similar results to the bare ZnSe or the neutral ZnSe | MEMI systems, wherein CO₂ was dissociated into the gas phase. Further insight on this first intermediate was obtained by visualizing the Bader charges and magnetisations of the C and O atoms closest (O_A) and farthest (O_B) from the surface, revealing that the photogenerated electron is delocalised between the activated CO₂ and the surface. Specifically, C, O_A and O_B were found to have magnetisations of 0.15, 0.13 and 0.12 μ_B and Bader charges of +1.54, -1.10 and -1.14 *e*, which indicates that activation of the CO₂ on a Zn site yields an adsorbed species with a negative Bader charge of -0.7 *e* and a radical behaviour, which we denote as *CO₂^{δ-}.

To determine the feasibility of ZnSe | MEMI to catalyse the CO₂RR in a mechanism containing *CO₂^{δ-} as the first intermediate, we then performed a reactivity study by proposing two possible pathways, i) a neutral mechanism in which CO₂ is activated via a PCET to form *COOH, followed by a subsequent PCET and desorption of CO_(g) (Path *a* in Figure 5.8) or ii) a mechanism in the presence of a photogenerated electron on the surface in which CO₂ is activated to the aforementioned *CO₂^{δ-} intermediate, which undergoes a PCET to form a *COOH intermediate with a potential negative charge density (*COOH^{δ-}) and a subsequent PCET desorbing CO_(g) (Path *b* in Figure 5.8).

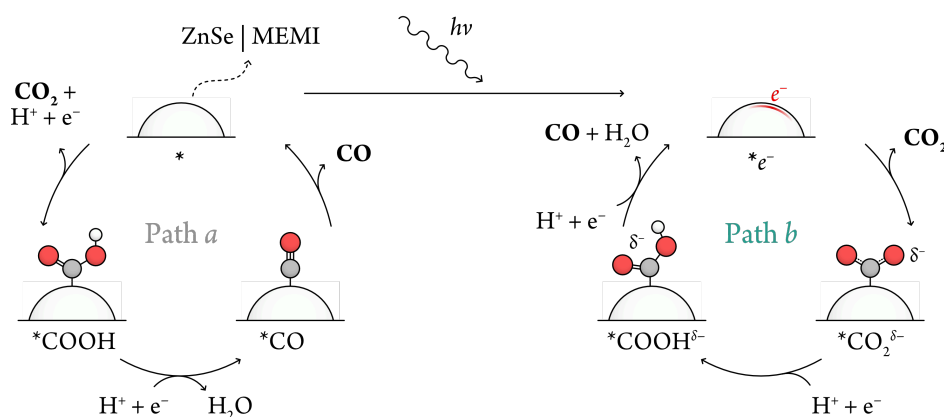


Figure 5.8 Proposed pathways for the MEMI-promoted CO₂RR on the ZnSe surface. Path *a* depicts a neutral mechanism in the absence of a photogenerated electron, where CO₂ is activated on the surface to *COOH through a PCET. Path *b* represents a mechanism in which the ZnSe surface, containing a photogenerated electron, activates the CO₂ by transferring negative charge to a MEMI-stabilised *CO₂^{δ-} intermediate.

The feasibility of Paths *a* and *b* was assessed by calculating the adsorption energies of their respective reaction intermediates, leading to the Gibbs energy profile shown in Figure 5.9. Importantly, we predict that activation of CO₂ is the most energy demanding step in both mechanisms; however, our calculations show that formation of *CO₂^{δ-} via Path *b* requires a much lower energy of 0.77 eV compared to the more endergonic activation step to *COOH in Path *a*, which requires an energy of 2.14 eV. These results are in good agreement with the experimental results obtained at different pH conditions; this analysis showed that lower pH values increased

HER yields but had a negligible effect on the CO₂RR. Accordingly, this implies that the most energy demanding step in the reaction may indeed not be mediated by a process involving a proton transfer, which further supports the energetic feasibility of Path *b* with respect to Path *a*.

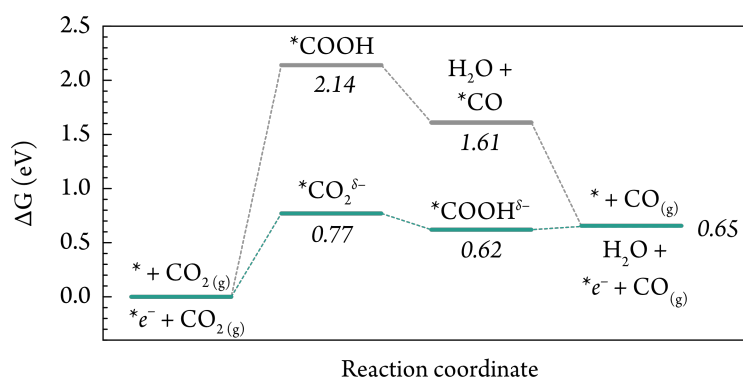


Figure 5.9 Calculated Gibbs energy diagrams for the CO₂ to CO reduction via Path *a* (in grey) and Path *b* (in turquoise) at the experimental conditions.

Next, we investigated the subsequent steps in the proposed reaction mechanisms. On the one hand, we predict that the very endergonic formation of *COOH in Path *a* is succeeded by an exergonic formation of *CO and subsequent spontaneous desorption. On the other hand, our calculations showed that the initial activation of CO to *CO₂^{δ-} in Path *b* is followed by a slightly exergonic step to form the *COOH^{δ-} intermediate and an endergonic step to yield desorbed CO, which only requires an energy of 0.03 eV. Similarly to *CO₂^{δ-}, the nature of the intermediates in both pathways was confirmed by performing a Bader charge analysis and visualising the atomic magnetisations, which confirmed the negative charge ($-0.65 e$) on the *COOH^{δ-} intermediate of Path *b* and a slight radical build-up in the *COOH intermediate of Path *a*. A representation of the four intermediates involved in both pathways is shown in Figure 5.10, with their corresponding atomic magnetisations and Bader charges.

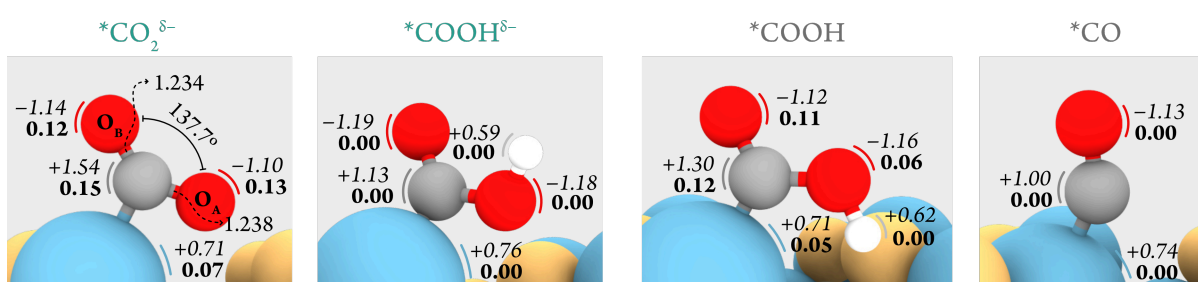


Figure 5.10 Side view representation of the calculated intermediates in Path *a* (grey label) and Path *b* (turquoise label) on ZnSe | MEMI, following the pathways depicted in Figure 5.8. Atomic Bader charges (in e) are displayed in italics beside each atom, while magnetisations (in μ_B) are shown in bold. Values of relevant bond lengths and angles are also depicted for the *CO₂^{δ-} intermediate. Neighbouring MEMI ligands have been omitted for clarity. Colour code is the same as in Figure 5.6.

Overall, our reactivity studies of the ZnSe | MEMI system predict that the CO₂RR occurs predominantly on surface Zn sites in a mechanism promoted by a photogenerated electron and neighbouring MEMI ligands. It is worth mentioning that either the CO₂RR and the competing HER occur atop the same surface Zn sites onto which MEMI ligands are adsorbed. Nonetheless, we believe that the presence of MEMI ligands influence both reactions in a different fashion; while the coverage of MEMI ligands decrease the number of surface Zn sites onto which HER readily occurs, its presence is necessary for the adsorption of the CO₂RR intermediates on the remaining sites. Moreover, simulations showed that the adsorption and activation of CO₂ is the most energetically demanding step, which highlights the importance of the interactions between the MEMI ligands and this intermediate to enhance catalytic activity. Therefore, we will devote the following sections to unravel the nature of the interactions between the MEMI ligands and the *CO₂^{δ-}, and to rationalise the ability of the dithiol ligands to enhance the CO₂RR activity on the ZnSe | Ni(cycP) based on similar effects.

5.6. Ligand effects on CO₂RR selectivity

The nature of the stabilising interactions between the MEMI ligands and *CO₂^{δ-} was investigated by computing $s(\mathbf{r})$ as a function of ρ by means of the Critic2 software.²²⁸ In short, these interactions are represented as peaks in $s(\mathbf{r})$, wherein negative and positive values of $\text{sign}(\lambda_2)\rho$ depict attractive and repulsive interactions, respectively, allowing for the pseudo-quantitative determination of the interaction strength. Accordingly, the NCIs between the MEMI coverage and the *CO₂^{δ-} onto a surface Zn site are plotted in Figure 5.11 A, and represented as electron density isosurfaces in Figure 5.11 B.

An analysis of the NCIs reveals that two relatively strong attractive interactions stand out, namely peaks 1 and 2 in Figure 5.11 A. At more positive values (less attractive interactions), we observe series of weakly attractive interactions (region 3 and peak 4) in ranges closer to the origin, and a set of weakly repulsive interactions in region 5. Moreover, the value of $\text{sign}(\lambda_2)\rho$ associated these peaks shows that the strength of these repulsive interactions is approximately half that of the interactions corresponding to peaks 1 and 2, which highlights that the bulk of the stabilisation arises from attractive NCIs between the ligand and the first intermediate. Subsequently, the isosurfaces associated with the highlighted NCIs in Figure 5.11 A were individually analysed, and are represented in Figure 5.11 C. This reveals that the most attractive NCIs in peaks 1 and 2 correspond to a π -p interaction between the aromatic imidazole ring and the 2p orbital of O_A, and a H-bond between O_B and a H atom from a neighbouring MEMI ligand, respectively. Importantly, the ability of the imidazole ring to stabilise a neighbouring *CO₂^{δ-} through a set of H-bonding and π -p interactions is in good agreement with the mechanisms proposed in the literature.⁹³ Furthermore, we predict that the rest of attractive NCIs (corresponding to peaks 3 and 4 in Figure 5.11 A) correspond to weaker π -p interactions with farther C atoms in the ring and vdW interactions between O_B and H atoms of the MEMI ligands. Finally, all repulsive interactions are predicted to result from weak steric effects. Hence, we believe that this combination of highly

attractive and slightly repulsive interactions favour the activation of CO₂ on the surface, and ultimately promotes the reduction of CO₂ to CO.

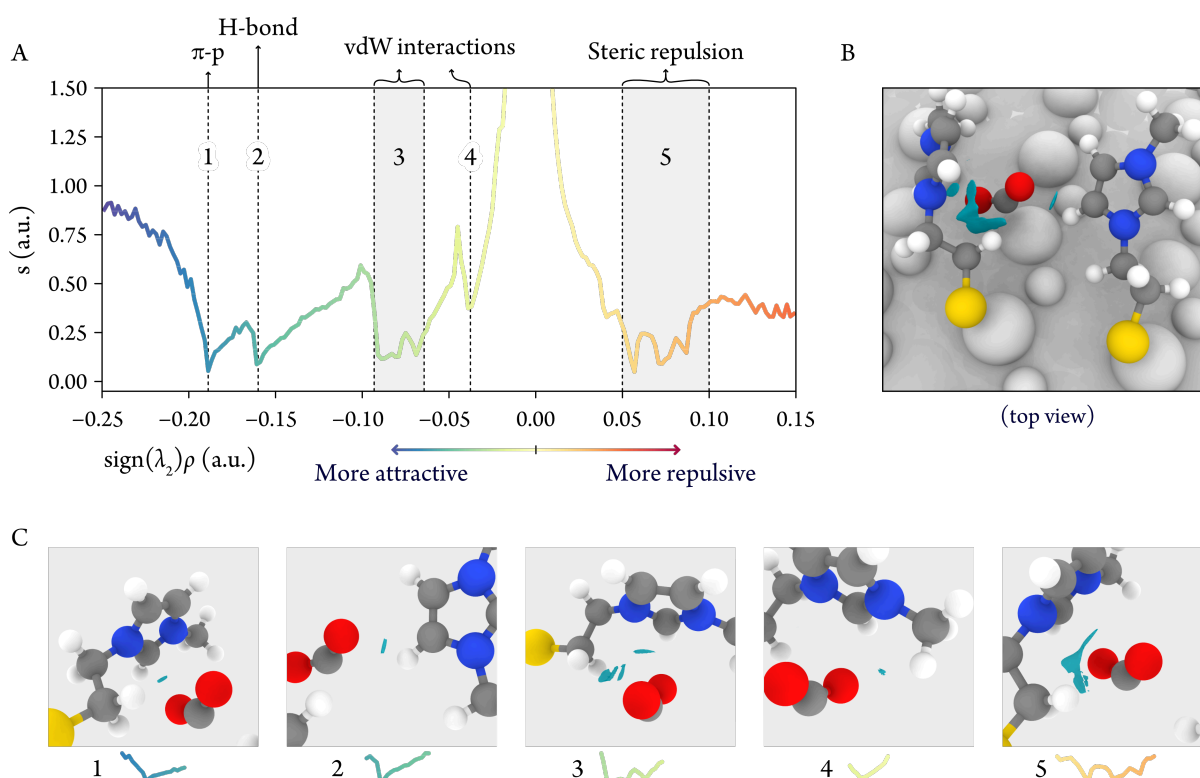


Figure 5.11 A) Plot of the reduced density gradient ($s(\mathbf{r})$) as a function of the electron density multiplied by the sign of the second eigenvalue of the Hessian matrix ($\text{sign}(\lambda_2)\rho$) for the ZnSe | MEMI system with the adsorbed $^*\text{CO}_2^{\delta-}$ intermediate. Peaks correspond to attractive and repulsive NCIs, assigned based on the value of $\text{sign}(\lambda_2)\rho$ below and above 0 a.u., respectively. Thus, the further the peak is from the origin, the stronger the attractive or repulsive nature of the interaction. B) NCIs between the MEMI ligands and $^*\text{CO}_2^{\delta-}$ represented as blue isosurfaces with an isovalue of $0.3 \text{ e}^-/(\text{a.u.})^3$. C) Relevant NCIs identified in A) represented as blue isosurfaces with isovalues of $0.5 \text{ e}^-/(\text{a.u.})^3$ (for peak 4) and $0.3 \text{ e}^-/(\text{a.u.})^3$ (for the rest). Surface atoms in C) have been omitted for clarity.

5.6.1. Tailoring ligand-functionalised hybrid ZnSe QDs as CO₂ reduction photocatalysts

In order to support the experimental results on the bare ZnSe QD and in the presence of the Ni(cycP) co-catalyst, we performed a similar investigation on representative ZnSe | nDT and ZnSe | Ni(cycP) | nDT systems, as discussed in previous sections. Firstly, the ability of EDT, HexDT and OctDT to monodentately stabilise the $^*\text{CO}_2^{\delta-}$ intermediate on the bare ZnSe QD and in the presence of a photogenerated electron was investigated. Importantly, all attempts to adsorb $^*\text{CO}_2^{\delta-}$ and stabilise it upon interaction with HexDT and OctDT in the second coordination sphere were unsuccessful, and resulted in desorption of CO₂ and relaxation of the free thiol group away from the surface. However, due to the shorter-reaching nature and fewer degrees of freedom of EDT, calculations showed that this ligand could effectively interact with $^*\text{CO}_2^{\delta-}$ on a neighbouring Zn site and stabilise its adsorption. Furthermore, we believe that this effect will be similar for subsequent

reaction intermediates, which may be a good indicator of the ability of EDT to adsorb on the surface and promote the CO₂RR more effectively compared to longer ligands, in agreement with experiments. NCIs between EDT and the *CO₂^{δ-} intermediate in the ZnSe | EDT system are represented in Figure 5.12 A, which reveals the presence of a dimmer H-bond between the free thiol group and the intermediate, as well as vdW interactions. This weaker effect on the stabilisation of CO₂ compared to the previously discussed ZnSe | MEMI system is confirmed by a larger C–O–C angle of 142.3°.

Next, we sought to assess the NCIs between the EDT, HexDT and OctDT ligands and the *CO₂^{δ-} adsorbed on the Ni centre in the ZnSe | Ni(cycP) | nDT systems. Firstly, we investigated the interactions between EDT in position *H* (EDT_H), depicted in Figure 5.6 C, and the intermediate in ZnSe | Ni(cycP) | EDT. Interestingly, an analysis of the NCIs (represented in Figure 5.12 B) shows that the shorter length of EDT yields only one slightly attractive H-bond arising from interactions between the free thiol and the second coordination sphere, with a less attractive nature relative to the results obtained on ZnSe | EDT. Thus, we believe that the slight enhancement in CO production (albeit within the margin of error) observed experimentally in ZnSe | Ni(cycP) | EDT compared to ZnSe | Ni(cycP) may be due to EDT additionally facilitating the surface-promoted mechanism onto free Zn sites.

After determining the inability of EDT to effectively stabilise the first potential CO₂RR intermediate in the ZnSe | Ni(cycP) | EDT system, we then turned our attention to assessing the competence of the longer HexDT and OctDT ligands to yield attractive interactions with the Ni-bound *CO₂^{δ-}. In order to account for all possible ligand configurations, NCIs between *CO₂^{δ-} and monodentate HexDT and OctDT ligands in positions A to G (sites from which they can interact with the intermediates, as represented in Figure 5.6 C) were calculated. The results of this thorough NCI analysis, including the interactions represented as isosurfaces in the structure and as plots of $s(\mathbf{r})$, are depicted in Figure 5.13.

The analysis of the NCIs reveals that the use of longer dithiol ligands not only allows for the effective interaction with the intermediates from multiple adsorption sites, but the resulting interactions are in some cases dramatically more attractive compared to those using EDT. Our calculations show that ZnSe | Ni(cycP) with both HexDT and OctDT on sites *B*, *C*, *E* and *F* display very attractive NCIs with peaks of $s(\mathbf{r})$ at ranges of $\text{sign}(\lambda_2)\rho$ from *ca.* -0.1 to -0.2 a.u., depicting H-bonds up to 3 times stronger than in ZnSe | Ni(cycP) | EDT. Moreover, we predict that these strongly attractive H-bonds from the ligands on the aforementioned sites will not be accompanied by any significant repulsive interactions. Similarly to the effect observed in ZnSe | EDT, we envision that these attractive NCIs will potentially stabilise all intermediates in the CO₂RR and facilitate CO production, which supports the increased CO yields observed in experiments on the ZnSe | Ni(cycP) | HexDT and OctDT systems. Furthermore, due to the inability of HexDT and OctDT to activate CO₂ onto Zn sites and facilitate a surface-promoted mechanism, we believe that the enhancement in CO production using longer dithiols arises exclusively from their stabilising effects on the co-catalyst promoted pathway.

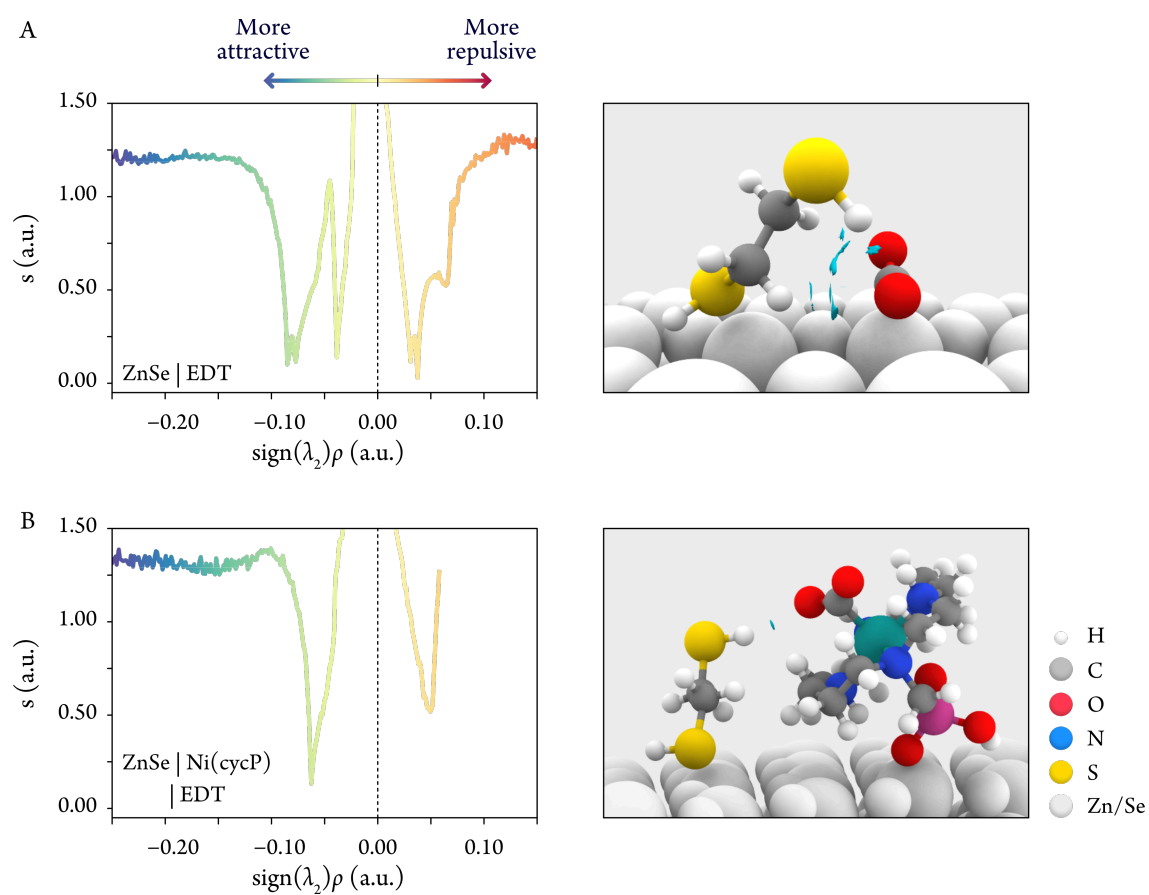


Figure 5.12 Plots displaying the NCIs between EDT and the $^*\text{CO}_2^{\delta-}$ intermediate on the ZnSe | EDT (A) and the ZnSe | Ni(cycP) | EDT (B) systems. The outlines of the peaks arising from plotting $s(\mathbf{r})$ as a function of $\text{sign}(\lambda_2)\rho$ are displayed on the leftmost panels, and the NCIs between EDT and the $^*\text{CO}_2^{\delta-}$ intermediate are depicted as blue isosurfaces with an isovalue of $0.3 e^-/(\text{a.u.})^3$ on the right.

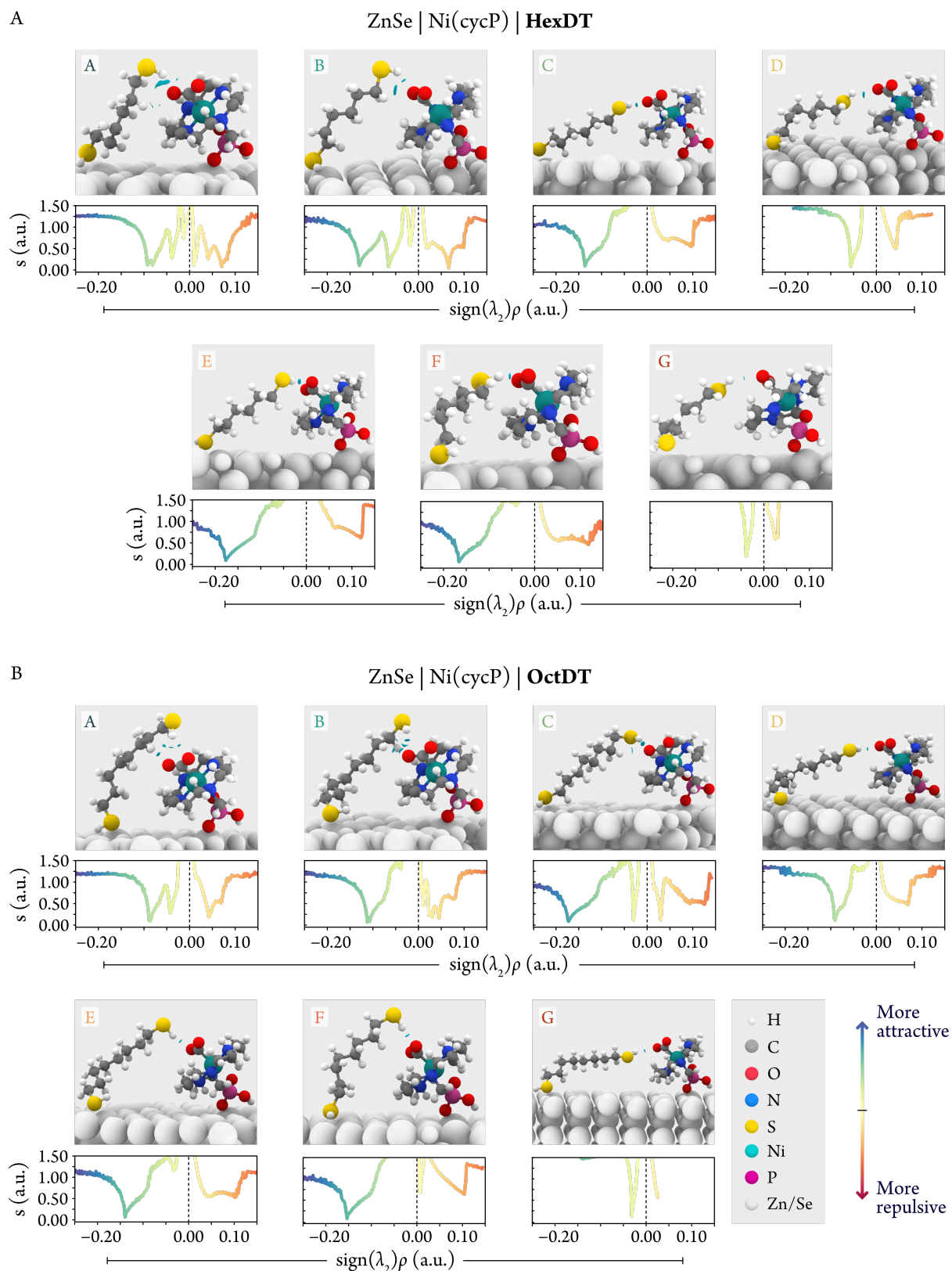


Figure 5.13 Representation of the NCIs between the $^*CO_2^{\delta-}$ intermediate and HexDT (A) or OctDT (B) on each adsorption site from which they can reach the second coordination sphere of the Ni centre with a free thiol in their monodentate conformations (A to G in Figure 5.6). The NCIs are represented in the topmost panels as blue isosurfaces with isovalues of $0.3 e^-/(a.u.)^3$, and depicted as plots of $s(\mathbf{r})$ as a function of $sign(\lambda_2)\rho$ in the bottom panels.

5.7. Conclusions

The superior catalytic CO₂ to CO conversion on ZnSe QDs functionalised with MEMI ligands observed experimentally was investigated by means of periodic DFT calculations. This was achieved by modelling the predominant surface of the QD using the Wulff construction method and performing an analysis of the MEMI ligand coverage on the resulting surface, which resulted in a 50% of the surface Zn sites covered by MEMI ligands. After determining the surface resting state, we assessed the competence of the MEMI coverage for activating CO₂ on the surface with and without the presence of a photogenerated electron—yielding an adsorbed *CO₂^{δ-} species with negative charge density build-up and radical behaviour—, which we believe is the first reaction intermediate based on the experimental results. Ultimately, we predict that MEMI ligands are able to stabilise this first intermediate only in the presence of a photogenerated electron in a cooperative process. To confirm that *CO₂^{δ-} is indeed the first intermediate in the catalysed reaction, we proposed and elucidated two distinct pathways leading to CO production, namely a neutral pathway in which CO₂ is adsorbed and converted to *COOH through a PCET in a neutral mechanism, or a pathway mediated by the presence of a photogenerated electron on the surface, yielding a *CO₂^{δ-} intermediate which undergoes subsequent PCET steps. Based on the energetics of both mechanisms, we predict the latter to be predominant given its lower value of the most endergonic step energy compared to the neutral mechanism (0.77 vs 2.14 eV), in both cases corresponding to CO₂ activation on a surface Zn site. Moreover, we predict that these active sites for the CO₂RR are also active for the competing HER only in the presence of a photogenerated electron, but while the MEMI coverage facilitates the former by stabilising the intermediates on the surface, it hinders the latter by reducing the amount of sites onto which H is adsorbed. Finally, the stabilising nature of the MEMI ligands on the highest energy intermediate was assessed by performing an analysis of the NCIs, which revealed that *CO₂^{δ-} is subjected to strongly attractive π-p interactions and H-bonding between O and the aromatic imidazole ring from neighbouring MEMI ligands.

Based on the evidence that NCIs in the second coordination sphere promote the CO₂RR by stabilising the reaction intermediates, we then sought to rationalise the experimentally observed enhancement in CO production on the ZnSe QD in the absence and the presence of a Ni(cycP) molecular co-catalyst and using dithiol ligands of different lengths. In order to do this, the experimental coverage of 3 representative dithiol ligands (EDT, HexDT and OctDT) was simulated in the absence and presence of Ni(cycP). Importantly, we predict that the coverage of dithiols on the Ni(cycP)-functionalised ZnSe QD contains monodentate ligands which can interact with the second coordination sphere of the Ni metal centre. Furthermore, our calculations show that these monodentate ligands can be assessed individually as their adsorption energy is not influenced by the presence of surrounding bidentate ligands in the coverage. Therefore, we modelled the coverage of the Ni(cycP)-functionalised QD by simulating a monodentate ligand adsorbed on Zn sites from which the free thiol can reach the metal centre, yielding 1 configuration for EDT and 7 for both HexDT and OctDT. Next, we

built up from these coverage models to investigate the ability of the three ligands to stabilise the $^*\text{CO}_2^{\delta-}$ intermediate in a surface pathway or a co-catalyst mediated pathway. Accordingly, our results suggest that the first intermediate can only be stabilised atop surface Zn sites in the presence of a shorter EDT ligand and a photogenerated electron, which explains the good results observed experimentally for this ligand compared to larger dithiols in the absence of the Ni co-catalyst. Further NCI analyses of the interactions demonstrate the ability of EDT to stabilise the $^*\text{CO}_2^{\delta-}$ intermediate *via* H-bonding from its free thiol group and an O atom of $^*\text{CO}_2^{\delta-}$. In the co-catalyst mediated mechanism, we showed that the length of EDT is insufficient to effectively generate these stabilising NCIs with the reaction intermediates; however, our simulations on all possible configurations of monodentate HexDT and OctDT reveal that the increased length of these ligands can yield strong H-bonds with $^*\text{CO}_2^{\delta-}$ and possibly subsequent intermediates, which supports the good CO production rates of the Ni(cycP)-functionalised ZnSe QD observed experimentally in the presence of longer dithiols. However, to more accurately describe the effects on the enhancement in CO production on these systems, a complete reactivity study is underway.

In conclusion, these studies reveal the importance of understanding the interactions in the second coordination sphere for the photocatalytic CO₂RR by means of a thorough mechanistic study and pseudo-quantitative analysis of the NCIs. Ultimately, we believe that the insight obtained from this work will prove essential for the future rational design of efficient state-of-the-art photocatalysts for CO₂ conversion into usable chemical feedstocks.

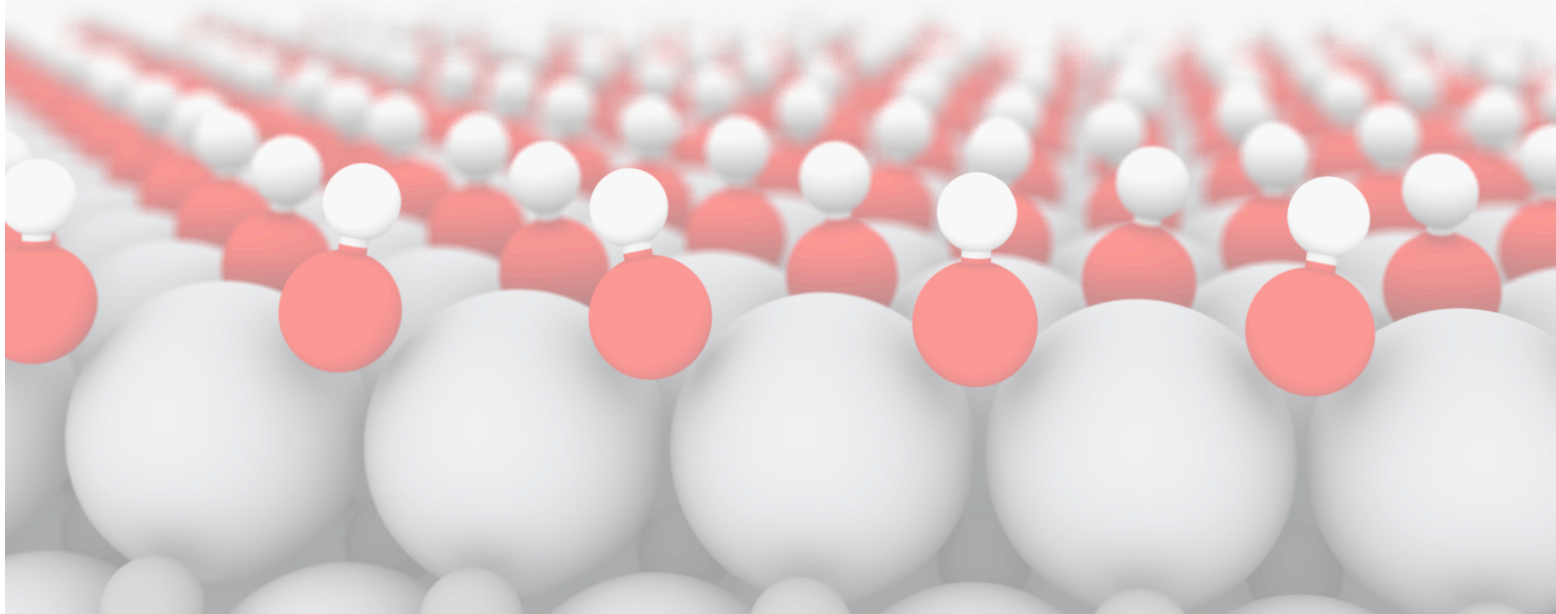
“ Looking back, we were the luckiest people in the world; there was no choice but to be pioneers; no time to be beginners. – **Margaret Hamilton**

In a retrospective piece for NASA, 2008

CHAPTER

6

Coverage-led Design of MXenes for Electrocatalysis



6.1. Introduction

Since the formulation of the CHE model in 2004,⁸² which simplified the theoretical study of heterogeneous electrocatalytic systems, interest in this field has experienced a dramatic increase. This prompted the study of a wide range of reactions under different electrochemical conditions, such as the ones discussed in previous sections. Nonetheless, most theoretical electrocatalytic studies have been historically focused on analysing the behaviour of bare, non-functionalised catalysts under electrochemical conditions to draw relevant figures of merit.^{100,231} However, we know that species present in solution can play a crucial role in the reactivity,²³² and these seldom are only simple spectators or sources of surface poisoning, but also active participants in many reaction mechanisms.^{66,233,234} Moreover, accurately determining the presence of surface coverages on the catalysts' resting state is especially relevant under aqueous electrochemical conditions, as applying different external potentials is theorised to promote one or another surface termination.²³⁵ This knowledge has prompted some interest in assessing the surface coverage as a fundamental step to accurately depict reaction mechanisms in electrochemical conditions;²³⁶ however, we believe more effort needs to be put into investigating how to efficiently *use* the surface coverage present in electrochemical conditions to design and discover novel electrocatalysts. Therefore, in this chapter we will thoroughly discuss how to accurately depict the surface coverage and its behaviour on state-of-the-art 2-D materials; subsequently, we will address how the pH and applied potential can be optimised to increase the stability and activity of the investigated surface coverages for their application in a wide range of electrocatalytic reactions.

With this aim, we will focus on discussing the nature of the surface coverage of one of the most promising 2-D materials for electrocatalysis, namely MXenes. These materials are a family of 2-D metal carbides and nitrides obtained from etching of their respective MAX phases with the general formula $M_{n+1}AX_n$, where n ranges from 1 to 4, M denotes an early transition metal (e.g. Sc, Ti, Zr, Hf, V, Nb, Ta, Cr, or Mo), A stands for an element from groups 13–16 (e.g. Al, Ga, In, Tl, Si, Ge, Sn, Pb, P, As, Bi, S, or Te), and X for carbon or nitrogen.²³⁷ Therefore, MXenes⁺⁺⁺ are defined by the general formula $M_{n+1}X_n$ (where $n = 1$ to 4).²³⁸ These can be either monometallic or bimetallic, wherein atoms in the latter can be either arranged randomly (solid solutions) or present an out-of-plane (*o*-MXenes) or in-plane ordering (*i*-MXenes)—where the two different transition metals are positioned either in a *sandwich* configuration or distributed periodically along the plane, respectively, with a hexagonal structure with a $P6_3/mmc$ symmetry group. Furthermore, the minor metal in bimetallic solid solutions and *i*-MXenes can be etched to obtain MXenes with vacancies; these configurations are represented in Figure 6.1. Because of their high tunability and electronic properties, MXenes have been simulated for a myriad of applications such as supercapacitors,²³⁹ wireless communications²⁴⁰ and energy storage,^{237,241} as well as in a number of electrochemical reactions, including nitrogen reduction,²⁴² CO oxidation,²⁴³ OER,²⁴³ and HER.^{241,244,245} These applications are often governed by the surface termination of MXenes, as these have been demonstrated to be generally functionalised with a wide range of adsorbates such as Cl, I, Se, Br and Te,^{246,247} and in aqueous solution and electrochemical conditions by one or more monolayers of H, OH and O adsorbates originating from the applied potential and water intercalation between MXene flakes.²³⁵ Hence, MXenes are most commonly written as $M_{n+1}X_nT_x$, wherein T denotes the ever-present terminal species on each side of the MXene slab which, interestingly, have proven to confer MXenes with a superior thermodynamic stability.²⁴⁸ In addition, some MXenes have been found to be 2-D topological insulators⁺⁺⁺.^{249,250} This results in some MXenes changing their electronic behaviour upon functionalisation: for instance, Ti_2CO_2 (Ti_2C MXene functionalised with O atoms on each side) has been theorised to display a band gap of *ca.* 0.92 eV (as predicted using hybrid functionals), in contrast with its bare counterpart which behaves as a metal.²⁵⁰ In addition, the presence of mixed coverages of oxygen and hydroxyl groups with various binding strengths governs the activity of MXenes toward HER. Specifically, this reaction is believed to primarily occur onto the O adsorbates; this has been demonstrated theoretically, as ΔG_{H^+} on some $M_{n+1}X_nO_2$ MXenes was found to be close to thermoneutral.^{244,251} Therefore, an assessment of the surface coverage at experimental conditions is key for understanding the properties and reactivity of MXenes in electrochemical conditions.

Since their discovery in 2011,²⁵² thousands of MXenes containing various transition metals have been theoretically studied and predicted,^{247,253} however, only a handful have been synthesized to date, as shown in Table 6.1.^{238,252,254–272} In this chapter, we will unravel the nature of the coverage of the monometallic and bime-

⁺⁺⁺ MXenes are named after the two species present in the structure and the *-ene* termination—analogue to *graphene*—to highlight their bidimensional nature.

⁺⁺⁺ They display gapless states at the edges and insulating states at the bulk, which is dominated by spin-orbit coupling.

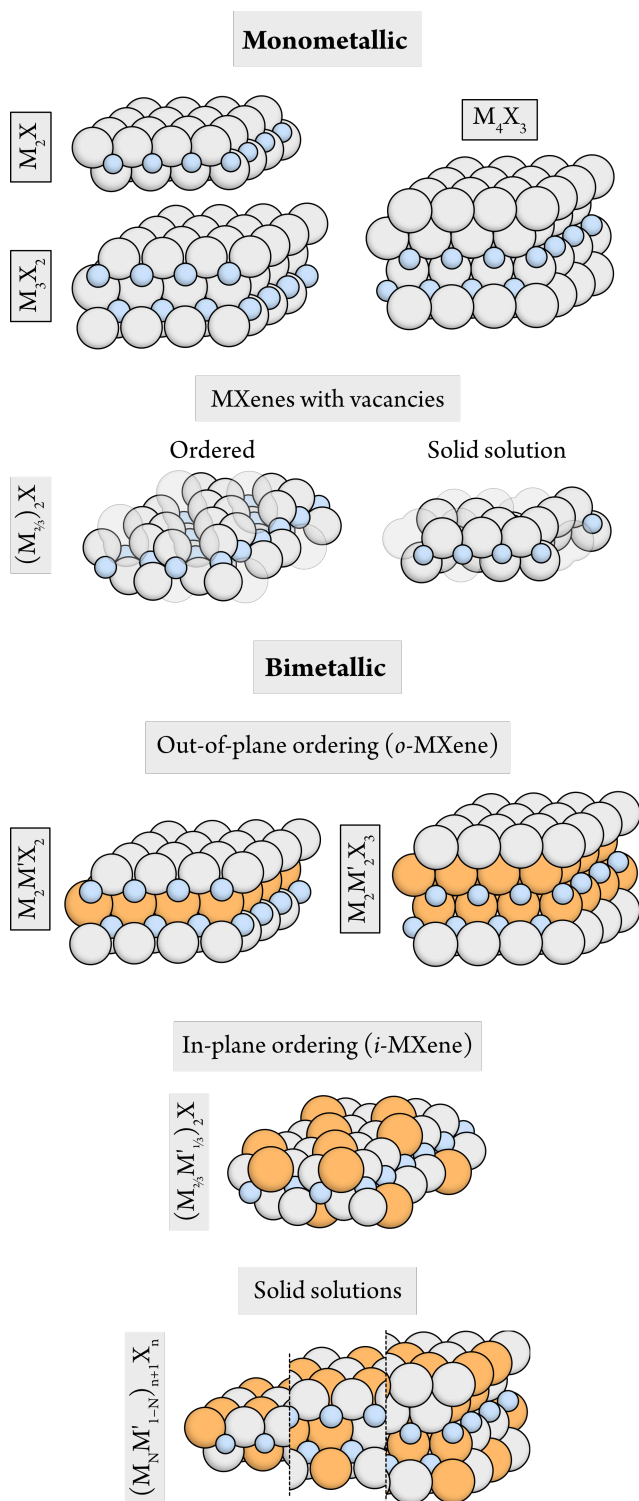


Figure 6.1 Representation of the different MXene types that have been experimentally synthesized. Metals M and M' are represented as orange and grey spheres, while the C/N atoms are depicted in light blue. MXene types investigated in this thesis are labelled with a black outline.

Table 6.1 Formulae of the MXenes that have been synthesized ($n = 1$ to 4), along with their corresponding original source in the literature. MXenes with both in-plane and out-of-plane ordering are depicted in blue, while solid solution MXenes are represented in dark orange. MXenes studied in this section are denoted in bold.

n	MXene	Year and reference(s)
1	Ti₂N	2017 ²⁶⁴
	Ti₂C	2012 ²⁵⁴
	V₂C	2013 ²⁵⁵
	(V _{1-x} Ti _x) ₂ C	2017 ^{256,267}
	W _{1.33} C	2018 ²⁷⁰
	Nb _{1.33} C	2018 ²⁶⁹
	Mo₂N	2017 ²⁶⁶
	Mo₂C	2015 ²⁵⁹
	V₂N	2017 ²⁶⁶
	Nb₂C	2013 ²⁵⁵
	TiNbC	2012 ²⁵⁴
	Mo _{1.33} C	2017 ²⁶⁵
	Mo _{1.33} Y _{0.66} C	2018 ²⁷¹
	2	Ti₃(C,N)₂
Ti₃C₂		2011 ²⁵²
(Cr₂Ti)₂C₂		2015 ²⁵⁸
(Mo₂Sc)₂C₂		2017 ²⁶³
(Ti _{0.5} V _{0.5}) ₃ C ₂		2014 ²⁵⁶
Hf₃C₂		2017 ²⁶⁸
Zr₃C₂		2016 ²⁶²
(Cr₂V)₂C₂		2014 ²⁵⁶
(Mo₂Ti)₂C₂	2015 ²⁵⁸	
3	Ti₄N₃	2016 ²⁶⁰
	Nb₄C₃	2014 ²⁵⁷
	(Nb _{0.5} V _{0.5}) ₄ C ₃	2014 ²⁵⁶
	(Nb _{0.8} Zr _{0.2}) ₄ C ₃	2016 ²⁶¹
	V₄C₃	2018 ²⁷²
	Ta₄C₃	2012 ²⁵⁸
	(Nb _{0.8} Ti _{0.2}) ₄ C ₃	2016 ²⁶¹
(Mo₂Ti₂)C₃	2015 ²⁵⁸	
4	(Mo ₄ V) ₄ C ₄	2020 ²³⁸

tallic *o*-MXenes that have been synthesized to date (outlined structures in Figure 6.1 and MXenes in bold in Table 6.1). This discussion will be divided into four parts: firstly, the surface coverage of *o*-MXenes under electrochemical conditions will be determined; secondly, the relative stability of MXenes and their coverage phases will be assessed in order to optimise the reaction conditions; next, the influence of the surface coverage on the electron conductivity of MXenes will be studied; finally, the insight obtained from this thorough analysis of the surface coverage will be used to predict the source of HER—the main competing reaction in electrochemical reactions and in the formation of surface coverages—at different applied potentials.

6.2. Computational details

Periodic DFT calculations reported in this chapter were performed using the PBE functional as implemented in the VASP software, version 5.4.1.^{223,224} The core electrons of all studied transition metals and C, N, H and O atoms were replaced by PAW potentials,¹⁴⁹ while their valence electrons were expanded in plane waves with a kinetic energy cut-off of 520 eV. To obtain a more accurate representation of the electronic structure, *p* semi-core states (those in the second outermost electron shell) of Ti, Mo, V, Nb, Cr and Hf and *s* semi-core states of Sc and Zr were also treated as valence states. Reciprocal space within the first Brillouin zone was sampled using a *k*-point density of 25 Å. These parameters are identical to those used in the calculations of all structures within the Materials Project,²²⁵ which allows for a fair energetic comparison between the MXenes investigated herein and the bulk structures collected in that database. To simulate the potential topological insulating nature of the calculated MXenes, spin-orbit coupling effects were taken into account by assessing electron spins non-collinearly.

All structures were optimised using a maximum step size of 0.03 Å and a force-based convergence criteria of 0.02 eV Å⁻¹. MXene *p*(1×1) slabs with symmetry $\bar{P}3m1$ were constructed using the crystal bases specified in Table 6.2. In all slab structures, 15 Å of vacuum was added in the direction perpendicular to the surface. The lattice parameter of the surface slabs—initially set to 3.0 Å—was pre-optimised by relaxing the cell size and shape; subsequently, lattice parameters were fine-tuned varying *a* and *b* simultaneously from -1 to +1 % of the obtained value with a step size of 0.5 % and fitting the resulting energies using the Birch–Murnaghan EOS.

Surface coverages of H, OH and O adsorbates were assessed by considering the functionalization of all the available surface sites (*hcp*, *fcc*, *top* and *bridge*, as represented in Figure 2.16) onto both sides of the *p*(1×1) slab, by means of a Delaunay triangulation and procedural adsorption of species as implemented in the *autocoverage* program.^{§§§§} Mixed O/OH coverages were investigated by sequentially adsorbing H atop O atoms onto their most stable adsorption sites in a *p*(2×2) slab containing 4 O adsorbates on each side of the slab. Surface line and Pourbaix diagrams identifying coverage phases at various conditions of pH and *U* were constructed as

^{§§§§} The source code for this program is accessible on the following repository: <https://www.craft.do/s/b2te0pT8PEZluG>

described in Section 2.7.2 and implemented in a python code.^{*****} The Gibbs energies of adsorption of all the functionalised species were calculated relative to the bare MXene, using equations similar to those in Eqs. (2.92) to (2.94).

Table 6.2 Crystal bases describing the atomic positions in the unit cell of the calculated MXene slabs. τ corresponds to the slab thickness parameter, which is set to 2.5 for all structures and varies upon relaxation.

MXene	Expanded formula	Element	Fractional coordinates		
			X	Y	Z
M_2X	$M-X-M'$	M	$\frac{2}{3}$	$\frac{1}{3}$	$\frac{1}{2} \times \tau$
		X	0	0	0
		M'	$\frac{1}{3}$	$\frac{2}{3}$	$-\frac{1}{2} \times \tau$
M_3X_2	$M_1-X-M_2-X'-M_1'$	M_1	$\frac{1}{3}$	$\frac{2}{3}$	τ
		X	$\frac{2}{3}$	$\frac{1}{3}$	$\frac{1}{2} \times \tau$
		M_2	0	0	0
		X'	$\frac{1}{3}$	$\frac{2}{3}$	$-\frac{1}{2} \times \tau$
		M_1'	$\frac{2}{3}$	$\frac{1}{3}$	$-\tau$
M_4X_3	$M_1-X-M_2-X'-M_2''-X''-M_1'$	M_1	0	0	$1.5 \times \tau$
		X	$\frac{1}{3}$	$\frac{2}{3}$	τ
		M_2	$\frac{2}{3}$	$\frac{1}{3}$	$\frac{1}{2} \times \tau$
		X'	0	0	0
		M_2''	$\frac{1}{3}$	$\frac{2}{3}$	$-\frac{1}{2} \times \tau$
		X''	$\frac{2}{3}$	$\frac{1}{3}$	$-\tau$
		M_1'	0	0	$-1.5 \times \tau$

Gibbs energy corrections were computed using the Thermochemistry Module implemented in the ASE package²²⁶ at pH = 0 and the temperature and pressure of 298 K and 1 atm. All structures involving an electrochemical water layer (Section 2.6.1) were performed on $p(3 \times 3)$ slabs, where water molecules in the OHP are at least 4 Å away from the surface termination. For the reaction steps involving a PCET, the CHE model was used (Section 2.7.1). All TS structures were located by means of the CI-NEB algorithm (Section 2.8.1), using four images along the reaction coordinate; subsequently, the nature of all stationary points was confirmed by frequency analysis with a numerical Hessian matrix obtained by atomic displacements of 0.01 Å via the finite difference method, only considering the vibrational modes of the adsorbates.

Surface energies of the covered MXene slabs were calculated as discussed elsewhere,^{234,238} and are defined as:

$$\gamma_{hkl} = \frac{G_{slab} - N_M \mu_M - N_X \mu_X - \sum_j N_j \mu_j}{2A} \quad (6.1)$$

Where G_{slab} is the Gibbs energy of the MXene slab with a given surface coverage; $N_M \mu_M$ is the chemical potential (chemical energy per mole of substance¹⁷⁵) of the bulk metal comprising the MXene multiplied by the

^{*****} The source code of both scripts are available on the following website: <https://www.craft.do/s/7M2uCh0gQnFEW3>

amount of metal atoms in the MXene slab; $N_X\mu_X$ is the chemical potential of C/N (for which graphite and a N_2 molecule in the gas phase were taken as a reference) multiplied by the number of C/N atoms in the MXene slab; and $N_j\mu_j$ is the chemical potential of all the adsorbates (H, O and/or OH) present in the slab, which can be described in terms of the chemical potentials of H_2 and H_2O , as discussed in Section 2.7.2.

Pourbaix diagrams showing the thermodynamically most stable phases of the atoms making up each functionalised MXene were constructed considering all the structures present in the Materials Project database;²⁷³ subsequently, the relative stability of the functionalised MXenes with respect to the thermodynamically most stable phase was calculated at each point of U and pH, generating a stability heatmap as described elsewhere.^{274,275} This will be discussed in more detail in subsequent sections.

6.3. Coverage analysis of MXenes

We began our assessment of the morphology and subsequent potential reactivity of the MXene surfaces by performing a thorough analysis of the coverage phases present in aqueous solution (wherein both sides of the MXene slab can be functionalised with H, OH or O).²³⁵ This analysis yielded exergonic functionalisation of all MXenes with 1, 2 or 3 H atoms and 1 O species on each side of a $p(1\times 1)$ unit cell (covering all *fcc*, *hcp* and/or *top* sites). The full coverage of one type of surface adsorption site by a unique adsorbate is commonly denoted as *adsorbate monolayer* (ML) in literature; herein, these surface coverages are labelled $n\theta_{X^*}$, where n denotes the number of MLs on the surface, and X^* denotes the adsorbed species. In addition to the complete coverage of either H or O, partial and full MLs of H^* atop the θ_{O^*} coverage were also assessed, containing 0.25, 0.50, 0.75 and 1 ML of H^* , which are labelled $(\theta_{O^*} \times \frac{1}{4}\theta_{H^*})$, $(\theta_{O^*} \times \frac{1}{2}\theta_{H^*})$, $(\theta_{O^*} \times \frac{3}{4}\theta_{H^*})$ and $(\theta_{O^*} \times 1\theta_{H^*})$, respectively. Although it has been shown that MXenes are also functionalised by F derived from the etching process, this will not be included in the following discussion.

First, the Gibbs energy of the different adsorbates on all considered coverages was calculated and plotted as a function of the applied potential. The different effect that U_{SHE} has on the adsorption energy of each species (which is discussed in Section 2.7.2) yields the ΔG vs. U_{SHE} plots represented in Figure 6.2 for all studied MXenes. Importantly, these plots are essential for determining the most stable surface coverage at different reaction conditions. Hence, we predict that all MXenes will be readily covered by O-containing surface coverages at pH 0 and $U = 0 V_{SHE}$. Specifically, Ti_2C , Mo_2N , Ti_2N , Hf_3C_2 , Zr_3C_2 , Mo_2TiC_2 , Ta_4C_3 and Ti_4N_3 will be covered by θ_{O^*} at $U = 0 V_{SHE}$, while Mo_2C , Nb_2C , V_2C , V_2N , Ti_3C_2 , Cr_2TiC_2 , Cr_2VC_2 , Nb_4C_3 , V_4C_3 and $Mo_2Ti_2C_3$ will be terminated by $(\theta_{O^*} \times \frac{1}{4}\theta_{H^*})$, and Mo_2ScC_2 by $(\theta_{O^*} \times \frac{1}{2}\theta_{H^*})$. However, our calculations show that the ΔG of O and OH surface coverages will become more endergonic at lower values of U_{SHE} , which in turn favours the adsorption of H, as expected. Hence, at relatively small negative values of U_{SHE} , we predict all MXenes to be fully covered with $1\theta_{H^*}$, which increases to $2\theta_{H^*}$ and $3\theta_{H^*}$ at larger negative values.

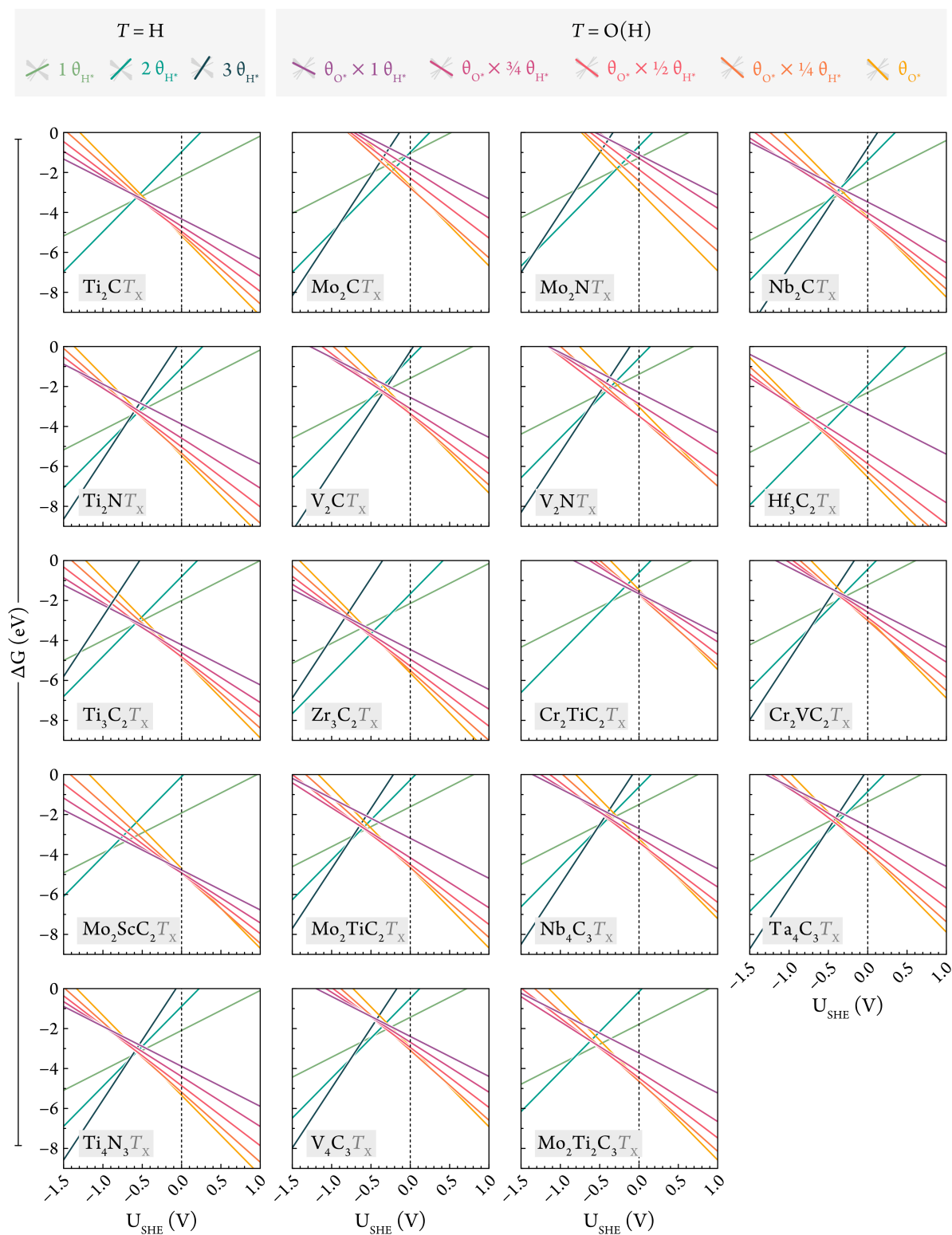


Figure 6.2 Gibbs energy diagrams for full coverages of H, O and OH, or mixed O/OH coverages at pH 0 on both sides of the considered *o*-MXenes. For details about these calculations, see Section 2.7.2.

In order to better visualize the existing coverage at electrochemical conditions of U_{SHE} and pH, the surface Pourbaix diagrams of all considered MXenes are represented in Figure 6.3. These plots are specially relevant

for accurately assessing the surface morphology at reaction conditions; however, to rationally design electrocatalysts that make use of these surface coverages, we need to address how stable functionalised MXenes are and whether the reaction conditions can be tuned to improve their thermodynamic stability.

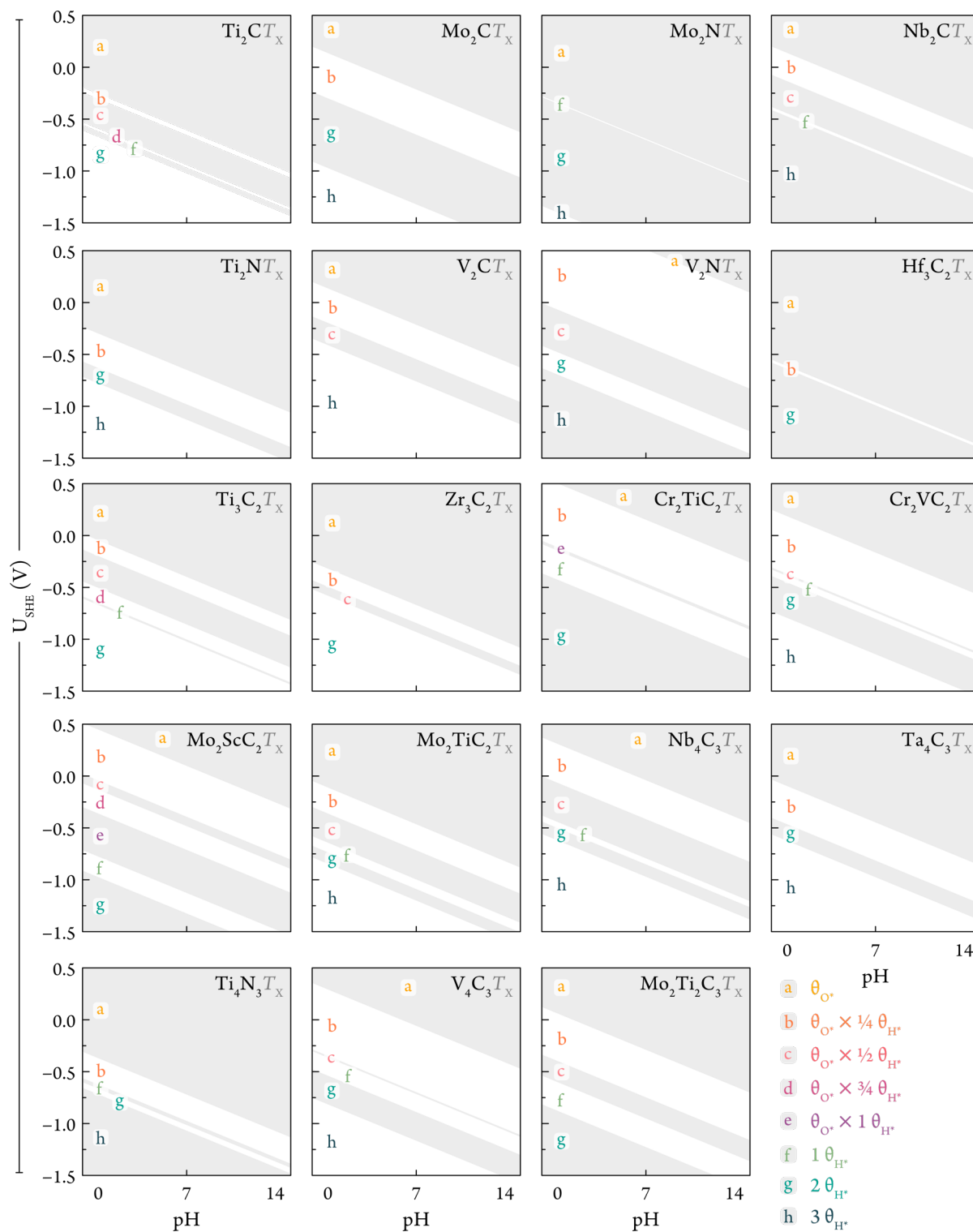


Figure 6.3 Calculated Pourbaix diagrams displaying the predominant surface coverages of *o*-MXenes at different applied potentials and pH values. See Section 2.7.2 for details.

6.4. Relative stability of MXenes

Despite their promising applications demonstrated by first-principle calculations, the widespread development of MXenes in relevant catalytic processes is hindered by their low stability. In particular, MXenes have been shown to be easily oxidised at ambient conditions and require to be stored under an anaerobic atmosphere and at low temperatures.²⁷⁶ Hence, a considerable effort has been put into understanding the effects driving MXene degradation;^{277,278} this has recently led to the synthesis of highly stable MXenes (characterised by a reduced number of defects that act as nucleation sites for degradation), which are more suitable for large-scale applications.²⁷⁹ However, fewer studies have been conducted to assess the relative stabilities of MXenes for electrochemical applications—i.e. how the conditions of pH and applied potential can be optimised to use MXenes as efficient electrocatalysts.

To assess the relative stability of MXene slabs with different stoichiometries, we calculated the surface energies of all synthesized *o*-MXenes as a function of the applied potential, as defined by (6.1) and represented in Figure 6.4, wherein each panel highlights a pair of MXenes with similar element composition but different stoichiometries. This provides a description of the energy required to form each functionalised MXene slab at each potential, and therefore, is a good indicator of their thermodynamic stability. These diagrams depict the stabilising nature of the terminations at larger negative and positive potentials, under which adsorption of H and O MLs, respectively, become more exergonic. Importantly, Figure 6.4 also predicts that increasing the thickness of the MXenes results in more negative surface energies compared to the bulk components of the slabs at all potentials. Therefore, these results suggest that thicker MXenes are theoretically thermodynamically more stable at all ranges of U , in agreement with experiments reported in the literature.²⁷⁸

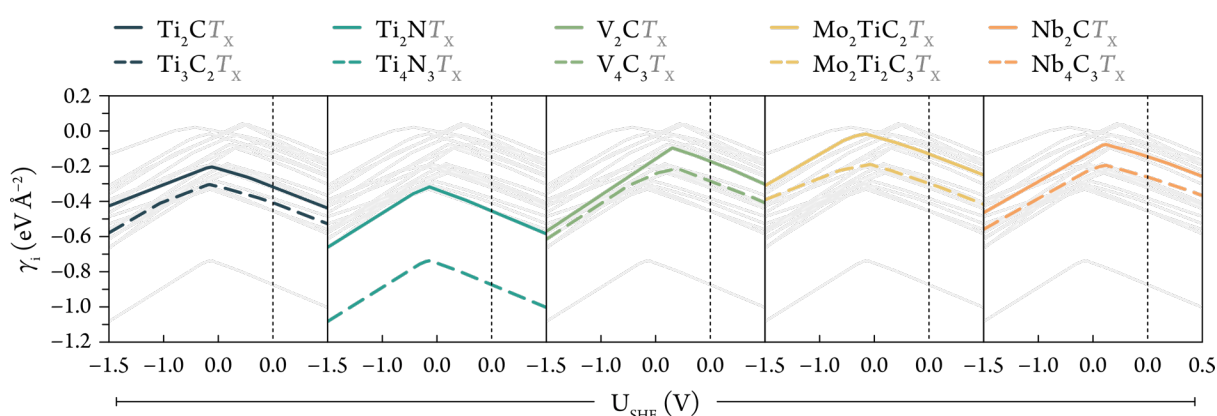


Figure 6.4 Representation of the surface energy of the bare MXenes as a function of the applied potential. Each panel highlights a pair of MXenes with identical atomic composition but different stoichiometry. Slope changes in surface energy are attributed to phase changes in the surface coverage, as depicted in Figure 6.3.

Having elucidated the relative stabilities of MXenes with different stoichiometries and compositions, we then sought to determine the optimal conditions of pH and U for every termination in Figure 6.3. This is of utmost importance for the rational design of functionalised materials for electrocatalysis, where the conditions of pH and U can be tuned not only for obtaining a desired active surface but to limit catalyst degradation. To do so, we determined the thermodynamically stable phases arising the combinations of the species forming each MXene whose properties are available on the Materials Project database,²²⁵ which is represented as a Pourbaix diagram where each phase is delimited by lines. Based on this Pourbaix diagram, we then calculated the energy of each functionalised MXene with respect to the most stable phase at every point of U vs. pH (i.e. the Pourbaix energy, ΔG_{pbx}).²⁷⁵ Nonetheless, as we are interested in uncovering the conditions at which a given coverage is predicted to be more stable, we then plotted the difference in relative stability within each termination ($\Delta\Delta G_{\text{pbx}}$) as a heatmap; this is displayed for all possible surface coverages of Ti_2CT_x in Figure 6.5 A, where lighter and darker regions represent conditions where the system is less and more stable, respectively. Specifically, these diagrams reveal that Ti_2C covered by $1 \theta_{\text{O}^*}$ (Ti_2CO_2) presents a wide range of U and pH at which the stability is most optimal (dark blue area),⁺⁺⁺⁺ where it predominantly degrades to $\text{TiO}_{2(\text{s})}$ (Materials Project ID mp-554278) and $\text{CH}_{4(\text{g})}$; while the former product has been detected through in the form of both anatase and rutile phases upon oxidation of Ti-based MXenes,^{278,280} the latter has been recently observed in gas chromatography experiments on Ti_2C , Ti_3C_2 , Ti_3CN , and Nb_2C .²⁷⁸ Furthermore, this wide region of stability is observed to a lesser extent in the Pourbaix diagrams of the mixed O/OH coverages; in contrast, optimal conditions for stabilising Ti_2C covered by $1 \theta_{\text{H}^*}$ and $2 \theta_{\text{H}^*}$ are delimited to lower pH and negative U values.

Besides the relevant information that the individual Pourbaix diagrams for the terminated surfaces provide, consideration of the surface coverage diagrams presented in Figure 6.3 yields an important conclusion. While we predict that stability of the Ti_2C MXene terminated by H, O or mixed O/OH coverages can be optimised at a certain range of pH and U , the most stable regions may lie outside the range of prevalence of this surface coverage; in other words, attempting to optimise the stability of a given coverage by modifying the electrochemical conditions may be futile, for this coverage may not be present at the target pH and U . Because of this, we envisioned that a more practical representation of the thermodynamic Pourbaix diagrams could be obtained by combining the surface diagrams depicted in Figure 6.3 (as displayed in Figure 6.5 B), wherein the relative stability of each surface coverage is delimited to the range where each coverage predominates. The final thermodynamic and surface coverage Pourbaix diagram for Ti_2CT_x displaying the ranges of predominance of each termination and its relative stability, along with the most stable phases to which the covered MXene ultimately degrades, is represented in Figure 6.5 C. Therefore, for all studied MXenes we must consider i) what surface coverage is present at electrochemical conditions, ii) whether the thermodynamic stability of the covered MXene can be improved by tuning the pH and U without modifying the surface morphology, and iii)

⁺⁺⁺⁺ It is worth highlighting that, as aforementioned, MXenes have been shown to be predominantly unstable in an oxygen atmosphere; the stabilities reported herein are relative to the most stable phase achievable with each considered coverage.

6.5. Electron conductivity of functionalized MXenes

To complement the thorough analysis of the MXene terminations present at electrochemical conditions, we modelled the electron conductivity of the studied MXenes to ascertain whether their base-line metallic nature is altered upon functionalisation with either H, OH or O MLs. The semiconductive nature of Ti_2CO_2 was confirmed by assessing its band diagram via non-collinear calculations with spin-orbit coupling and investigating the relevant points along the 1st BZ of the hexagonal MXene lattice, with the most characteristic k -path identified as Γ -M-K- Γ .

The band diagram of Ti_2CO_2 is represented in Figure 6.7 along with the band diagrams of the bare, H-, and OH-covered Ti_2C . The former was found to contain an indirect band gap of 0.89 eV, which is very close to the values of 0.88 to 0.92 eV reported in literature using hybrid functionals^{250,281} and considerably far from the 0.24 eV obtained with spin-polarised GGA calculations;²⁸¹ this highlights the importance of accounting for spin-orbit coupling effects to accurately represent the electronic nature of MXenes. Based on these results, we subsequently explored the possibility of all other o -MXenes to become semiconductors upon functionalisation with O by calculating their electronic band structure, as depicted in Figure 6.8. Our results indicate that all the other experimentally synthesized o -MXenes are metallic in all instances. This is further demonstrated in the computed band diagrams for the rest of covered MXenes, which are represented in the Appendix.

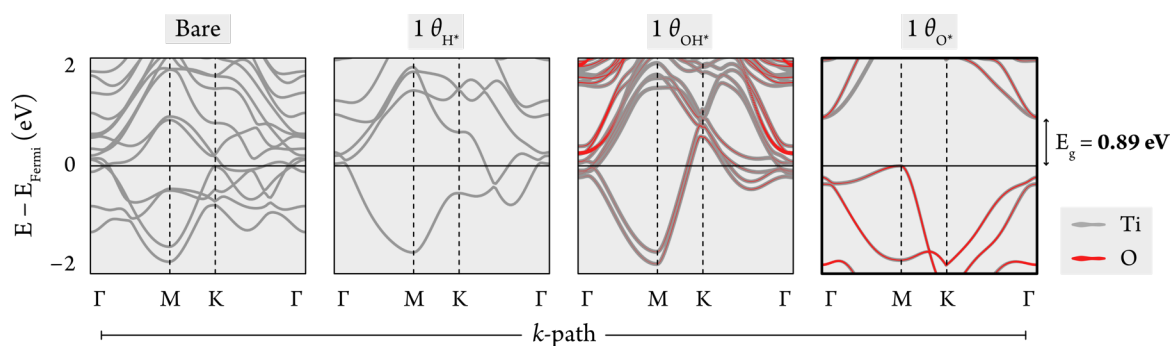


Figure 6.7 Electronic band structures of the bare Ti_2C MXene and with H, OH and O coverages.

Then, we sought to further demonstrate the necessity to consider spin-orbit coupling in our calculations by performing an analysis of the spin texture in the VB and CB of Ti_2CO_2 within a range of -0.2 to 0.2 \AA^{-1} in the X^{-1} and Y^{-1} directions from Γ -point—depicting the direct band gap observed in the rightmost panel of Figure 6.7. The 3-D band diagram of the considered regions in the VB and CB for the assessment of the spin texture is presented in Figure 6.9 A. The assessment of the spin texture along the CB shows that electrons therein primarily contain a spin with a direction normal to the plane, which is represented in Figure 6.9 B. However, a similar analysis reveals that electrons in the VB behave non-collinearly, as demonstrated by the apparent in-plane spin components of the majority of electrons, as depicted in Figure 6.9 C. In view of these results, we

decided to including spin-orbit coupling in subsequent calculations to explore the electrocatalytic applications of MXenes.

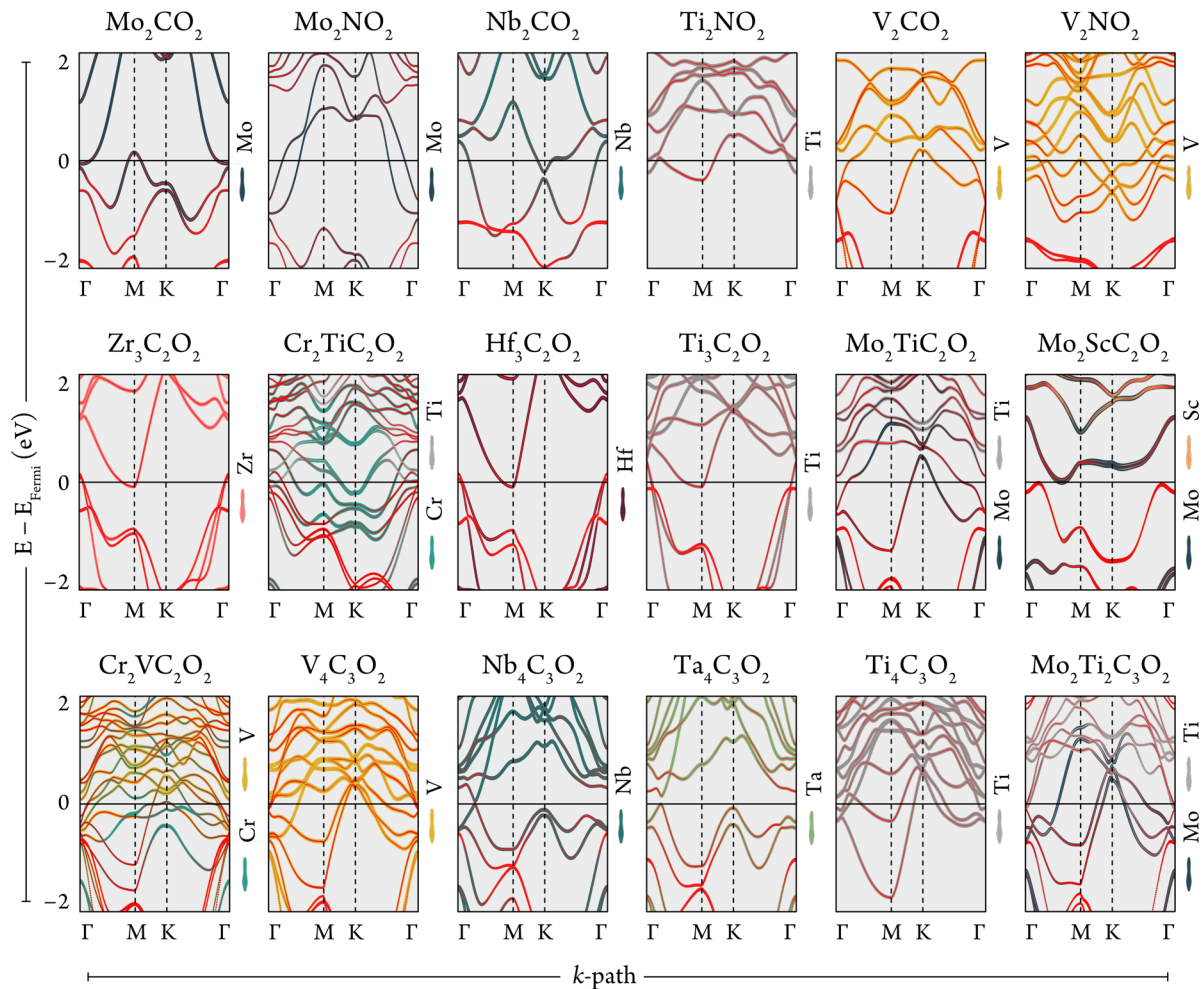


Figure 6.8 Electronic band structures of all studied O-covered MXenes (except for Ti_2CO_2 , which is shown in the rightmost panel of Figure 6.7). The contributions of the $\text{O}(2p)$ orbitals and transition metal d orbitals are depicted in different colours.

So far, we have shown that the coverage of MXenes under electrochemical conditions can be determined by computing surface Pourbaix diagrams. In addition, we have discussed the role that surface coverages have on the thermodynamic stability of MXenes, and how we can tune electrochemical conditions to optimise their stability. Finally, we have briefly reviewed the effects that this coverage has on the electronic properties of MXenes. In the next section, we will investigate the influence of the surface coverage on the activity of the MXenes towards the HER, where the concepts and results discussed hitherto will become relevant.

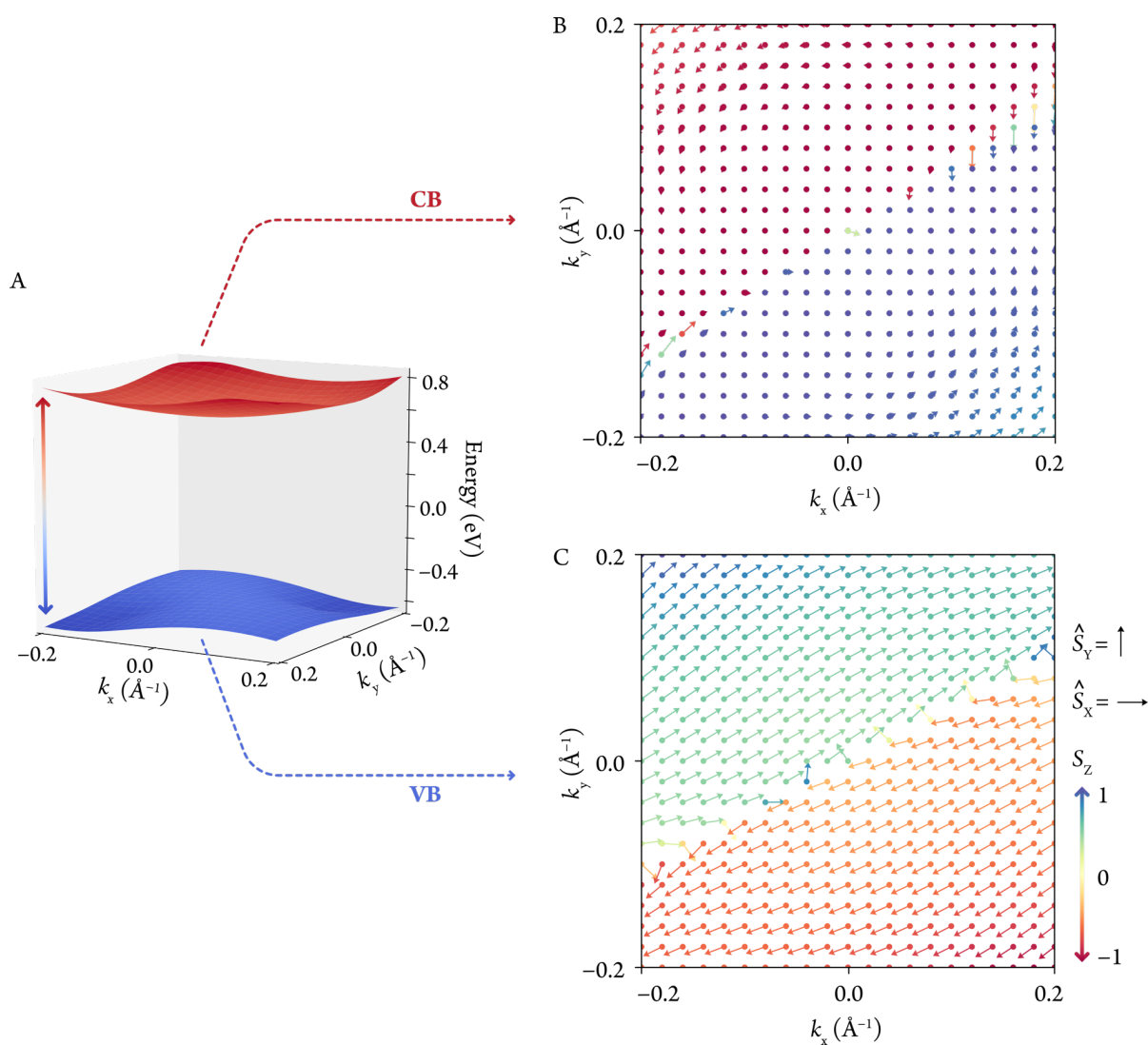


Figure 6.9 In A, 3D band structure of Ti_2CO_2 around Γ -point. In B and C, spin textures of the CB and VB, respectively, showing the \vec{S}_x and \vec{S}_y components of the spin as arrows, while the colour of each arrow denotes the magnitude and direction of the \vec{S}_z out-of-plane component.

6.6. Coverage-dependent hydrogen evolution

To assess the electrocatalytic activity of MXenes, we investigated the ability of these materials to promote the HER under electrochemical conditions. This analysis consisted of a kinetic study of the Volmer, Tafel and Heyrovsky steps, wherein H atoms from the surface coverage (sourced from H^* and OH^* adsorbates) are used to evolve $\text{H}_{2(\text{g})}$. With the kinetic insights derived from the different surface-terminated MXenes, we expect to understand the relationship between surface coverage and HER activity of experimentally synthesized *o*-MXenes.

6.6.1. Kinetic and mechanistic study

The HER activity of MXenes was investigated by choosing a representative structure which ideally displayed potential activity towards this reaction based on theoretical evidence. Accordingly, preliminary theoretical studies show that O atoms in Ti_2CO_2 can act as adsorption sites for H^* with a $\Delta G_{\text{H}^*} \sim 0$ eV at pH 0.²⁴⁴ Therefore, this section focuses on assessing the HER on Ti_2CT_x at different electrochemical conditions, in an attempt to generalise the HER activity of the simulated *o*-MXenes.

The kinetics of the HER occurring atop the θ_{O^*} coverage were investigated by considering two cases. Firstly, the study of the Tafel step involving the coupling of two H atoms from HO^* adsorbates of the $(\theta_{\text{O}^*} \times \frac{1}{2} \theta_{\text{H}^*})$ coverage to produce H_2 . This situation was deemed as the most feasible pathway that could potentially yield H_2 , since the recombination of the H atoms in that coverage leaves the surface covered by θ_{O^*} , which is the prevailing termination at standard conditions. To more accurately approximate the MEP for this reaction, both HO^* adsorbates were positioned on neighbouring *fcc* adsorption sites of a $p(3 \times 3)$ slab, in contrast with the most stable configuration for this coverage wherein HO^* species are preferentially adsorbed equidistantly and as far away from each other as possible. Subsequently, a CI-NEB of the formation of H_2 from the recombination of the H atoms revealed a TS displaying an imaginary frequency of -2016 cm^{-1} with a large activation barrier of 2.13 eV, where the H atoms were separated by a distance of 1.042 Å, as shown in Figure 6.10 A. This large activation barrier may be explained with the initial large distance between the H atoms, as these are separated by 2.877 Å in the considered $(\theta_{\text{O}^*} \times \frac{1}{2} \theta_{\text{H}^*})$ coverage. Furthermore, the charge redistribution within the TS was investigated by computing charge density difference within the plane intersecting the relevant O and H atoms, shown in the rightmost panel of Figure 6.10 A. This analysis revealed that charge from the O–H bond was depleted (as demonstrated by the dark red region between the O and the H atoms) and used to form the H–H bond (as indicated by the blue region between these atoms).

In view of the high activation energy which renders the Tafel step too energy demanding, we next investigated the ability of the H atoms adsorbed onto surface O^* to produce H_2 via a Heyrovsky mechanism. This was simulated using an electrochemical water layer—as discussed in Section 2.6.1—and the Ti_2C MXene functionalised with a θ_{OH^*} coverage onto which the water layer was able to physisorb (at a distance of *ca.* 3 Å) without major structural deformation. This coverage was chosen based on its ability to successfully stabilise the water layer on the OHP; the results from this analysis were deemed representative of those expected for the HER using H^* atoms atop other mixed O/OH coverages. Subsequently, we calculated the interaction of a H-down atom from a H_3O^+ ion and a H from an OH^* adsorbate, yielding H_2 and the surface with a $(\theta_{\text{O}^*} \times [\theta_{\text{H}^*} - 1\text{H}^*])$ coverage. The CI-NEB analysis, represented in the leftmost panel of Figure 6.10 B, reveals a TS with a potential energy activation barrier of only 0.13 eV, that is, 2.18 eV lower than the Tafel mechanism. Moreover, this TS (represented in the middle panel of Figure 6.10 B) is characterised by an imaginary frequency of -1029 cm^{-1} and a H–H distance of 2.607 Å. Similarly to the Tafel mechanism, a charge density difference

analysis reveals pronounced charge depletions (red area) between the involved O and H atoms, pointing at the breaking of the O–H bonds. Due to the lower kinetic barrier of this process compared to the Tafel mechanism, we propose that the HER on Ti_2CO_2 will occur through a Volmer-Heyrovsky pathway, as shown elsewhere.²⁴⁴

Having elucidated the predominant pathway governing the HER activity on Ti_2CO_2 , we then sought to assess the nature of this process on the hydrogen coverages with which Ti_2C is predominantly functionalised at negative potentials. We began by calculating the Volmer step so as to adsorb a H atom on a $1 \theta_{\text{H}^*}$ coverage with 1H^* vacancy, $(1 \theta_{\text{H}^*} - 1 \text{H}^*)$. This system was chosen due to its ability to stabilise an electrochemical water layer physisorbed on the functionalised surface, as shown in Figure 6.10 C. Moreover, this structure provides a good representation of the maximum energy required to adsorb 1H^* on the considered coverage—i.e. if this process is already kinetically fast, we can assume that the adsorption of all present H^* species in $(1 \theta_{\text{H}^*} - 1 \text{H}^*)$ will follow a similar trend, since they are subject to less repulsion from fewer surrounding H adsorbates. As can be observed in the CI-NEB analysis shown in the leftmost panel of Figure 6.10 D, our calculations predict that the Volmer step proceeds through a barrierless process. Similarly to Ti_2CO_2 , the kinetics of the subsequent Tafel and Heyrovsky steps were assessed using the $2 \theta_{\text{H}^*}$ coverage of Ti_2C , which is predominant across a wide range of negative potentials. On the one hand, the analysis of the Tafel step was investigated by approaching two neighbouring H atoms, which diffused atop a Ti and subsequently desorbed forming H_2 . On the other hand, the Heyrovsky step was assessed between the protonated water layer and the $2 \theta_{\text{H}^*}$ coverage, which subsequently produced H_2 gas and a $(2 \theta_{\text{H}^*} - 1 \text{H}^*)$ covered surface. Similarly to the Volmer step, the Tafel and Heyrovsky mechanisms on the studied coverages were found to occur in a barrierless process; this demonstrates that, at the ranges of potential where this coverage is predominant, both the Volmer–Heyrovsky and Volmer–Tafel steps are kinetically fast.

After establishing the kinetic feasibility of the HER on both the bare and O-covered Ti_2C MXenes, we then sought to unravel the source of hydrogen evolution at each applied potential through a thorough mechanistic analysis. In this study, the bare surface was sequentially functionalised with H^* and O^* species leading to the coverages discussed in previous sections. In addition, we considered the ability of H-containing coverages to undergo the aforementioned barrierless Tafel and Heyrovsky steps and produce H_2 , which necessarily compete with the subsequent hydrogenation of the surface. The energy diagrams of these processes at pH 0 and $U = 0 \text{V}_{\text{SHE}}$ and $-0.60 \text{V}_{\text{SHE}}$ are depicted in Figure 6.11. In these, we present two distinct pathways: one where Ti_2C is functionalised with $1 \theta_{\text{H}^*}$ or $2 \theta_{\text{H}^*}$, and another where it is functionalised with $1 \theta_{\text{O}^*}$, which is subsequently terminated with H to form mixed O/OH and OH coverages. For the former, both Heyrovsky and Tafel steps are included, while for the latter, only Heyrovsky steps are deemed kinetically feasible. At standard conditions, we predict the lowest energy step to correspond to the surface with the $1 \theta_{\text{O}^*}$ coverage, as depicted in the surface Pourbaix diagrams. As we increase the negative potential, we also increase the endergonicity of the $1 \theta_{\text{O}^*}$

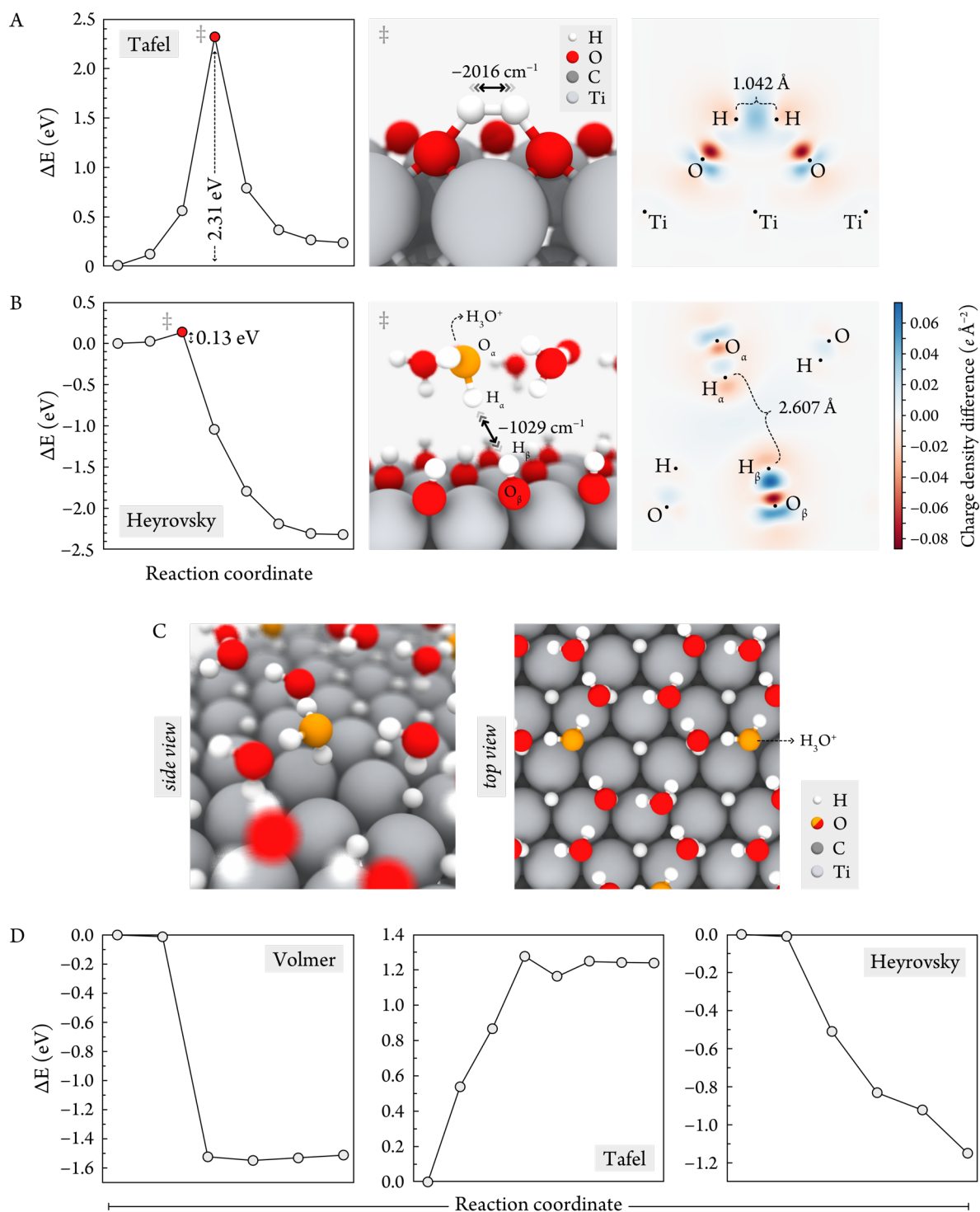


Figure 6.10 A and B) On the left, energies of the images along the CI-NEB of the Tafel and Heyrovsky mechanisms on Ti_2C for the formation of H_2 from the coverages $(\theta_{\text{O}^*} \times \frac{1}{2} \theta_{\text{H}^*})$ and $1 \theta_{\text{OH}^*}$, respectively. Images corresponding to the TS (red points) are represented in the middle panels, showing the value and direction of the characteristic imaginary frequencies. Charge density difference analyses across the interaction plane are represented in the rightmost panels, where the atom centres are represented as dots. C) Initial structure used for calculating the Volmer step onto the $(1 \theta_{\text{H}^*} - 1 \text{H}^*)$ coverage, containing a water layer with a hydronium ion whose O atom is represented in orange for clarity. D) Energies of the images along the CI-NEB calculations for the Volmer, Tafel and Heyrovsky steps on the surface coverages $(1 \theta_{\text{H}^*} - 1 \text{H}^*)$, $2 \theta_{\text{H}^*}$ and $2 \theta_{\text{H}^*}$, respectively.

coverage compared to the H and mixed O/OH coverages, which ultimately facilitates the generation of a ($\theta_{\text{O}^*} \times \frac{1}{4} \theta_{\text{H}^*}$) coverage at *ca.* $-0.20 \text{ V}_{\text{SHE}}$. However, we predict that this coverage will spontaneously yield H_2 via a Heyrovsky mechanism. A similar effect is appreciated at larger negative potentials, where generation of subsequent O-containing coverages competes with H_2 formation.

As observed in Figure 6.3, which shows the most stable coverages at each applied potential for every MXene, the application of a potential of *ca.* $-0.5 \text{ V}_{\text{SHE}}$ favours the adsorption of a stable coverage of $1 \theta_{\text{H}^*}$; at this potential, we predict this coverage to be HER inactive due to the high energy required to generate the resulting bare surface after H_2 desorption. However, at more negative potentials where generation of the $2 \theta_{\text{H}^*}$ coverage becomes exergonic ($-0.60 \text{ V}_{\text{SHE}}$), we predict that H_2 formation will become energetically feasible through a Heyrovsky mechanism with the second H ML.

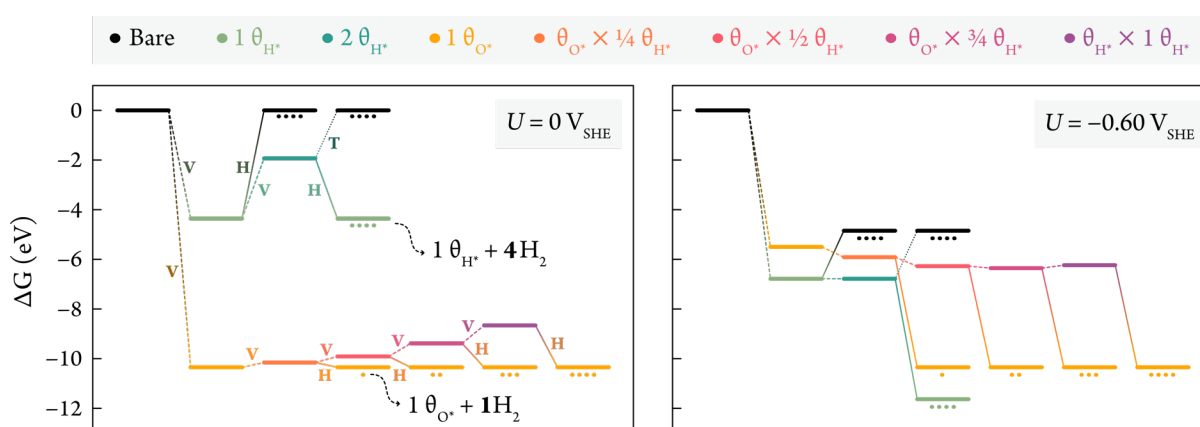


Figure 6.11 Gibbs energy diagrams for the formation of the considered coverages and generation of H_2 on $p(2 \times 2)\text{-Ti}_2\text{C}$ at $0.00 \text{ V}_{\text{SHE}}$ and $-0.60 \text{ V}_{\text{SHE}}$. Each dot under the terminal energy levels denotes one molecule of H_2 generated. Volmer, Tafel and Heyrovsky steps are represented as dashed, dotted and solid lines between reaction intermediates, and are labelled as V, T and H in the leftmost plot, respectively. Energy levels are colour-coded based on the present surface coverage.

Hence, this analysis sheds light on the ability of the surface coverages to undergo HER at different applied potentials. In particular, we predict that HER on Ti_2C primarily occurs via a Volmer–Heyrovsky mechanism involving H atoms on a O-covered or bare surface, and that this process competes with the generation of subsequent MLs of H. Accordingly, higher negative potentials increase the exergonicity of H_2 generation compared to the stable formation of surface coverages. Therefore, we predict that the HER on Ti_2C is not limited by the kinetics of the reaction, and protons in the IHP effectively act as source of H for the Heyrovsky mechanism which readily occurs at low negative applied potentials.

6.6.2. Basal plane vs. edge reactivity

It has been previously reported that HER active sites on 2-D metal dichalcogenides are the edge and basal plane vacancies,²⁸² which is in contrast with studies on MXenes which propose that the HER occurs on the basal plane. To confirm this, we investigated the adsorption energy of H on a $n = 2$ Ti carbide MXene (Ti_3C_2) strip of width $\sim 7 \text{ \AA}$, which displayed a larger number of potentially active edge sites compared to its $n = 1$ counterpart. The top and isometric views of the MXene strip are displayed in Figure 6.12 A, along with all adsorption sites considered. Of these, 8 sites were identified onto which H could be stabilized. These adsorption sites along with their calculated ΔG_{H} are depicted in Figure 6.12 B. In addition, we also investigated the same sites for O adsorption, and these results are presented in Figure 6.12 C.

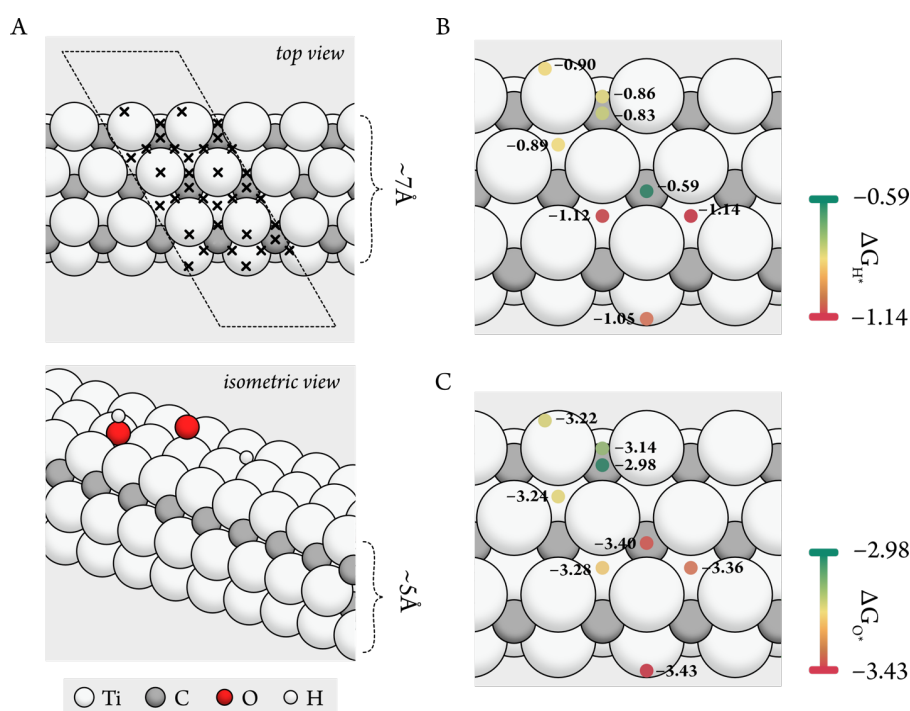


Figure 6.12 A) On the top, top view of the Ti_3C_2 stripe used for edge coverage and reactivity analysis, where all considered adsorption sites on the slab are depicted as crosses. On the bottom, isometric view of the Ti_3C_2 strip showing arbitrary H, OH and O adsorbates for illustration purposes. B and C) Top view of the slab depicting as dots the sites where H^* and O^* adsorbates, respectively, are stabilised; these are coloured based on their Gibbs binding energy—more endergonic adsorptions are depicted in green, while more exergonic adsorptions are represented in red. ΔG_{H} and ΔG_{O} values are given in bold beside each adsorption site.

This analysis reveals that the sites onto which H adsorption is most endergonic (and, therefore, are more active towards HER at negative potentials)^{****} correspond to a HCP site in the basal plane, with a ΔG_{H} of -0.59 eV .

^{****} As a preliminary study and subject to further investigations, we assume that adsorbate-adsorbate interactions does not substantially influence the adsorbate binding energy.

This is 0.31 eV and 0.46 eV higher than the binding of H atop edge Ti sites on the first and second metal layers, respectively. A similar result was obtained with the adsorption of O, where the most endergonic adsorption was located on a basal HCP site. Hence, we predict that the coverage-dependent reactivity of Ti_3C_2 MXene predominantly occurs on the basal plane which presents a lower affinity for the species in the electrolyte, and therefore, these are more prone to reaction and subsequent desorption.

6.6.3. Coverage-driven HER at low overpotentials

The theoretical HER activity of electrocatalysts is commonly represented as a volcano plot showing the theoretical overpotential as a function of the Gibbs energy of adsorption of H. This provides a quantitative indicator of the potential of a set of electrocatalysts, and has been previously applied for the theoretical investigation of MXenes.^{241,244} This representation, however, falls short of being a useful tool for electrocatalytic processes, as usually we are not only interested in obtaining a good HER catalyst at low overpotentials, but also in determining whether the considered electrocatalyst will be HER active at a given pH and U .

For this purpose, we sought to relate the observed surface Pourbaix coverages with the apparent HER activity. To serve as proof of concept, this assessment was carried out for MXenes which are terminated by O and mixed O/OH coverages in their resting state at pH 0 and $U = 0 \text{ V}_{\text{SHE}}$, and whose subsequent coverage achievable by increasing the negative potential also displays both O^* and HO^* species. As demonstrated by our mechanistic analysis depicted in Figure 6.11, HER is triggered upon change of the coverage phase within the same coverage regime. For instance, in the case that the θ_{O^*} and the $(\theta_{\text{O}^*} \times \frac{1}{4} \theta_{\text{H}^*})$ coverages are at equilibrium at standard conditions, the energy required to chemisorb a H^* atom to form the latter coverage—which subsequently undergoes a Heyrovsky mechanism to produce H_2 —is thermoneutral. Therefore, the threshold for H_2 generation is determined by the point of intersect between $(\theta_{\text{O}^*} \times n \theta_{\text{H}^*})$ and $(\theta_{\text{O}^*} \times m \theta_{\text{H}^*})$ ($n < m = 0, \frac{1}{4}, \frac{1}{2}$ or $\frac{3}{4}$) at each potential. Hence, a more accurate HER descriptor can be obtained by assessing the difference in the Gibbs energy between the first and the second-most stable coverage at $U = 0 \text{ V}_{\text{SHE}}$, for all ranges of potential ($\Delta\Delta G_{\text{ads}}$). These diagrams are represented for a set of calculated *o*-MXenes in Figure 6.13.

In these diagrams, the HER is predicted to be energetically feasible at conditions of pH and U above the threshold line (depicted in gold), with values of $\Delta\Delta G_{\text{ads}} < 0.2 \text{ eV}$. Below the threshold line, H_2 generation is predicted to become exergonic, and HER will occur spontaneously. Therefore, MXenes where the threshold line begins close to the origin are considered to be HER active at standard conditions in the conventional interpretation of the HER descriptor. Hence, at the theoretical level considered herein, we predict V_2N and Nb_4C_3 to be very active towards the HER at low overpotentials. Conversely, we expect MXenes such as Ti_2N , Zr_3C_2 , or Cr_2VC_2 to demand larger overpotentials. Although it has been shown that some Ti-, Mo- and V-based MXenes are active towards the HER at low overpotentials in acidic conditions,²⁸³ further experimental studies need to be carried out to rationalise our theoretical observations. Importantly, the diagrams shown in Figure 6.13 are specially relevant for the use of MXenes in electrocatalysis, as it offers a quantitative interpretation of

the HER activity at different electrochemical conditions by assessing the Gibbs energy of adsorption of the predominant surface coverages. For instance, a similar interpretation holds for the HER activity arising from H atoms in the H-coverage regime at reducing potentials, where we predict H₂ to be mainly evolved via a Volmer-Heyrovsky mechanism involving the electrolyte and the last H (most endergonically) adsorbed on the 2 θ_{H} coverage.

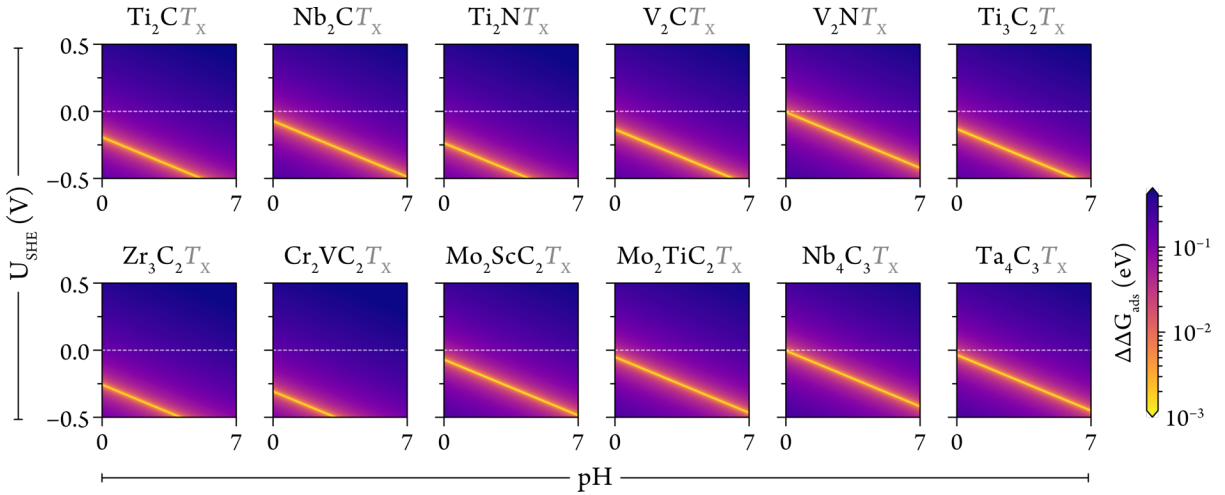


Figure 6.13 Diagrams displaying the adsorption energy differences between the coverage present at $U = 0$ V_{SHE} and pH 0 and the next coverage achievable by lowering the potential at pH 0, for MXenes in which either termination is composed by $(\theta_{\text{O}} \times n \theta_{\text{H}})$ ($n = 0, 1/4, 1/2, 3/4, 1$).

6.7. Conclusions

The effect of the surface coverage of 2-D materials for electrocatalytic applications is often neglected or underestimated. In an effort to better understand how the coverage can be accurately assessed and understood, we carried out a thorough investigation of all 2-D *o*-MXenes synthesized to date. This analysis of the coverage considered species present in aqueous electrolytes, *i.e.* H, O and OH.

Firstly, surface Pourbaix diagrams showing the predominant coverage phases as a function of pH and U_{SHE} were constructed. These diagrams highlighted the ability of MXenes to be functionalised with various terminations at different applied potentials; whilst application of positive potentials favoured the adsorption of O, negative potentials promoted H-covered surfaces. Our calculations also show that the presence of adsorbates can increase the stability of MXenes, which is also directly proportional to their slab thickness. The relative stabilities of each surface coverage was investigated by constructing a thermodynamic Pourbaix diagram, which depicts the optimal conditions of pH and U_{SHE} at which every coverage can be achieved, which also denotes the main degradation products. Subsequently, the influence of the surface coverage on the electronic properties of the calculated *o*-MXenes was investigated by computing their electronic band diagrams including spin-orbit

coupling. This analysis revealed that metallic Ti_2C behaves as a semiconductor upon functionalisation with O, whereas all other studied covered MXenes display metallic properties.

After unravelling the nature of the surface coverage of all synthesized *o*-MXenes and its effect on the electron conductivity, we then sought to rationalise the influence of the various coverages on the activity of the surface towards the HER. Firstly, the kinetics of the Volmer, Tafel and Heyrovsky steps were investigated on the two identified coverage regimes, i.e. on the surface covered with O and mixed O/OH coverages, and on the surface covered by 1 or 2 MLs of H. This analysis revealed that the high energetics of the Tafel step in this regime renders this process unfeasible; in contrast, our simulations show that H atoms atop O coverages are capable of undergoing Heyrovsky steps with a low kinetic barrier. A similar investigation on the H-covered MXene revealed that surface H atoms contained therein undergo Volmer, Tafel and Heyrovsky steps without an activation barrier. After determining the fast kinetics of this reaction, we then performed a mechanistic study that revealed the source of HER at each point of applied potential, which is generally governed by Heyrovsky steps from H atoms on the surface coverage. In addition, we determined that activity towards the HER stems from adsorption sites on the basal plane. Finally, this insight was used for the construction of more accurate representations for the coverage-dependent HER activity of MXenes at different conditions of pH and U_{SHE} , based on the difference in Gibbs energies between the first and second most stable adsorbates at pH 0.

In conclusion, this theoretical study of the surface coverage of state-of-the-art 2-D materials has demonstrated that understanding the resting state and its effects on reactivity is a key process for an accurate description of the nature and reactivity of the catalyst. In addition, this study showcases the importance of accurately assessing the HER either to design efficient catalysts for this reaction, or to suppress its activity—so as to increase the selectivity of the catalyst towards a desired reduction product—by precisely tuning the electrochemical conditions. Hence, we envision that an accurate assessment of the surface coverage can enable a novel route for the rational design of electrocatalysts for a wide range of reactions.

In the following chapter, this knowledge will be applied for the design of MXenes for the sustainable production of chemical feedstocks via a mechanism mediated by H surface coverages at low negative potentials.

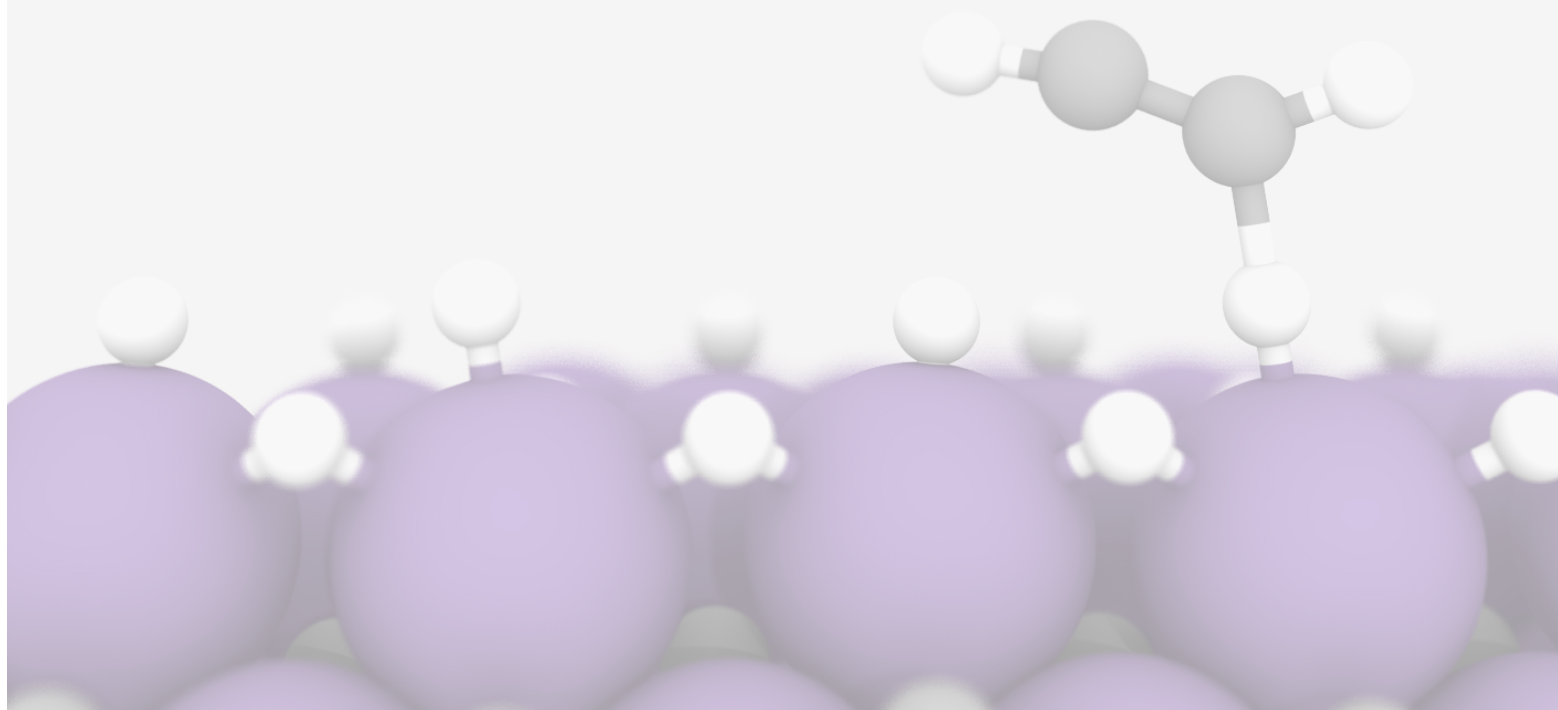
“ Yet if there were no hazards there would be no achievement,
no sense of adventure. – **Arthur C. Clarke**

Rendezvous with Rama, 1973

CHAPTER

7

2-D MXenes for Electrochemical Hydrogenations



7.1. Introduction

Surface terminations on 2-D MXenes have been widely recognised as the origin of the excellent activity of these materials for the thermal catalysis of a wide range of reactions. For instance, recent studies have shown that O* species present on the basal plane of MXenes are the main active sites for the dehydrogenation of hydrocarbons, such as ethylbenzene²⁸⁴ or propane.²⁸⁵ Similarly, O* terminations have been predicted to promote C–H activation in methane²³⁴ (electrochemically) and in light alkanes (thermally),²⁸⁵ where the activity can be described by the coverage affinity towards H, and have been shown to facilitate the activation of double bonds in light alkenes.²⁸⁶ Nonetheless, the vast majority of the works assessing the coverage-mediated catalytic activity of MXenes focus on the resting state at standard conditions, where the presence of terminal O* species is ubiquitous. As we have seen in the previous chapter, this scenario is not representative of the surface morphology at reducing potentials, wherein θ_{H^*} coverages are predominant. Furthermore, while the existence of θ_{H^*} coverages has been extensively demonstrated theoretically,²³⁵ the nature and potential catalytic applications of these phases have been seldom explored.

The insight acquired from the thorough coverage analysis of the MXenes, along with the knowledge that H* species forming the θ_{H^*} coverages at reducing potentials are electron-rich and potentially behave as hydrides,²³⁵ prompted us to study the applications of MXenes as potential ECH catalysts.²⁸⁷ Hence, the next sections will

be dedicated to assessing the suitability of the MXenes studied in the previous chapter for this purpose; firstly, by investigating a case study involving the hydrogenation of an organic substrate—which was subsequently supported by experiments from our collaborators—; secondly, by determining the catalytic activity of a wide range of MXenes for the coverage-dependent hydrogenation of acetylene. This study will be aimed at rationally designing the morphology and stability of the surface coverage of MXenes, in a novel approach which will also take into account the thorough assessment of the HER activity to limit the effect of this competing reaction and improve the selectivity and yield towards the desired hydrogenated products.

7.1.1. Rational design of electrochemical hydrogenation catalysts

We envision that a suitable MXene catalyst for coverage-mediated ECH reactions should possess 3 key properties: firstly, it must display a H-coverage regime at low reducing potentials; secondly, this coverage must be stable at the operando conditions relative to the all conditions of pH and U ; finally, it must be readily available commercially. In the quest to obtain MXene structures which meet these criteria, we assessed the surface and stability Pourbaix diagrams of all currently synthesized *o*-MXenes, as discussed in Sections 6.3 and 6.4. From the diagrams shown in Figure 6.3 and Figure 6.6, one MXene in particular stands out from the rest, namely Mo_2CT_x . This MXene displays a 2 θ_{H^+} coverage at a potential range of *ca.* $-0.25 \text{ V}_{\text{SHE}}$ to $-0.80 \text{ V}_{\text{SHE}}$, whose relative thermodynamic stability is optimised at all values of U and pH at which this coverage predominates. Interestingly, a theoretical study on the thermal hydrogenation of ethylene (which was published during preparation of this thesis) reported a δ -MoC(001) surface with a similar surface morphology as Mo_2CT_x as a good candidate for hydrogenations. Therein, the authors also proposed that the surface H coverage plays a crucial role.²⁸⁸ Other MXenes that are potentially active for the coverage-promoted ECH based on the overpotential needed to create a predominant H coverage and its subsequent stability include all studied V-based MXenes, Mo_2NT_x , and $\text{Ti}_3\text{C}_2\text{T}_x$. Despite its lower relative stability and slightly harsher reducing conditions needed to develop a H coverage compared to Mo_2CT_x , $\text{Ti}_3\text{C}_2\text{T}_x$ stands out for being by far the most studied and commercially available of all the synthesized MXenes. Therefore, we dedicated the bulk of the theoretical studies discussed herein on exploring the ECH activity of H-covered $\text{Ti}_3\text{C}_2\text{T}_x$, Mo_2CT_x and V_2CT_x .

7.2. Computational methods

All calculations reported in this chapter have been performed at the theoretical level described in Section 6.2. Structures of the H-terminated MXenes have been calculated by considering the functionalization of all the available adsorption sites on both sides of the slab, as described in Section 6.3. Similarly to the study of the surface coverages, Gibbs energy corrections were computed using the Thermochemistry Module implemented in the ASE package²²⁶ at pH = 0 and the temperature and pressure of 298 K and 1 atm. For the reaction steps involving a H^+/e^- pair, the CHE model was used (see Section 2.7.1 for details).

The hydrogenation mechanism on the different MXenes was modelled on a $p(2\times 2)$ and $p(3\times 3)$ slabs for the reaction with acetylene and pentynol, respectively. These slabs were created from the $p(1\times 1)$ structure used in the coverage analysis. Structures were optimised using the parameters discussed in Section 6.2.

The effect of the solvent was taken into account through single-point calculations using an implicit solvent model with $\epsilon_r = 80$, as implemented in the VASPsol package.²⁸⁹ The calculated energies in solution include electrostatic, cavitation, and dispersion contributions.

7.3. Electrochemical hydrogenation of unsaturated alcohols

As we already reviewed in Section 1.3.4, when coupled to renewable energy sources, ECH holds great promise as a sustainable alternative for the production of key commodity chemicals, wherein the source of H is the aqueous electrolyte rather than relying on high pressures of H_2 gas. However, most studies on the ECH of unsaturated organic molecules have focused on assessing catalyst materials that have been previously found to be active for thermal hydrogenations such as Pd, mainly by employing on-site-generated H_2 .²⁹⁰ Interestingly, Ti-based MXenes have recently been theoretically predicted to be potentially active towards the thermal hydrogenation of furfural to furfuryl alcohol in the presence of H_2 , reaching activities of up to $145 \text{ mmol g}^{-1} \text{ h}^{-1}$ in a process mediated by H^* and HO^* surface adsorbates.²⁹¹ Nonetheless, to the best of our knowledge MXenes have yet to be explored for the ECH of organic molecules at low reducing potentials.

The ability of MXenes to carry out the ECH was assessed using $Ti_3C_2T_x$ ($T_x = 2 \theta_{H^*}$) and 4-pentyn-1-ol (simply pentynol hereafter) as the model surface and substrate, respectively. This alkyne was chosen based on its high availability, and its liquid nature and miscibility with water, which facilitates the determination of the products yield by NMR. We propose that this ECH reaction involves the interaction of the surface with a $2 \theta_{H^*}$ coverage (predominant on this MXene at potentials lower than *ca.* -0.6 V_{SHE}), wherein the H atoms cover all *fcc* and *hcp* sites and display atomic charges of $-0.41 e$ and $-0.36 e$, respectively, as determined by Bader charge analysis.²⁹² Thus, we envision that the H's adsorbed more endergonically atop *hcp* sites are able to interact with the substrate molecules within the OHP, wherein the alkyne can be hydrogenated to the alkene (4-penten-1-ol, pentenol hereafter) or all the way to the alkane (pentanol hereafter) in a Heyrovsky-type mechanism, as schematised in Figure 7.1. Thus, we carried out a mechanistic study of the hydrogenation of

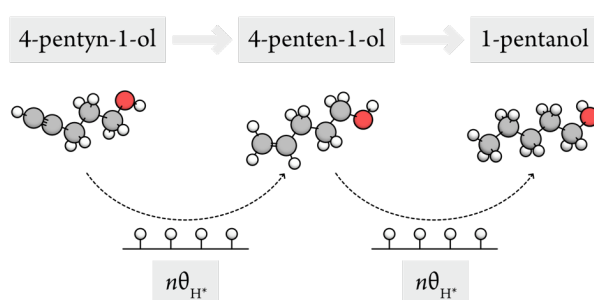


Figure 7.1 Schematic representation of the proposed Heyrovsky-type mechanism for the hydrogenation of 4-pentyn-1-ol to 4-penten-1-ol and 1-pentanol on a H-covered MXene surface.

pentynol to pentenol, as well as the over-hydrogenation of pentenol to pentanol, on $\text{Ti}_3\text{C}_2\text{T}_x$ with a $2\theta_{\text{H}}$ coverage ($\text{Ti}_3\text{C}_2\text{H}_4$, consisting of 2 ML of H atoms covering all *fcc* and *hcp* sites).

First, the lowest energy configuration of pentynol on $\text{Ti}_3\text{C}_2\text{H}_4$ was found to lay *ca.* 4.5 Å away from the surface in a flat configuration (A^* , as represented in Figure 7.2 A), with a relative Gibbs energy of -0.16 eV. Interestingly, hydrogenation of C_1 and C_2 atoms by interacting with 2 H atoms from surface *hcp* sites was found to occur in an asynchronous mechanism, wherein the first H was transferred to C_1 with a barrier of 0.68 eV through a TS with an imaginary frequency of 722 cm^{-1} ($\text{AB}^{*\dagger}$ in Figure 7.2 A). This process resulted in the

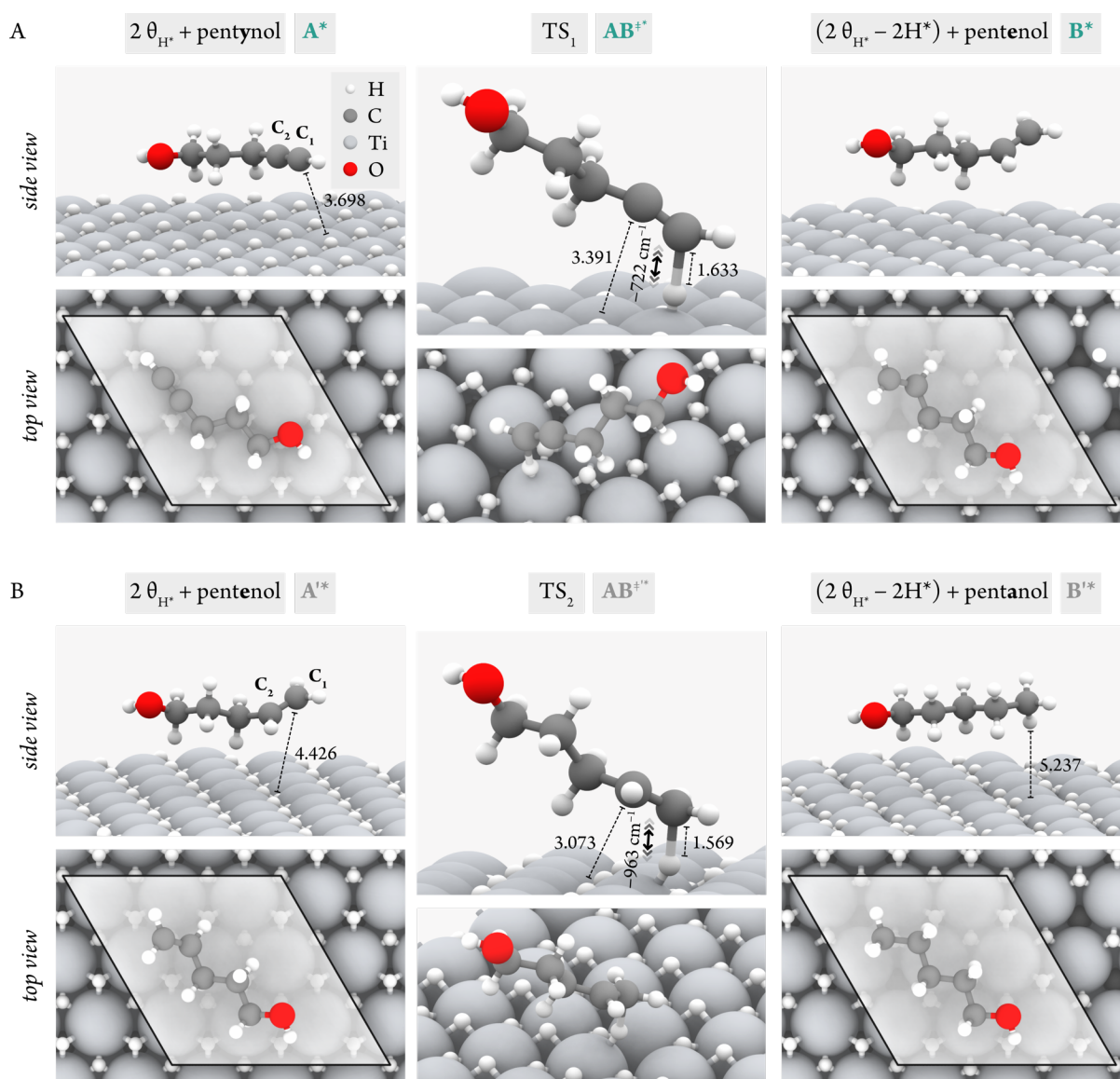


Figure 7.2 A) Side and top views of the reactant (left panels), TS (middle panels) and product (right panels) structures in the mechanism for the ECH of pentynol to pentenol on $\text{Ti}_3\text{C}_2\text{H}_4$. B) Side and top views of the reactant (left panels), TS (middle panels) and product (right panels) structures in the mechanism for the ECH of pentenol to pentanol on $\text{Ti}_3\text{C}_2\text{H}_4$. The direction of the characteristic vibrational modes in the TS structures are represented with bidirectional arrows, along with the magnitude of the characteristic frequency. Relevant bond lengths are shown in Å.

second H being transferred to C₂ spontaneously yielding pentenol and the surface coverage without 2 H atoms (B* in Figure 7.2 A) in an overall highly exergonic process. Finally, the desorption of pentenol into the solvent was found to require a small energy of 0.14 eV. In addition to the proposed pathway, the alternative mechanism wherein C₂ was initially hydrogenated instead of C₁ was also calculated, although the transition state found for this process (shown in Figure 7.3) displayed an activation barrier *ca.* 0.6 eV higher and therefore was deemed very unlikely.

Having elucidated the feasibility of the proposed pathway for the hydrogenation of pentynol to pentanol, we then assessed the ability of the 2 θ_{H^+} coverage of Ti₃C₂T_x for the over-hydrogenation of pentenol to pentanol. Similarly to pentynol, pentenol was found to be physisorbed at a distance of *ca.* 4.4 Å from the 2 θ_{H^+} coverage (A** in Figure 7.2 B) with a Gibbs adsorption energy of -0.22 eV. The hydrogenation of pentenol to pentanol was found to be highly exergonic and to involve a first order saddle point (AB^{‡*} in Figure 7.2 B) with an imaginary frequency of -963 cm⁻¹; this is characterised by a first H transfer from an *hcp* site to C₁ with an energy barrier of 0.59 eV, followed by a barrierless transfer of a second *hcp* H to C₂. Finally, the desorption of pentanol (B** in Figure 7.2 B) into the gas phase was predicted to require 0.13 eV.

The energetics of both proposed mechanisms (Figure 7.4) reveals that Ti₃C₂T_x covered by 2 θ_{H^+} is an excellent electrocatalyst for the ECH of pentynol to both pentenol and pentanol. Therefore, we predict that this reaction will be facilitated at the potential range where this coverage is predominant (below -0.59 V_{SHE}) and stable (at neutral pH) as seen in Figure 6.3 and Figure 6.6. Furthermore, we envision that the Faradaic efficiency of this reaction can be optimised at potentials closer to the crossing point where the 2 θ_{H^+} coverage becomes more

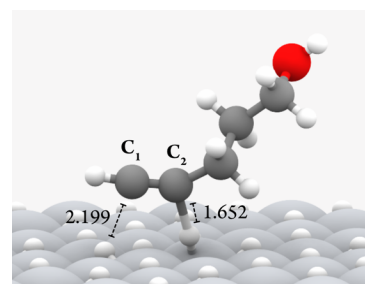


Figure 7.3 TS structure of the hydrogenation of pentynol to pentenol through an alternative pathway wherein C₂ is firstly hydrogenated. Relevant bond lengths are shown in Å.

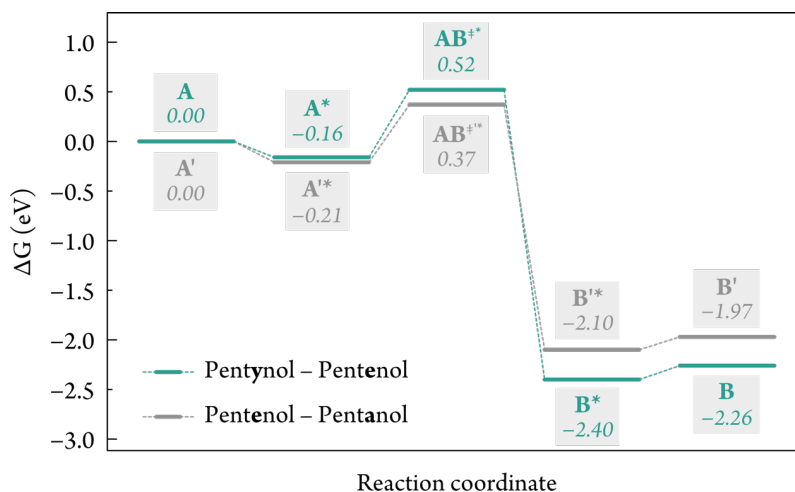


Figure 7.4 Gibbs energy diagrams for the ECH of pentynol to pentenol (blue path) and pentenol to pentanol (grey path) on the Ti₃C₂ MXene with a coverage of 2 θ_{H^+} . A and A' correspond to pentynol and pentenol in the gas phase and the Ti₃C₂ surface covered with 2 θ_{H^+} , respectively; B and B' correspond to pentenol and pentanol in the gas phase and the Ti₃C₂ surface covered with (2 θ_{H^+} - 2 H*). The intermediates A*, B*, A** and B**, and TS structures AB^{‡*} and AB^{‡*} are represented in Figure 7.2.

stable than the $1 \theta_{\text{H}^+}$ coverage (i.e. neighbouring $-0.59 \text{ V}_{\text{SHE}}$), where HER activity arising from a Heyrovsky mechanism between the electrochemical water layer and the *hcp* H atoms on the $2 \theta_{\text{H}^+}$ coverage is minimised.

The ability of $\text{Ti}_3\text{C}_2\text{T}_x$ to hydrogenate pentynol at low reducing potentials was demonstrated experimentally by our collaborators in the group of Prof. Paula Colavita at Trinity College Dublin. This was achieved by drop casting a carbon cloth coated with an ink containing a 0.3 mg mL^{-1} solution of the MXene into electrolytes at pH 1, 4 and 7. After saturating the electrolyte with N_2 and performing chronoamperometric scans to clean the surface of impurities, 10 mM of pentynol was added into the cathodic side of the cell, followed by a further chronoamperometric scan of 4 h. The aliquot was subsequently investigated by NMR, wherein any peaks corresponding to triple, double and single C–C bonds were identified allowing for quantification of the concentrations of their respective substrates. This analysis showed that $\text{Ti}_3\text{C}_2\text{T}_x$ could effectively promote the ECH of pentynol at pH 7, as shown in Figure 7.5.

Interestingly, experiments also revealed that, while both pentynol conversion to pentenol and Faradaic efficiencies were negligible at potentials above $-0.55 \text{ V}_{\text{RHE}}$ ($-0.96 \text{ V}_{\text{SHE}}$ at pH 7), pentynol to pentenol conversion rates peaked at ca. $-0.65 \text{ V}_{\text{RHE}}$ ($-1.06 \text{ V}_{\text{SHE}}$ at pH 7) and remained constant at more reducing potentials. Most importantly, we note that this potential threshold is very similar to the observed upper limit for the predominance of H coverage, which hints that this reaction is, indeed, governed by surface H atoms. Furthermore, experiments show that the Faradaic efficiency towards pentenol goes from ca. 10 % at $-0.65 \text{ V}_{\text{RHE}}$ to 32 % at $-0.75 \text{ V}_{\text{RHE}}$, and subsequently decreases

to lower values at more negative potentials (being HER the main reaction occurring at the electrode). Based on our simulations, we believe that this behaviour can be attributed to the further stabilisation of the H coverage regime with respect to the O coverage regime at potentials around $-0.75 \text{ V}_{\text{RHE}}$, which may favour the coverage-led pentynol hydrogenation. On the contrary, we envision HER to compete more effectively with the ECH of pentynol at more reducing potentials, leading to a decrease in the Faradaic efficiency. It must be noted that current calculations predict both the hydrogenation and over-hydrogenation processes to be energetically feasible; however, experimental results show the absence of the over-hydrogenated pentanol species in the products, hinting at the ability of $\text{Ti}_3\text{C}_2\text{T}_x$ to selectively hydrogenate pentynol to pentenol. This may be due to the higher solubility in water of pentynol (miscible in water) compared to pentenol (57 g L^{-1}) which may favour

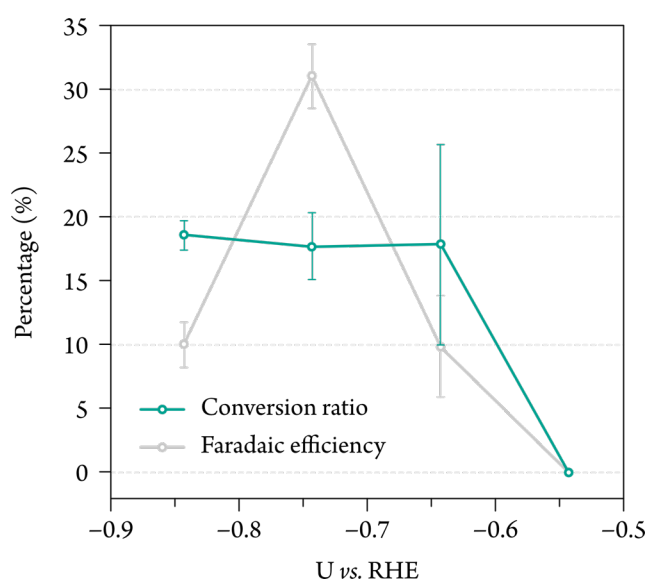


Figure 7.5 Experimental conversion and Faradaic efficiency towards pentenol in the ECH of pentynol as a function of the applied potential at pH 7. No peaks corresponding to traces of pentanol were detected in the NMR spectra.

the diffusion of the former to the reactive surface, although further calculations are ongoing to elucidate the mechanism leading to these unforeseen results.

7.4. Electrochemical hydrogenation of acetylene

Having elucidated the role of the H-covered Ti_3C_2 MXene for the ECH of a model terminal alkyne and confirmed its activity experimentally, we envisioned that the ability of pentynol to undergo the ECH on $\text{Ti}_3\text{C}_2\text{T}_x$ could be extrapolated to a wide range of H-covered MXenes and terminal alkynes. Therefore, we then explored the viability of MXenes as electrocatalysts for the selective ECH of acetylene to ethylene, one of the most widely produced chemical feedstocks in industry (see Section 1.3.4). Similarly

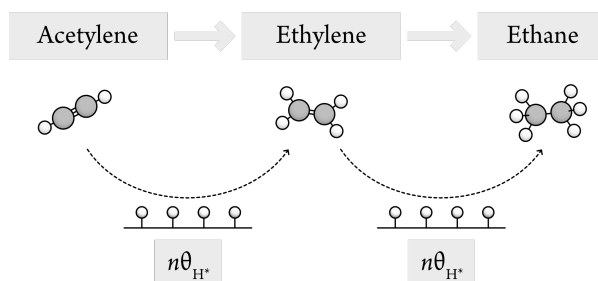


Figure 7.6 Schematic representation of the proposed reaction mechanism for the hydrogenation of acetylene to ethylene and ethane on a MXene surface covered by H atoms.

to the case of pentynol, we propose a reaction pathway in which acetylene can undergo a first coverage-driven hydrogenation through a concerted Heyrovsky-type mechanism yielding ethylene, which then can undergo over-hydrogenation to ethane as schematised in Figure 7.6. Due to the ability of the Mo_2C MXene to display a H coverage at low reducing potentials with a high relative stability, and the similar structures reported experimentally for thermal hydrogenations (see Section 7.1.1), in the next sections we will initially focus on the ECH of acetylene on this MXene at potential ranging from $-0.25 \text{ V}_{\text{SHE}}$ to $-0.80 \text{ V}_{\text{SHE}}$, wherein the $2 \theta_{\text{H}^*}$ coverage (with H atoms covering all *fcc* and, next, all *top* sites) is predominant.

To shed light on the nature of the H MLs on the aforementioned coverage, we performed a Bader charge analysis.²⁹² Similarly to the case of H atoms atop the *fcc* and *hcp* sites of Ti_3C_2 , we found that H atoms covering the *fcc* and *top* sites of Mo_2C feature atomic charges of $-0.29 e$ and $-0.20 e$, respectively; therefore, we concluded that terminal H atoms on Mo_2C also behave as hydride-like species, rendering this MXene as a suitable electrocatalyst for the ECH of acetylene, as we described in the next sections.

7.4.1. Semi-hydrogenation of acetylene

After confirming that the surface of the Mo_2C MXene can be functionalized with electron-rich H atoms at relatively low potentials, we set out to explore its viability as an electrocatalyst for the selective ECH of acetylene. With this aim, we first investigated the adsorption of acetylene on the Mo_2C surface with a $2 \theta_{\text{H}^*}$ coverage. Our calculations indicate that the most stable configuration corresponds to the acetylene molecule in a physisorbed state with an orientation parallel to the surface and sitting above two H atoms on *top* and *fcc* sites at a distance of *ca.* 5.0 \AA (I_1 in Figure 7.7), with a slightly endergonic Gibbs energy of adsorption of 0.14

eV. From this structure, we subsequently examined the interaction between the physisorbed acetylene and the surface *top* H atoms (which displayed more endergonic adsorption energies) by performing a CI-NEB analysis wherein both H atoms are transferred simultaneously. This yielded an exergonically physisorbed ethylene atop the $2 \theta_{\text{H}^*}$ coverage with 2H^* vacancies (denoted $(2 \theta_{\text{H}^*} - 2 \text{H}^*)$ and labelled as I_2 in Figure 7.7). Similarly to the hydrogenation of pentynol, this was found to proceed through a first-order saddle point with an energy barrier of 0.71 eV and an imaginary frequency of -547 cm^{-1} (TS_1 in Figure 7.7, whose nature will be discussed in detail in the following sections). Specifically, this corresponded to the transfer of the first H (H_α) to the C closest to the surface (C_α); subsequent transfer of the second H (H_β) to the C farthest from the surface (C_β) was found to occur in a barrierless process. This asynchronous mechanism was confirmed by assessing a possible sequential hydrogenation through a C_2H_3 intermediate, which further demonstrated the absence of a saddle point along the MEP describing the transfer of H_β .

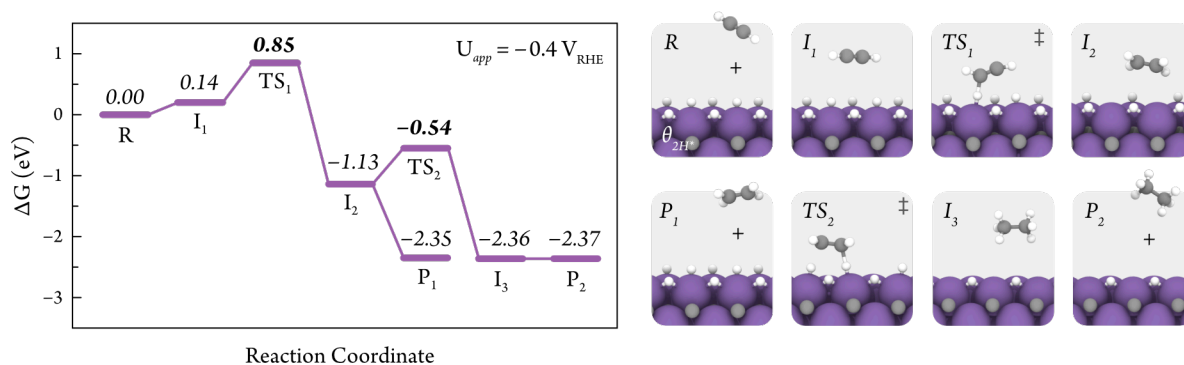


Figure 7.7 Gibbs energy diagram of the reaction mechanism for the ECH of acetylene (R) to ethylene (P_1) and ethane (P_2) on the Mo_2C MXene with a $2 \theta_{\text{H}^*}$ coverage at an applied potential of $-0.4 \text{ V}_{\text{RHE}}$.

7.4.2. Assessment of the selectivity

Overall, the DFT calculations presented thus far predict that the earth-abundant Mo_2C MXene with a $2 \theta_{\text{H}^*}$ surface coverage can promote the ECH of acetylene to ethylene under ambient conditions, requiring low applied potentials ($\leq -0.25 \text{ V}_{\text{RHE}}$) and an activation energy which is perfectly surmountable at room temperature. With this knowledge, we then assessed the selectivity of the system by modelling the over-hydrogenation of ethylene to ethane using the same approach adopted in the modelling of the ECH of acetylene to ethylene. To do so, we first calculated the adsorption of the physisorbed ethylene, which yielded a stable conformation parallel to the surface at a distance of *ca.* 5 Å. Subsequently, we performed a CI-NEB analysis to assess the interaction of the physisorbed ethylene with 2 neighbouring surface H atoms on *top* positions in the $(2 \theta_{\text{H}^*} - 2 \text{H}^*)$ coverage to yield ethane (I_3 in Figure 7.7). Similarly to the ECH of acetylene, this process was found to occur through a TS structure (TS_2 in Figure 7.7) consisting of an asynchronous concerted H transfer, with an imaginary frequency of -881 cm^{-1} and an energy barrier of 0.59 eV, slightly lower to that predicted for the semi-hydrogenation of acetylene. Finally, our simulations show that the resulting ethylene is physisorbed

atop the $2\theta_{\text{H}^*}$ coverage with 4 H vacancies (denoted $(2\theta_{\text{H}^*} - 4\text{H}^*)$), and notably, its Gibbs energy of adsorption lies 1.23 eV below the previous intermediate; this indicates that the competing over-hydrogenation and subsequent desorption of the alkane (P_2 in Figure 7.7) is highly thermodynamically favourable.

Despite the similar energetics between the ECH of acetylene to ethylene and the undesired over-hydrogenation to ethane point to Mo_2C as an electrocatalyst with poor selectivity, a closer examination of other competing processes under electrochemical conditions proves otherwise. More specifically, we note that the over-hydrogenation of ethylene competes with the desorption of the olefin and the concomitant regeneration of the 2H^* vacancies on *top* positions in the $(2\theta_{\text{H}^*} - 2\text{H}^*)$ coverage (P_1 in Figure 7.7). Importantly, this latter step is an electrochemical process which involves 2 PCETs, and therefore, it is expected to become more favourable at more reducing potentials (as shown in Equation (2.94)). In particular, our calculations predict that, at $U = -0.4 \text{ V}_{\text{RHE}}$, the regeneration of the initial $2\theta_{\text{H}^*}$ coverage is thermodynamically favoured by 1.01 eV compared to the transition state associated with the over-hydrogenation of ethylene. Hence, given the broad range of potentials at which the $2\theta_{\text{H}^*}$ coverage is predicted to be stable on Mo_2C (from $-0.25 \text{ V}_{\text{SHE}}$ to $-0.80 \text{ V}_{\text{RHE}}$), it follows that the dissociation of ethylene and the recovery of the catalyst resting state can be potentially lowered by over 1.6 eV with respect to over-hydrogenation transition state, and at a low potential of $-0.40 \text{ V}_{\text{SHE}}$, this product is predicted to lay 1.81 eV below TS_2 , as displayed in the Gibbs energy diagram of Figure 7.7. Therefore, the selectivity of the Mo_2C MXene will be given by the competitive adsorption of acetylene and ethylene. Hence, we concluded that the investigated MXene may be considered as a promising electrocatalyst for the selective ECH of acetylene to ethylene under ambient conditions at relatively low reducing potentials. Furthermore, we predict that catalyst selectivity can be further improved by applying a more negative bias provided it is within the region of stability of the H-covered MXene surface and it remains within the region where HER is predicted to be minimised, based on our discussion in Section 6.6.

7.5. Charge density difference analysis

To gain a deeper insight on the nature of the H atoms involved in the concerted ECH mechanism, we performed a charge density difference analysis on the TS_1 and TS_2 structures shown for the hydrogenation of acetylene to ethylene and ethylene to ethane, respectively (Figure 7.8 A). The result of this analysis, presented in Figure 7.8 B, allowed us to rationalize the asynchronous concerted hydrogenation of acetylene and ethylene with the charge redistribution within the plane intersecting with the relevant atoms (C_α , C_β , H_α and H_β) of the reacting species. Firstly, we observed that electron density is transferred from H_α to C_α , as indicated by the loss of charge density at the $\text{Mo}-\text{H}_\alpha$ bonds (darker red area) and the gain of charge density at the newly formed $\text{C}_\alpha-\text{H}_\alpha$ bond (dark blue area) in both hydrogenations. This flow of electron density is further evidenced by the net Bader charge on the H_α atoms, which decreases from $-0.20 e$ to -0.04 (-0.06) e in TS_1 (TS_2). In addition, the isosurfaces in Figure 7.8 B indicate a net loss of electron density along the $\text{C}_\alpha-\text{C}_\beta$ bond, confirming the reduction

of the triple and double bond in TS_1 and TS_2 , respectively. The electron density distribution upon the interaction of acetylene and ethylene with H_α eventually leads to the injection of negative charge into the furthest C_β atom, which is demonstrated by the computed Bader charges of C_β of $-0.49 e$ and $-0.17 e$ in TS_1 and TS_2 , respectively. Hence, C_β behaves like a carbanion, which eventually triggers the abstraction of the neighbouring H_β as a proton with the subsequent net loss of electron density of the adjacent Mo centre (light red region).

These results shed light on the nature of the interactions driving the semi- and over-hydrogenation

of acetylene on the H-covered Mo_2C MXene. After assessing the role of the atoms involved in the reaction and establishing a potential pathway for the selective ECH of acetylene to ethylene, we then explored the reactivity of other MXenes towards this process, which we discuss in detail in the following section.

7.6. MXene stoichiometry and metal-dependence of acetylene hydrogenation

With the intention of investigating the catalytic activity of a broader range of MXenes for the selective ECH of acetylene, we aimed at studying how the choice of the metal and the stoichiometry of the MXene influences the energetics and charge distributions of the species in the proposed Heyrovsky-type mechanism. For this purpose, we performed a benchmark the activity of the two most promising MXenes for the ECH based on their surface coverage, i.e. Mo_2C and V_2C , as discussed in Section 7.1.1. In addition to these readily available MXenes, we investigated the effect of the MXene stoichiometry by assessing the activity of their respective theoretical $n = 3$ phases, i.e. Mo_3C_2 and V_3C_2 , containing a $2 \theta_{\text{H}^+}$ coverage. Similarly to the case of Mo_2C , the aforementioned termination in Mo_3C_2 , V_2C and V_3C_2 was found to be predominantly formed by H atoms

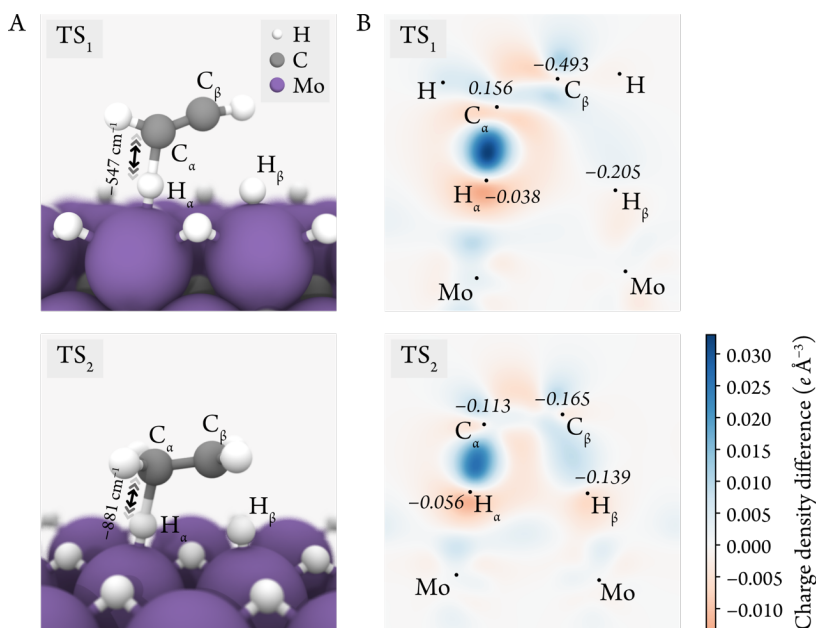


Figure 7.8 A) Side view representations of the TS structures for the concerted ECH of acetylene to ethylene (top) and ethylene to ethane (bottom) on Mo_2C with a $2 \theta_{\text{H}^+}$ coverage. The imaginary frequencies are depicted beside the arrows showcasing the motion of the corresponding vibrational mode. B) Charge density differences analyses across the interaction plane of the structures in A. Regions experiencing a net loss or gain of electron density are displayed in red and blue, respectively. The centre of atoms in the interaction plane are depicted as black dots in the charge density difference heatmap. Bader charges (a.u.) of relevant atoms in the TS structures (i.e. C_α , H_α , C_β and H_β) are also displayed.

covering all *fcc* and *top* sites, the latter being the most endergonically adsorbed and, therefore, the most prone to interact with species in the OHP. Finally, the mechanistic analysis on these two MXenes and their bulkier counterparts was complemented by assessing the ECH of acetylene on Ti_3C_2 , the most readily available MXene which, according to our simulations, can promote the ECH of pentynol via a mechanism facilitated by H atoms on *hcp* sites as the source of H.

Similarly to the study of Mo_2C , we firstly determined the electron-rich nature of the surface H on the other investigated MXenes by performing a Bader charge analysis. This revealed that H on *top* positions of the $2\theta_{\text{H}^*}$ coverage of Mo_3C_2 , V_2C and V_3C_2 , and H atoms on *hcp* positions of Ti_3C_2 (which were already discussed in Section 7.3) have a hydride-like nature, with atomic charges of -0.19 , -0.23 , -0.18 and $-0.36 e$, respectively. Next, we conducted a mechanistic study by firstly assessing the adsorption of acetylene on the H-covered surfaces of the investigated MXenes; this resulted in the Gibbs energy diagrams shown in Figure 7.9. Initially, acetylene is physisorbed at a distance of *ca.* 5 \AA with Gibbs binding energies ranging from 0.03 (on Mo_3C_2) to 0.29 eV (on Ti_3C_2). A subsequent CI-NEB analysis of the semi-hydrogenation of acetylene revealed a similar TS in all cases, wherein the physisorbed acetylene interacted with H atoms on *hcp* (in Ti_3C_2) or *top* positions (in the remaining MXenes), leading to the asynchronous concerted transfer of two H atoms to yield a physisorbed ethylene molecule and a $(2\theta_{\text{H}^*} - 2\text{H}^*)$ coverage. The calculated TSs are characterised by imaginary frequencies ranging from -419 to -803 cm^{-1} and low energy barriers ranging from 0.35 eV (V_2C) to 0.71 eV (Mo_2C). Interestingly, we predict that, while the source of H in Ti_3C_2 are the H atoms adsorbed on *hcp* sites, these spontaneously migrate to *top* sites upon interaction with the physisorbed acetylene, where they can more effectively reach the C centres.

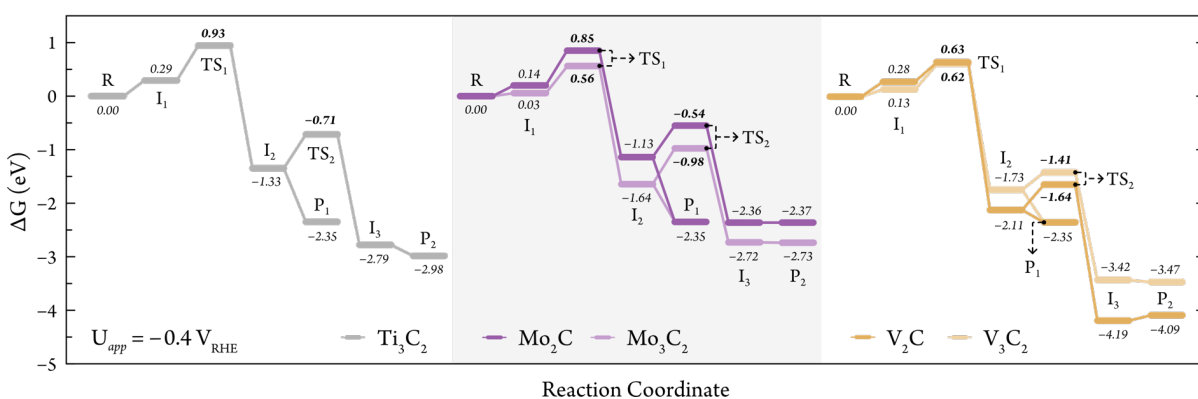


Figure 7.9 Computed Gibbs energy diagrams for the ECH of acetylene on Ti_3C_2 , Mo_2C , Mo_3C_2 , V_2C and V_3C_2 MXenes at an applied potential of $-0.4 \text{ V}_{\text{RHE}}$. Labels for the reaction intermediates are the same as those shown for Mo_2C in Figure 7.7; similar structures were obtained for the other MXenes.

The competing over-hydrogenation of ethylene to ethane was also investigated on the selected MXenes starting from the physisorbed ethylene on the $(2\theta_{\text{H}^*} - 2\text{H}^*)$ coverage interacting with two remaining H atoms on the

most endergonically adsorbed H ML. This was predicted to proceed through a TS with similarly low energy barriers ranging from 0.32 (V_3C_2) to 0.66 eV (Mo_3C_2), characterised by the asynchronous concerted transfer of both H atoms with imaginary frequencies ranging from -770 (V_3C_2) to -922 cm^{-1} (V_2C). Subsequently, the generation of a physisorbed ethane on all structures atop a ($2 \theta_{H^*} - 4 H^*$) coverage was found to be highly exergonic in all cases (≤ -2.36 eV), followed by an almost thermoneutral desorption of the alkane.

Although this scenario points to the studied MXenes being highly active towards the over-hydrogenation of acetylene to ethane, a consideration of the electrochemical conditions reveals that, similarly to the investigated reaction pathway on Mo_2C , the desorption of ethylene and recovery of the surface H vacancies (as depicted in the P_1 steps of Figure 7.9) is favoured by 0.71 to 1.81 eV compared to TS_2 at an applied potential of $-0.4 V_{RHE}$. Importantly, this finding suggests that all investigated MXenes (and, potentially, all synthesized MXenes) are active towards the selective ECH of acetylene to ethylene, wherein the choice of metal or stoichiometry has little to no influence on the computed energies of the proposed reaction pathway. It must be noted, however, that MXenes with $n > 1$ stoichiometries are predicted to be more stable than their thinner counterparts (as discussed in Section 6.4), and therefore, are more suitable for catalytic applications.

To unravel the nature of the atoms involved in the concerted acetylene hydrogenation, we performed a charge density difference analysis between the surface with the H coverage and the interacting acetylene across the interaction plane within TS_1 in the studied MXenes (represented in the top panels of Figure 7.10 with relevant bond distances and imaginary frequencies). The charge density difference heatmaps derived from this analysis are depicted in the bottom panels of Figure 7.10. Further insight was obtained from the Bader charge analysis of C_α , C_β , H_α and H_β , whose effective charges, along with those in TS_2 and in the H atoms forming the 2 MLs in the coverage at experimental conditions, are presented in Table 7.1.

The analysis of the charge redistribution within TS_1 in the studied MXenes reveals similar results to the ones found for Mo_2C . Firstly, charge depletion between H_α and the neighbouring metal indicates the dissociation of the M–H bond and subsequent formation of the $H_\alpha-C_\alpha$ bond, as demonstrated by the red and dark blue areas within the heatmaps, respectively. Secondly, the ability of the hydride-like H_α atoms to donate charge to the newly formed bonds is made evident by the increase in their Bader charge in both TS_1 and TS_2 compared to its initial state on the $2 \theta_{H^*}$ coverage; this can be seen in Table 7.1, where H atoms in the topmost top positions, with a Bader charge of $-0.20 e$, display a more positive value of -0.04 and $-0.06 e$ when transferred as H_α in TS_1 and TS_2 , respectively. Finally, in all studied cases we predict that C_β has a carbanion character (with a more negative charge compared to C_α , with the largest difference found in Mo-based MXenes) and can abstract H_β as a proton in a barrierless process. Hence, this charge density difference confirms the importance of the hydride-like H_α for the ECH of acetylene, and further demonstrates the ECH capabilities of a broader range of MXenes. Guided by these results, experiments on the ability of MXenes to catalyse the ECH of acetylene are currently ongoing in the group of Prof. Paula Colavita in Trinity College Dublin.

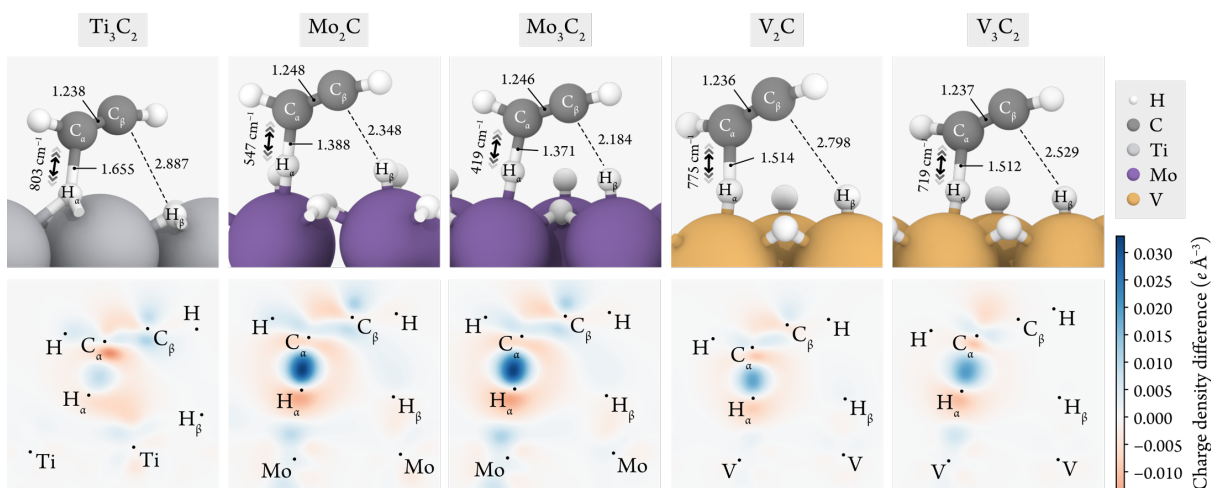


Figure 7.10 On the topmost panels, side view representations of the TS structures for the concerted ECH of acetylene to ethylene on Ti_3C_2 , Mo_2C , Mo_3C_2 , V_2C and V_3C_2 with a $2\theta_{\text{H}^+}$ coverage. Relevant bond distances are shown in Å, whereas imaginary frequencies are depicted beside the arrows showcasing the motion of the corresponding vibrational mode. The bottom panels illustrate the charge density differences across the interaction plane of each MXene structure. Regions experiencing a net loss of electron density are displayed in red, while regions gaining electron density are depicted in blue. The centre of the atoms within the interaction plane are represented as dots in the charge density difference heatmaps.

Table 7.1 Bader charges (in a.u.) of the relevant H and C atoms (i.e. C_α , H_α , C_β and H_β , as specified in Figure 7.10) in the calculated TS structures for the ECH of acetylene to ethylene and the over-hydrogenation to ethane on the studied MXenes (left), and of the different H atoms on the $2\theta_{\text{H}^+}$ coverage of the bare MXene (right).

	Atom	TS ₁	TS ₂	Atom	$2\theta_{\text{H}^+}$
Mo_2C	H_α	-0.04	-0.06	$\text{H}(fcc)$	-0.29
	C_α	+0.16	-0.11	$\text{H}(top)$	-0.20
	H_β	-0.21	-0.14	-	-
	C_β	-0.49	-0.16	-	-
Mo_3C_2	H_α	-0.02	-0.08	$\text{H}(fcc)$	-0.26
	C_α	+0.19	-0.05	$\text{H}(top)$	-0.19
	H_β	-0.18	-0.13	-	-
	C_β	-0.52	-0.16	-	-
V_2C	H_α	-0.08	-0.12	$\text{H}(fcc)$	-0.30
	C_α	-0.12	-0.14	$\text{H}(top)$	-0.23
	H_β	-0.24	-0.14	-	-
	C_β	-0.18	-0.12	-	-
V_3C_2	H_α	-0.07	-0.14	$\text{H}(fcc)$	-0.29
	C_α	+0.09	-0.11	$\text{H}(top)$	-0.18
	H_β	-0.23	-0.15	-	-
	C_β	-0.47	-0.11	-	-
Ti_3C_2	H_α	-0.22	-0.18	$\text{H}(fcc)$	-0.41
	C_α	-0.04	-0.16	$\text{H}(hcp)$	-0.36
	H_β	+0.19	-0.32	-	-
	C_β	-0.44	-0.18	-	-

7.7. Conclusions

The ability of MXenes to catalyse the ECH of small organic substrates in a proposed H-coverage-mediated Heyrovsky-type mechanism was investigated in two cases. Firstly, the ECH of a model substrate, 4-pentyn-1-ol, was assessed on the $2 \theta_{\text{H}^+}$ coverage of Ti_3C_2 , a readily available MXene displaying a wide range of potentials at which this coverage is predominant and relatively stable (below $-0.60 \text{ V}_{\text{SHE}}$). The H atoms making up the MLs of coverage were found to display a negative charge build-up giving them hydride-like attributes, which rendered them potentially active for hydrogenation reactions. Consequently, the partial and over-hydrogenation of 4-pentyn-1-ol to 4-penten-1-ol and 1-pentanol, respectively, was investigated. A careful examination of the kinetics of this reaction revealed that the ECH of pentynol to pentenol and pentenol to pentanol proceeded through transition states with relatively low energy barriers. Interestingly, the transfer of both H atoms from the most endergonically adsorbed H ML to the terminal C atoms of the organic substrate was predicted to occur via an asynchronous mechanism, wherein the transfer of the first H was determined to be the RDS, whereas the second H was transferred spontaneously. Therefore, we predict the Ti_3C_2 MXene to be active for the hydrogenation of 4-pentyn-1-ol at potentials below $-0.6 \text{ V}_{\text{SHE}}$. Our theoretical predictions have been proven experimentally by our collaborators in the group of Prof. Colavita in Trinity College Dublin, who demonstrated that Ti_3C_2 is able to promote the ECH of pentynol to pentenol at potentials corresponding to our observed range of predominant H-coverage regime. Further calculations are ongoing to unravel the origin of the selectivity on this MXene.

In this chapter, we also demonstrated that a broader range of MXenes could be used for the ECH of more relevant alkynes through a similar Heyrovsky-type mechanism, such as the selective ECH of acetylene to ethylene. For this purpose, we selected a MXene which was predicted to be the most potentially active for this reaction (based on our thorough analysis on the predominant surface coverages and their relative stabilities from Chapter 6), namely Mo_2C . A mechanistic study on the ECH of acetylene on the $2 \theta_{\text{H}^+}$ coverage of Mo_2C showed that acetylene was able to undergo a hydrogenation to ethylene via interaction with 2 top H atoms of the surface coverage, in an asynchronous concerted mechanism involving a TS with a relatively low energy barrier. The undesired over-hydrogenation of ethylene to ethane was also investigated, which was predicted to be highly exergonic and involved a TS with a similarly low energy barrier, showing an almost identical concerted H transfer. However, upon introduction of the negative potential required for the generation of the reactive H coverage, we predict that dissociation of ethylene and recovery of the surface H vacancies—which involves 2 PCET steps—will effectively compete with the over-hydrogenation, and this step will be 1.81 eV lower in energy compared to the second TS at $U = -0.40 \text{ V}_{\text{SHE}}$. Therefore, our simulations show that this system is a promising catalyst for the selective ECH of acetylene. Next, the effect of the constituent metal on the activity was investigated by studying this reaction on V_2C and Ti_3C_2 , while the influence of the MXene stoichiometry was assessed by simulating Mo_3C_2 and V_3C_2 . Most importantly, our calculations showed that all studied

MXenes are potentially active towards the selective ECH of acetylene to ethylene, as demonstrated by the similar energy diagrams and location of intermediates as Mo_2C . Charge density difference analyses of the TS in the semi-hydrogenation of acetylene on the considered MXenes showed similar charge redistributions, where the role of the firstly transferred H (acting as a hydride), carbanion formation and consequent proton abstraction is found to be of great significance.

Hence, this project showcases how the surface coverage of MXenes under electrochemical conditions can be leveraged for relevant electrocatalytic applications. In this case study, unravelling the surface coverage of all synthesized MXenes allowed us to rationally design, for the first time, MXenes as efficient electrocatalysts for the ECH of terminal alkynes, which is also confirmed by experimental studies. The proposed highly active Heyrovsky-type alkyne hydrogenation mechanism is carried out at low negative potentials and overcomes the main drawbacks from current synthetic routes: firstly, it uses protons in the solution as the source of hydrogen, avoiding the use of high pressures of H_2 gas; secondly, since alkyne hydrogenation is carried out without its chemisorption and activation, polymerisation of the reactants and formation of surface coke (which has been shown to deactivate the catalyst and reduce selectivity) is prevented. Furthermore, this potential towards the ECH was theorised to be transferrable to a series of MXenes and model substrates as demonstrated in the ECH of acetylene, which paves the way for the use of MXenes not only as electrocatalysts for the ECH of terminal alkynes, but as electrocatalysts for a wide range of electroreductions driven by the H surface coverage.

“ *Only if we understand, can we care. Only if we care, we will help. Only if we help, we shall be saved.* – **Jane Goodall**

Jane Goodall: 40 Years at Gombe, 1999

CHAPTER

8

General Conclusions and Future Work

In this thesis, heterogeneous systems based on Earth-abundant elements have been investigated for their use in industrially relevant photo- and electroreduction reactions. These systems are discussed in Chapters 4 to 7, each containing their project-specific conclusions; in the following, a concise summary of these studies, followed by a short discussion of the future approaches our results point towards, is presented.

8.1. Conclusions

Firstly, we explored the performance of metal-free N-doped C electrodes for the ORR in alkaline conditions. Guided by the experimental findings from our collaborators, we investigated the effect of graphitic-N and pyridinic-N doping with different concentrations on the catalytic activity and selectivity towards the 2-electron or 4-electron reduction to hydrogen peroxide or water, respectively. The results from our mechanistic study show that the most active sites on theoretical cluster models containing uniquely pyridinic-N or graphitic-N dopants promote the undesired 2-electron reduction product. Interestingly, the presence of both dopants in the system was found to be essential for achieving a good energetic distribution of the reaction intermediates and favour the 4-electron reduction with low onset potentials, in agreement with experiments. These results offer an in-depth insight on the role of different N dopants on C-based electrodes for a tailored ORR activity and selectivity, which is highly relevant for the development of novel metal-free electrodes for fuel cells.

Next, we investigated the influence of ligand-adsorbate interactions on the stabilisation of key intermediates in the photocatalytic CO₂RR on ZnSe QDs. Firstly, we found that imidazolium-based ligands are able to facilitate the reaction on the bare QD by stabilising the CO₂*⁻ intermediate through NCIs. Based on these findings, we then assessed the effect of the length of dithiol ligands in the presence and absence of a Ni-based molecular co-catalyst. According to our calculations, shorter-reaching ligands facilitate a surface-promoted CO₂RR pathway, whereas longer ligands favour the reaction on the Ni co-catalyst. These results are in good agreement with the experimental observations from our collaborators, and pave the way for the use of tailored capping ligands for the development of novel QD-based systems as CO₂RR photocatalysts.

Finally, the surface coverage of the *o*-MXenes synthesized to date was thoroughly investigated, including a novel thermodynamic stability assessment and an investigation of the competing HER. Interestingly, most studied MXenes were found to display predominant H coverages at low negative potentials, which prompted us to study MXenes for the ECH of unsaturated organic substrates. In particular, Ti₃C₂ was identified as a promising catalyst for the ECH of pentynol based on a coverage-driven mechanistic study. This MXene was then found to be highly selective towards pentenol, based on the findings from our experimental collaborators. Next, studies on the ECH of acetylene using Mo, Ti and V-based MXenes predicted these structures to be very active towards the ECH of small terminal alkynes at low negative potentials via a Heyrovsky-type process mediated by electron-rich H coverages. These results emphasize the role of the surface coverage in electrocatalysis, and is the first instance where MXenes have been shown to be active for ECH.

Overall, in this thesis we have elucidated the reduction reaction mechanisms of relevant photocatalytic and electrocatalytic processes relevant to energy storage and conversion. Specifically, understanding the effects of the dopant distribution, ligand phase composition and the presence of an electrochemically generated coverage has been shown to be key for the development of ORR, CO₂RR and HER and ECH catalysts, respectively. Altogether, the results reported herein highlight the importance of periodic DFT calculations for untangling the activity of heterogeneous catalysts for their use in solar- and power-to-X technologies.

8.2. Future work

The insights obtained in the results discussed herein shine light on the steps to take in future photo- and electrocatalytic applications. Firstly, we have been able to demonstrate the cooperative effect between N dopants in C materials for the ORR. We believe that future studies should focus on providing a better insight on how the dopant distribution and location can be tuned to optimise these effects, as well as assessing the viability of other dopant species. This will be paramount for the design of sustainable fuel cells using Earth-abundant materials.

Secondly, we have shown that non-covalent interactions are essential in order to drive the photocatalytic CO₂RR using ligand-capped ZnSe QDs. We believe that future works on this subject should provide approaches to better understand these interactions. Furthermore, given the success obtained by using both imidazolium and dithiol-containing ligands, we expect follow up studies to aim at designing new ligand phases to enhance these interactions and improve the reaction selectivities and yields.

Finally, we have provided a novel approach for the hydrogenation of terminal alkynes using a Heyrovsky-type mechanism which has barely been explored in previous works. This has been applied theoretically for the hydrogenation of acetylene and also experimentally for the hydrogenation of pentynol. However, we suggest future works to study the hydrogenation other industry-relevant species using this pathway using both MXenes and novel and potentially more stable catalysts which can be more easily scaled up.

In general, the results presented in this thesis highlight the importance of determining the surface coverage, dopant distribution and ligand phase composition for an accurate understanding of the effects unfolding in any photo- and electrocatalytic process. These factors, and specially the surface coverage, are seldom considered in state-of-the-art electrocatalytic studies and, in most cases where they are taken into account, their role is often underestimated. Therefore, we believe that future theoretical catalytic studies should begin with a thorough study of the basal plane at the studied conditions to obtain more realistic results. Although an initial approach to this issue has been presented in this thesis, we hope that future studies will provide more insight on further mixed coverages and additional adsorbates, potentially using high-throughput screening of surface sites and machine learning techniques.

References

- [1] Ohtomo, Y.; Kakegawa, T.; Ishida, A.; Nagase, T.; Rosing, M. T. *Nat. Geosci.* **2014**, *7*, 25–28.
- [2] Gilbert, W. *Nature* **1986**, *319*, 618–618.
- [3] Huheey, J. E.; Keiter, E. A.; Keiter, R. L. *Inorganic chemistry: principles of structure and reactivity*, 4th ed.; HarperCollins College Publishers: New York, NY, 1993.
- [4] Wigley, T. M. L.; Brimblecombe, P. *Nature* **1981**, *291*, 213–215.
- [5] Yung, Y. L.; McElroy, M. B. *Science* **1979**, *203*, 1002–1004.
- [6] Navarro-González, R.; McKay, C. P.; Mvondo, D. N. *Nature* **2001**, *412*, 61–64.
- [7] Berg, J. M.; Tymoczko, J. L.; Stryer, L.; Stryer, L. *Biochemistry*, 5th ed.; W.H. Freeman: New York, 2002.
- [8] Arrhenius, S. Z. *Für Phys. Chem.* **1889**, *4U*, 96–116.
- [9] Eyring, H. *J. Chem. Phys.* **1935**, *3*, 107–115.
- [10] Evans, M. G.; Polanyi, M. *Trans. Faraday Soc.* **1935**, *31*, 875–894.
- [11] Crichton, R. R. Zinc – Lewis Acid and Gene Regulator. In *Biological Inorganic Chemistry*; Elsevier, 2012; pp 229–246.
- [12] Hagen, J. Homogeneous Catalysis with Transition Metal Catalysts. In *Industrial Catalysis*; Wiley-VCH Verlag GmbH & Co. KGaA: Weinheim, Germany, 2015; pp 17–46.
- [13] Nørskov, J. K.; Studt, F.; Abild-Pedersen, F.; Bligaard, T. *Fundamental Concepts in Heterogeneous Catalysis*; John Wiley & Sons, Inc: Hoboken, NJ, USA, 2014.
- [14] Somorjai, G. A. Active Sites in Heterogeneous Catalysis. In *Advances in Catalysis*; Elsevier, 1977; Vol. 26, pp 1–68.
- [15] Jin, R.; Li, G.; Sharma, S.; Li, Y.; Du, X. *Chem. Rev.* **2021**, *121*, 567–648.
- [16] Guo, D.; Shibuya, R.; Akiba, C.; Saji, S.; Kondo, T.; Nakamura, J. *Science* **2016**, *351*, 361–365.
- [17] Pablo-García, S.; Álvarez-Moreno, M.; López, N. *Int. J. Quantum Chem.* **2021**, *121*, e26382.
- [18] Medford, A. J.; Vojvodic, A.; Hummelshøj, J. S.; Voss, J.; Abild-Pedersen, F.; Studt, F.; Bligaard, T.; Nilsson, A.; Nørskov, J. K. *J. Catal.* **2015**, *328*, 36–42.
- [19] Koper, M. T. M. *J. Electroanal. Chem.* **2011**, *660*, 254–260.
- [20] Nørskov, J. K.; Bligaard, T.; Logadottir, A.; Kitchin, J. R.; Chen, J. G.; Pandalov, S.; Stimming, U. *J. Electrochem. Soc.* **2005**, *152*, J23.
- [21] Singh, A. R.; Rohr, B. A.; Statt, M. J.; Schwalbe, J. A.; Cargnello, M.; Nørskov, J. K. *ACS Catal.* **2019**, *9*, 8316–8324.
- [22] Birdja, Y. Y.; Pérez-Gallent, E.; Figueiredo, M. C.; Göttle, A. J.; Calle-Vallejo, F.; Koper, M. T. M. *Nat. Energy* **2019**, *4*, 732–745.
- [23] Langmuir, I. *J. Am. Chem. Soc.* **1918**, *40*, 1361–1403.
- [24] Hinshelwood, C. N. *The Kinetics of Chemical Change in Gaseous Systems*; Oxford University Press and Humphrey Milford: London, 1926.
- [25] Horiuti, I.; Polanyi, M. *Trans. Faraday Soc.* **1934**, *30*, 1164–1172.
- [26] López, N.; Vargas-Fuentes, C. *Chem. Commun.* **2012**, *48*, 1379–1391.
- [27] Baxter, R. J.; Hu, P. *J. Chem. Phys.* **2002**, *116*, 4379–4381.
- [28] Horiuti, J.; Polanyi, M. *Nature* **1933**, *132*, 819–819.
- [29] Horiuti, J.; Ikusima, M. *Proc. Imp. Acad.* **1939**, *15*, 39–44.
- [30] Trasatti, S. The Absolute Electrode Potential: An Explanatory Note: (Recommendations 1986).
- [31] Craig, M. J.; Coulter, G.; Dolan, E.; Soriano-López, J.; Mates-Torres, E.; Schmitt, W.; García-Melchor, M. *Nat. Commun.* **2019**, *10*, 4993.
- [32] Soriano-López, J.; Schmitt, W.; García-Melchor, M. *Curr. Opin. Electrochem.* **2018**, *7*, 22–30.
- [33] Bard, A. J.; Faulkner, L. R. *Electrochemical methods: fundamentals and applications*, 2nd ed.; Wiley: New York, 2001.
- [34] McCrory, C. C. L.; Jung, S.; Peters, J. C.; Jaramillo, T. F. *J. Am. Chem. Soc.* **2013**, *135*, 16977–16987.

- [35] Perry, S. C.; Pangotra, D.; Vieira, L.; Csepei, L.-I.; Sieber, V.; Wang, L.; Ponce de León, C.; Walsh, F. C. *Nat. Rev. Chem.* **2019**, *3*, 442–458.
- [36] Seh, Z. W.; Kibsgaard, J.; Dickens, C. F.; Chorkendorff, I.; Nørskov, J. K.; Jaramillo, T. F. *Science* **2017**, *355*, eaad4998.
- [37] Weinberg, D. R.; Gagliardi, C. J.; Hull, J. F.; Murphy, C. F.; Kent, C. A.; Westlake, B. C.; Paul, A.; Ess, D. H.; McCafferty, D. G.; Meyer, T. J. *Chem. Rev.* **2012**, *112*, 4016–4093.
- [38] Tyburski, R.; Liu, T.; Glover, S. D.; Hammarström, L. J. *Am. Chem. Soc.* **2021**, *143*, 560–576.
- [39] Tarantino, K. T.; Liu, P.; Knowles, R. R. *J. Am. Chem. Soc.* **2013**, *135*, 10022–10025.
- [40] Koper, M. T. M. *Phys. Chem. Chem. Phys.* **2013**, *15*, 1399–1407.
- [41] Marcus, R. A. J. *Chem. Phys.* **1956**, *24*, 966–978.
- [42] de Aguirre, A.; Funes-Ardoiz, I.; Maseras, F. *Inorganics* **2019**, *7*, 32.
- [43] Antoniadou, M.; Daskalaki, V. M.; Balis, N.; Kondarides, D. I.; Kordulis, C.; Lianos, P. *Appl. Catal. B Environ.* **2011**, *107*, 188–196.
- [44] Schneider, J.; Matsuoka, M.; Takeuchi, M.; Zhang, J.; Horiuchi, Y.; Anpo, M.; Bahnemann, D. W. *Chem. Rev.* **2014**, *114*, 9919–9986.
- [45] Chan, S.-F.; Chou, M.; Creutz, C.; Matsubara, T.; Sutin, N. *J. Am. Chem. Soc.* **1981**, *103*, 369–379.
- [46] Bellin, J. S.; Alexander, R.; Mahoney, R. D. *Photochem. Photobiol.* **1973**, *17*, 17–24.
- [47] Pellegrin, Y.; Odobel, F. C. R. *Chim.* **2017**, *20*, 283–295.
- [48] Kashefi, K.; Holmes, D. E.; Reysenbach, A.-L.; Lovley, D. R. *Appl. Environ. Microbiol.* **2002**, *68*, 1735–1742.
- [49] Schneider, J.; Bahnemann, D. W. *J. Phys. Chem. Lett.* **2013**, *4*, 3479–3483.
- [50] Fujishima, A.; Honda, K. *Nature* **1972**, *238*, 37–38.
- [51] Yang, J.; Wang, D.; Han, H.; Li, C. *Acc. Chem. Res.* **2013**, *46*, 1900–1909.
- [52] Kudo, A.; Miseki, Y. *Chem. Soc. Rev.* **2009**, *38*, 253–278.
- [53] (a) Walter, M. G.; Warren, E. L.; McKone, J. R.; Boettcher, S. W.; Mi, Q.; Santori, E. A.; Lewis, N. S. *Chem. Rev.* **2010**, *110*, 6446–6473. (b) Walter, M. G.; Warren, E. L.; McKone, J. R.; Boettcher, S. W.; Mi, Q.; Santori, E. A.; Lewis, N. S. *Chem. Rev.* **2011**, *111*, 5815.
- [54] Chen, S.; Takata, T.; Domen, K. *Nat. Rev. Mater.* **2017**, *2*, 17050.
- [55] Serpone, N. *J. Photochem. Photobiol. A: Chem.* **1997**, *104*, 1–12.
- [56] Rego de Vasconcelos, B.; Lavoie, J.-M. *Front. Chem.* **2019**, *7*, 392.
- [57] Chehade, Z.; Mansilla, C.; Lucchese, P.; Hilliard, S.; Proost, J. *Int. J. Hydrog. Energy* **2019**, *44*, 27637–27655.
- [58] Thomas, C. E. *Int. J. Hydrog. Energy* **2009**, *34*, 6005–6020.
- [59] Wulf, C.; Linßen, J.; Zapp, P. *Energy Procedia* **2018**, *155*, 367–378.
- [60] Foit, S. R.; Vinke, I. C.; de Haart, L. G. J.; Eichel, R.-A. *Angew. Chem. Int. Ed.* **2017**, *56*, 5402–5411.
- [61] Lee, W. J.; Li, C.; Prajitno, H.; Yoo, J.; Patel, J.; Yang, Y.; Lim, S. *Catal. Today* **2021**, *368*, 2–19.
- [62] Shinagawa, T.; Garcia-Esparza, A. T.; Takanabe, K. *Sci. Rep.* **2015**, *5*, 13801.
- [63] Conway, B. E.; Tilak, B. V. *Electrochim. Acta* **2002**, *47*, 3571–3594.
- [64] Li, C.; Baek, J.-B. *ACS Omega* **2020**, *5*, 31–40.
- [65] Hansen, J. N.; Prats, H.; Toudahl, K. K.; Mørch Secher, N.; Chan, K.; Kibsgaard, J.; Chorkendorff, I. *ACS Energy Lett.* **2021**, *6*, 1175–1180.
- [66] Tang, M. T.; Liu, X.; Ji, Y.; Nørskov, J. K.; Chan, K. *J. Phys. Chem. C* **2020**, *124*, 28083–28092.
- [67] Greeley, J.; Jaramillo, T. F.; Bonde, J.; Chorkendorff, I.; Nørskov, J. K. *Nat. Mater.* **2006**, *5*, 909–913.
- [68] Benck, J. D.; Hellstern, T. R.; Kibsgaard, J.; Chakthranont, P.; Jaramillo, T. F. *ACS Catal.* **2014**, *4*, 3957–3971.
- [69] Lukowski, M. A.; Daniel, A. S.; Meng, F.; Forticaux, A.; Li, L.; Jin, S. *J. Am. Chem. Soc.* **2013**, *135*, 10274–10277.
- [70] Yan, Y.; Xia, B.; Xu, Z.; Wang, X. *ACS Catal.* **2014**, *4*, 1693–1705.
- [71] Lindgren, P.; Kastlunger, G.; Peterson, A. A. *ACS Catal.* **2020**, *10*, 121–128.
- [72] Exner, K. S. *Electrochem. Sci. Adv.* **2021**, e2100101.

- [73] Baek, D. S.; Lee, J.; Lim, J. S.; Joo, S. H. *Mater. Chem. Front.* **2021**, *5*, 4042–4058.
- [74] Dubouis, N.; Grimaud, A. *Chem. Sci.* **2019**, *10*, 9165–9181.
- [75] McCrum, I. T.; Koper, M. T. M. *Nat. Energy* **2020**, *5*, 891–899.
- [76] Steele, B. C. H.; Heinzl, A. *Nature* **2001**, *414*, 345–352.
- [77] Staffell, I.; Scamman, D.; Velazquez Abad, A.; Balcombe, P.; Dodds, P. E.; Ekins, P.; Shah, N.; Ward, K. R. *Energy Environ. Sci.* **2019**, *12*, 463–491.
- [78] Gómez-Marín, A. M.; Rizo, R.; Feliu, J. M. *Beilstein J. Nanotechnol.* **2013**, *4*, 956–967.
- [79] Cheng, T.; Goddard III, W. A.; An, Q.; Xiao, H.; Merinov, B.; Morozov, S. *Phys. Chem. Chem. Phys.* **2017**, *19*, 2666–2673.
- [80] Ma, R.; Lin, G.; Zhou, Y.; Liu, Q.; Zhang, T.; Shan, G.; Yang, M.; Wang, J. *Npj Comput. Mater.* **2019**, *5*, 78.
- [81] Ramaswamy, N.; Mukerjee, S. J. *Phys. Chem. C* **2011**, *115*, 18015–18026.
- [82] Nørskov, J. K.; Rossmeisl, J.; Logadottir, A.; Lindqvist, L.; Kitchin, J. R.; Bligaard, T.; Jónsson, H. *J. Phys. Chem. B* **2004**, *108*, 17886–17892.
- [83] International Energy Agency. *Energy Technol. Perspect.* **2020**, 174.
- [84] Glasgow Climate Pact, Glasgow Climate Change Conference - October/November 2021 Decisions. 2021.
- [85] Chang, X.; Wang, T.; Gong, J. *Energy Environ. Sci.* **2016**, *9*, 2177–2196.
- [86] Qiao, J.; Liu, Y.; Hong, F.; Zhang, J. *Chem. Soc. Rev.* **2014**, *43*, 631–675.
- [87] Jin, S.; Hao, Z.; Zhang, K.; Yan, Z.; Chen, J. *Angew. Chem. Int. Ed.* **2021**, *133*, 20795–20816.
- [88] König, M.; Vaes, J.; Klemm, E.; Pant, D. *iScience* **2019**, *19*, 135–160.
- [89] Fu, J.; Zhu, B.; Jiang, C.; Cheng, B.; You, W.; Yu, J. *Small* **2017**, *13*, 1603938.
- [90] Luo, W.; Zhang, J.; Li, M.; Züttel, A. *ACS Catal.* **2019**, *9*, 3783–3791.
- [91] Das, S.; Pérez-Ramírez, J.; Gong, J.; Dewangan, N.; Hidajat, K.; Gates, B. C.; Kawi, S. *Chem. Soc. Rev.* **2020**, *49*, 2937–3004.
- [92] Ishida, H.; Tanaka, H.; Tanaka, K.; Tanaka, T. *J. Chem. Soc., Chem. Commun.* **1987**, 131–132.
- [93] Lau, G. P. S.; Schreier, M.; Vasilyev, D.; Scopelliti, R.; Grätzel, M.; Dyson, P. J. *J. Am. Chem. Soc.* **2016**, *138*, 7820–7823.
- [94] Hori, Y.; Wakebe, H.; Tsukamoto, T.; Koga, O. *Electrochim. Acta* **1994**, *39*, 1833–1839.
- [95] Peng, X.; Karakalos, S. G.; Mustain, W. E. *ACS Appl. Mater. Interfaces* **2018**, *10*, 1734–1742.
- [96] Zhu, W.; Michalsky, R.; Metin, Ö.; Lv, H.; Guo, S.; Wright, C. J.; Sun, X.; Peterson, A. A.; Sun, S. *J. Am. Chem. Soc.* **2013**, *135* (45), 16833–16836.
- [97] Nitopi, S.; Bertheussen, E.; Scott, S. B.; Liu, X.; Engstfeld, A. K.; Horch, S.; Seger, B.; Stephens, I. E. L.; Chan, K.; Hahn, C.; Nørskov, J. K.; Jaramillo, T. F.; Chorkendorff, I. *Chem. Rev.* **2019**, *119*, 7610–7672.
- [98] Choi, C.; Kwon, S.; Cheng, T.; Xu, M.; Tieu, P.; Lee, C.; Cai, J.; Lee, H. M.; Pan, X.; Duan, X.; Goddard III, W. A.; Huang, Y. *Nat. Catal.* **2020**, *3*, 804–812.
- [99] Durand, W. J.; Peterson, A. A.; Studt, F.; Abild-Pedersen, F.; Nørskov, J. K. *Surf. Sci.* **2011**, *605*, 1354–1359.
- [100] Peterson, A. A.; Abild-Pedersen, F.; Studt, F.; Rossmeisl, J.; Nørskov, J. K. *Energy Environ. Sci.* **2010**, *3*, 1311–1315.
- [101] Vijay, S.; Ju, W.; Brückner, S.; Tsang, S.-C.; Strasser, P.; Chan, K. *Nat. Catal.* **2021**, *4*, 1024–1031.
- [102] Gauthier, J. A.; Fields, M.; Bajdich, M.; Chen, L. D.; Sandberg, R. B.; Chan, K.; Nørskov, J. K. *J. Phys. Chem. C* **2019**, *123*, 29278–29283.
- [103] Sun, Z.; Ma, T.; Tao, H.; Fan, Q.; Han, B. *Chem* **2017**, *3*, 560–587.
- [104] De Luna, P.; Hahn, C.; Higgins, D.; Jaffer, S. A.; Jaramillo, T. F.; Sargent, E. H. *Science* **2019**, *364*, eaav3506.
- [105] Vilé, G.; Albani, D.; Almora-Barrios, N.; López, N.; Pérez-Ramírez, J. *ChemCatChem* **2016**, *8*, 21–33.
- [106] Borodziński, A.; Bond, G. C. *Catal. Rev.* **2006**, *48*, 91–144.
- [107] Albers, P.; Pietsch, J.; Parker, S. F. *J. Mol. Catal. A: Chem.* **2001**, *173*, 275–286.
- [108] Kaiser, S. K.; Lin, R.; Mitchell, S.; Fako, E.; Krumeich, F.; Hauert, R.; Safonova, O. V.; Kondratenko, V. A.; Kondratenko, E. V.; Collins, S. M.; Midgley, P. A.; López, N.; Pérez-Ramírez, J. *Chem. Sci.* **2019**, *10*, 359–369.

- [109] Larsson, M.; Jansson, J.; Asplund, S. *J. Catal.* **1998**, *178*, 49–57.
- [110] Zhao, J.; Zha, S.; Mu, R.; Zhao, Z.-J.; Gong, J. *J. Phys. Chem. C* **2018**, *122*, 6005–6013.
- [111] Anderson, J. A.; Mellor, J.; Wells, R. P. K. *J. Catal.* **2009**, *261*, 208–216.
- [112] Hu, M.; Zhao, S.; Liu, S.; Chen, C.; Chen, W.; Zhu, W.; Liang, C.; Cheong, W.-C.; Wang, Y.; Yu, Y.; Peng, Q.; Zhou, K.; Li, J.; Li, Y. *Adv. Mater.* **2018**, *30*, 1801878.
- [113] Marshall, S. T.; O'Brien, M.; Oetter, B.; Corpuz, A.; Richards, R. M.; Schwartz, D. K.; Medlin, J. W. *Nat. Mater.* **2010**, *9*, 853–858.
- [114] Jin, Q.; He, Y.; Miao, M.; Guan, C.; Du, Y.; Feng, J.; Li, D. *Appl. Catal. A: Gen.* **2015**, *500*, 3–11.
- [115] García-Melchor, M.; López, N. *J. Phys. Chem. C* **2014**, *118*, 10921–10926.
- [116] Vilé, G.; Bridier, B.; Wichert, J.; Pérez-Ramírez, J. *Angew. Chem. Int. Ed.* **2012**, *51*, 8620–8623.
- [117] (a) García-Melchor, M.; Bellarosa, L.; López, N. *ACS Catal.* **2014**, *4*, 4015–4020. (b) García-Melchor, M.; Bellarosa, L.; López, N. *ACS Catal.* **2015**, *5*, 1525.
- [118] Kruppe, C. M.; Krooswyk, J. D.; Trenary, M. *ACS Catal.* **2017**, *7*, 8042–8049.
- [119] Riley, C.; Zhou, S.; Kunwar, D.; De La Riva, A.; Peterson, E.; Payne, R.; Gao, L.; Lin, S.; Guo, H.; Datye, A. *J. Am. Chem. Soc.* **2018**, *140*, 12964–12973.
- [120] Primo, A.; Neatu, F.; Florea, M.; Parvulescu, V.; Garcia, H. *Nat. Commun.* **2014**, *5*, 5291.
- [121] Bełtowska-Brzezinska, M.; Łuczak, T.; Mączka, M.; Baltruschat, H.; Müller, U. *J. Electroanal. Chem.* **2002**, *519*, 101–110.
- [122] Li, B.; Ge, H. *Sci. Adv.* **2019**, *5*, eaaw2774.
- [123] Shi, R.; Wang, Z.; Zhao, Y.; Waterhouse, G. I. N.; Li, Z.; Zhang, B.; Sun, Z.; Xia, C.; Wang, H.; Zhang, T. *Nat. Catal.* **2021**, *4*, 565–574.
- [124] Bu, J.; Liu, Z.; Ma, W.; Zhang, L.; Wang, T.; Zhang, H.; Zhang, Q.; Feng, X.; Zhang, J. *Nat. Catal.* **2021**, *4*, 557–564.
- [125] Yang, B.; Gong, X.-Q.; Wang, H.-F.; Cao, X.-M.; Rooney, J. J.; Hu, P. *J. Am. Chem. Soc.* **2013**, *135*, 15244–15250.
- [126] Vilé, G.; Baudouin, D.; Remediakis, I. N.; Copéret, C.; López, N.; Pérez-Ramírez, J. *ChemCatChem* **2013**, *5*, 3750–3759.
- [127] Vignola, E.; Steinmann, S. N.; Al Farra, A.; Vandegheuchte, B. D.; Curulla, D.; Sautet, P. *ACS Catal.* **2018**, *8*, 1662–1671.
- [128] Dong, Y.; Ebrahimi, M.; Tillekaratne, A.; Simonovis, J. P.; Zaera, F. *Phys. Chem. Chem. Phys.* **2016**, *18*, 19248–19258.
- [129] Hartree, D. R. *Math. Proc. Camb. Philos. Soc.* **1928**, *24*, 111–132.
- [130] Contreras-García, J.; Johnson, E. R.; Keinan, S.; Chaudret, R.; Piquemal, J.-P.; Beratan, D. N.; Yang, W. *J. Chem. Theory Comput.* **2011**, *7*, 625–632.
- [131] Roothaan, C. C. J. *Rev. Mod. Phys.* **1951**, *23*, 69–89.
- [132] Thomas, L. H. *Math. Proc. Camb. Philos. Soc.* **1927**, *23*, 542–548.
- [133] Contreras-García, J.; Boto, R. A.; Izquierdo-Ruiz, F.; Reva, I.; Woller, T.; Alonso, M. *Theor. Chem. Acc.* **2016**, *135*, 242.
- [134] (a) Perdew, J. P.; Burke, K.; Ernzerhof, M. *Phys. Rev. Lett.* **1996**, *77*, 3865–3868. (b) Perdew, J. P.; Burke, K.; Ernzerhof, M. *Phys. Rev. Lett.* **1997**, *78*, 1396.
- [135] Perdew, J. P.; Ziesche, P.; Eschrig, H. *Electronic structure of solids '91*; Akademie Verlag, Berlin, 1991.
- [136] Becke, A. D. *Phys. Rev. A* **1988**, *38*, 3098–3100.
- [137] Lee, C.; Yang, W.; Parr, R. G. *Phys. Rev. B* **1988**, *37*, 785–789.
- [138] Chai, J.-D.; Head-Gordon, M. *Phys. Chem. Chem. Phys.* **2008**, *10*, 6615–6620.
- [139] Chai, J.-D.; Head-Gordon, M. *J. Chem. Phys.* **2008**, *128*, 084106.
- [140] Becke, A. D. *J. Chem. Phys.* **1997**, *107*, 8554–8560.
- [141] Behan, J. A.; Hoque, Md. K.; Stamatina, S. N.; Perova, T. S.; Vilella-Arribas, L.; García-Melchor, M.; Colavita, P. E. *J. Phys. Chem. C* **2018**, *122*, 20763–20773.
- [142] Peñas-Defrutos, M. N.; Bartolomé, C.; García-Melchor, M.; Espinet, P. *Chem. Commun.* **2018**, *54*, 984–987.
- [143] Hermann, C. Z. *Für Krist. – Cryst. Mater.* **1928**, *68*, 257–287.
- [144] Hermann, C. Z. *Für Krist. – Cryst. Mater.* **1931**, *76*, 559–561.

- [145] Bragg, W. H.; Bragg, W. L. *Proc. R. Soc. Lond. A* **1913**, *88*, 428–438.
- [146] Ewald, P. P. *Acta Cryst. A* **1969**, *A25*, 103–108.
- [147] Ashcroft, N. W.; Mermin, N. D. *Solid State Physics*; Holt, Rinehart and Winston: New York, 1976.
- [148] Hasan, M. Z.; Kane, C. L. *Rev. Mod. Phys.* **2010**, *82*, 3045–3067.
- [149] Blöchl, P. E. *Phys. Rev. B* **1994**, *50*, 17953–17979.
- [150] Grimme, S. *WIREs Comput. Mol. Sci.* **2011**, *1*, 211–228.
- [151] Grimme, S. *J. Comput. Chem.* **2006**, *27*, 1787–1799.
- [152] Grimme, S.; Antony, J.; Ehrlich, S.; Krieg, H. *J. Chem. Phys.* **2010**, *132*, 154104.
- [153] Caldeweyher, E.; Ehlert, S.; Hansen, A.; Neugebauer, H.; Spicher, S.; Bannwarth, C.; Grimme, S. *J. Chem. Phys.* **2019**, *150*, 154122.
- [154] Warshel, A.; Levitt, M. *J. Mol. Biol.* **1976**, *103*, 227–249.
- [155] Ogasawara, H.; Brena, B.; Nordlund, D.; Nyberg, M.; Pelmenchikov, A.; Pettersson, L. G. M.; Nilsson, A. *Phys. Rev. Lett.* **2002**, *89*, 276102.
- [156] Hansen, H. A.; Rossmeisl, J.; Nørskov, J. K. *Phys. Chem. Chem. Phys.* **2008**, *10*, 3722–3730.
- [157] Kastlunger, G.; Lindgren, P.; Peterson, A. A. *J. Phys. Chem. C* **2018**, *122*, 12771–12781.
- [158] Chen, L. D.; Bajdich, M.; Martirez, J. M. P.; Krauter, C. M.; Gauthier, J. A.; Carter, E. A.; Luntz, A. C.; Chan, K.; Nørskov, J. K. *Nat. Commun.* **2018**, *9*, 3202.
- [159] Marenich, A. V.; Cramer, C. J.; Truhlar, D. G. *J. Phys. Chem. B* **2009**, *113*, 6378–6396.
- [160] Mennucci, B. *WIREs Comput. Mol. Sci.* **2012**, *2*, 386–404.
- [161] Miertuš, S.; Scrocco, E.; Tomasi, J. *Chem. Phys.* **1981**, *55*, 117–129.
- [162] Alfonso, D. R.; Tafen, D. N.; Kauffmann, D. R. *Catalysts* **2018**, *8*, 424.
- [163] Jerkiewicz, G. *ACS Catal.* **2020**, *10*, 8409–8417.
- [164] Debye, P. *Math. Ann.* **1909**, *67*, 535–558.
- [165] Hestenes, M. R.; Stiefel, E. *J. Res. Natl. Bur. Stand.* **1952**, *49*, 409–436.
- [166] Verbeke, J.; Cools, R. *Int. J. Math. Educ. Sci. Technol.* **1995**, *26*, 177–193.
- [167] Powell, M. J. D. Variable Metric Methods for Constrained Optimization. In *Mathematical Programming The State of the Art*; Bachem, A., Korte, B., Grötschel, M., Eds.; Springer Berlin Heidelberg: Berlin, Heidelberg, 1983; pp 288–311.
- [168] Halgren, T. A.; Lipscomb, W. N. *Chem. Phys. Lett.* **1977**, *49*, 225–232.
- [169] Elber, R.; Karplus, M. *Chem. Phys. Lett.* **1987**, *139*, 375–380.
- [170] Mills, G.; Jónsson, H. *Phys. Rev. Lett.* **1994**, *72*, 1124–1127.
- [171] Jónsson, H.; Mills, G.; Jacobsen, K. W. Nudged Elastic Band Method for Finding Minimum Energy Paths of Transitions. In *Classical and Quantum Dynamics in Condensed Phase Simulations*; WORLD SCIENTIFIC: LERICI, Villa Marigola, 1998; pp 385–404.
- [172] Henkelman, G.; Uberuaga, B. P.; Jónsson, H. *J. Chem. Phys.* **2000**, *113*, 9901–9904.
- [173] Murnaghan, F. D. *Proc. Natl. Acad. Sci.* **1944**, *30*, 244–247.
- [174] Birch, F. *Phys. Rev.* **1947**, *71*, 809–824.
- [175] Gibbs, J. W. *Trans. Conn. Acad. Arts Sci.* **1874**, *3*, 343–524.
- [176] Wulff, G. *Z. Für Kryst. Mineral.* **1901**, *34*, 449–530.
- [177] Barmparis, G. D.; Lodziana, Z.; Lopez, N.; Remediakis, I. N. *Beilstein J. Nanotechnol.* **2015**, *6*, 361–368.
- [178] Rahm, J. M.; Erhart, P. *J. Open Source Softw.* **2020**, *5*, 1944.
- [179] Ong, S. P.; Richards, W. D.; Jain, A.; Hautier, G.; Kocher, M.; Cholia, S.; Gunter, D.; Chevrier, V. L.; Persson, K. A.; Ceder, G. *Comput. Mater. Sci.* **2013**, *68*, 314–319.
- [180] Montoya, J. H.; Persson, K. A. *Npj Comput. Mater.* **2017**, *3*, 14.
- [181] Warshay, M.; Prokopius, P. R. *J. Power Sources* **1990**, *29*, 193–200.
- [182] Nie, Y.; Li, L.; Wei, Z. *Chem. Soc. Rev.* **2015**, *44*, 2168–2201.
- [183] Greeley, J.; Stephens, I. E. L.; Bondarenko, A. S.; Johansson, T. P.; Hansen, H. A.; Jaramillo, T. F.; Rossmeisl, J.; Chorkendorff, I.; Nørskov, J. K. *Nat. Chem.* **2009**, *1*, 552–556.
- [184] Escudero-Escribano, M.; Malacrida, P.; Hansen, M. H.; Vej-Hansen, U. G.; Velazquez-Palenzuela, A.; Tripkovic, V.; Schiotz, J.; Rossmeisl, J.; Stephens, I. E. L.; Chorkendorff, I. *Science* **2016**, *352*, 73–76.
- [185] Lim, B.; Jiang, M.; Camargo, P. H. C.; Cho, E. C.; Tao, J.; Lu, X.; Zhu, Y.; Xia, Y. *Science* **2009**, *324*, 1302–1305.

- [186] Li, Y.; Tong, Y.; Peng, F. *J. Energy Chem.* **2020**, *48*, 308–321.
- [187] Zhou, Y.; Chen, G.; Zhang, J. *J. Mater. Chem. A* **2020**, *8*, 20849–20869.
- [188] Gong, K.; Du, F.; Xia, Z.; Durstock, M.; Dai, L. *Science* **2009**, *323*, 760–764.
- [189] Qu, L.; Liu, Y.; Baek, J.-B.; Dai, L. *ACS Nano* **2010**, *4*, 1321–1326.
- [190] Wang, X.; Lee, J. S.; Zhu, Q.; Liu, J.; Wang, Y.; Dai, S. *Chem. Mater.* **2010**, *22*, 2178–2180.
- [191] Yu, L.; Pan, X.; Cao, X.; Hu, P.; Bao, X. *J. Catal.* **2011**, *282*, 183–190.
- [192] Kim, H. W.; Bukas, V. J.; Park, H.; Park, S.; Diederichsen, K. M.; Lim, J.; Cho, Y. H.; Kim, J.; Kim, W.; Han, T. H.; Voss, J.; Luntz, A. C.; McCloskey, B. D. *ACS Catal.* **2020**, *10*, 852–863.
- [193] Zhang, L.; Xia, Z. *J. Phys. Chem. C* **2011**, *115*, 11170–11176.
- [194] Kim, H.; Lee, K.; Woo, S. I.; Jung, Y. *Phys. Chem. Chem. Phys.* **2011**, *13*, 17505.
- [195] Studt, F. *Catal. Lett.* **2013**, *143*, 58–60.
- [196] Ning, X.; Li, Y.; Ming, J.; Wang, Q.; Wang, H.; Cao, Y.; Peng, F.; Yang, Y.; Yu, H. *Chem. Sci.* **2019**, *10*, 1589–1596.
- [197] Faisal, S. N.; Haque, E.; Noorbehesht, N.; Zhang, W.; Harris, A. T.; Church, T. L.; Minett, A. I. *RSC Adv.* **2017**, *7*, 17950–17958.
- [198] Behan, J. A.; Iannaci, A.; Domínguez, C.; Stamatina, S. N.; Hoque, Md. K.; Vasconcelos, J. M.; Perova, T. S.; Colavita, P. E. *Carbon* **2019**, *148*, 224–230.
- [199] Lai, L.; Potts, J. R.; Zhan, D.; Wang, L.; Poh, C. K.; Tang, C.; Gong, H.; Shen, Z.; Lin, J.; Ruoff, R. S. *Energy Environ. Sci.* **2012**, *5*, 7936–7942.
- [200] Gaussian 09, Revision E.01, M. J. Frisch, G. W. Trucks, H. B. Schlegel, G. E. Scuseria, M. A. Robb, J. R. Cheeseman, G. Scalmani, V. Barone, G. A. Petersson, H. Nakatsuji, X. Li, M. Caricato, A. Marenich, J. Bloino, B. G. Janesko, R. Gomperts, B. Mennucci, H. P. Hratchian, J. V. Ortiz, A. F. Izmaylov, J. L. Sonnenberg, D. Williams-Young, F. Ding, F. Lipparini, F. Egidi, J. Goings, B. Peng, A. Petrone, T. Henderson, D. Ranasinghe, V. G. Zakrzewski, J. Gao, N. Rega, G. Zheng, W. Liang, M. Hada, M. Ehara, K. Toyota, R. Fukuda, J. Hasegawa, M. Ishida, T. Nakajima, Y. Honda, O. Kitao, H. Nakai, T. Vreven, K. Throssell, J. A. Montgomery, Jr., J. E. Peralta, F. Ogliaro, M. Bearpark, J. J. Heyd, E. Brothers, K. N. Kudin, V. N. Staroverov, T. Keith, R. Kobayashi, J. Normand, K. Raghavachari, A. Rendell, J. C. Burant, S. S. Iyengar, J. Tomasi, M. Cossi, J. M. Millam, M. Klene, C. Adamo, R. Cammi, J. W. Ochterski, R. L. Martin, K. Morokuma, O. Farkas, J. B. Foresman, and D. J. Fox, Gaussian, Inc., Wallingford CT, 2016.
- [201] Kelly, C. P.; Cramer, C. J.; Truhlar, D. G. *J. Phys. Chem. B* **2007**, *111*, 408–422.
- [202] Ramaswamy, N.; Mukerjee, S. *Adv. Phys. Chem.* **2012**, *2012*, 491604.
- [203] Lai, Q.; Zheng, J.; Tang, Z.; Bi, D.; Zhao, J.; Liang, Y. *Angew. Chem. Int. Ed.* **2020**, *59*, 11999–12006.
- [204] Tai, S.-H.; Chang, B. K. *RSC Adv.* **2019**, *9*, 6035–6041.
- [205] Hung, C.-T.; Yu, N.; Chen, C.-T.; Wu, P.-H.; Han, X.; Kao, Y.-S.; Liu, T.-C.; Chu, Y.; Deng, F.; Zheng, A.; Liu, S.-B. *J. Mater. Chem. A* **2014**, *2*, 20030–20037.
- [206] Wu, H.-L.; Li, X.-B.; Tung, C.-H.; Wu, L.-Z. *Adv. Mater.* **2019**, *31*, 1900709.
- [207] Kuznetsova, V. A.; Mates-Torres, E.; Prochukhan, N.; Marcastel, M.; Purcell-Milton, F.; O'Brien, J.; Visheratina, A. K.; Martinez-Carmona, M.; Gromova, Y.; Garcia-Melchor, M.; Gun'ko, Y. K. *ACS Nano* **2019**, *13*, 13560–13572.
- [208] Wang, C.; Thompson, R. L.; Baltrus, J.; Matraga, C. *J. Phys. Chem. Lett.* **2010**, *1*, 48–53.
- [209] Wang, J.; Xia, T.; Wang, L.; Zheng, X.; Qi, Z.; Gao, C.; Zhu, J.; Li, Z.; Xu, H.; Xiong, Y. *Angew. Chem. Int. Ed.* **2018**, *57*, 16447–16451.
- [210] Kuehnel, M. F.; Orchard, K. L.; Dalle, K. E.; Reisner, E. *J. Am. Chem. Soc.* **2017**, *139*, 7217–7223.
- [211] Zhou, R.; Guzman, M. I. *J. Phys. Chem. C* **2014**, *118*, 11649–11656.
- [212] Froehlich, J. D.; Kubiak, C. P. *Inorg. Chem.* **2012**, *51*, 3932–3934.
- [213] Kuehnel, M. F.; Sahn, C. D.; Neri, G.; Lee, J. R.; Orchard, K. L.; Cowan, A. J.; Reisner, E. *Chem. Sci.* **2018**, *9*, 2501–2509.
- [214] Lim, H.-K.; Kwon, Y.; Kim, H. S.; Jeon, J.; Kim, Y.-H.; Lim, J.-A.; Kim, B.-S.; Choi, J.; Kim, H. *ACS Catal.* **2018**, *8*, 2420–2427.
- [215] Umireddi, A. K.; Sharma, S. K.; Pala, R. G. S. *Catal. Sci. Technol.* **2022**, Advance article. DOI: 10.1039/D1CY01584B.
- [216] Lin, J.; Ding, Z.; Hou, Y.; Wang, X. *Sci. Rep.* **2013**, *3*, 1056.

- [217] Yang, D.; Zhu, Q.; Han, B. *The Innovation* **2020**, *1*, 100016.
- [218] Rosen, B. A.; Salehi-Khojin, A.; Thorson, M. R.; Zhu, W.; Whipple, D. T.; Kenis, P. J. A.; Masel, R. I. *Science* **2011**, *334*, 643–644.
- [219] Sun, L.; Ramesha, G. K.; Kamat, P. V.; Brennecke, J. F. *Langmuir* **2014**, *30*, 6302–6308.
- [220] Kemna, A.; García Rey, N.; Braunschweig, B. *ACS Catal.* **2019**, *9*, 6284–6292.
- [221] Wang, Y.; Hatakeyama, M.; Ogata, K.; Wakabayashi, M.; Jin, F.; Nakamura, S. *Phys. Chem. Chem. Phys.* **2015**, *17*, 23521–23531.
- [222] García Rey, N.; Dlott, D. D. *Phys. Chem. Chem. Phys.* **2017**, *19*, 10491–10501.
- [223] Kresse, G.; Furthmüller, J. *Phys. Rev. B* **1996**, *54*, 11169–11186.
- [224] Kresse, G.; Furthmüller, J. *Comput. Mater. Sci.* **1996**, *6*, 15–50.
- [225] Jain, A.; Ong, S. P.; Hautier, G.; Chen, W.; Richards, W. D.; Dacek, S.; Cholia, S.; Gunter, D.; Skinner, D.; Ceder, G.; Persson, K. A. *APL Mater.* **2013**, *1*, 011002.
- [226] Hjorth Larsen, A.; Jørgen Mortensen, J.; Blomqvist, J.; Castelli, I. E.; Christensen, R.; Dulak, M.; Friis, J.; Groves, M. N.; Hammer, B.; Hargus, C.; Hermes, E. D.; Jennings, P. C.; Bjerre Jensen, P.; Kermode, J.; Kitchin, J. R.; Leonhard Kolsbjerg, E.; Kubal, J.; Kaasbjerg, K.; Lysgaard, S.; Bergmann Maronsson, J.; Maxson, T.; Olsen, T.; Pastewka, L.; Peterson, A.; Rostgaard, C.; Schiøtz, J.; Schütt, O.; Strange, M.; Thygesen, K. S.; Vegge, T.; Vilhelmsen, L.; Walter, M.; Zeng, Z.; Jacobsen, K. W. *J. Phys.: Condens. Matter* **2017**, *29*, 273002.
- [227] Ehlers, A. W.; Böhme, M.; Dapprich, S.; Gobbi, A.; Höllwarth, A.; Jonas, V.; Köhler, K. F.; Stegmann, R.; Veldkamp, A.; Frenking, G. *Chem. Phys. Lett.* **1993**, *208*, 111–114.
- [228] Otero-de-la-Roza, A.; Johnson, E. R.; Luaña, V. *Comput. Phys. Commun.* **2014**, *185*, 1007–1018.
- [229] (a) Shahzad, K.; Olego, D. J.; Van de Walle, C. G. *Phys. Rev. B* **1988**, *38*, 1417–1426. (b) Shahzad, K.; Olego, D. J.; Van de Walle, C. G. *Phys. Rev. B* **1991**, *43*, 1830.
- [230] Barnard, A. S.; Feigl, C. A.; Russo, S. P. *Nanoscale* **2010**, *2*, 2294–2301.
- [231] Liu, H.; Wang, H.; Jing, Z.; Wu, K.; Cheng, Y.; Xiao, B. *J. Phys. Chem. C* **2020**, *124*, 25769–25774.
- [232] Ludwig, T.; Singh, A. R.; Nørskov, J. K. *J. Phys. Chem. C* **2021**, *125*, 21943–21957.
- [233] Sandberg, R. B.; Montoya, J. H.; Chan, K.; Nørskov, J. K. *Surf. Sci.* **2016**, *654*, 56–62.
- [234] Kang, Y.; Li, Z.; Lv, X.; Song, W.; Wei, Y.; Zhang, X.; Liu, J.; Zhao, Z. *J. Catal.* **2021**, *393*, 20–29.
- [235] Fredrickson, K. D.; Anasori, B.; Seh, Z. W.; Gogotsi, Y.; Vojvodic, A. *J. Phys. Chem. C* **2016**, *120*, 28432–28440.
- [236] Ulissi, Z. W.; Singh, A. R.; Tsai, C.; Nørskov, J. K. *J. Phys. Chem. Lett.* **2016**, *7*, 3931–3935.
- [237] Anasori, B.; Lukatskaya, M. R.; Gogotsi, Y. *Nat. Rev. Mater.* **2017**, *2*, 16098.
- [238] Deysher, G.; Shuck, C. E.; Hantanasirisakul, K.; Frey, N. C.; Foucher, A. C.; Maleski, K.; Sarycheva, A.; Shenoy, V. B.; Stach, E. A.; Anasori, B.; Gogotsi, Y. *ACS Nano* **2020**, *14*, 204–217.
- [239] Kumar, K. S.; Choudhary, N.; Jung, Y.; Thomas, J. *ACS Energy Lett.* **2018**, *3*, 482–495.
- [240] Sarycheva, A.; Polemi, A.; Liu, Y.; Dandekar, K.; Anasori, B.; Gogotsi, Y. *Sci. Adv.* **2018**, *4*, eaau0920.
- [241] Seh, Z. W.; Fredrickson, K. D.; Anasori, B.; Kibsgaard, J.; Strickler, A. L.; Lukatskaya, M. R.; Gogotsi, Y.; Jaramillo, T. F.; Vojvodic, A. *ACS Energy Lett.* **2016**, *1*, 589–594.
- [242] Gao, Y.; Cao, Y.; Zhuo, H.; Sun, X.; Gu, Y.; Zhuang, G.; Deng, S.; Zhong, X.; Wei, Z.; Li, X.; Wang, J. *Catal. Today* **2020**, *339*, 120–126.
- [243] Cheng, C.; Zhang, X.; Wang, M.; Wang, S.; Yang, Z. *Phys. Chem. Chem. Phys.* **2018**, *20*, 3504–3513.
- [244] Gao, G.; O’Mullane, A. P.; Du, A. *ACS Catal.* **2017**, *7*, 494–500.
- [245] Handoko, A. D.; Fredrickson, K. D.; Anasori, B.; Convey, K. W.; Johnson, L. R.; Gogotsi, Y.; Vojvodic, A.; Seh, Z. W. *ACS Appl. Energy Mater.* **2018**, *1*, 173–180.
- [246] Kamysbayev, V.; Filatov, A. S.; Hu, H.; Rui, X.; Lagunas, F.; Wang, D.; Klie, R. F.; Talapin, D. V. *Science* **2020**, *369*, 979–983.
- [247] Rajan, A. C.; Mishra, A.; Satsangi, S.; Vaish, R.; Mizuseki, H.; Lee, K.-R.; Singh, A. K. *Chem. Mater.* **2018**, *30*, 4031–4038.
- [248] Ashton, M.; Mathew, K.; Hennig, R. G.; Sinnott, S. B. *J. Phys. Chem. C* **2016**, *120*, 3550–3556.
- [249] Khazaei, M.; Ranjbar, A.; Arai, M.; Sasaki, T.; Yunoki, S. *J. Mater. Chem. C* **2017**, *5*, 2488–2503.
- [250] Champagne, A.; Charlier, J.-C. *J. Phys. Mater.* **2020**, *3*, 032006.

- [251] Jin, D.; Johnson, L. R.; Raman, A. S.; Ming, X.; Gao, Y.; Du, F.; Wei, Y.; Chen, G.; Vojvodic, A.; Gogotsi, Y.; Meng, X. *J. Phys. Chem. C* **2020**, *124*, 10584–10592.
- [252] Naguib, M.; Kurtoglu, M.; Presser, V.; Lu, J.; Niu, J.; Heon, M.; Hultman, L.; Gogotsi, Y.; Barsoum, M. W. *Adv. Mater.* **2011**, *23*, 4248–4253.
- [253] Ponce-Pérez, R.; Gutierrez-Ojeda, S. J.; Guerrero-Sánchez, J.; Moreno-Armenta, M. G. *Sci. Rep.* **2021**, *11*, 12393.
- [254] Naguib, M.; Mashtalir, O.; Carle, J.; Presser, V.; Lu, J.; Hultman, L.; Gogotsi, Y.; Barsoum, M. W. *ACS Nano* **2012**, *6*, 1322–1331.
- [255] Naguib, M.; Halim, J.; Lu, J.; Cook, K. M.; Hultman, L.; Gogotsi, Y.; Barsoum, M. W. *J. Am. Chem. Soc.* **2013**, *135*, 15966–15969.
- [256] Abdelmalak, M. N. *PhD Thesis – MXenes: A New Family of Two-Dimensional Materials and Its Application as Electrodes for Li-Ion Batteries*; Drexel University, 2014.
- [257] Ghidui, M.; Naguib, M.; Shi, C.; Mashtalir, O.; Pan, L. M.; Zhang, B.; Yang, J.; Gogotsi, Y.; Billinge, S. J. L.; Barsoum, M. W. *Chem. Commun.* **2014**, *50*, 9517–9520.
- [258] Anasori, B.; Xie, Y.; Beidaghi, M.; Lu, J.; Hosler, B. C.; Hultman, L.; Kent, P. R. C.; Gogotsi, Y.; Barsoum, M. W. *ACS Nano* **2015**, *9*, 9507–9516.
- [259] Meshkian, R.; Näslund, L.-Å.; Halim, J.; Lu, J.; Barsoum, M. W.; Rosen, J. *Scr. Mater.* **2015**, *108*, 147–150.
- [260] Urbankowski, P.; Anasori, B.; Makaryan, T.; Er, D.; Kota, S.; Walsh, P. L.; Zhao, M.; Shenoy, V. B.; Barsoum, M. W.; Gogotsi, Y. *Nanoscale* **2016**, *8*, 11385–11391.
- [261] Yang, J.; Naguib, M.; Ghidui, M.; Pan, L.; Gu, J.; Nanda, J.; Halim, J.; Gogotsi, Y.; Barsoum, M. W. *J. Am. Ceram. Soc.* **2016**, *99*, 660–666.
- [262] Zhou, J.; Zha, X.; Chen, F. Y.; Ye, Q.; Eklund, P.; Du, S.; Huang, Q. *Angew. Chem. Int. Ed.* **2016**, *55*, 5008–5013.
- [263] Meshkian, R.; Tao, Q.; Dahlqvist, M.; Lu, J.; Hultman, L.; Rosen, J. *Acta Mater.* **2017**, *125*, 476–480.
- [264] Soundiraraju, B.; George, B. K. *ACS Nano* **2017**, *11*, 8892–8900.
- [265] Tao, Q.; Dahlqvist, M.; Lu, J.; Kota, S.; Meshkian, R.; Halim, J.; Palisaitis, J.; Hultman, L.; Barsoum, M. W.; Persson, P. O. Å.; Rosen, J. *Nat. Commun.* **2017**, *8*, 14949.
- [266] Urbankowski, P.; Anasori, B.; Hantanasirisakul, K.; Yang, L.; Zhang, L.; Haines, B.; May, S. J.; Billinge, S. J. L.; Gogotsi, Y. *Nanoscale* **2017**, *9*, 17722–17730.
- [267] Zhou, J.; Gao, S.; Guo, Z.; Sun, Z. *Ceram. Int.* **2017**, *43*, 11450–11454.
- [268] Zhou, J.; Zha, X.; Zhou, X.; Chen, F.; Gao, G.; Wang, S.; Shen, C.; Chen, T.; Zhi, C.; Eklund, P.; Du, S.; Xue, J.; Shi, W.; Chai, Z.; Huang, Q. *ACS Nano* **2017**, *11*, 3841–3850.
- [269] Halim, J.; Palisaitis, J.; Lu, J.; Thörnberg, J.; Moon, E. J.; Precner, M.; Eklund, P.; Persson, P. O. Å.; Barsoum, M. W.; Rosen, J. *ACS Appl. Nano Mater.* **2018**, *1*, 2455–2460.
- [270] Meshkian, R.; Dahlqvist, M.; Lu, J.; Wickman, B.; Halim, J.; Thörnberg, J.; Tao, Q.; Li, S.; Intikhab, S.; Snyder, J.; Barsoum, M. W.; Yildizhan, M.; Palisaitis, J.; Hultman, L.; Persson, P. O. Å.; Rosen, J. *Adv. Mater.* **2018**, *30*, 1706409.
- [271] Persson, I.; el Ghazaly, A.; Tao, Q.; Halim, J.; Kota, S.; Darakchieva, V.; Palisaitis, J.; Barsoum, M. W.; Rosen, J.; Persson, P. O. Å. *Small* **2018**, *14*, 1703676.
- [272] Tran, M. H.; Schäfer, T.; Shahraei, A.; Dürrschnabel, M.; Molina-Luna, L.; Kramm, U. I.; Birkel, C. S. *ACS Appl. Energy Mater.* **2018**, *1*, 3908–3914.
- [273] Persson, K. A.; Waldwick, B.; Lazic, P.; Ceder, G. *Phys. Rev. B* **2012**, *85*, 235438.
- [274] Singh, A. K.; Zhou, L.; Shinde, A.; Suram, S. K.; Montoya, J. H.; Winston, D.; Gregoire, J. M.; Persson, K. A. *Chem. Mater.* **2017**, *29*, 10159–10167.
- [275] Patel, A. M.; Nørskov, J. K.; Persson, K. A.; Montoya, J. H. *Phys. Chem. Chem. Phys.* **2019**, *21*, 25323–25327.
- [276] Zhang, C. J.; Pinilla, S.; McEvoy, N.; Cullen, C. P.; Anasori, B.; Long, E.; Park, S.-H.; Seral-Ascaso, A.; Shmeliov, A.; Krishnan, D.; Morant, C.; Liu, X.; Duesberg, G. S.; Gogotsi, Y.; Nicolosi, V. *Chem. Mater.* **2017**, *29*, 4848–4856.
- [277] Persson, I.; Halim, J.; Hansen, T. W.; Wagner, J. B.; Darakchieva, V.; Palisaitis, J.; Rosen, J.; Persson, P. O. Å. *Adv. Funct. Mater.* **2020**, *30*, 1909005.

- [278] Huang, S.; Mochalin, V. N. *ACS Nano* **2020**, *14*, 110251–10257.
- [279] Mathis, T. S.; Maleski, K.; Goad, A.; Sarycheva, A.; Anayee, M.; Foucher, A. C.; Hantanasirisakul, K.; Shuck, C. E.; Stach, E. A.; Gogotsi, Y. *ACS Nano* **2021**, *15*, 6420–6429.
- [280] Hieu, V. Q.; Phung, T. K.; Nguyen, T.-Q.; Khan, A.; Doan, V. D.; Tran, V. A.; Le, V. T. *Chemosphere* **2021**, *276*, 130154.
- [281] Xie, Y.; Kent, P. R. C. *Phys. Rev. B* **2013**, *87*, 235441.
- [282] Park, S.; Park, J.; Abroshan, H.; Zhang, L.; Kim, J. K.; Zhang, J.; Guo, J.; Siahrostami, S.; Zheng, X. *ACS Energy Lett.* **2018**, *3*, 2685–2693.
- [283] Zubair, M.; Ul Hassan, M. M.; Mehran, M. T.; Baig, M. M.; Hussain, S.; Shahzad, F. *Int. J. Hydrog. Energy* **2022**, *47*, 2794–2818.
- [284] Diao, J.; Hu, M.; Lian, Z.; Li, Z.; Zhang, H.; Huang, F.; Li, B.; Wang, X.; Su, D. S.; Liu, H. *ACS Catal.* **2018**, *8*, 10051–10057.
- [285] Niu, K.; Chi, L.; Rosen, J.; Björk, J. *Phys. Chem. Chem. Phys.* **2020**, *22*, 18622–18630.
- [286] Torres, D.; Lopez, N.; Illas, F. *J. Catal.* **2006**, *243*, 404–409.
- [287] Copéret, C.; Estes, D. P.; Larmier, K.; Searles, K. *Chem. Rev.* **2016**, *116*, 8463–8505.
- [288] Jimenez-Orozco, C.; Flórez, E.; Viñes, F.; Rodriguez, J. A.; Illas, F. *ACS Catal.* **2020**, *10*, 6213–6222.
- [289] Mathew, K.; Sundararaman, R.; Letchworth-Weaver, K.; Arias, T. A.; Hennig, R. G. *J. Chem. Phys.* **2014**, *140*, 084106.
- [290] Shi, Z.; Li, N.; Lu, H.-K.; Chen, X.; Zheng, H.; Yuan, Y.; Ye, K.-Y. *Curr. Opin. Electrochem.* **2021**, *28*, 100713.
- [291] Naguib, M.; Tang, W.; Browning, K. L.; Veith, G. M.; Maliekkal, V.; Neurock, M.; Villa, A. *ChemCatChem* **2020**, *12*, 5733–5742.
- [292] Tang, W.; Sanville, E.; Henkelman, G. *J. Phys.: Condens. Matter* **2009**, *21*, 084204.

Appendix

Band diagrams of bare and covered *o*-MXenes

In the following, the band diagrams of all synthesized *o*-MXenes in their bare configuration, and with 1 ML of H, OH and O are shown. This depicts the metallic nature of all investigated terminated MXenes at different electrochemical conditions, except for the semiconductor O-covered Ti_2C .

